Development of a biomimetic multitube system for the study of ADPKD

Sarah Myram

▶ **To cite this version:**

Sarah Myram. Development of a biomimetic multitube system for the study of ADPKD. Life Sciences [q-bio]. Sorbonne Universite, 2020. English. NNT : . tel-04643279v1

HAL Id: tel-04643279

https://hal.science/tel-04643279v1

Submitted on 4 Apr 2023 (v1), last revised 10 Jul 2024 (v2)

HAL is a multi-disciplinary open access archive for the deposit and dissemination of scientific research documents, whether they are published or not. The documents may come from teaching and research institutions in France or abroad, or from public or private research centers.

L'archive ouverte pluridisciplinaire **HAL**, est destinée au dépôt et à la diffusion de documents scientifiques de niveau recherche, publiés ou non, émanant des établissements d'enseignement et de recherche français ou étrangers, des laboratoires publics ou privés.

Sorbonne Université

Ecole doctorale « Physiologie, physiopathologie et thérapeutique »

Institut Curie, UMR 168 / Equipes Macromolécules en Biologie et en Médecine (MMBM) et Physico-biologie aux mésoéchelles (PBME)

Développement d'un système multitube biomimétique pour l'étude de l'ADPKD

Par Sarah Myram

Thèse de doctorat de Biophysique

Dirigée par Sylvie Coscoy et Stéphanie Descroix

Présentée et soutenue publiquement le 16 janvier 2020

Devant un jury composé de :

Mme Joëlle SOBCZAK-THEPOT

M Laurent MALAQUIN (Rapporteur)

Mme Sylvie DUFOUR (Rapporteur)

Mme Sophie SAUNIER (Examinateur)

M Marco PONTOGLIO (Examinateur)

Mme Sylvie COSCOY (Directrice de thèse)

Mme Stéphanie DESCROIX (Co-directrice de thèse)

Dédicace

Ackowledgements

Abbreviations

PSP: phenolsuphonephtalein

PCT: Proximal Convoluted Tubule

DCT: Distal Convoluted Tubule

JGA: JuxtaGlomerular Apparatus

GFR: Glomerular Filtration Rate

PCT: Proximal Convoluted Tubular cells

ECM: Extracellular Matrix

ATP: Adenosine TriPhosphate

NO: Nitric Oxid

SNS: Sympathetic Nervous System

ADH: Antidiuretic Hormone

ANP: Natriuretic Hormone

PTH: Parathyroid Hormone

ACE: Angiotensin-Converting Enzyme

PC1: Polycystin 1

PC2: Polycystin 2

ADPKD: Autosomal Dominant Polycystic Kidney Disease

PKD: Polycystic Kidney Disease

ESRD: End Stage Renal Disease

TKV: Total Kidney Volume

UTI: Urinary Tract Infections

PLD: Polycystic Liver Disease

ICA: IntraCranial Aneurysms

TRP: Transient Receptor Potential

ER: Endoplasmic Reticulum

IP3R: Inositol 1, 4, 5-Triphosphate Receptor

pIMCD: primary Inner Medullary Collecting Duct

YAP: Yes-Associated Protein

cAMP: cyclic Adenosine MonoPhosphate

PCP: Planar Cell Polarity

Fjx1: Four-jointed 1

CFTR: Cystic Fibrosis Transmembrane conductance Regulator

V2R: Vasopressin-2 Receptor

ARB: Angiotensin Receptor Blocker

ACEI: Angiotensin Converting Enzyme Inhibitors

KO: Knockout

OOC: Organ-On-Chip

PDMS: polydimethylsiloxane

ADME: Absorption, Distribution, Metabolism, and Excretion

TE: Tissue Engineering

hPTEC: human Proximal Tubule Epithelial Cells

GMEC: Glomerular Microvascular Endothelial Cells

COC: Cyclic Olefin Copolymer

TABLE OF CONTENTS

Introduction:

ADPKD or Autosomal Polycystic Kidney Disease is one of the most frequent inherited nephropathy caused by mutations in *PKD1* or *PKD2* gene encoding the polycystin proteins. Affecting millions of people worldwide, its major hallmarks evolve during a lifetime, becoming noticeable around forty years old [1][2]. This renal disorder is characterized by the formation of numerous fluid-filled cysts extending from adjacent nephrotic tubules, which progressively leads to renal failure in adulthood. Nevertheless, as this disease is often diagnosed lately, the only treatments recommended are dialysis and kidney transplant, the last resort. Therefore, relying on the novel and emerging Organ-on-chip field developed to recapitulate many tissues and organs tri-dimensional architecture in their microenvironment, in addition to their functions, we scrutinized on the kidney-on-chip devices. Significant advances were realized in the fabrication of biologically relevant tissues and organs such as kidneys, as powerful tools to facilitate drug development and personalized-medicine applications [3]. Nonetheless, none of them were designed to specifically reproduce a renal disorder, in particular ADPKD. Therefore, to decipher the mechanisms involved in cystogenesis process during ADPKD evolution and ease drug screening in the near future, we developed an innovative kidney-on-chip platform for this PhD project.

Relating a general overview on the renal physiology discovery and organ-on-chip field emergence, we focused on ADPKD in parallel to the kidney-on-chip domain in this first chapter. Afterwards, we outlined the development of our innovative multitube device to model ADPKD hallmarks, which will be described in the chapter II. First implemented with MDCK cells, a common renal cell line, ADPKD cellular models were then seeded in this microphysiological device. In the chapter III, the behavior of ADPKD cell lines will be characterized on 2D flat surfaces in comparison to their dynamics within 3D tubular scaffold. Eventually, the different improvements of our innovative multitube platform, and the biological assays to further characterize this kidney-on-chip ADPKD modelling will be mentioned in the fourth chapter.

Chapter 1: State of the art

Drawings illustrating the anatomy of the human kidney, from Richard Bright's Report of Medical Cases Longman, drew in 1827, Wellcome Library, London.
On the top, drawing representing kidney texture beneath the outer layer, and on the bottom, sketch of a cross-section showing the internal kidney anatomy.
Source: The British Museum website.

Table of content

1) Kidney, a vital organ

Nephrology is a medical speciality regarding the study of the kidneys: its anatomy, its physiology as well as the diseases associated. This term has been used for the first time at the end of the 20th century, after being referred as "kidney medicine". **Richard Bright** (1789-1858), who gave his name to the Bright's disease that gathers any type of kidney pathologies, is considered as the founder of this speciality [4].

a) Historical discovery of the kidney and its function

Kidneys are part of the urinary system. Present in two copies in the organism, they are reddish bean-shaped organs divided in two parts: the adrenal gland, and the renal capsule (Fig.1A). To better understand the terms used by the first scientists seeking about renal functions, a global overview on kidney anatomy is given. A detailed description of kidney structure will be reported in part I) 1) b) of this chapter.

The **renal capsule** contains the nephrons that are subdivided into two parts: the renal corpuscle and the renal tubules. The **renal corpuscle** is composed of the glomerulus, referred as the Malpighian bodies when it has been discovered, and the Bowman's capsule. It encompasses the glomerular capillaries that join the afferent arteriole upstream, and reunite to form the efferent arteriole downstream. The **renal tubules**, likewise, are surrounded by peritubular capillaries that are the extensions of the efferent arteriole (Fig.1B).

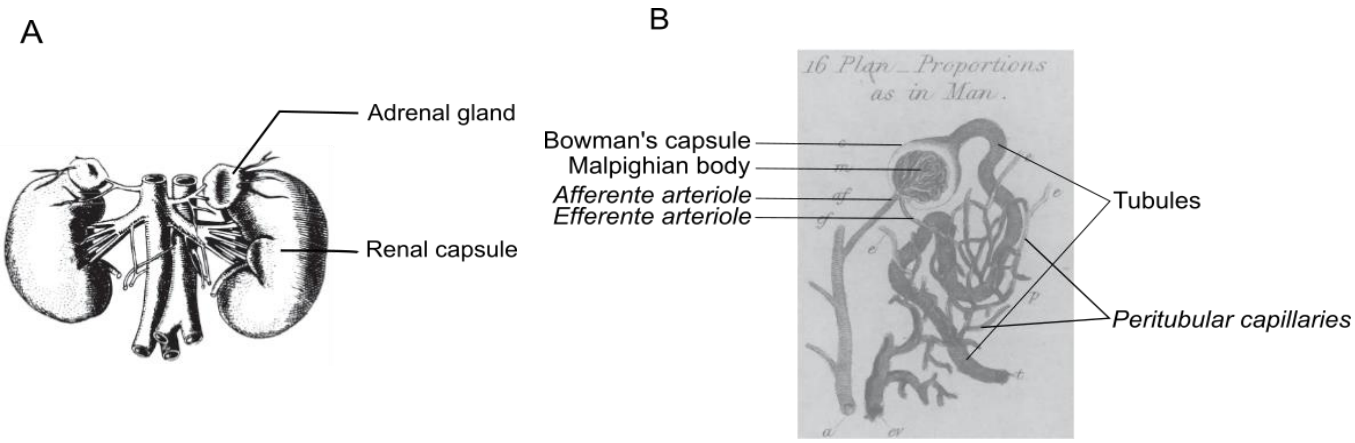

Figure 1: Illustrations of kidney external and internal anatomy from the beginning of renal physiology studies. A: Bartolommeo Eustachio's (1520-1574) depiction of the kidneys and suprarenal glands' external anatomy (from Lancisi's book). B: Illustration of a nephron from the Human kidney. The Bowman's capsule and Malpighian bodies compose the renal corpuscle. The Malpighian bodies constitute the glomerular capillaries link to the afferent and efferent arterioles. The renal corpuscle is followed by tubules surrounded by peritubular capillaries. Schematic adapted from original legends and drawing [2].

Source: [2, 3]

Between 1841 and 1924, scientists focused on kidneys anatomy and urine formation process in order to understand the nature of the body fluids. Everything started with the observations of the morphology of this endocrine and vital organ through a microscope, during the 16th century.

After the emergence of the first microscopes in the Netherlands, an Italian biologist, **Marcello Malpighi**, examined the anatomy of animal and plant tissues. In 1660, he focused on frog internal organs anatomy and deciphered the capillaries of the lung, the link between pulmonary veins and arteries involved in the blood circulation [4]–[7]. Then, in a classic essay "De viscerum structura" published in 1666, he characterized the kidney morphology of different animals and humans by injecting a solution of black fluid and wine within the renal artery. He was the first one to describe the lobular appearance of the kidney surface, interpreting it as the vestige of the lobular structure of the fetal kidney. He could not distinguish the anatomical link

between the glands, which are the renal corpuscles or glomeruli, and the tubules, although he realized that urine and blood were separated in these glomeruli.

This approach was the first one focused on a meticulous observation of the kidney anatomy and functions. Since then, it took 182 years to make a major breakthrough with a controversy on renal anatomy and physiology, more precisely on urine formation steps within specific renal structures [7].

In 1842, a paper relating **William Bowman**'s work precisely depicted the structure of Malpighi's bodies using a microscope ten times more powerful than the one used by Marcello Malpighi (Fig.2). He tracked a solution of potassium bichromate from the glomeruli to the renal artery to determine the path through which the fluids go within the kidneys. What is now called the Bowman's capsule is the extension of the basement membrane of the tubes, within the Malpighi's corpuscles, surrounded by glomerular capillaries and ending with peritubular capillaries around the tubules. Between adjacent capillaries, he observed recurrent anastomoses.

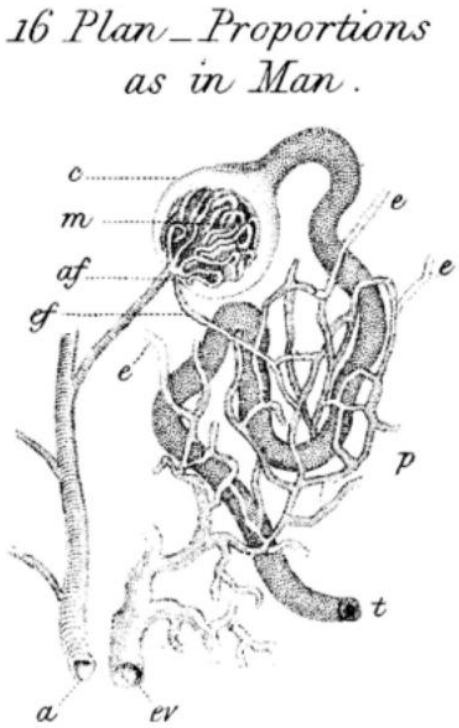

Figure 2: Bowman's drawing representing a man's nephron with the reel proportions (magnification of the Fig.3). a; arterial branch, af: afferent vessel of Malpighian body, e or ef: efferent vessel of Malpighian body, m: Malpighian tuft, p: plexus of the tubes, t: tubes. Sources: [1-4]

He also noticed that one glomerulus is connected to one tubule, and that the tubules gathered with each other to join and form collecting ducts [4]–[7]. According to his accurate observations based on many diverse animal dissections, he hypothesized that only water goes through the glomerulus, which allows urea, uric acid, salts, and other small solutes secreted by the tubules to stay in solution in the kidneys. Thus, assuming that urine formation is due to fluid secretion within the kidneys, Bowman made a significant contribution to the renal physiology understanding [7].

In the meantime, **Carl Friedrich Wilhelm Ludwig**, a German physician and physiologist, also observed and injected several solutions (albumin, dye, ink, etc…) within kidneys of different animals. He ended up with the same conclusion as Bowman on the blood circulation pathway in the kidneys, unaware of Bowman's work. Besides, he focused on urine chemical composition comparing it to serum composition. He found out that urea, sulphate and phosphate are more concentrated in urine than in the serum. He postulated that glomeruli filtrate blood, and tubules reabsorb but do not secrete blood constituents to allow urine formation. Indeed, the filtrate volume of blood is much larger that urine volume excreted: Ludwig concluded that most of the filtrate must be reabsorbed by the renal tubular epithelium. He then performed another important experiment on a semi-permeable membrane between urine and blood to refine his first observations. Applying a pressure, the blood crosses the membrane without the proteins, which suggested that blood was filtered through the small pores of the membrane. Knowing that the blood and urine composition was similar but not at the same concentration, Ludwig deduced that urine derived from blood. He also understood that urine formation begins with a simple physical or mechanical process of filtration, which is an admirable tour de force. Proteins and cells are separated from the blood to form a filtrate with all urine constituents through the capillaries. This mechanism relied on the glomerulus structure and hydrodynamics from which he predicted the hydrostatic pressure and flow profiles in the renal bloodstream (Fig.3). His theory, published between 1842 and 1861, elucidated several observations such as glucose and uric acid presence in the urine when their concentrations is high in the blood, and derived from hemodynamic laws that Bowman neglected. Ludwig and his students bolstered renal innervation role to monitor renal circulation and urine formation. However, they could not demonstrate which drives this mechanism: perfusion pressure or blood flow in the glomeruli and tubules.

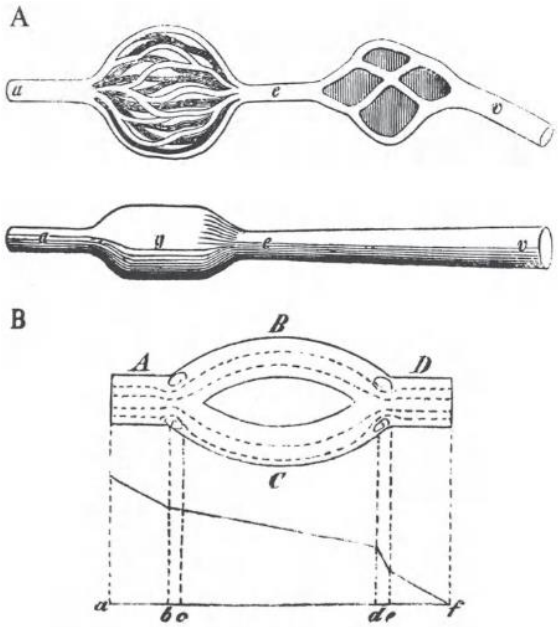

Figure 3: Ludwig's schematics of renal microvasculature and the pressure profile associated. A: On the top, glomerular capillaries (right) with the peritubular capillaries (left). On the bottom, the renal blood vessels relative cross sectional area. a: Afferent arteriole, g: glomerular capillaries, e: efferent arteriole, v: venule. B: Illustration of the pressure profile across the capillary bed. The lowercase letters correspond to the position in the renal vascular bed. A, a: afferent arteriole, b,c: origin of the two glomerular capillaries (B,C), d,e: union of two capillaries to form D, the efferent arteriole and the beginning of the peritubular capillary, f: end of the peritubular capillary network. The line shows a decrease pressure along the nephron.
Source: [3, 4]

So far, two theories were competing: Bowman's theory suggesting that urine formation starts with glomerular secretion and Ludwig's theory claiming that it begins with glomerular filtration followed by tubule reabsorption.

Between 1874 and 1883, another German physiologist named **Rudolph Peter Heinrich Heidenhain**, questioned Ludwig's theory and supported Bowman's theory, relying on his observations of secretion fluids within different organs. In 1883, in the chapter "*Excretion of Solutes in the Urine*", he rejected Ludwig's filtration theory in the kidney. Notwithstanding, he supported the secretory mechanism [6]. Indeed, he studied the histology of glandular tissues involved in saliva, milk, gastric and intestinal secretions. With the secretory theory in mind, Heidenhain realized injections experiments of indigo carmine dye into rabbits. He observed the

dye in the lumen and cells of renal tubules, but not in the glomerulus [1, 4]. From these experiments, he concluded that active transport in the renal epithelial cells lead the blood constituents to the tubules, independently of any glomerular activity. In other words, Heidenhain asserted that the "active force" of the cells, an unidentifiable "vital" cells activity, pushed the "diffusate" from the plasma through the glomerulus, and expelled it to the tubule lumen.

Thus, according to Heidenhain, urine is only formed by a secretion process in the kidneys. Even without strong evidences, the scientific community agreed with Heidenhain's assumption that remained the dominant one for the next 35 years.

In 1917, **Arthur Robertson Cushny**, a Scottish pharmacologist and physiologist published the book "*The Secretion of the Urine*" bringing a crucial help in renal functions knowledge. Re-evaluating the different theories, he combined Heidenhain's and Ludwig's theories to propose a "modern view" of renal function. Blood filtration could lead to the formation of an enormous volume of filtrate that is partially reabsorbed along the tubules to explain the concentration of the solutes in the plasma and the urine. Cushny accepted the main concept of Ludwig's theory: the first step of urine formation is the blood filtration in the glomerulus, but he did not admit the protein-free filtrate composition. Hence, he agreed with the hydrodynamic laws used by Ludwig to induce blood filtration, and with the active force of the cells to reabsorb solutes illustrated by Heidenhain. Nevertheless, he suggested a new concept of "threshold and no-threshold bodies" or the substances crossing the tubules to modify the filtrate formed in the glomerulus. Cushny asserted that threshold bodies at a low concentration are reabsorbed by the tubules, and are excreted in the urine at higher concentration [6].

By the end of World War I, Cushny's argument on kidney functions, despite the lack of experimental evidences, influenced and highly stimulated students on renal physiology [4]–[7].

A few years later, **Alfred Newton Richards**, an American pharmacologist, proposed an experiment in which the renal blood flow is kept constant using a kidney perfusion. However, his research was interrupted by World War I before he was being discharged from the service in 1918. Back in the laboratory, he met **Joseph Treloar Wearn** who was captivated by his experiments on the circulation in the living frog's kidney. Working together, Richards

learned how to insert a sharpened glass capillary pipette into a red blood cell with a micromanipulator, while Wearn grasped how to visualize the kidney of an anesthetized frog under a microscope. Afterward, Wearn suggested to collect glomerular fluid and bladder urine simultaneously, with the micropuncture technique, in order to analyze and compare their composition (Fig.4). From that time, another turning in renal physiology history began. They pointed out that the glomerular filtrate contains chloride and glucose, but not always the urine, depending on their concentration in the bloodstream. Moreover, Wearn also administrated indigo carmine dye in the kidney of an anesthetized frog. He noticed that the glomerular fluid collected had a light blue colour, whereas the urine was darker, which is in conflict with Heidenhain's statement. With all these experiments, they demonstrated, in 1924, that blood filtration through the glomerular capillaries formed a protein-free filtrate followed by tubules reabsorption of the filtrate, and ended up with urine formation. An 80-year-old controversy has finally been settled.

Richard's laboratory published several relevant papers about glomerular and tubules fluid composition from frog and snake, during the next 15 years. Relying on microanalytic methods, and another technique to divide tubule segments, they determined fluids composition in each section of the tubule. Humble, Richards shared his advances in renal physiology with the many investigators who brought important progresses in the knowledge of kidney function. Ten years later, in 1940, the same experiments were done on mammalian kidneys and were similar to those obtained with amphibians.

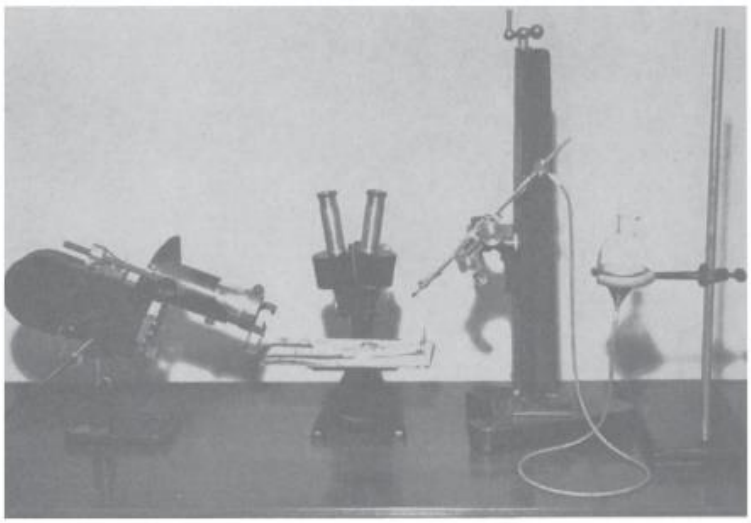

Figure 4: Set-up developed and used by Richards, Wearn, and the students from Richards' laboratory. With this system, it was possible to visualize the renal circulation of an anesthetized frog, and to micropunture their glomeruli and tubules. From left to right: Light for the transillumination, the binocular microscope with frog board, the micropipette holder in Palmer stand, and the mercury-levelling board.
Source: [3]

Eventually, **Eli Kennerly Marshall Jr** completed Richards and colleagues research between 1924 and 1926, providing a strong proof of concept on renal tubules reabsorption, but also secretion of solutes. Indeed, he intravenously administrated a dye used as a clinical kidney function test, the phenolsuphonephtalein (PSP), in dogs and collected urine and blood samples. He discovered that PSP concentration was higher in the kidneys than in the other organs, and that it was in excess in the urine compared to its concentration in the filtrate. He assumed that secretion should occur to eliminate substances into the urine [6]. However, the Second World War took place, and interrupted further renal physiological investigations. We had to wait the 1950s for the development of new approaches in the renal physiology domain, which leads to *in vitro* perfusion techniques in different tubule sections immersed in a bath containing other solutes.

Thus, in 1924, Wearn and Richards' experiments highlighted the mechanisms of urine formation, in accordance with filtration-reabsorption Ludwig's theory, resolving an 80-year-old controversy in the modern era of renal physiology [7]. Together, the scientists demonstrated that the glomerulus filtrates the blood to split filtrate from the plasma, and that most of this filtrate is reabsorbed in the tubules [6] (Fig.5).

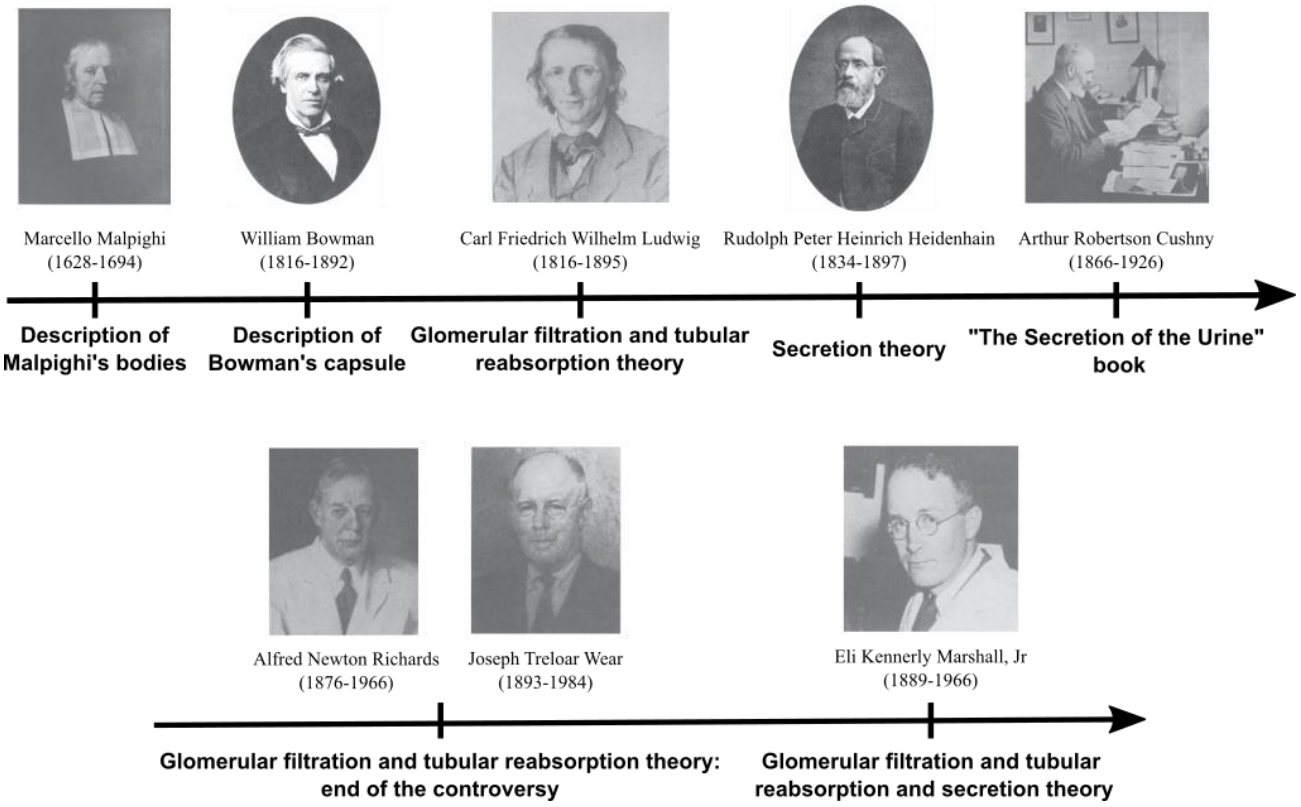

Figure 5: Portraits of prominent scientists who allowed renal physiology development and understanding in renal functions. Below, the main discovery is indicated.
Source: [1, 3]

b) Kidney morphology and structure

Kidneys are endocrine vital organs with several homeostatic functions to maintain the internal environment balance, an aspect on which we will focus in the next part of this chapter I) 1) c). They are divided into two parts: the adrenal gland for the endocrine functions, and the renal capsule for the homeostasis function (Fig.6A).

Kidney external anatomy:

Part of the urinary system, the paired kidneys are reddish bean-shaped organs located in the retroperitoneal space, between the peritoneum and the posterior wall of the human abdomen (Fig.6A). The peritoneum is a serous membrane composing the lining of the abdominal cavity that covers and supports most of the intra-abdominal organs. The right kidney is slightly lower than the left because the liver fills the space on the right superior side of the kidney.

An adult kidney is about 10-12 cm length, 5-7 cm width, 3 cm thick, and has a mass of around 135-150 g. The rounded, outer convex surface of each kidney faces the vertebral column, and near the centre of the concave border, the indented surface is called the renal hilum or hilum. From this structure emerges the ureter that carries urine out of the kidneys to the bladder, along with blood vessels, lymphatic vessels and nerves (Fig.6B) [5][6].

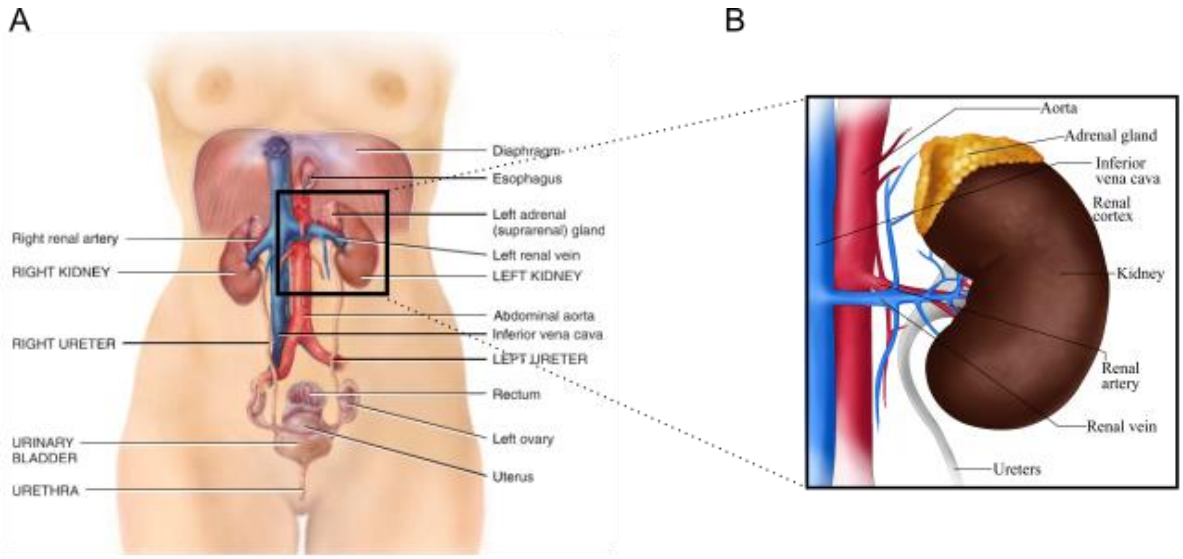

Figure 6: Illustrations of the localization of the kidneys in the organism, and its external anatomy. A: Anterior view of the urinary system in a female. B: Anterior view of the left kidney.

Source: adapted from reference [5].

Each kidney is encompassed in three layers of tissue: from the outside to the inside: the renal fascia covered by an adipose capsule, itself wrapped in a renal capsule that is the deepest layer (Fig.7). The renal fascia is the superficial and thin layer of connective tissue in contact with the peritoneum to anchor the kidney to the abdominal wall and the other structures. Then, the adipose capsule, composed of fatty tissue, protects the kidney from trauma and holds it firmly in the abdominal cavity. Finally, the renal capsule also protects the kidney against trauma and maintains its shape. It is a smooth, transparent layer of dense irregular connective tissue that is continuous with the outer coat of the ureter.

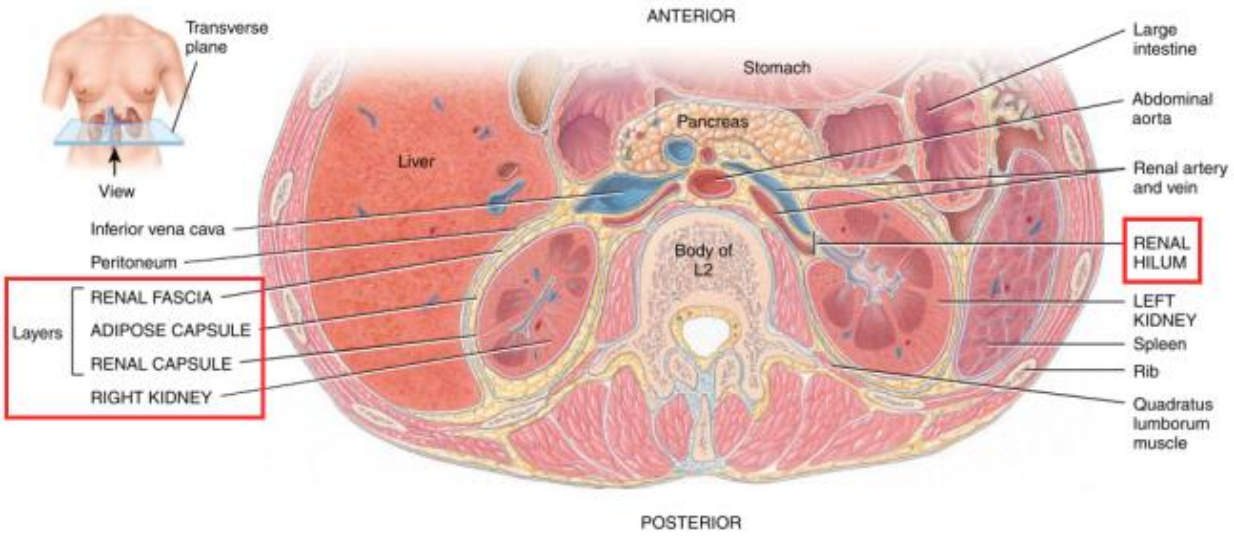

Figure 7: Schematic of the inferior view of the abdomen transverse section (second vertebra lumbar). The three layers embedding the kidneys have been framed, as well as the renal hilum from which emerges the ureter.
Source: adapted from reference [5].

Kidney internal anatomy:

Within the kidney, two specific regions are visible: an outer light red region called the renal cortex, and a darker reddish-brown inner region called the medulla (Fig.8). They form the **parenchyma**: the functional section of the kidney. The medulla part contains several cone-shaped renal pyramids with the largest base facing the renal cortex, and the narrowest part or renal papilla, pointing towards the renal hilum. The renal pyramids are arranged radially around the hilum. The renal cortex, surrounding the medulla with its smooth texture, elongates from the renal capsule to the apex of the renal pyramid. It also projects between renal pyramids, which is called renal columns.

A primary urine, or filtrate, is formed in the renal pyramids and drained into cuplike structures called the minor and major calices. A minor calyx collects urine from the papillary ducts of one renal papilla (tip of a renal pyramid), and delivers it to a major calyx. There are eight to eighteen minor calyces and two or three major calyces in each kidney. Transformed into urine in the calyces where no reabsorption occurs, the urine is drained into a large cavity, the renal pelvis, and then excreted through the ureter to the urinary bladder [5][6]. From the calyces to the ureter, smooth muscle tissues drive the urine towards the bladder thanks to peristalsis movements. The

renal pelvis, the calyces, and branches of the renal blood vessels and nerves are contained in the renal sinus, which is a cavity prolonging to the hilum (Fig.9).

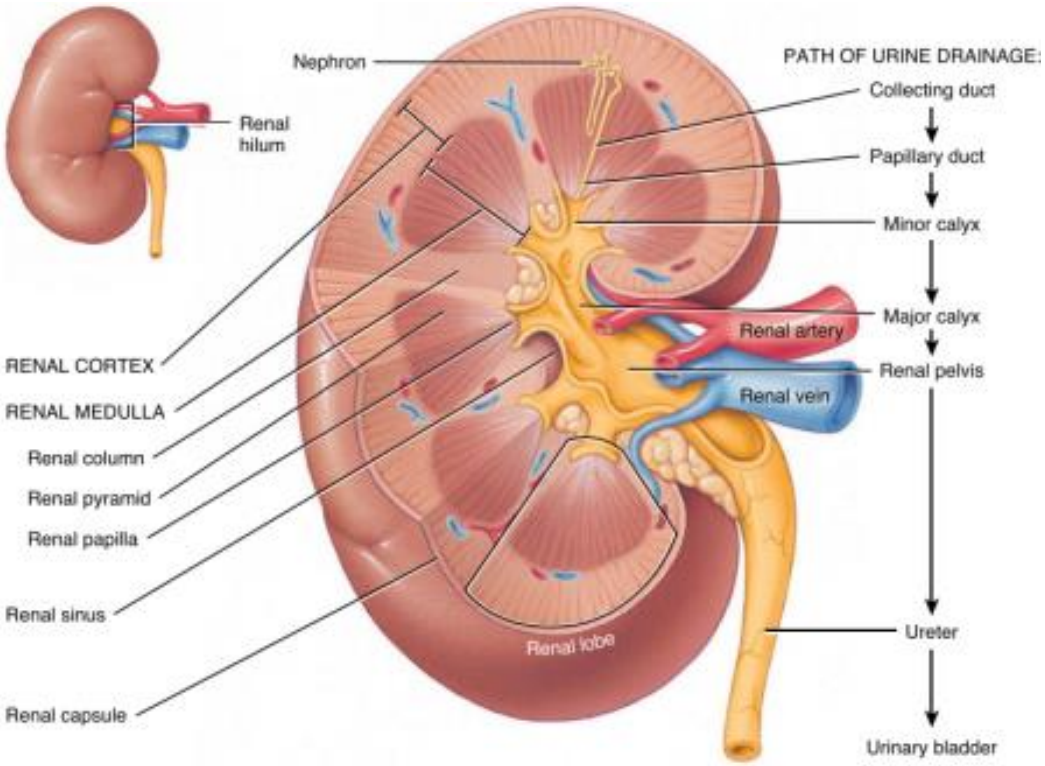

Figure 8: Schematic of the interior view of the right kidney, focused on its different regions. The urinary pathway is indicated on the right.
Source: [5]

The parenchyma, composed of renal cortex and renal pyramids, contains the functional and structural unit of the kidney: **the nephrons**. Those units have a specific shape in the renal cortex, more precisely between the outer cortical zone and the inner juxtamedullary zone. There are around one million nephrons per kidney, parallel to each other, tightly packed, with a highly reproducible geometry (Fig.9). They consist of two main parts: a renal corpuscle for the blood filtration, followed by a succession of tubules of different diameters to allow urine formation. The nephrons lie within the renal cortex: the nephron loop elongates into the renal medulla, forms a hairpin turn, and returns to the renal cortex. Those structures are very close to an abundant blood supply, which will be described progressively.

The **renal corpuscle** is composed of a compact interconnected capillary loop called the **glomerulus** (plural is glomeruli) or glomerular capillaries, surrounded by a double-walled epithelial cup, the **Bowman's capsule** or glomerular capsule. Blood is filtered in this capsule and transformed into a filtrate that passes into the renal tubule to form urine [9] (Fig.9). The urine, composed of wastes and other useless solutes, is then eliminated from the body through its excretion in the urinary bladder.

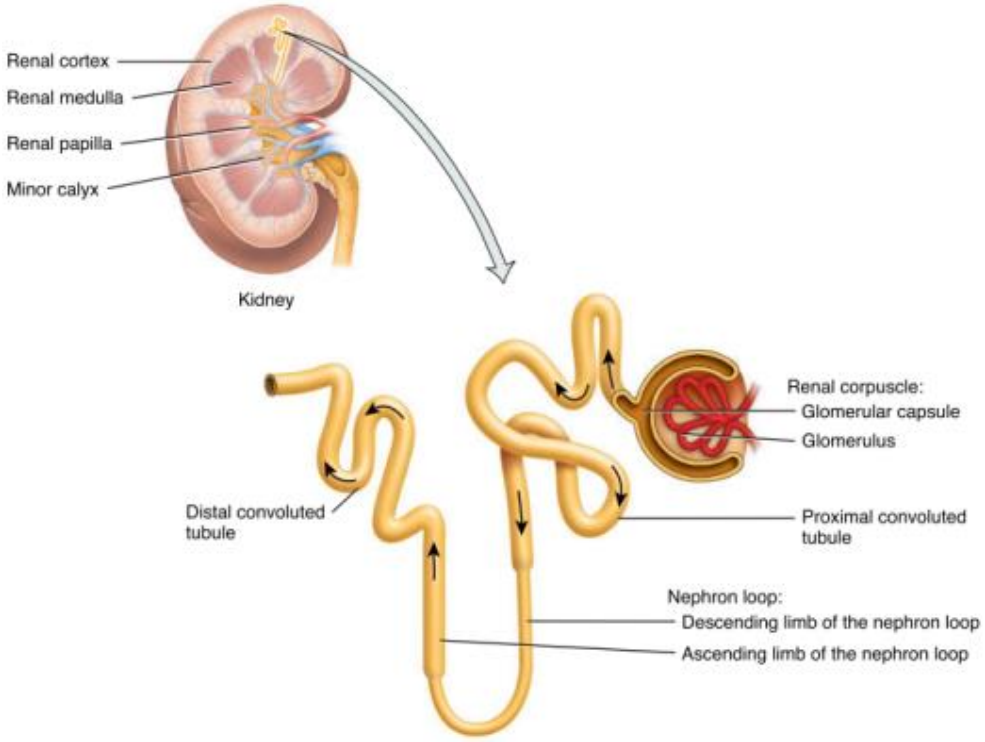

Figure 9: Schematic illustrating the nephron's sections. On the top left, the left kidney with the localization of the nephrons. On the bottom right, magnification on a nephron.
Source: [5]

Let start with the **renal corpuscle** that is responsible for the initial step of urine formation: the separation of proteins from the blood plasma. Within the renal corpuscle, three layers forming the visceral layer overlap to filtrate the blood and to produce a filtrate: the *endothelial cells* forming the glomerular capillaries, the thick *basal membrane* of the capillaries, and a *monolayer of epithelial cells* lying on the basal membrane and facing the Bowman's capsule [9]. The first layer is composed of endothelial cells punctured with many pores. This is due to the thickness of the endothelial cells that are fenestrae, thin and have few mitochondria [10]. Those endothelial cells are attached to a capillary basement membrane or basal lamina consisting of glycoproteins and proteoglycans. The main glycoproteins expressed are type IV collagen, laminin and fibronectin. The third layer is composed of modified simple

squamous epithelial cells called **podocytes** with many footlike projections, **pedicels** that surround the layer of endothelial cells and are embedded in the basement membrane [5][6]. Those pedicels are coated with glycocalyx, like the endothelial cells [10]. Wrapping this inner structure, a parietal layer composed of simple squamous epithelium forms the outer wall of the Bowman's capsule. The filtrate goes through the space between adjacent pedicels to reach the space between the parietal and visceral layers, a space called the capsular space, before going through the renal tube [8]. Besides, another cell type, the mesangial cells, is located between and within the glomerular capillary loops. They phagocyte and remove useless trapped components from the basal membrane and the endothelial cells: they are macrophages [9]. They also contain myofilaments which allow them to contract like vascular smooth muscle cells to influence the filtration process, and in response to different stimuli (Fig.10).

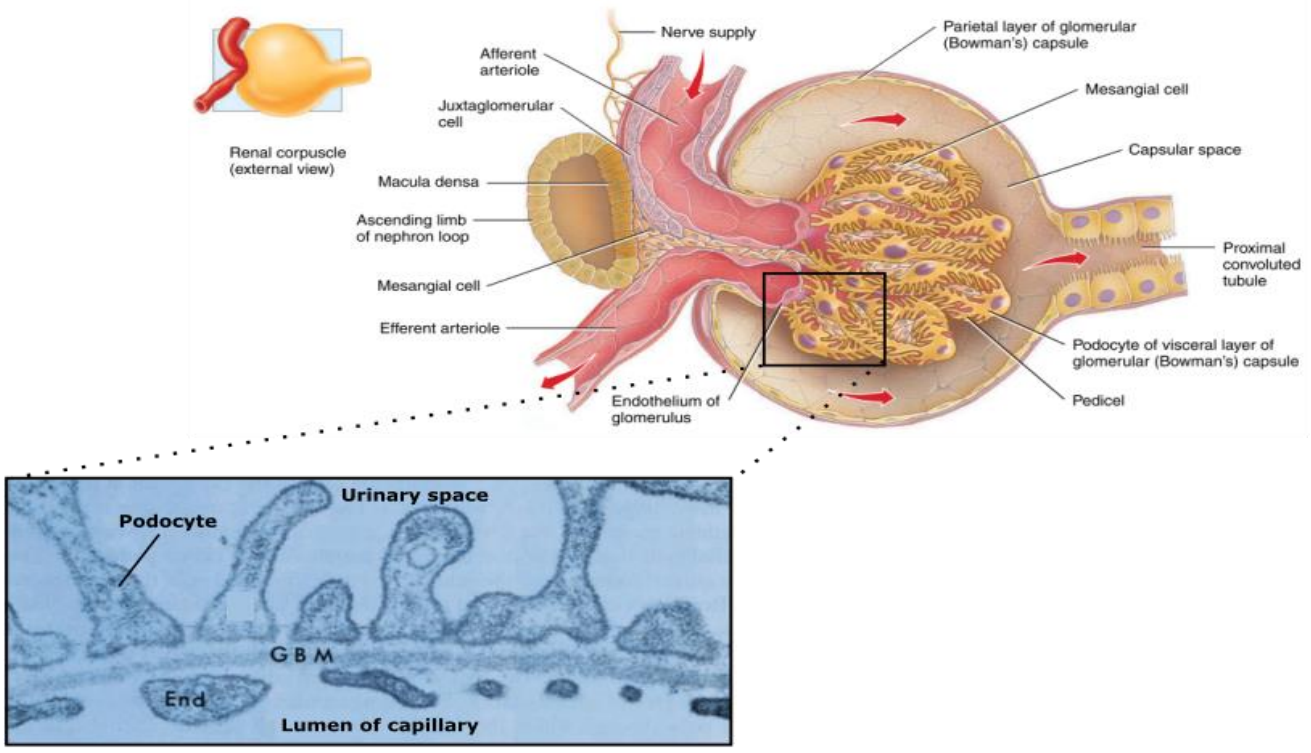

Figure 10: Illustrations of the internal view of a renal corpuscle. A: Schematic of a renal corpuscle with the blood pathway indicated by the red arrows. B: Cross-section focusing on the visceral layer of a renal corpuscle, with End: endothelial cells, GBM: glomerular basement membrane.
Source: adapted from references [5, 6].

The filtrate is then ejected in the **renal tubule** split in three main parts: the **proximal convoluted tubule (PCT)** that is an extension of the glomerular capsule, the **loop of Henle** and

the **distal convoluted tubule (DCT)** that is away from the PCT. They are qualified as convoluted because they are coiled and not straight [5][6]. Along the tubule, a monolayer of epithelial cells lines with the basal membrane, but their shape and thickness vary from segment to segment [9]. They all present tight junctions to physically join them together, and control the permeability (Fig.9).

The **proximal convoluted tubule** drains the Bowman's capsule and goes down toward the medulla. The cell layer is made of simple cuboidal epithelial cells with a prominent brush border of microvilli on their apical surface facing the lumen. Like in the small intestine, the microvilli increase the surface area for reabsorption and secretion. This segment leads to the loop of Henle that is divided in two main parts: the descending thin limb, the ascending thin limb and/or the ascending thick limb, depending on the localisation of the loop within the medulla. The **descending thin limb of Henle's loop, or the descending thin limb** is in the medulla where it forms a hairpin loop before going up alongside to itself. The parallel segment is the **ascending thin limb of Henle's loop, or the ascending thin limb**. The hairpin loop penetrates deeply within the medulla, which constitutes the long loop. It is composed of the descending thin limb and the ascending thin limb with simple squamous epithelial cells. The thin ascending limb is then elongated, and thickens to form the **ascending thick limb** consisting of simple cuboidal to low columnar epithelial cells. Nevertheless, in the renal cortex, short-loop nephrons do not have a thin ascending limb, but a thick ascending limb that begins just after the hairpin loop of the thin descending limb (Fig.11).

Cortical nephrons or short-loop nephrons represent about 80-85% of the total nephrons. The other 15-20% of the nephrons are juxtamedullary nephrons or long-loop nephrons, at the edge between the cortical and the medulla regions. Indeed, their renal corpuscles is deep in the cortex, close to the medulla, and their long loop extends deeper in the medulla. Those nephrons favour the excretion of very dilute or concentrated urine (see details below, in the subchapter I) 1) c)). Moreover, both types of nephrons (short or long) receive one afferent arteriole that splits into the glomerulus. Then, the glomerular capillaries join to form the efferent arteriole to carry blood out of the renal corpuscle. The glomerular capillaries are the only capillaries in the body to be between two arterioles, rather than between an arteriole and a venule. Because of this

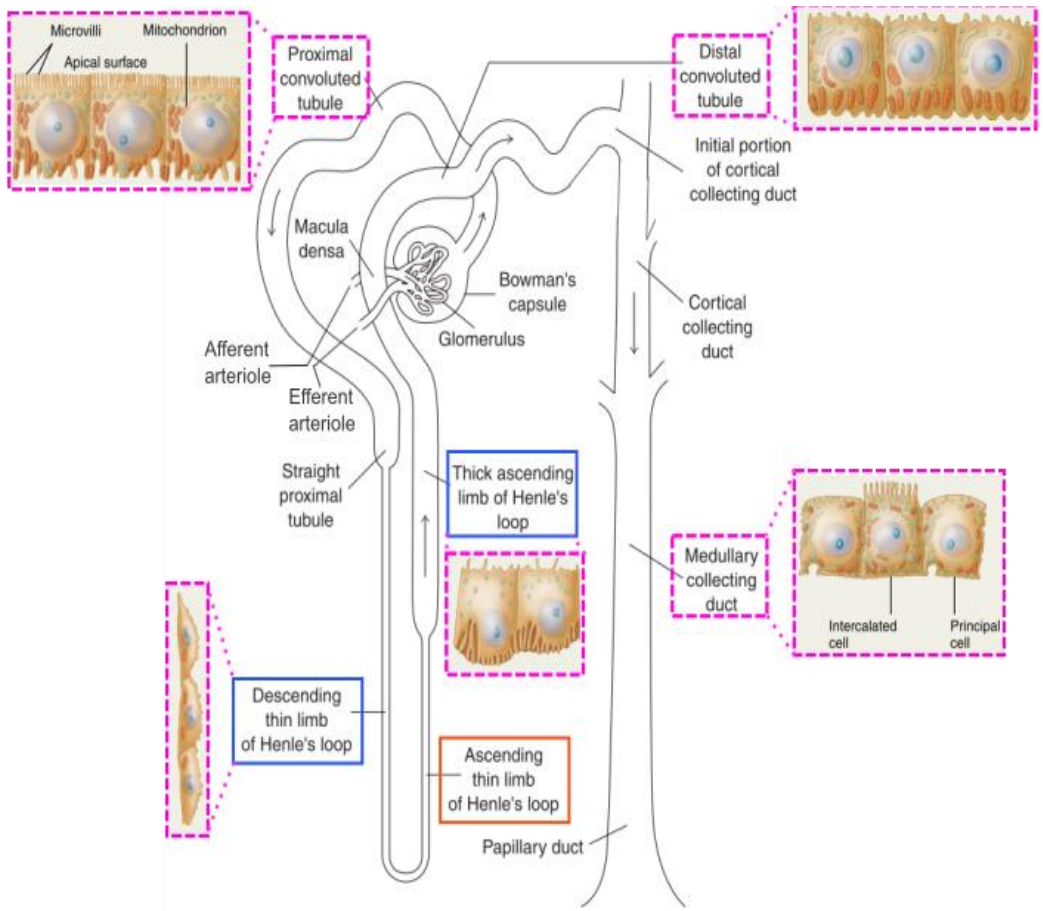

Figure 11: Schematic representing the relationships between each sections of a long-looped nephron. The orange rectangle highlights the section missing in the short loop nephrons, whereas the blue rectangles correspond to the sections present in both types of nephrons (short and long). The purple insets illustrate the cell types and shape in each section of the nephron. Note that in the descending and ascending thin limbs, the epithelial cell type is the same.

network, the glomerulus is part of the urinary and cardiovascular systems. Then, the efferent arteriole divides and forms the peritubular capillaries that surround the nephrons tubules in the renal cortex. In the renal medulla, some efferent arterioles extend in long, loop-shaped capillaries called **vasa recta** to supply in blood the nephrons of this region. Finally, the blood draining through the vasa recta and the peritubular capillaries reaches the cortical radiate veins, the arcuate veins and the interlobar veins running between the renal pyramids. It ends up in the renal vein. This last one is in the renal hilum, where it drives the blood to the inferior vena cava. Renal nerves belong to the autonomic nervous system and are sympathetic nerves regulating

blood flow through the kidney. They are vasomotor nerves leading to renal arterioles vasodilatation or vasoconstriction (Fig.12).

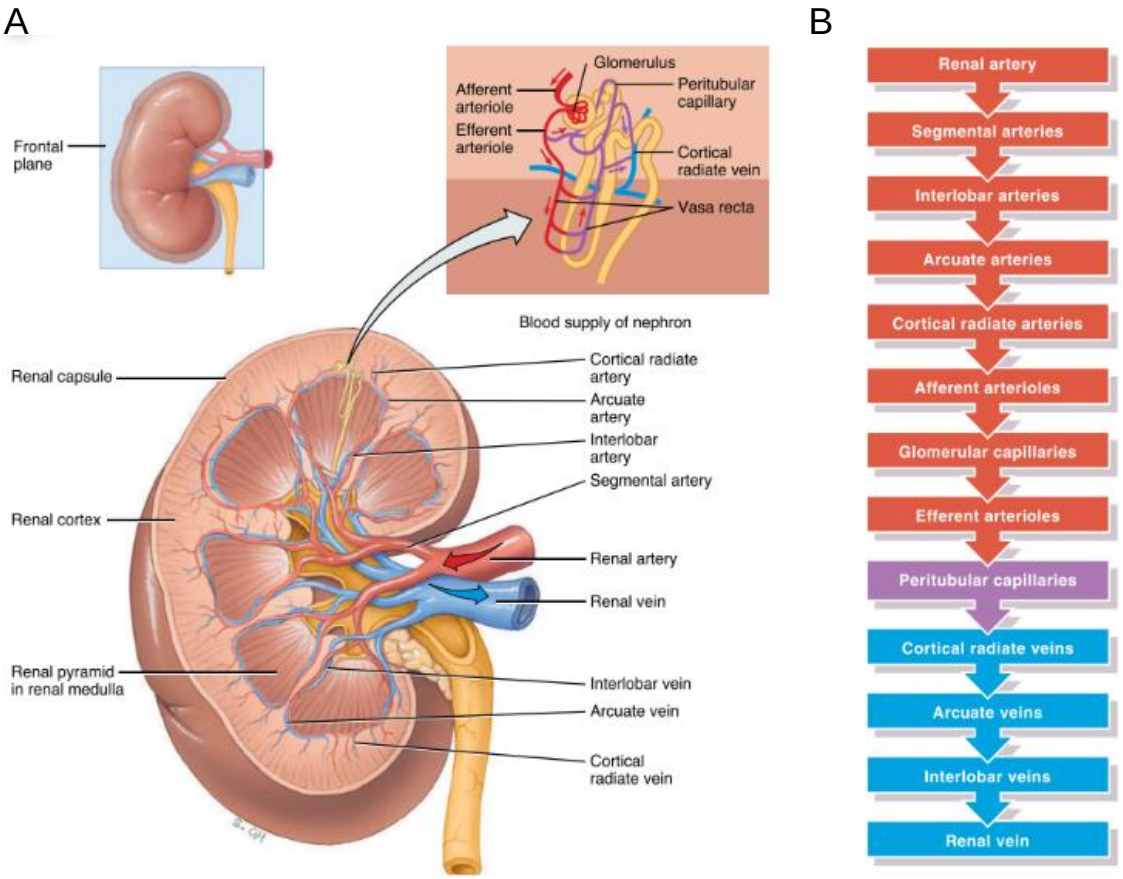

Figure 12: Schematics representing the renal innervation and the blood flow pathway through the kidney. A: Inset focusing on a nephron and its bloodstream. B: Schematic showing the blood pathway through the renal innervation.
Source: [5]

The renal bloodstream network and the nephrons are very close to each other. Between them, an interstitium containing fluid and cells such as fibroblasts, allows the secretion of collagen, proteoglycans, and glycoproteins [9].

For both type of nephrons, the last part of the ascending limb (thin or thick) goes between the afferent and efferent arterioles linked to the renal corpuscle from which it is originated. The cells in this region are crowded and specialized columnar cells known as **macula densa**. Next to the macula densa, the endothelial cells forming the afferent capillaries (and sometimes the efferent arteriole too) align with modified smooth muscle fibers called **juxtaglomerular cells**. The macula densa in addition to the juxtaglomerular cells compose **the**

juxtaglomerular apparatus (JGA) that helps the blood pressure regulation in the kidney (Fig.10).

Eventually, the **distal convoluted tubule** starts not far away from the macula densa, and is prolonged into the collecting tubule. In the second half of the DCT and the collecting duct, two different cell types coexist: the principal cells and the intercalated cells (type A and type B) (Fig.11). The principal cells express receptors for the Antidiuretic Hormone (ADH) and the aldosterone, to regulate fluid volume (see details below, part I) 1) c)). The intercalated cells, less numerous, act on the homeostasis of blood pH. Several distal convoluted tubules from many nephrons merge to form a large cortical collecting duct that joins others to make a larger **collecting duct.** All of those collecting ducts associate together and converge into a hundred large **papillary ducts**, which drain urine into the minor and major calyces to reach the ureter. The urine composition entering the calyces is not impaired anymore; it is temporarily stored in the urinary bladder, and intermittently eliminated.

Hence, the kidney has about one million nephrons from birth, but less collecting ducts, and even less papillary ducts. The impairment of a nephron does not induce the formation of new ones, which means that kidney injury is not detected until its functions decline to less than 25%. Indeed, the remaining functional nephrons adjust their functions to handle the deficiency of the impaired one. In a normal case, the increase of kidney size is due to the growth of individual nephrons. In a pathological case, the injured kidney could be surgically removed, which will induce the hypertrophy (enlargement) of the other one. The healthy kidney will then be able to filter at 80% of the rate of two normal kidneys.

To summarize, urine pathway through the different parts of the kidney is a long way before reaching the urinary bladder. Blood arriving to the afferent arteriole reaches the renal corpuscle where it is transformed to produce a filtrate through the glomerulus. The filtrate is then expulsed in the efferent arteriole and in the different sections of the renal tubule. It crosses the renal cortex, goes down to the medulla, before going up in the cortex and then in the medullary collecting ducts. The filtrate becomes urine that reaches the renal calyces where it cannot be modified. Urine fills the ureter and the urinary bladder where it is stored and then eliminated.

Presently, let us focus on the processes leading to blood transformation into urine within the kidneys, and the roles of each structural part in this mechanism.

c) Physiological functions

Kidneys maintain the homeostasis of blood volume and composition. They represent less than 0.5% of total body mass, and receive about 20-25% of the cardiac output. In adults, the renal blood flow in both kidneys is about 1.2 L/min. The blood is then transformed into urine relying on three mechanisms within the different sections of the nephrons: **glomerular filtration**, **tubular reabsorption** and **tubular secretion**. Usually, the volume of glomerular filtrate every day is around 150 liters. However, more than 99% of the glomerular filtrate goes back to the renal bloodstream by tubular reabsorption, which indicates that only 1-2 liters is excreted in the urine [8].

i) Blood's filtration

The first step of urine formation consists in blood filtration occurring in the glomerulus, into the Bowman's capsule. The blood crosses the three layers composing the filtration membrane described above (section I) 1) b) of this chapter) to produce a filtrate containing very small molecules. Each layer has a role, and the deeper blood enters the glomerulus, the more the filtration is refined (Fig.13).

The first layer composed of endothelial cells is more permeable than the endothelium of other capillaries in the body, and is negatively charged because of the presence of glycocalyx, a thick layer of polymeric proteins. It is punctured with many small pores of about 0.07-0.1 µm diameter, which is due to the thickness (up to 500 nm) of the endothelial cells that are fenestrae. It allows the passage of small positively charged solutes from the blood, except red blood cells and platelets. The mesanglial cells, located between the afferent and efferent arterioles, contribute to the glomerular filtration thanks to their contractile properties [8]. Then, the basal membrane operates as a molecular sieve that retains large molecules, with a molecular weight above 68 kDa, and rejects negatively charged proteins as well. The albumin, main protein in the plasma with a diameter of 0.007 µm, crosses the filtration membrane in very low amount (<1%). This membrane also regulates water flow [10]. Besides, podocytes possess negative charges to reject smaller negatively charged proteins. They add up to the basal membrane barrier functions and maintain it. They are also able to phagocyte macromolecules, like the mesanglial cells. The footlike extensions, pedicels, have a space between them: the filtration slit. This one extent in a thin membrane called slit membrane. Small molecules such as water,

glucose, with a diameter smaller than 6-7 nm, go across this slit membrane. Plasma proteins with a tiny size, as well as solutes like ammonia, urea and ions can also cross this membrane. The whole filtration membrane, with its three layers, has a thickness of only 0.1 mm. Positively charged proteins go through this filtration membrane more easily than neutral proteins [9].

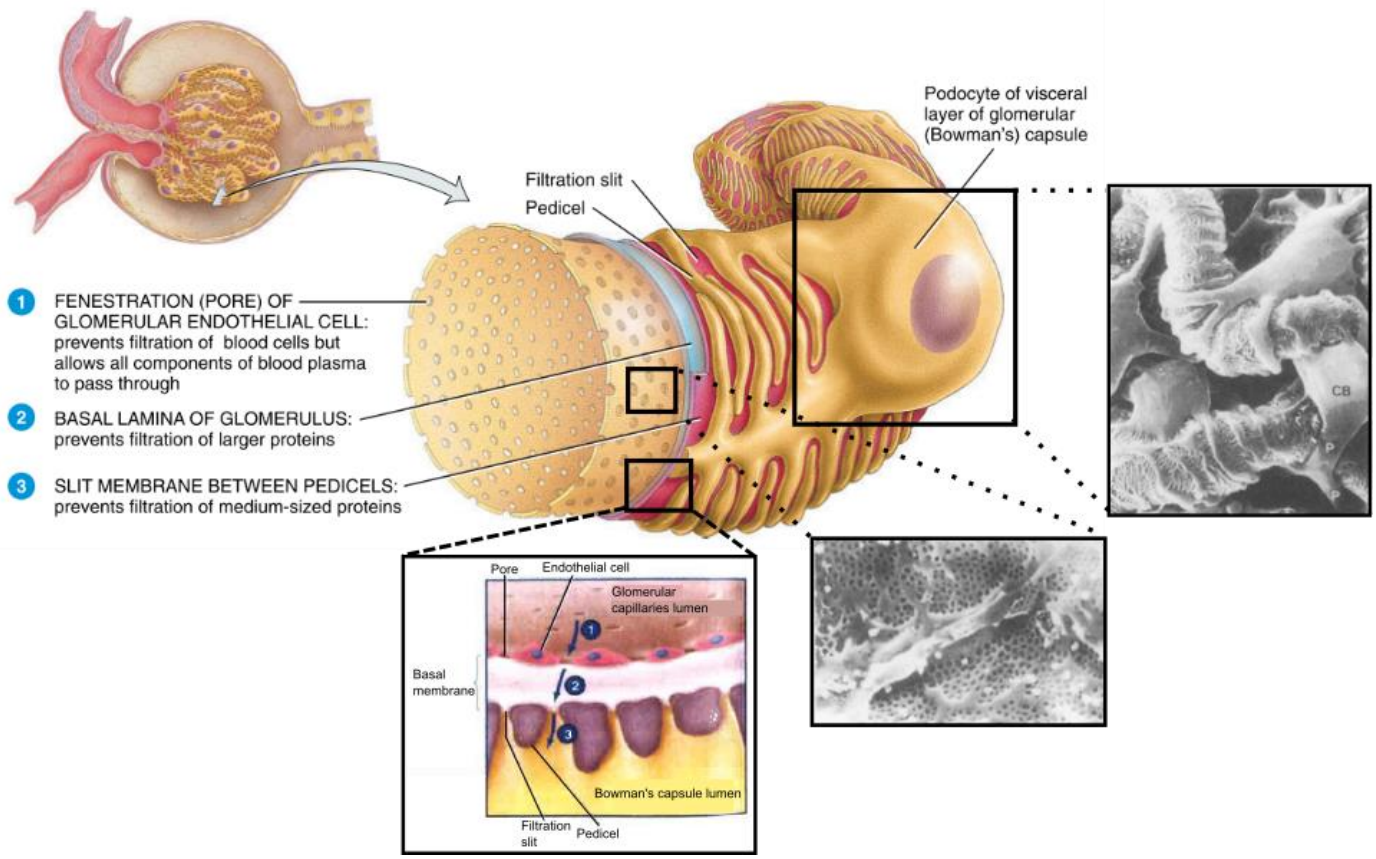

Figure 13: Schematics representing the filtration membrane within the glomerulus, and scanning electron micrographs of two structures. A: Schematic focusing on the filtration membrane layers and structure. B: Inset illustrating the outer surface of the rat glomerular capillaries with CB, the cell body of a podocyte. Pedicels looking like interdigitating process extend from this podocyte. Scale bar: X3000 approximately. C: Inset showing the inner surface of a rat glomerular capillary, and focusing on the porous membrane. Scale bar: X16000. D: Magnification on the glomerular filtration membrane illustrating the filtrate pathway.
Source: adapted from [5] and [7].

Hence, three levels of controls, in size and charge of proteins, are present in the renal corpuscle to obtain a filtrate without large proteins [8]–[10].

A physical force is applied to push the blood through the glomerulus for the filtration step, and then drives the filtrate through the tubule. The afferent arteriole diameter is larger than the efferent arteriole one, which induces a high pressure in the glomerular capillaries, and a high resistance in the glomerulus. Moreover, the glomerular capillaries are long and extensive, which is regulated by the mesenglial cells. Indeed, they contract or relax to decrease or increase, respectively, the surface area for the filtration. When they relax, the glomerular capillaries surface area is large, which allows a high glomerular filtration. Inversely, their contraction leads to a decrease surface area which favours a lower glomerular filtration.

The glomerular filtration relies on two main forces called Starling's forces: the **hydrostatic pressure (P)** and the **osmotic pressure (π)**. The hydrostatic pressure (45-55 mmHg) exerted by the blood in the glomerular capillaries (P_{cap}) drives water and solutes filtration through the filtration membrane. A hydrostatic pressure in the Bowman's capsule (P_{bc}) (15 mmHg) applied against the filtration membrane, and an osmotic pressure (π_{cap} = 25 mmHg in the beginning) due to the presence of proteins in the filtrate counteract the filtration [6]. Indeed, in the glomerular capillaries, the anatomical arrangement of the blood vessels favours fluid movement across the capillaries. The blood crosses the arteries, afferent arteriole, glomerular capillaries, efferent arteriole, peritubular capillaries, venules and the veins (Fig.14). The pressure exerted on the filtration membrane, 55-45 mmHg, is higher than in the capillaries of most other vascular beds (around 32 mmHg). It stays constant and slightly decreases along the length of the glomerular capillaries because of the efferent arteriole that promotes a certain resistance. This force induces the formation of the filtrate. The osmotic pressure progressively increases with the volume water leaving the glomerular capillaries, and as a consequence, the protein concentration increases [10]. In the efferent arteriole, the hydrostatic pressure decreases, as well as in the peritubular capillaries. As the osmotic pressure is elevated in the glomerular capillaries, the fluid is progressively reabsorbed in the peritubular capillaries to reduce it [5][7]. The total pressure favouring filtration is the Net filtration pressure defined as the subtraction of the hydrostatic pressure in the glomerular capillaries (P_{cap}), the hydrostatic pressure in the Bowman's capsule (P_{bc}) and the osmotic pressure in the capillaries (π_{cap}).

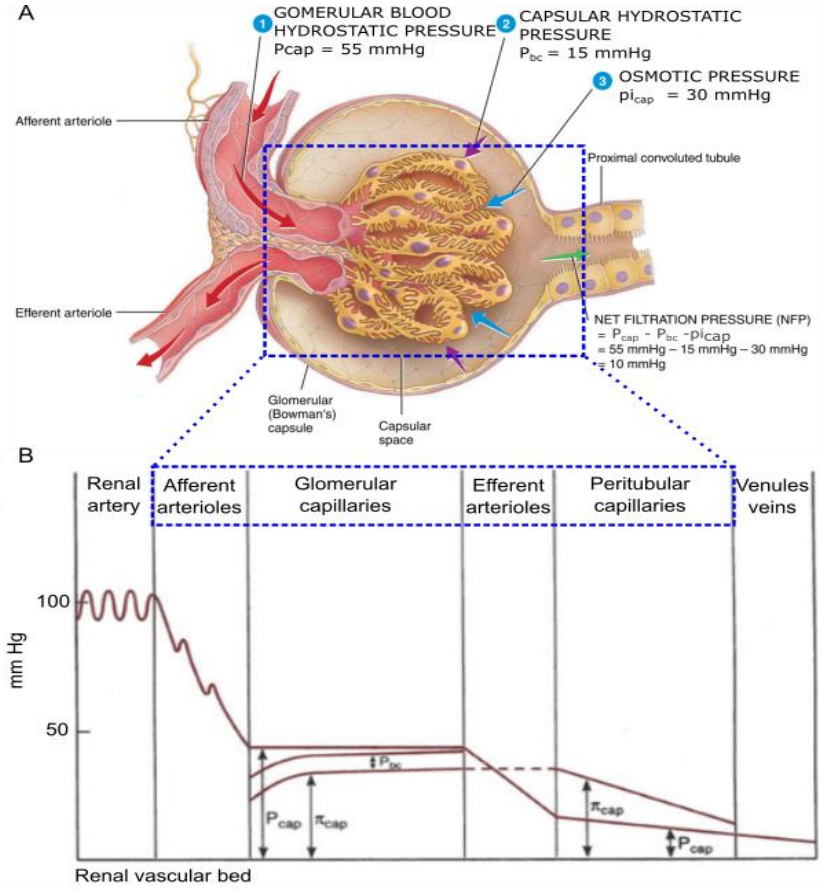

Figure 14: Blood flow distribution within the glomerulus and the renal bloodstream. A: Schematic of the internal view of the renal corpuscle illustrating blood flow pathway through the glomerulus. B: Graph representing the mean blood pressure evolution between the renal artery and the renal vein. The pressure in the glomerular capillaries, Pcap, allows the filtrate formation. The hydrostatic pressure in the Bowman's capsule (Pbc) and the osmotic pressure due to proteins concentration in the plasma (pi cap) resist to the glomerular pressure.
Source: adapted from [5] and [7].

In terms of filtrate formation rate within the glomeruli of both kidneys, **Glomerular Filtration Rate or GFR** is about 120 ml/min, which means 180 L/day. Human has about 3L of plasma from which derives the filtrate. As a consequence, the whole plasma is filtered several times per day (60 times) to eliminate metabolic and toxic wastes from the body. The GFR is relatively constant in the kidneys in order to maintain the homeostasis of body fluids. Indeed, with a high GFR, the reabsorption of some substances may not occur, whereas with a low GFR, the reabsorption of all the filtrate may happen, as well as certain wastes that will not be excreted in the urine. Indeed, a hypervolemia promotes the GFR increase, and inversely, it decreases with hypovolemia. The regulation of the glomerular blood flow relies on the control of the

afferent and efferent arterioles diameters. As mentioned previously, afferent arteriole constriction leads to blood flow decrease, whereas its dilation induces a rise of the blood flow. Nevertheless, aging and renal diseases usually induce a reduction of the GFR [9].

ii) Tubular reabsorption and secretion

After blood filtration, the filtrate enters the proximal convoluted tubule (PCT) where its composition changes along each section of the tubule because of the reabsorption and secretion processes (Fig.15). Cells lining the tubule and the collecting duct reabsorbed 99% of the filtered water and solutes essential for the body. Indeed, the term reabsorption means the return of substances in the bloodstream, whereas absorption indicates the entry of new substances into the body, such as in the gastrointestinal tract.

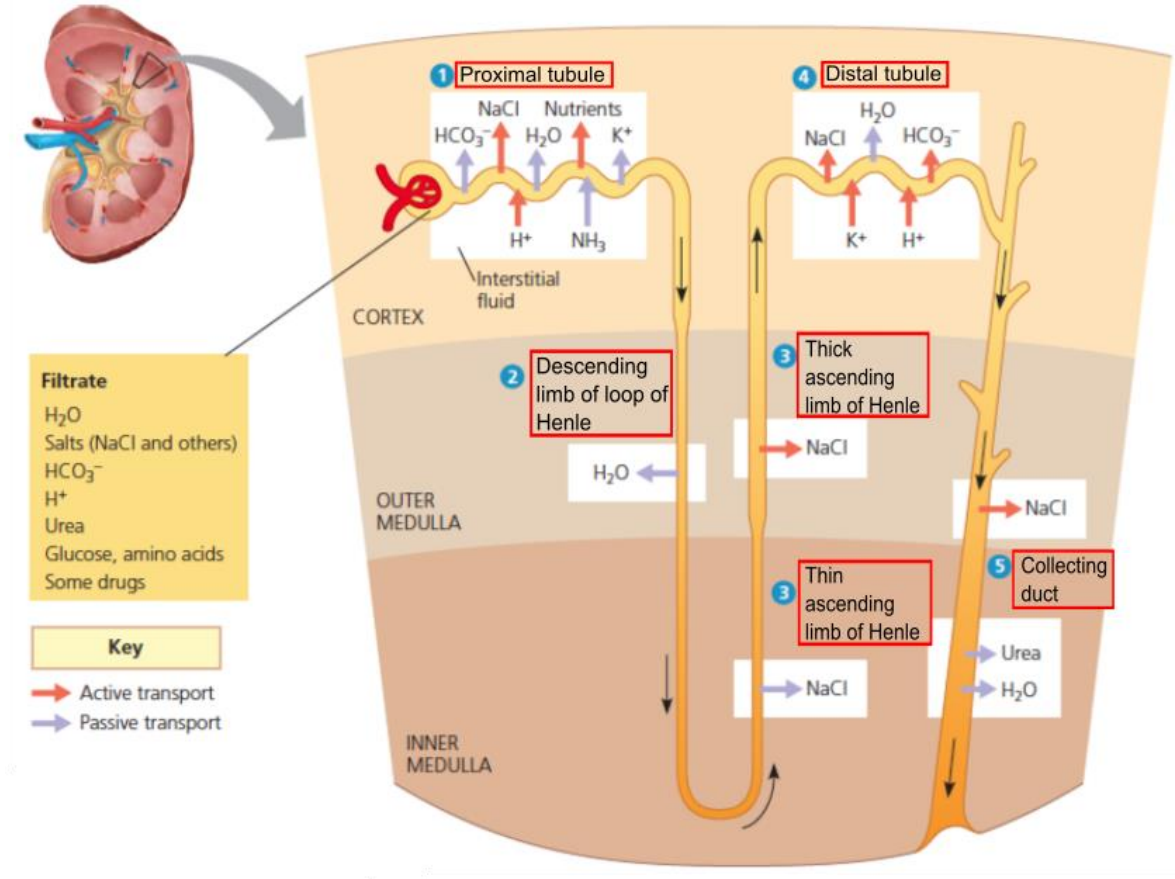

Figure 15: Schematic representing the main fluids components and solutes movements along each section of the tubule, through active and passive transports processes.
Source: adapted from « Physique des grandes fonctions des organismes vivants » course.

All cells lining the renal tubule express a sodium-potassium pump (Na/K ATPases) in their basolateral side to ensure sodium reabsorption in a one-way process. Indeed, they hydrolyse ATP within the cytosol of the cell to eject sodium (Na^+) towards the interstitium and the peritubular capillaries. As other cells in the body, their intracellular concentration in sodium is very low because of the activity of this pump [8].

PCT reabsorbed the largest amount of solutes and water from filtered fluid by active and passive transports. The cells lining the tubules are oriented: their apical side faces the tubule lumen, whereas their basolateral part is in contact with the interstitium that is close to the renal bloodstream. This orientation favours exchanges between the lumen where the fluid goes, the interstitium and the peritubular capillaries (Fig.16B). The cells reabsorb ions and organic solutes in an active way, using specific transporters to maintain the homeostasis, and create an osmotic gradient. In the first half of the proximal convoluted tubule, cells reabsorb all the glucose, amino acids, lactic acid, water-soluble vitamins and other nutrients by Na^+ symporters located in the apical membrane. For instance, PCT cells secrete one proton (H^+) in the lumen while reabsorbing one sodium ion in the cells using an antiporter, which decreases the sodium concentration in the tubule lumen (Fig.16A). The proton concentration participates to the regulation of blood pH: it induces bicarbonate reabsorption or synthesis within the tubule cells (Fig.16B). The bicarbonate diffuses through the basolateral membrane to reach the peritubular capillaries where it regulates blood pH. In parallel, solutes reabsorption drives an osmotic gradient leading to water reabsorption by osmosis. Cells lining along the PCT and the descending limb of the nephron loop are highly permeable: they express a water channel called Aquaporin-1. This protein, localized at the apical and basolateral sides of the PCT cells, rises water movement from the lumen towards the cells [8]–[10]. Removing water from the lumen leads to a high osmolarity. In the second half of the PCT, an electrochemical gradient takes place: anions (Cl^-) diffuse in the peritubular capillaries which induces the paracellular reabsorption of cations (K^+, Ca^{2+}, Mg^{2+}) between two adjacent cells, to balance the gradient in the interstitium. The PCT cells also secrete ammonium and urea, two toxic metabolic wastes from the catabolism of amino acids, or synthesized in their own cytoplasm. Free of many solutes and other nutrients, the fluid osmolarity in the lumen is similar to the one in the peritubular capillaries. It goes through the descending limb where a lot of cations (Na^+, K^+, Ca^{2+}, Mg^{2+}) are reabsorbed towards the interstitium and the renal bloodstream, as well as a few amount of anions (Cl^-). This low gradient of anions in the cells leads to water movements in this part of the loop. Arriving in the ascending limb, water cannot be reabsorbed: the osmolarity in the

tubule decreases progressively. In the early distal convoluted tubule (DCT), water reabsorption is coupled to ions (Na^+, Ca^{2+}, Cl^-) entry in the tubular cells. The fluid then arrives at the end of the DCT where the amount of water, solutes reabsorption (Na^+, K^+, $HCO3^-$), and solutes secretion (H^+, K^+) depend on the body's need. In this tubular section, the sodium-potassium pump is constantly and significantly active, which indicates that the sodium concentration is quite low in the lumen. To adjust this disequilibrium, sodium passively diffuses from the cells, to the interstitium and towards the peritubular capillaries. Moreover, unlike active sodium transports in the other tubular sections, in the DCT, sodium passes through the cellular apical membrane using leakage channels. The potassium (K^+) excreted in the urine is mainly due to potassium diffusion from the DCT cells towards the lumen, and their passage through leakage channels too.

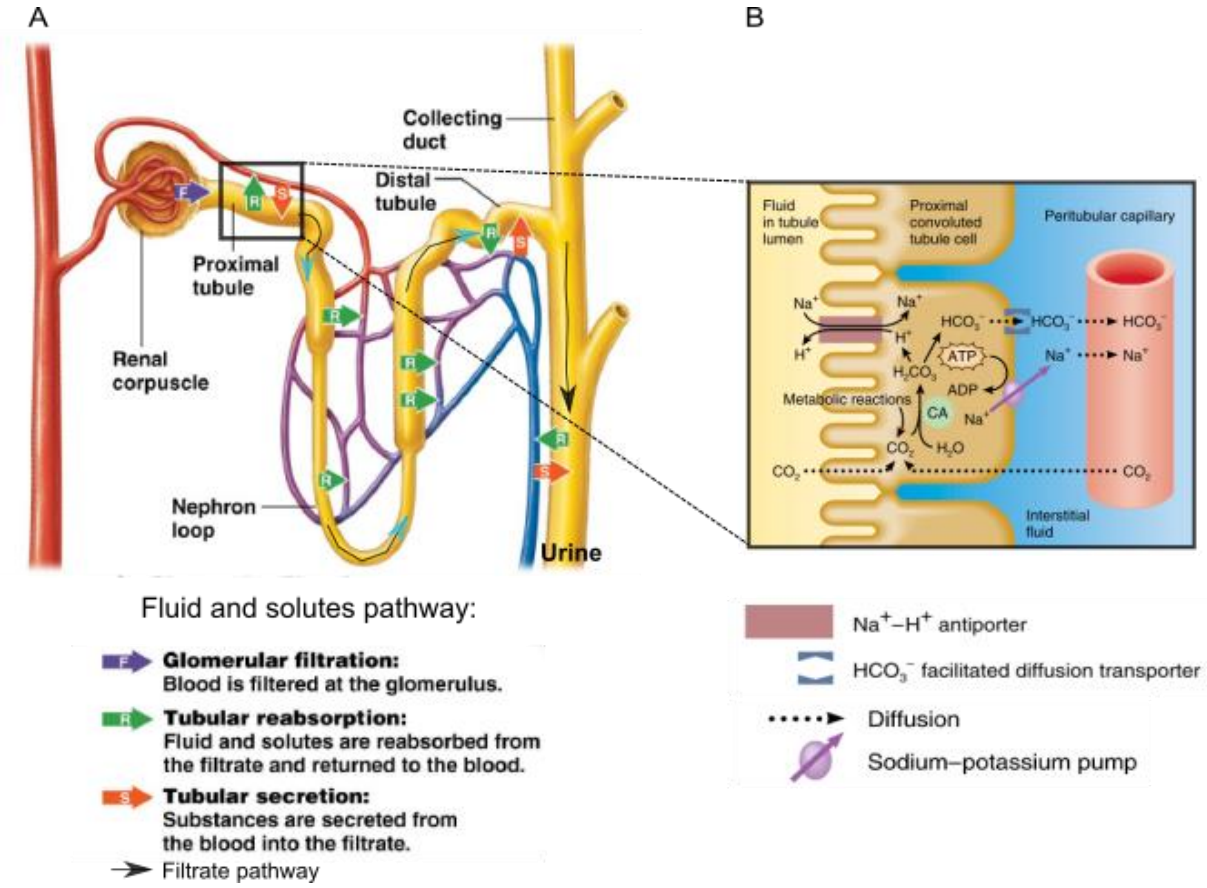

Figure 16: Ions, fluid and solutes flow distribution within the glomerulus and the renal bloodstream. A: Summary of fluid and solutes pathway through the nephron, and the exchanges to produce urine. B: Illustrations of the antiporter Na^+/H^+ functioning: Na^+ reabsorption within the PCT cell and H^+ secretion in the tubular lumen, with HCO^{3-} metabolism.

Source: adapted from [5] and Urinary system.

Eventually, at the end of the fluid pathway through the different tubular segment, 90-95% of the filtered solutes have been reabsorbed and returned to the renal bloodstream. Ions (K^+, H^+), metabolic and toxic wastes have been secreted in the urine to maintain blood pH and remove substances from the body [8] (Fig.16B). The accumulation of those metabolic wastes are toxic for the organism, specifically for the central nervous system. They also secrete foreign substances from the diet such as drugs, environmental toxins, and derivatives from hormonal catabolism. All of those components are progressively eliminated from the body when they are synthesized.

iii) Hormonal and neuronal regulation of the homeostasis

Urine formation relies on blood filtration followed by the reabsorption and secretion of solutes and other nutrients to maintain the homeostasis. Each step is monitored at different levels: renal autoregulation, hormonal and neuronal mechanisms are involved.

The GFR and renal blood flow stayed quite constant overtime, even when practicing exercises, thanks to the **renal autoregulation**. It is based on two mechanisms: the myogenic process and the tubuloglomerular feedback. The **myogenic mechanism** regulates renal blood flow and GFR within seconds after blood pressure or arterial pressure changing. Indeed, when the blood flow rate increases, the GFR increases as well, which stretches the afferent arteriole. The smooth muscle fibers around this arteriole then contract to reduce the blood flow and the GFR, establishing an equilibrium. The reverse phenomenon occurs in response to a low blood flow and GFR: the smooth muscle fibers dilate leading to a decrease of GFR. Moreover, another slower mechanism takes place to act on water and solutes reabsorption in the renal tubule cells: the **tubuloglomerular feedback**. Indeed, the macula densa inhibits the secretion of nitric oxide (NO), a vasodilatator, by the juxtaglomerular cells when GFR is above a normal value. The absence of NO promotes the afferent arteriole constriction to reduce the blood flow, and favours ions and water reabsorption in the PCT and the nephron loop. The GFR and the blood flow go back to normal. As with the myogenic mechanism, this cascade of molecular events is reversible [5][6].

Furthermore, the sympathetic nervous system (SNS) supplies kidneys with nerves through which it secretes a vasoconstrictor hormone, the norepinephrine. This hormone, synthesized by the adrenal gland, induces the contraction of the smooth muscle fibers surrounding the afferent arteriole, in response to a high GFR. The blood flow then drops, as

well as the GFR, which promotes a urine output reduction to increase blood volume or hypervolemia, and distributes the blood flow to other organs. Similarly, the norepinephrine affects the efferent arteriole when the SNS is moderately stimulated. Although this neuronal axe is involved in GFR decline, it is predominantly activated for emergency cases such as during a haemorrhage. Otherwise, the renal autoregulation monitors the GFR changes.

Another level of control influences the GFR variations overtime, playing on different steps of the urine formation along the nephrotic segments: the **hormonal regulation**. Five hormones are involved in ions and water reabsorption/secretion to regulate the GFR: the **renine-angiotensine-aldosterone axe**, the **Antidiuretic Hormone (ADH)**, the Atrial Natriuretic Hormone (ANP) and the Parathyroid Hormone (PTH). We will focus on three of them, the main targets used in pharmacology to improve some renal disorders.

The first system depends on three molecular actors: **renine-angiotensine-aldosterone**. In response to hypovolemia and hypotension, the juxtaglomerular cells secrete the enzyme renine. This enzyme cleaves the angiotensinogen protein from the liver to produce angiotensin I. This peptide is then cleaved by another enzyme, the angiotensin-converting enzyme (ACE) to form the angiotensin II. Eventually, this last active hormonal form constricts the afferent arteriole to decrease the GFR, which induces active ions reabsorption and reduces hypokalaemia, hypernatremia in the PCT. It then enhances the secretion of the aldosterone, another hormone playing on ions reabsorption/secretion. Together, those three molecules lead to an increase of blood volume, and thus, of the arterial pressure.

It is also possible to regulate plasma osmolarity and hypovolemia, acting on the epithelial permeability of the late DCT and collecting duct, last sections of the nephron. Indeed, a low plasma osmolarity is detected by the osmoreceptors located in the hypothalamus, which leads to **ADH** secretion in the bloodstream. The Antidiuretic Hormone (ADH), also called vasopressin, promotes the exocytosis of a channel water, the aquaporine-2 (AQP2), in the apical membrane of DCT and collecting duct. As a consequence, these sections become more permeable to water reabsorption, which favours hypervolemia, plasma osmolarity drop, and more concentrated urine. The AQP2 exocytosis progressively decreases as the ADH level in the renal bloodstream declines, leading to less water reabsorption and a return to normal osmolarity. This hormonal mechanism is particularly stimulated in case of severe dehydration or haemorrhage. With less ADH secretion, urine is more diluted.

iv) Tubular excretion: regulation of urine concentration

One of the main kidney function is to maintain the blood osmolarity at 300 mOsmol/liter, which depends on urine volume and concentration. Local osmolarity, varying between 300 and 1200 mOsmol/liter in the interstitial fluid and in the renal medulla, is preserved all along the renal tubule by two mechanisms. The first one takes place during the filtration/reabsorption/secretion processes and has been described above. The second one is called the **countercurrent flow**, which means that the fluid flows in two opposite directions. Two countercurrent mechanisms occur in the kidney: the countercurrent multiplication and the countercurrent exchange. Blood circulation in the peritubular capillaries and fluid circulation within the tubule flow in two opposite directions, and in closed parallelly disposed tubules. Tubular fluid goes through the descending limb where only water is reabsorbed to progressively increase the osmotic gradient in this tubule. Then, it flows in the impermeable ascending limb (devoids of aquaporins) where ions (Na^+, Cl^-) are reabsorbed by active transporters. The long nephron loop goes deeply in the medulla, where the countercurrent is amplified: the loop runs as a **countercurrent multiplier** (Fig.17). Arriving in the early DCT, the urine is diluted, but is then concentrated again. Indeed, the late DCT and collecting duct localised in the medulla are more permeable to water and urea, which increases urine concentration. The countercurrent flow leads to more concentrated urine excreted, but at a low volume. In the meantime, the **countercurrent exchanger** favours exchanges between the blood of the vasa recta belonging to the peritubular capillaries, and the interstitial fluids in the medulla, which is due to the countercurrent flow (Fig.17). Indeed, the vasa recta, close to the descending and ascending limb where the countercurrent flow occurs, exchanges solutes and water with those tubules. It works as a countercurrent exchanger to keep the gradient created by the countercurrent multiplication, and supply the renal medulla with oxygen, and nutrients [8]–[10]. Then, the fluid excreted

enters the calyces where no further reabsorption takes place: urine drains into the bladder to be temporarily stored and eliminated.

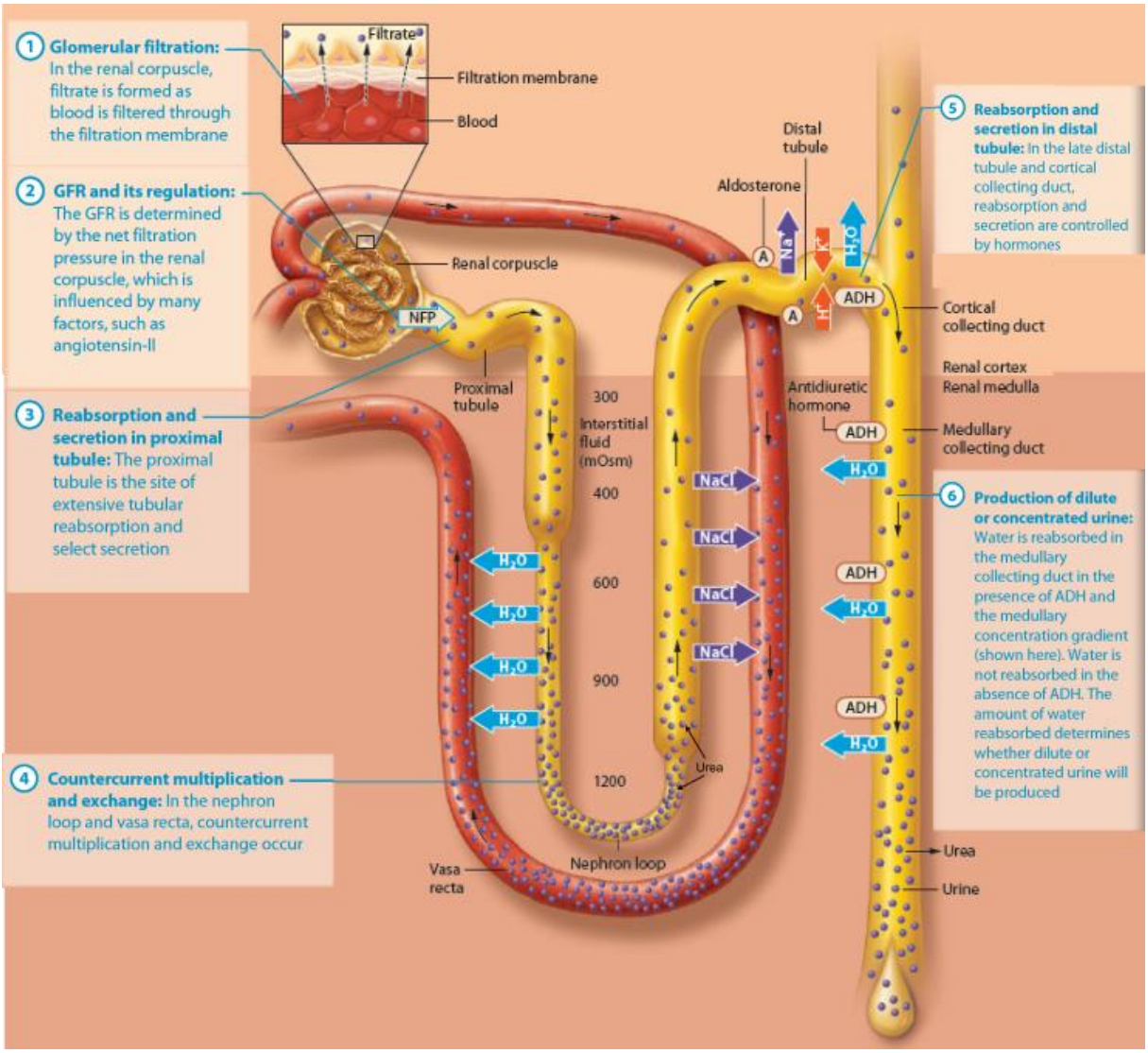

Figure 17: Schematics illustrating the countercurrent functioning, and urine formation along the renal tubule, with ions and water exchanges. The countercurrent, multiplier and exchanger, favours concentrated or diluted urine formation along the renal tubule, and the urea recycling between the interstitium and the tubule.

Source: adapted from Urinary system course.

2) ADPKD or Autosomal Polycystic Kidney Disease

a) Clinical presentation of ADPKD

i) ADPKD symptoms

Potentially lethal, the ADPKD affects millions of people all over the world, and is the fourth most common cause of end-stage renal failure worldwide [1][2]. With its unmistakable hallmarks mainly generated by a unique gene's power, the whole functions dependent anatomy of the kidney is impaired. Indeed, this organ's architecture is commonly sublimely intertwined with its physiological functions [11].

Most of the patients suffering from Autosomal Dominant Polycystic Kidney Disease (ADPKD) have a family history of Polycystic Kidney Disease (PKD). Although in 10% of the cases, this common renal disorder is due to a new mutation, ADPKD can be caused by mutation in two different genes, *PKD1* or *PKD2* [1], [2], [11]–[14]. Indeed, around 85% of ADPKD patients display a mutation in the *PKD1* (polycystic kidney disease-1) gene, while approximately 15% are caused by a mutation in the *PKD2* (polycystic kidney disease-2) gene. *PKD1* and *PKD2* genes encode the polycystin-1 (PC1) and polycystin-2 (PC2) proteins, respectively [1], [2], [11]–[14]. The type 2 ADPKD (ADPKD2) caused by a mutation in *PKD2* gene, displays less severe symptoms, but similar to the type 1 [1], [15]–[18] [19]. Kidneys and cysts, that are fluid-filled cavities composed of dedifferentiated epithelial cells deriving from preexisting tubules, have a smaller size and shape. The end stage renal disease (ESRD) emerges later: around 70 years old in average, meaning 20 years later than with the ADPKD1 [1], [2], [11]–[13]. The clinical presentation of both types of ADPKD is close, and almost all patients will develop renal cysts. Nevertheless, patients with *PKD1* mutations develop twice as many cysts as patients expressing a mutation in *PKD2* gene, and the cystogenesis begins earlier [13].

ADPKD is characterized by enlarged kidneys in which progressive numerous and bilateral fluid-filled cysts extend from renal tubular epithelial cells [11][13][20][21]. The irreversible progressive expansion of cysts compresses and propagates throughout the renal parenchyma, which eventually leads to renal failure in adulthood [9][11][20]. This physiological process occurs during a lifetime, and the progressive loss of kidney functions takes place around the age of 40 to 50 years old, when kidneys are largely encysted

[8][10][11][20] (Fig.18). Half of the patients suffering from ADPKD will need dialysis or transplantation to compensate the ESRD associated with renal dysfunctions [8][9].

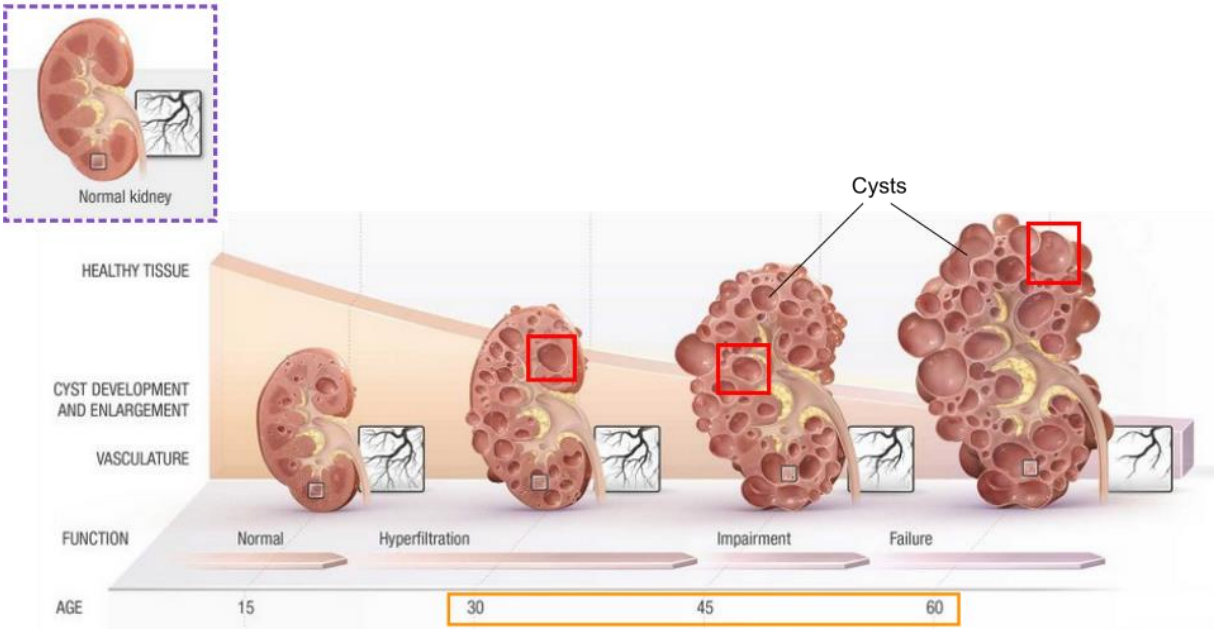

Figure 18: Schematic illustrating ADPKD evolution. From healthy kidney (purple insets), cysts progressively expend and grow (red insets), which is correlated to an increase of the kidney size. Over time, kidney functions decline (orange inset): able to perform hyperfiltration by compensation, a threshold inducing renal failure is reached. Meanwhile, renal bloodstream degenerates with cysts growth.
Source: adapted from

ii) Renal and extra-renal complications

Besides renal phenotypes due to ADPKD evolution, this disease is related to renal and extra-renal complications impairing the functions of several organs (heart, lung, liver, gut) [1]–[4][7]. Cardiovascular and gastrointestinal abnormalities lead to hypertension, one of the major complication of ADPKD. This strong risk factor favors a reduced GFR (Glomerular Filtration Rate), an increase Total Kidney Volume (TKV), and activation of the renin-angiotensin-aldosterone system described above [1][3][4][6][7]. Renal cystogenesis is also associated to kidney stones formation or nephrolithiasis for 25-35% of the patients [1][14]. Because of nephrons damage during ADPKD evolution, the stones are more likely localized in the renal tubules and collecting ducts than in the bladder or the ureter, which decreases urine volumes

and pH, and induces hypocitraturia (low amount of citrate in the urine). Some patients with ADPKD will also develop symptomatic urinary tract infections (UTI) that may manifest with cyst infection. All those renal complications occurring with APDKD development are combined with pain severity that is often independent of cysts and kidney size. This pain is experienced by around 60% of ADPKD patients before or after its diagnosis [25]–[28]. It is generally followed by hematuria (presence of blood in the urine), because of cyst rupture/hemorrhage [29]–[31]. The frequency of hematuria is correlated to kidney size, blood pressure and high risk of ESRD. Hence, the cysts growth over time and the subsequent enlargement of renal capsule favor abnormal posture and chronic musculoskeletal constraints [1].

On another note, ADPKD underlies side effects affecting different organs. Most patients suffering from ADPKD develop polycystic liver disease (PLD) with solitary hepatic cysts [32]. Progressive hepatic cysts growth favors liver enlargement compressing the surrounding tissues, and leading to a multitude of other symptoms that often remain asymptomatic. However, ADPKD patients may be affected with infected liver cysts that provoke pain among other things, although infected renal cysts is more common. Furthermore, ADPKD development induces cardiovascular complications such as pericardial effusion, valvular abnormalities, or coronary aneurysm. Aneurysms can also happen in the brain of patients with ADPKD, which is called intracranial aneurysms (ICA) [33][34]. Eventually, ADPKD further impacts the gastrointestinal and respiratory tracts mainly during the ESRD, when patients need renal transplant [35]. Indeed, polycystin proteins dysfunction may contribute to the development of diverticular disease, while PC1 mutation may disturb the respiratory tract and enlarge it, which triggers bronchiectasis.

iii) ADPKD diagnosis methods

Nowadays, two clinical situations have been established to assess ADPKD diagnosis. Depending on the history family presence or not, patients potentially suffering from ADPKD with or without symptoms take medical imaging, before a possible genetic test [8][14]. The initial imaging approach is the ultrasonography to confirm or exclude the diagnosis. Indeed, this method is widely available and non-invasive. However, its resolution is limited: it allows the detection of cysts above 1 cm diameter, although the high-definition ultrasound provides the identification of smaller cysts (2-3 mm) [13][36]. The total kidney volume (TKV) as well as cysts number, size, volume and topography are determined (Fig.19).

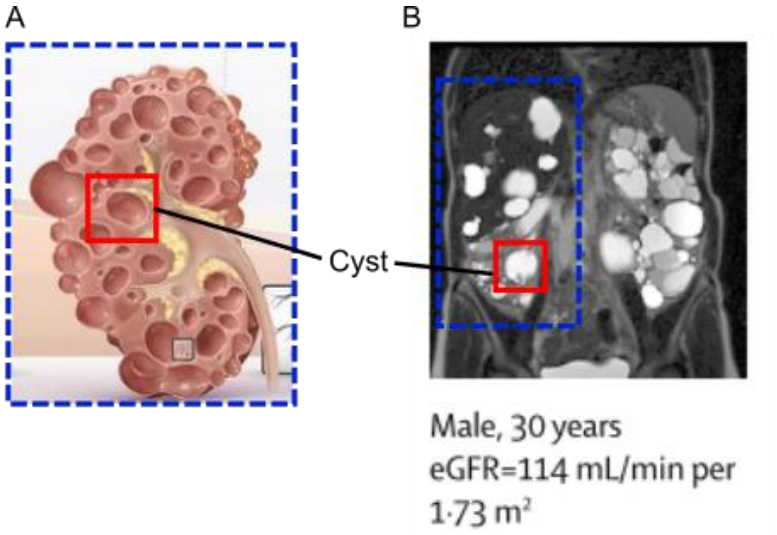

Figure 19: Renal imaging of a patient suffering from ADPKD. A: Schematic of an encysted kidney. The red inset focus on one cyst. B: MRI of a male patient in its early 30s for whom the molecular analysis revealed a non-truncating mutation in *PKD1* gene. The blue inset highlights one kidney whereas the red one indicates one cyst. eGFR: estimated Glomerular Filtration Rate.
Source: adapted from [12].

On the one hand, for patients with a history family, magnetic resonance imaging or MRI can improve and refine renal cysts detection to come up with a diagnosis. Indeed, MRI is significantly more sensitive than the ultrasound technic to characterize kidney architecture and cysts. Displaying more than ten kidney cysts, those patients suffer from ADPKD [13].

Furthermore, they exhibit an increase probability of cysts growth with age, which can be predicted thanks to MRI [1].

On the other hand, for patients with unknown family history (about 10-25% of patients with ADPKD), diagnosis based on imaging is not sufficient [36]–[38]. After having carefully excluded other renal cystic diseases, and performed different imaging methods, a genetic test is required to confirm ADPKD diagnosis. The ADPKD diagnosis is confirmed if the patient displays bilateral kidney enlargement with more than ten cysts [39].

Hence, ADPKD evolution and diagnosis depends on total kidney volume (TKV) and cysts volume in combination with renal and extra-renal complications such as hypertension, hematuria, nephrolithiasis, or cardiovascular and gastrointestinal abnormalities. It is also linked to the patient's gender and age: males experience more severe hypertension and renal dysfunctions than females [1].

For the next part, we will discuss the **molecular actors** involved in this disease, and **their effects** on the mechanical and architectural features of the kidneys.

b) ADPKD mechanical and molecular aspects

i) Structure and roles of PC1 and PC2

During the past few years, research extensively focused on the understanding of the functions of polycystins 1 and 2 (PC1 and PC2), as part of the knowledge on ADPKD. It has been shown that their expression level is fundamental to maintain the renal epithelium architecture (see below, I) 2) c)). Indeed, they are involved in many different signaling pathways regulating proliferation, apoptosis, cell adhesion or differentiation [8][10][11].

The two genes causing ADPKD were discovered with the same method, the positional cloning. In 1994, the first gene *PKD1* localized on the chromosome 16p13.3 was found, followed two years later by the discovery of the second gene *PKD2*, on the chromosome 4q21 [8][11][40]–[43].

PKD1 gene encodes PC1 protein, a 450kDa protein split in several segments needed for its intracellular localization and its functions. This protein consists of: a short C-terminus (198 amino acids) involved in the regulation of diverse signaling pathways, 11 transmembrane domains maintaining it at plasma membrane and endoplasmic reticulum, and a long N-terminal extremity (around 3000 amino acids) ensuring interactions between proteins and with the matrix. This extremity also mediates the sensing of mechanical stimuli (Fig.20, left diagram) [44]–[49].

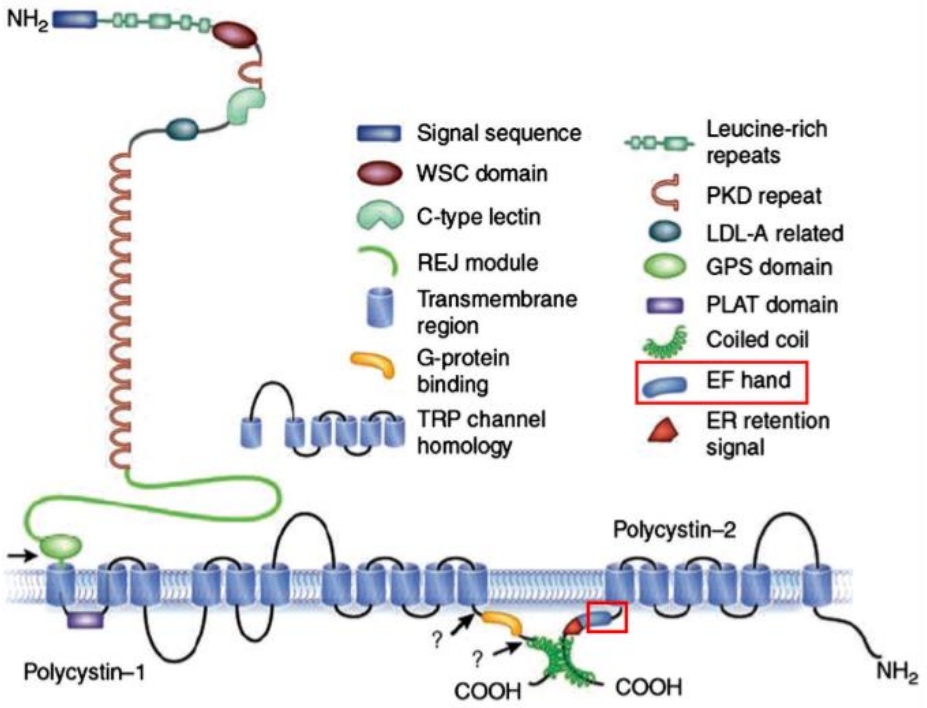

Figure 20: Illustrations of polycystin-1 (on the left) and polycystin-2 (on the right) structures, with their different domains allowing their interaction with other molecular partners. The red inset signals PC2 EF hand-calcium sensitive motif. Both proteins interact through their C-terminal extremities. Recently, it has been shown that PC1 may directly activate genes transcription by cleavage (possible cleavage sites indicated by the arrows), and translocation of the C-terminus to the nucleus. TRP: Transient Receptor Potential.
Source: adapted from [8]

PC1 N-terminus must be cleaved in its G protein-coupled receptor proteolytic site (GPS) to be fully functional. Otherwise, a full-length PC-1 protein favors ADPKD [48][50]. As a result, there is a pool of uncleaved PC1 within the renal cells, and another one of PC1 temporarily nonconvalently bound to the plasma membrane [51][52]. The C-terminal extremity

can also be cleaved in response to fluid flow decrease, as it was observed in mouse kidney model [53]. PC1 tail accumulates in the cytoplasm of cells lining ADPKD cysts in particular, and translocates in the nucleus where it can interact with transcription factors and activate different signaling pathways [54].

This transmembrane protein localizes at junctional complexes of polarized epithelial cells to favor cell-cell and cell-matrix contacts, playing a part in their establishment [55]–[58]. It is expressed in the epithelial cells of the developing and mature renal tubules, as well as in many other tissues such as heart, liver, bone, and endocrine glands [58]–[60].

Polycystin-2 (PC2), encoded by *PKD2* gene, belongs to the Transient Receptor Potential (TRP) family, and is a calcium-permeable nonselective cationic channel [55][56]. This channel is composed of 968 amino acids structured in six transmembrane domains, a short intracellular N-terminus, and a C-terminal extremity interacting with PC1 [1][3][4][32][43]. PC2 C-terminus consists of different segments: a coiled-coil region interacting with PC1, an EF-hand binding to calcium, and an endoplasmic reticulum retention domains to maintain this protein in the ER and the Golgi apparatus [55][57]–[60][68]. The EF-hand senses intracellular calcium concentration with a micromolar affinity [64] (Fig.20, right diagram). The C-terminus cleavage favors ADPKD.

PC2 is mainly expressed in the endoplasmic reticulum (ER) and the Golgi apparatus [69]. Within the ER that is a calcium intracellular store, PC2 monitors calcium release, in response to local increase intracellular calcium concentrations [1][32][70][71]. For this purpose, it combines with two other calcium channels: it inhibits the ryanodine receptor, and the inositol 1, 4, 5-triphosphate receptor (IP3R) to avoid calcium influx within intracellular stores [62][63]. PC2 is also found in the mitotic spindles where it is involved in cytoskeletal rearrangement and cytokynesis [74]–[76].

Both polycystin proteins interact through their C-terminal tails to form a complex [77]. They are localized in the primary cilium where they may sense flow variations and mechanical pressure in the kidney [78]. PC1 could directly sense urine flow, and mediates the activation of PC2 to regulate calcium influx in this organelle [76][79][80]. PC1 assists PC2 to form a functional calcium channel [81]. Nevertheless, Liu and coworkers recently outlined that PC2 can shape as a functional cation channel in the primary cilium of pIMCD cells (primary Inner Medullary Collecting duct) lacking PC1 expression. Their findings suggested that PC1-PC2

interaction is not essential for PC2 channel activity in the primary cilia [79], [82]. PC1-PC2 complex is also noticed at the plasma membrane, and in the ER [83]. In the focal contacts, polycystin proteins bind to a variety of the actin and microtubule cytoskeletal proteins (α-actinin, filamin, talin, vinculin, etc…), and junction proteins (intercellular and cell-matrix such as E-Cadherin, integrins, etc…) [1][32][61][85].

ii) Cystogenesis mechanisms

The ADPKD macroscopic hallmark is the **progressive and prominent fluid-filled cysts formation from the epithelial tubule**, which is a striking effect compare to the normally tightly tubules arrangement in a healthy kidney.

The first hypothesis mentioning cyst formation and propagation focused on three fundamental mechanisms: **cell proliferation** to line developing cystic cavities, **fluid secretion** within the cysts, and the **extracellular matrix remodeling** surrounding growing cysts [86]. Each of this mechanism is based on the stimulation of different signaling pathways that therapeutic treatments can target.

Cystic epithelial cells are dedifferentiated and persistently proliferative to surround the fluid-filled cavity, rather than to stretch the epithelial layer [87]–[89]. Indeed, early histologic studies mentioned that cystic cells are not larger than normal cells, but express more proto-oncogenes in rodent. This observations corroborate cell proliferation increase to promote cystogenesis, albeit it progresses over decades [90][91]. Furthermore, other studies described that cystic cell proliferation is induced by MAP kinase signaling pathway stimulation [92]. Indeed, PC1 truncated form cannot interact properly with PC2 to create a functional calcium channel, which lowers calcium intracellular concentrations and activates cAMP (Cyclic Adenosine Monophosphate). In turn, it enhances MAPK signaling pathway [93][94]. Lately, several clinical trials were performed, and mainly targeted signaling pathways involved in cell proliferation such as mTOR, Hippo or cAMP that favors fluid secretion within the cysts. Indeed, it was shown that Hippo signaling pathway is impaired in polycystic kidney diseases such as ADPKD. Hippo is involved in size organ control, by playing on cell proliferation and apoptosis in response to mechanical stimuli. Notably, it was observed that the last effector of this signaling pathway, the transcriptional co-activator YAP (Yes-associated Protein) is in the nucleus of cystic cells, whereas it is usually found in the cytoplasm. YAP could stimulate target

genes transcription leading to cell proliferation, and inhibiting cell apoptosis. This balance would drive cyst growth [95].

Renal cysts can derive from all renal tubular segments, between the Bowman's capsule and the collecting duct. In ADPKD patients, cysts can derive from different tubular segments (proximal or distal). However, according to some studies, most of the human cysts are originated from the distal tubule and the collecting duct [1]. When their size reaches between 2 and 3 mm, they detach from the parent tubule and migrate away [1].

A significant cell proliferation could induce a loss of planar cell polarity (PCP) during cell division within the tubes, and could initiate cyst formation [96]. Indeed, tubular epithelial cells mutated for PKD1 or PKD2 do not divide along the lumen axis, which favors tubule expansion instead of its elongation. The PCP signaling pathway indirectly regulates cyst growth, playing on the expression of some of its effectors like Fjx1 (Four-jointed). Indeed, a decline of Fjx1 mRNA was noted in mice depleted in Pkd1, and in response to renal tubular epithelium injury. Both the injury and the Pkd1 mutation could accelerate exponential cysts growth [96]. This pathway interferes with Hippo signaling pathway also involved in cyst expansion. Cell orientation during mitosis is one of the cellular and mechanical event promoting cyst development [97]. Then, cysts expend and compress the surrounding renal parenchyma because of transepithelial fluid reversion in the lumen: fluid secretion occurs instead of fluid absorption [12]. cAMP stimulation in cystic cells promotes chloride secretion and water movement (osmosis) by the apical cystic fibrosis transmembrane conductance regulator (CFTR) and the basolateral NKCCl cotransporter [73][74][98]–[100]. Indeed, injection of forskolin or secretin, two agonists of the adenylyl cyclase, a cAMP effector, stimulates fluid secretion in vitro and in an in vivo murin model [101]. Similarly, inhibitors of CFTR avoid chloride secretion which inhibits/prevents cysts growth [84][85]. Furthermore, another transporter, the Na+/K+ ATPase, influences the electrochemical gradient in cystic cells. Its mislocalization to the apical side instead of the basolateral side reverses the polarity for fluid absorption[104]–[106]. In addition, abnormal water absorption is mediated by aquaporin proteins (AQP1 and AQP2) along the renal tubule (see details in I) 1) b)). In particular, vasopressin proportionally increases AQP2 expression with the cyst size in human to worsen ADPKD [107].

In the meantime, cystogenesis favors structure and composition of the surrounding extracellular matrix (ECM) alteration [108]. Many proteins expression needed for its

remodeling shifts, such as collagens I and IV, metalloproteases activators and inhibitors, and integrins [1]. Nevertheless, the extracellular matrix composition, and in particular, its basal membrane on which renal epithelial cells lie, is crucial for cyst formation and propagation. Cysts constraint the functional renal parenchyma, and participate to its progressive failure during ADPKD. This phenomenon is associated with interstitial inflammation and fibrosis (an excess of fibrous connective tissue), which incites inflammatory mediators recruitment to promote cysts expansion [109]–[111].

iii) Clinical trials and current treatments

The slow progression of ADPKD, and the current methods used for the diagnosis and prognosis, contribute to a fast development of therapies. The race to find treatments delaying cystogenesis, to reduce the decline of kidney functions, and to improve patients life gave rise to several clinical trials with targeted therapies [112]–[116].

Most of the therapeutic molecules developed play on cell proliferation and/or fluid and electrolytes secretion to reduce cyst growth during ADPKD progression [117]. cAMP favors cell proliferation and fluid secretion by renal cystic cells. This effector stimulates the apical CFTR chloride channel aforementioned in the previous subsection (I) 2) b)ii)), and the ADH that activates the synthesis of the vasopressin-2 receptor (V2R), a water channel. A CFTR inhibitor, the CFTRinh172, and V2R antagonists, like Tolvaptan, were used: both slightly decreased cyst expansion [99] [118][117][118]. Trials with Tolvaptan were done on different PKD rodent models, as well as on ADPKD patients through the TEMPO (Tolvaptan Efficacy in Modifying PKD Outcomes) clinical trial. However, although it improved global renal functions (slowdown of cystogenesis, GFR, and renal pain decrease), ADPKD patients displayed liver function abnormalities, which limits its use [122]–[125]. Therefore, this treatment has been approved to improve ADPKD patient life in Japan, Canada and Europe. Similarly, somatostatin and its analogs (ocreotide, lanreotide, or pasireotide) slow cysts growth by inhibiting cAMP in liver and kidneys, in different animal models and chosen ADPKD patients [97]–[100][130]. Renal and liver functions are improved for a few patients, but gastrointestinal symptoms among others might limit their use [131].

Two other groups of molecules affect abnormal cell proliferation during cyst formation, and help controlling hypertension, first ADPKD complication. One of the main signaling pathway involved in controlling cell proliferation is mTOR, inhibited by different drugs

(sirolimus and everolimus, rapamycin) [101][102]. This inhibitor and its analogs have beneficial effects in animal models, but many side-effects in ADPKD patients, which restricts its potential utility [134][132][133]. Eventually, to treat the hypertension of ADPKD patients, a combination of two drugs inhibiting two different actors of the Renin-Angiotensin-Aldosterone axis are prescribed: the Angiotensin Receptor Blocker (ARB) and Angiotensin Converting Enzyme Inhibitors (ACEI) (see details about this axe I) 1) c)) [137].

All of the proposed therapies are, for the more hopeful, under clinical trials. They do not prevent eGFR decline in APDKD patients, albeit they slightly improve their daily life, especially when the disease reaches the end stage. Other therapies emerged to delay/suppress ESRD of the ADPKD, targeting the regulation of mitosis (Roscovitine, an anti-proliferative drug) for instance, inhibitors of the tyrosine kinase involved in the MAPK signaling pathway, etc [138].

c) Factors leading to the Snowball effect

i) Polycystin proteins dosage theory

Studies performed in *Pkd1* and *Pkd2* knockout mice, which means depleted for those genes, highlighted that their homozygous inactivation leads to complete loss of PC1 and PC2 expression. These complete inactivation is embryonically lethal [139]. Nevertheless, mice expressing homozygous *Pkd1* or *Pkd2* hypomorphic alleles, that generate a partial loss of gene function, live and develop ADPKD over time. Those first observations clearly indicate the significant importance of a threshold level for polycystin proteins expression in cystogenesis: the dosage-sensitive model of polycystins during ADPKD has been established [17][140]–[142]. In particular, the *PKD1* gene dosage (or *PKD2*) has a notable impact on ADPKD initiation and severity [17]. In line with those studies, a threshold level of dysfunctional polycystins has been established: 60% of dysfunctional PC1 favors late onset of ESRD in humans, and slows cystogenesis in knock-in mice [143]. Below 20% of normal PC1 dosage, the rate of cysts initiation and expansion drastically increases in mice [144]. Thus, PC1 dosage seems to play a central role in cyst growth rate (Fig.21).

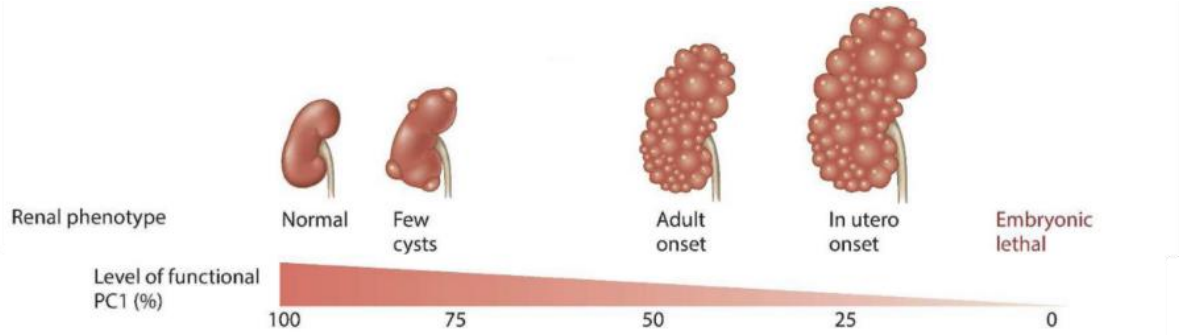

Figure 21: Diagram representing the dosage-sensitive model of polycystins during ADPKD. The level of functional PC1 depicted on the bottom influences the renal cystogenesis progress. A halving reduction of PC1 is associated with adult onset disease, whereas an absence of PC1 is lethal.
Source: adapted from [141]

Besides, ADPKD severity is caused by the time of gene inactivation, and thus, the time without PC1 and PC2 functional proteins. Indeed, temporarily controlled depletion of each polycystin proteins (PC1 or PC2) in mice kidneys has a worse effect on developing kidneys than on mature ones [145]–[147]. These observations emphasize that polycystins are required during cell proliferation occurring for post-natal renal development. Otherwise, cystogenesis process is favored.

ii) Somatic second-hit mutation theory

The gradual cyst expansion during the human lifetime suggests that the heterozygous mutation of *PKD1* or *PKD2* genes is not enough to favor this phenomenon [148]. A second mutation (environmental or stochastic factors) promoting the loss of the second allele is found in a significant proportion of cysts: this is the somatic **second hit mutation theory** [68]. Indeed, *Pkd1* mutated mice subjected to renal injury display an acceleration of cyst growth [149][150]. Moreover, heterozygous mice for Pkd1 or Pkd2 genes are more sensitive to renal injury that promotes inflammation and fibrosis [151].

Cysts derive from clonal growth of single cells within the tubules, which implies that all cells lining one cyst have the same genotype in the end. They frequently lose the remaining wild-type allele because of a somatic mutation [1][3][4][13]. Hence, each cyst harbors a distinct somatic mutation, and has a different size. To determine cystic constitution, mosaic embryos composed of *Pkd1*$^{-/-}$ cells and wild-type cells were generated. Gradually, *Pkd1*$^{-/-}$ cells replaced

the wild-type cells that underwent apoptosis, which suggests that cystogenesis is caused by a somatic second hit mutation in the *PKD1* gene, and programmed cell death in the surrounding cells [152] (Fig.22).

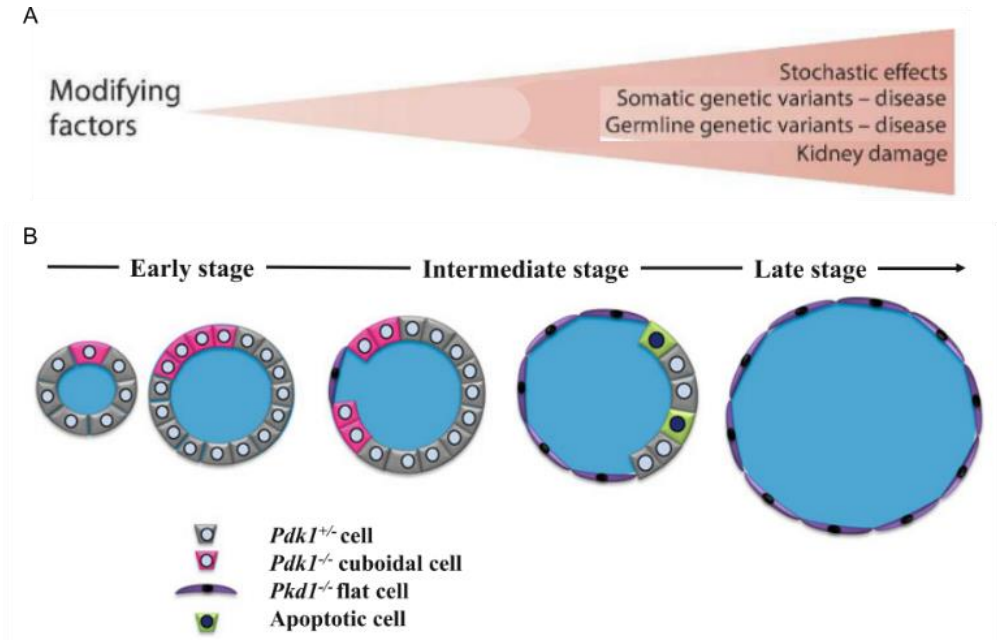

Figure 22: Diagram illustrating the cystogenesis progress during ADPKD. A: Arrow describing the genetic and somatic accumulation factors accelerating the functional allele loss of the *PKD1* gene, and promoting kidney dysfunction. B: Schematic of the cyst development between the early and late stage of the disease. At the ESRD, cysts are lined with flat *Pkd1* $^{-/-}$ cells, according to the cystogenesis model reported by Mochizuki and al. Source: adapted from [13, 141].

As a consequence, cyst cell composition is heterogeneous, with cells progressively shedding the wild-type allele of the *PKD1* (or *PKD2*) gene, which leads to the slow ADPKD evolution over the course of decades, and to cyst expansion [1][3][13]. The level of PC1 protein expression (and PC2 protein to a lesser extent), the penetrance of pathogenic alleles, and stage of development of kidney heterozygous for the *PKD1* gene play a role in ADPKD progression and severity [43][153].

iii) The snowball effect theory

Recent studies on ADPKD patients and specific mice models progressively developing ADPKD suggest that first cysts randomly form along the renal tubules. Those primary cysts then drive new cysts formation in their vicinity [22]. The secondary cysts cluster around early ones [11]. In particular, Peters and al were the first ones to describe this phenomenon in order to specifically recapitulate human ADPKD. To this end, they generated specific adult mice models in which kidney-specific Pkd1 deletion is induced by tamoxifen injections (iKsp-Pkd1 del). Using the lowest dose of tamoxifen (0.25 mg), only 8% of renal cells displayed scattered Pkd1 gene deletion, which neither promoted cystogenesis in six months, nor was the following renal injury induced to accelerate this process. Nevertheless, after a long dormant period with a low frequency of cyst formation, scattered Pkd1 deletion in association with renal injury favored a fast and exponential cyst growth. Other studies demonstrated that Pdk1 deletion in addition to renal injury increased cystogenesis, which was not observed in this work [11][150][151], [154]. The first renal cysts increased in size over time and continuously exert a force on the surrounding tissue. Indeed, nephrons are parallel and tightly packed, suggesting that the deformation of one tube may affect unimpaired adjacent tubules without cysts. This observation implies that first cyst formation may promote new cyst formation as a cascading and exponential effect: this is the "Snowball effect theory". This theory relates that tubule compression by first cysts triggers cystic snowball effect leading to abnormal signalling pathways activation within renal epithelial cells.

Furthermore, as aforementioned, the PC1-PC2 complex is localized in the primary cilium of renal epithelial cells where it acts as a mechanosensor. However, *Pkd1* gene depletion leads to a decline of PC1 expression, which cannot interact with PC2 in the primary cilia of renal epithelial cells. Although it has been reported that the PC2 protein can form a functional cation channel (preferentially K^+ and Na^+ influx instead of Ca^{2+} influx) compensating PC1 absence in the primary cilium, cystogenesis was observed in the new conditional mice models developed to decipher cilia involvement in the ADPKD. Indeed, those mice, Arl13b-EGFPtg:cPkd1 and Arl13b-EGFPtg:cPkd2 were conditionally knocked out for *Pkd1* or *Pkd2* genes upon doxycycline mix in the water drinking. They also expressed a transgene (Arl13b-EGFPtg) to visualize primary cilia during cystogenesis evolution [155]. This tiny and immotile hair-like organelle is essential to maintain epithelial cell differentiation, organ size and morphogenesis [76]. Displaying many receptors and channels on its plasma membrane, the

primary cilium integrates extracellular mechanical and chemical stimuli [156], [157]. In the renal epithelial cells, it shapes toward the tubule lumen where it senses fluid flows. Besides, in *Pkd1* KO (Knockout) murin models, albeit the length of cilia was not significantly different from the one of normal cells, those mutated cells were not able to sense flow variations to regulate fluid and solutes reabsorption/secretion processes along the tubule [1], [55], [156], [158], [159]. In ADPKD patients, cystic cells exhibit impaired ciliogenesis, which takes part in cyst formation and categorized this disease as a ciliopathy [160], [161].

Currently, the quest of new drugs is making a major stride to eliminate cystogenesis in ADPKD patients. Nevertheless, trials on animal models before clinical trials on only a few patients delay the discovery of potential more efficient molecules. There is a need in the existing research domain to develop an in vitro biomimetic models of this most common renal disorder, the ADPKD, to screen as many drugs as possible, and find out the most powerful and the least toxic. This leads us to the new and ongoing development of organ-on-chip era, more precisely, the kidney-on-chip, to open promising pharmacological approaches.

3) From Organ-on-chip to Kidney-on-chip development

a) Birth of the Organ-on-Chip field

To study human physiology and more specifically different diseases mechanisms such as renal disorders, scientists commonly used *in vivo* animal models like rodents or amphibians, from which the observations were not uncritically translated to human beings. Therefore, in the 1960s, with ethical concerns arising, Russel and Burch postulated the need of alternative methods based on the 3R principle: the Reduction, Refinement, and Replacement of animal experiments [162]. For this purpose, increasing *in vitro* models have been designed during the 20th century, leading to the Organ-On-a-chip field emergence [163].

i) Organ-On-Chips' platforms: an innovative device

The term Organ-On-Chip (OOC) was invented in 2010, by Donald Ingber who created a microfluidic chip to reproduce the human lung three dimensional cell-cell interactions, and functions [162][164][165]. It refers to an innovative *in vitro* model of a tissue or organ by

mimicking its micro-environmental architecture and creating its minimal functional units on a micrometric scale, under easily monitored physiological conditions (or microfluidic-based system). Unlike the *in vivo* complex models, the OOC systems yearn for a bottom-up approach to build realistic *in vitro* models, at the tissue and/or organ level complexity, with appropriate and biocompatible materials [162][166].

The platform on which the tissue adheres relies on microfabrication techniques. It involves a replica molding process or soft lithography, mainly using polydimethylsioxane (PDMS) as bulk material [162][3], [166], [167]. It is a soft synthetic polymeric silicon-based elastomer based on silicon that has many beneficial properties for biological applications in the microengineering domain such as being optically transparent and permeable to gas. However, because of its hydrophobicity favouring non-specific adsorption of molecules, its surface needs a treatment to control molecules concentration variation and cell adhesion [166][3][162]. Other materials such as thermoplastic (polystyrene, polycarbonate, or other polymers) can also be used and/or combined with PDMS, as a bulk material for the organ-on-a-chip [164]. Indeed, the chip designed during my thesis project relies on another substrate than PDMS, which will be detailed in the next chapter. Furthermore, to increase and improve its biocompatibility, this chip material can be coated with extracellular matrix (ECM) proteins such as collagen I, fibronectin, Matrigel or laminin. Those proteins can alternatively be used as hydrogels to shape the organ or tissue three-dimensional (3D) scaffold, with the appropriate rigidity, porosity, and degradation properties. In parallel to those natural hydrogels, synthetic and hybrid hydrogels associating both advantages of the natural and synthetic hydrogels can also be used [3]. In addition to 3D scaffold, microfluidic membrane can be integrated on the chip to reproduce the barriers and interfaces between cells and/or tissues like the lung-, intestine- or brain-on-chip [168]–[170]. Physical forces can be applied on this membrane: stretching to mimic the vasculature or the epithelium, shear stress, cyclic strain and/or mechanical constraints for instance [171]–[173]. Moreover, in recent years, technological advances in microengineering, in association with microfluidics, favour the addition of sensors (biosensors and electrical sensors) within the microchip for online monitoring. It provides real-time data on tissue metabolism, which is not easily measured in animal models. Eventually, to recreate a tissue-, organ-on-a-chip as close as possible to the physiological conditions, adequate and relevant cellular models are needed. Commonly, three cell sources are utilised in the OOC field: primary cells directly providing from a living organism, without any modification, immortalized cell lines deriving from chemically or virally modified primary cells [174], and stem cells (SCs)

collected within some organs and able to differentiated in all cell types in addition to their self-renewal capabilities/potential [162][3]. Those different categories of cellular samples, with a common tendency to come from human beings, have their advantages and drawbacks. Indeed, primary cells hardly extracted from the interest organ (liver, skin, skeletal muscle, fat) [175]–[178] are challenging to maintain in culture for a long period, even if their phenotype is close to the *in vivo* tissue [174]. In contrast, immortalized cell lines lose their senescence properties leading to alteration of their phenotype [179]. However, widely used in the OOC domain, those cells have a more homogeneous population than the primary cells extracted from different donors [172][173]. The stem cells, albeit being a powerful tool because of their pluripotency (capacity to differentiate in all cell types with physiological phenotype), raise ethical concerns about human SCs use and the possibility to create a patient-on-a-chip personalized platform [174][175]. From those SCs is born the reprograming technique for the induction of pluripotent stem cells honoured with a Nobel Prize in 2012. This method promotes the reprograming of biopsies or adult tissues (keratinocytes [184], pancreatic [185]) into SCs [176][177].

With these different tools in hand, microphysiological models development make huge strides lately, especially to increase knowledge about disease mechanisms and drug efficacy testing [163].

ii) Introduction to the Single- and Multi-Organ-on-Chips

Although animal experiments helped to understand and have a global view on human body functions, those models lack physiological and pathophysiological inter-species similarity [188]. The OOC, with accurate and reliable features in the organ functions and disease modelling, are crucial to improve pre-clinical drug screening and drug toxicity before clinical trials on humans [189]. Indeed, to test more targeted drugs for peculiar diseases, pharmaceutic industries became increasingly interested in OOC as screening 3D drug platforms, an intermediate between 2D cell culture and animal models [190] [191]–[193]. In that context, around 28 organ-on-a-chip companies in less than seven years have been developed to improve preclinical safety and efficacy testing, at low cost, with less time consuming and a better efficiency [194].

The first OOC was designed in 2010 by Donald Ingber aforementioned [165]. With the previously noted concept in mind, Ingber developed the first lung-on-chip, a simple device with a stretchable membrane to mimic the breathing movements seen in the lung. Made in PDMS, this microchip has three compartments: a central channel subdivided in two by a horizontal porous and elastomeric membrane, and two channels on both sides through which a vacuum pump applied a cyclic depression to stretch the PDMS membrane. The middle part is lined with epithelial cells on the top of the membrane, and endothelial cells on the bottom, to reproduce cell-cell interactions, metabolic exchanges, and biochemical gradients. On the top part, the alveolar epithelial cells face an air-liquid interface, just like in the lung during the physiological breathing movements. Opposite to those cells, microvascular endothelial cells have been co-cultured to recapitulate the alveolar-capillary interface (Fig.23). The PDMS flexible membrane is the key feature of this chip, allowing its versatile and widely use in the OOC field to study the physiology or pathophysiology of different organs.

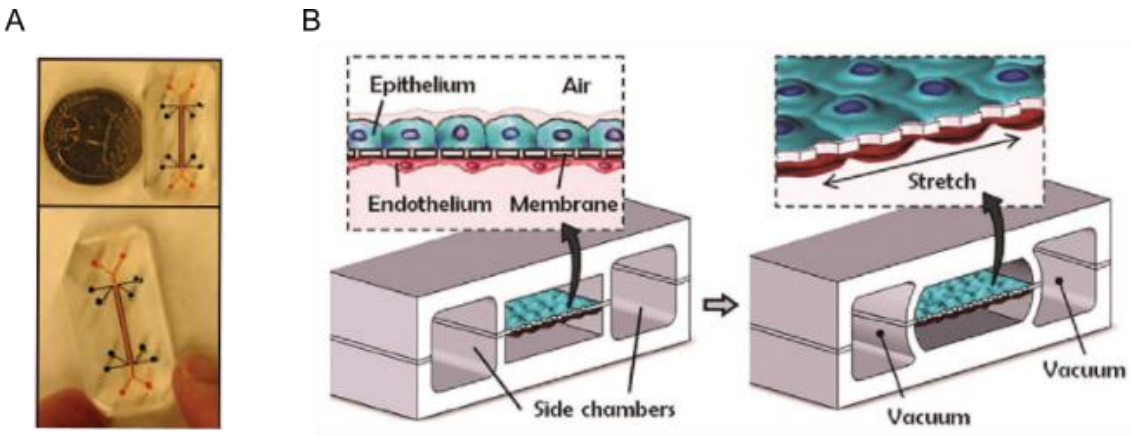

Figure 23: Illustrations of the Lung-on-chip developed by Ingber, the first organ-on-chip.
A: Pictures of the chip from the top view. The blue dye highlights the top part of the chip, and the red dye represents its bottom part. B: Schematic of the chip illustrating cells distribution within the central channel, and the mechanical force applied on it through the two other channels to favour tissue stretching.
Source: adapted from [164]

This approach was promptly followed by the development of numerous single OOC: blood vessels-, bones-, airways-, liver-, brain- or blood-brain-barrier-, gut-, and kidney-on-chip [168], [195]–[201]. It is worth noting that the liver is the first organ to metabolize drugs after their ingestion and their entering in the bloodstream. Therefore, liver toxicity is one the main

reason for drug withdrawal [23][13], [166]. Regarding the toxicological and pharmaceutical aspects, liver is the most interesting organ to study, which led to the development of many companies focused on liver-on-chips designing such as LiverChip [162], [166]. Moreover, anticancer accurate targeted therapies can fail in traditional 2D cell cultures. Therefore, there is a need to develop cancer-on-chip in order to recapitulate the complex nature and physiological tumor microenvironment (migration and angiogenesis processes in particular), and evaluate novel drugs efficiency [204], [205]. This first step in the OOC field coherently led to an increased sophistication of single-organ-on-chip to multi-organs-on-chip, to make a step forward towards human- or body-on-chip associated with targeted therapies [206]. As a way to mimic the interplay between different organs, the multi-organs-on-chip promotes the evaluation of the absorption, distribution, metabolism, and excretion (ADME) of a drug (Fig.24). First to start with the combination of two organs for the ADME process assessment, the group of Uwe Marx in Berlin (founder of TissUse company) combined a liver and a skin on the same chip in

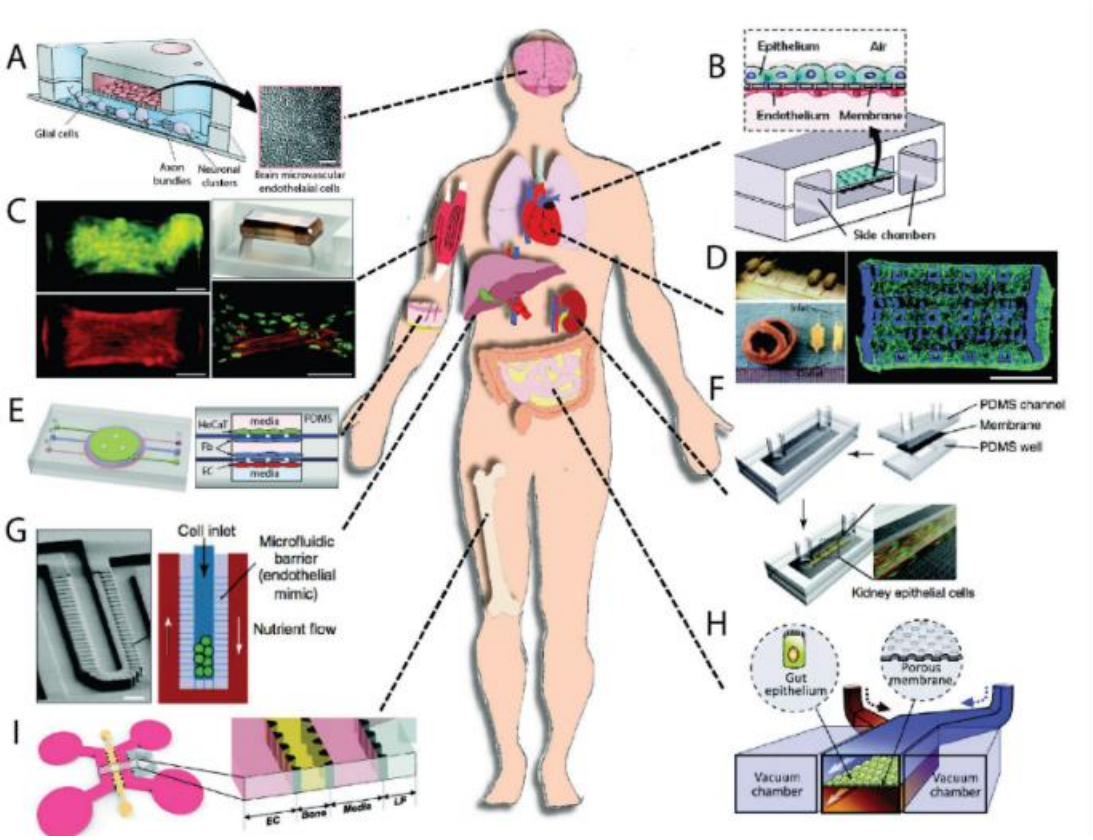

Figure 24: Illustration of the body-on-chip with the schematics and pictures of the current isolated organ-on-chip of interest that could be connected on a same chip one day, for pharmaceutical purposes.

Source: [167]

2012 [162]. They emphasised the allergic potential of a substance absorbed through the skin, and assessed its liver toxicity, which is of interest for the cosmetic industries too. Other teams associated two essential organs, kidney and liver in particular, to study drug metabolism and excretion [207], [208].

Shortly after, a four-organ-chip integrating human cells from liver, intestine, kidney and skin was developed in 2015 [209]. This microphysiological chip includes two layers made in PDMS for two fluid flow circuits, separated by a porous membrane. It is divided in four compartments in close interaction to co-culture four different cell types representing each organ, six air pressure fittings, and two reservoirs to collect fluids excreted from the kidney at the end of the drug metabolic course (Fig.25). Each compartment, in contact with a culture medium specific to its cell type, is linked to two fluid flow circuits by two peristaltic-on-chip micropumps for blood passing through the intestine, the liver and the skin, and excreted fluids from the kidney compartment. Both circuits overlap in the kidney compartment, and are consecutively actuated by pressure or vacuum application. Within this four-organ-chip, the organs integrity and functions interplaying with each other over a long period of 28 days has been exhibited for the first time. Afterward, other research groups developed multi-organ-ono-chip like liver-blood vessel-fat [210], liver-tumor-bone marrow [211] or liver-lung-fat tissues [212].

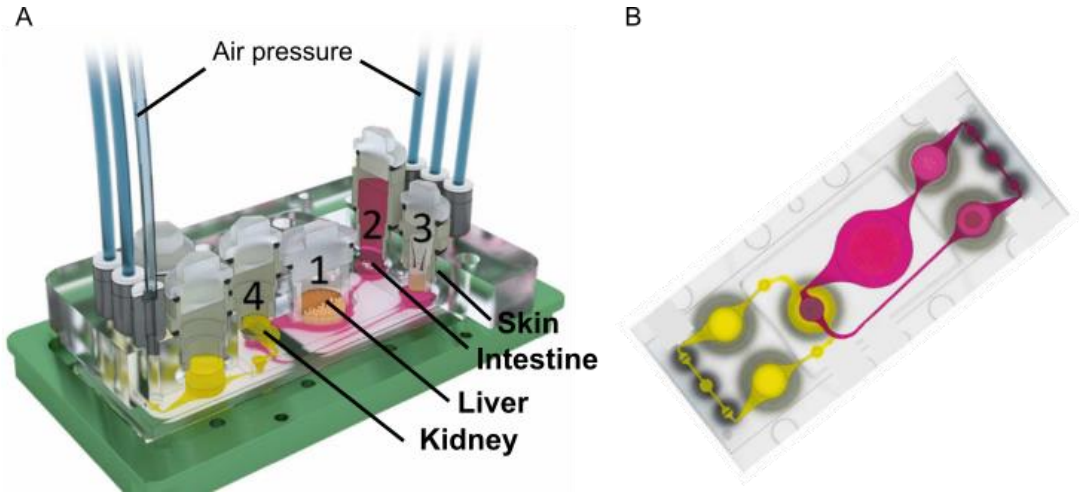

Figure 25: Illustrations of the Four-Organ-On-Chip. A: 3D view of the chip representing the cross-sectional view of the four interconnected organs with the liver (1), intestine (2), skin (3) and kidney (4). B: Diagram of the chip from the top view. The pink represents blood flow circulation, and the yellow illustrates the excreted fluids circulation from the kidney compartment.
Source: adapted from Source: adapted from [209]

Hence, the organ-on-chip field gave rise to the development of many single and multi-organ-on-chips to better understand isolated and interconnected organs, as well as to test drug efficacy and safety. Among them, kidneys, which are involved in toxic and metabolic wastes elimination from the body, are of great interest, notably regarding the development and discovery of novel pharmaceutical treatments. Lately, Kidney-on-chips designing is an attractive and growing field: to recreate its functions, as well as to mimic specific renal disorders such as ADPKD (details in I) 2)).

b) Kidney-On-Chip

i) Introduction to the Kidney-on-Chip area development

Over the past few years, several research teams yearn for creating *in vitro* tissue models to reproduce human kidney physiology and functions [213], [214]. It relies on tissue engineering (TE) development, a term introduced in 1987 to define tissues or organs creation from "principles and methods engineering and life sciences" *in vitro* "to restore, maintain or improve function" [215].

To address the kidney functions, five types of microphysiological kidney-on-chip were developed to model one segment of the nephron, the functional unit of the kidney (details I) 1)). All of them, and their characteristics are compared in the tables below (Fig.26 and 27). The most extensively part of the nephron mimicked is the proximal tubule [216]–[219]. Moreover, some attempts were done to reproduce the glomerulus that promotes blood filtration, or the nephron vasculature [220]. In particular, Musah and co-workers have developed one of the most advanced human glomerulus-on-chip to recapitulate the filtration membrane features, relying on the lung-on-chip. Indeed, using the design created by Ingber, the dimensions of the porous and stretchable membrane made in PDMS was adjusted to reproduce the glomerular filtration membrane. Composed of tiny holes of 7 µm diameters and spaced of 40 µm, its 50 µm height distinguishes two compartments. The membrane was coated with laminin-511 on both sides: the top channel lines with hiPCs differentiating in mature and functional human podocytes, while the bottom part lines with primary human glomerular endothelial cells. This GBM-podocytes-endothelial interface is flanked with two hollow vacuum channels to exert monitored

cyclic mechanical strain, a stretching of 1 Hz happening with every cardiac cycle, using a peristaltic pump. In parallel, two shear stress values are applied in each compartment: 7.10^{-3} dyn/cm^2 in the top urinary compartment, and $1.7.10^{-2}$ dyn/cm^2 in the bottom microvascular channel. Combining physiological dynamic constraints (stretching and fluid flow) on two opposite co-cultured cell layers, this human-glomerulus-on-a-chip is the first to exhibit molecular, functional and phenotypical features of human podocytes. In this microphysiological device, some characteristics of the glomerular filtration membrane in interaction with the glomerular capillaries were reconstituted, favouring renal toxicity assessments, drug development and disease modelling *in vitro* [221]. Nevertheless, a platform combining all the different segments of the nephron, including its vasculature, has not been designed for the moment.

In keeping with the platform developed by Ingber to recapitulate the lung-on-chip, Jang and co-workers designed a **simple multi-layer microfluidic chip** to analyse renal tubule cells. The chip consists of two compartments made in PDMS, and separated by a porous polyester membrane coated with collagen IV, one of the most abundant extracellular matrix protein expressed in the kidney, for cell adhesion. The top channel of 1mm width is seeded with primary inner medullary collecting duct (IMCD) cells from rat, and subsequently connected to a syringe pump applying a laminar shear stress of 1 dyn/cm^2, which refers to *in vivo* conditions. Opposed to this flow chamber, the bottom compartment pseudo-mimicking the interstitium is static: it is a reservoir of medium in contact with the basolateral part of the cells to stimulate them and favour exchanges (Fig.26_Model 1). In this device, the authors managed to recapitulate *in vivo*-like tubular environments in which primary renal cells display *in vivo*-like morphology (such as improved cell polarization) compare to static Transwell cultures. Renal metabolism, with water and ion reabsorption, was also assessed, to further support this device as a drug screening platform [222][162].

Similarly, Vedula and co-workers designed a chip with the same global structure than the one developed by Jang, but using another feature and material as a membrane. Indeed, made in polycarbonate, multilayers were superimposed and hot embossed with sub-micron surface topography that looks like grooves of 750 nm, structuring this porous membrane [223]. These **patterns**, whom size magnitude is observed in renal basement membrane[224], influence epithelial cells functions (barrier integrity) [225]–[230]. This membrane, coated with collagen IV on both sides, separated the filtrate lumen on the top, from the microvascular lumen on the

bottom. Indeed, human proximal tubular epithelial cells (hRPTEC) were co-cultured on the patterns, above the human microvascular endothelial cells (hMVEC), both channels overlapping and exchanging nutrients (Fig.26_Model 2). The co-culture on this proximal tubule-like reabsorptive barrier enhanced some of the epithelium metabolic activities evaluated, and its integrity. This device is one of the rare to include microvascular tissue to mimic reabsorptive barriers *in vitro* [223], [231].

Nevertheless, to get closer to renal physiological architecture and microenvironment, two other teams designed a microphysiological (MPS) device with **microtubular structures**, which remains challenging with the conventional photolithography technique. First, Weber and al recapitulated circular channels scaffold within a natural hydrogel, relying on the first studies made on primary renal epithelial cells seeded within hollow fibers, beforehand coated with an ECM protein (fibrin, or collagen IV) [232][233]. In the MPS, a microfiber of 125 µm was sandwiched between two parts in PDMS, in the centre of the chip. Collagen I was then injected to polymerize around the microfiber before its removal [234]. The tube was then coated with collagen IV, lined with human proximal tubule epithelial cells (hPTEC) and connected to a syringe pump to apply a flow rate of 0.5 µl/min (Fig.26_Model 3A). Within this 3-dimensional flow-directed hPTEC microphysiological system, the authors exhibited, for the first time, the fundamental biochemistry of renal tubule epithelium. Indeed, solutes and fluid transport as well as intracellular enzymatic functions (vitamin D metabolism), in addition to the *in vivo*-like tubule cell phenotype were recapitulated, compared to 2D culture or 3D static culture within a mix of hydrogels [219] [235], [236]. In the same vein, the device developed by Ladoux and al could be also considered as a kidney-on-chip device. Indeed, the chip had several aligned, regularly spaced and circular microtubes of different diameters (from 25 to 250 µm) made in PDMS, and coated with fibronectin (Fig.26_Model 3B) [237]. Metal wires made in copper or platinum were parallely disposed at one or two microns above a silicon wafer. The array of tubes were then covered with a PDMS layer to polymerize around them. The low height between the bottom part and the tubes beginning (1-2 µm) promoted the migration of MDKC and MFC10A cells used in this work to study tissue migration in a lumen.

	Model 1	Model 2	Model 3	
	Porous membrane		Circular scaffold	
Picture/schematic	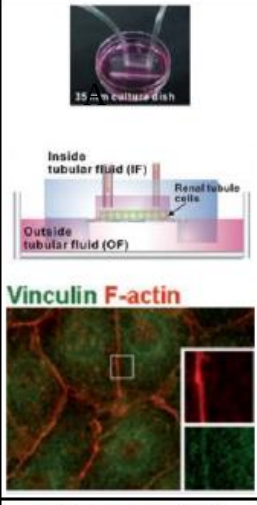	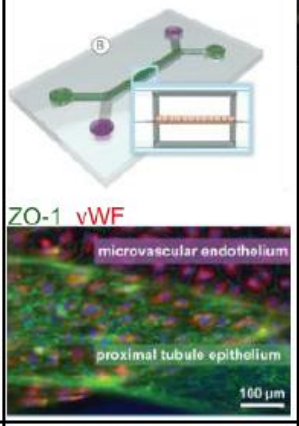	A 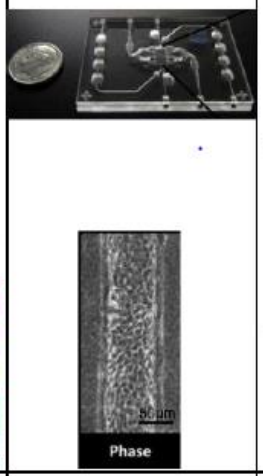	B 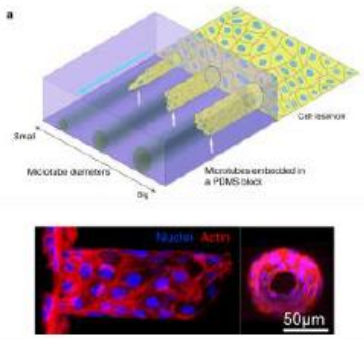
Cell type	Primary rat IMCD	hRPTEC and hMVEC	hPTEC	MDCK and MCF 10A
Flow?	Syringe pump: 1dyn/cm^2	No flow	Syringe pump: 0.5 µl/min	No flow
Channel size	1 mm	grooves = 750 µm	120 µm	25-250 µm
Channel shape	Rectangular	Rectangular	Circular	Circular
Coating?	Collagen IV	Collagen IV	Collagen IV	Collagen IV

Figure 26: Table comparing different Kidney-on-chips. Model 1: 222, model 2: 223, model 3A: 219, model 3B:237.

Source: adapted from Source: adapted from [222; 223; 219; 237]

Furthermore, another approach in association with microfluidics was developed: the **3D bioprinting** of organ-on-chip [217], [238], [239]. Homan and al designed a 3D human renal proximal tubule *in vitro*, embedded in an ECM and perfused via a peristaltic pump at a flow rate of 1 µl/min. The 3D bioprinting consisted of four main steps to form the convoluted proximal tubule: a first ink composed of silicon elastomer prints the convoluted filament or tubule in the gasket, and a thin layer of ECM (mix of fibrinogen and gelatin) was deposited above. Then, the fugitive sacrificial ink was printed on the ECM shaping in tubule, before its removal at 4°C. The tubule, molded in ECM, was then flushed several times to eliminate all residual of fugitive ink. A human proximal renal cell line (PTEC-TERT1) then lined in this convoluted tubule, whose diameter varies between 400 and 550 µm, far away from physiological conditions (Fig.27_Model 4A). As previously, *in vivo*-like cells morphology and metabolic activities (solutes transport, markers expression and localisation) were characterized [240]. Based on this technique, the same team printed two channels close to each other and lined with: PTEC-TERT1 in one channel, and human glomerular microvascular endothelial

cells (GMEC) in the adjacent one (Fig.27_Model 4B). Both channels were independently perfused with a closed-loop perfusion system. Within this 3D vascularized proximal tubule (3D VasPT) co-culturing two cell types, they highlighted renal reabsorption functions through the tubular-vascular exchanges [241].

	Model 4		Model 5
	3D bioprinting		Embedded cells within hydrogel
Picture/schematic	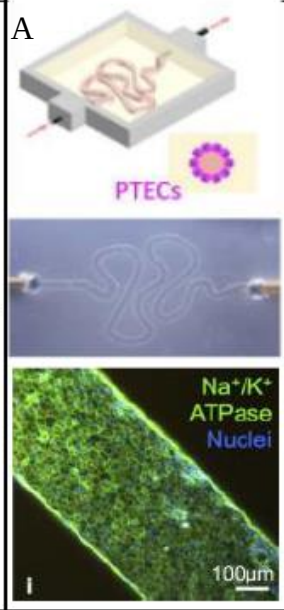	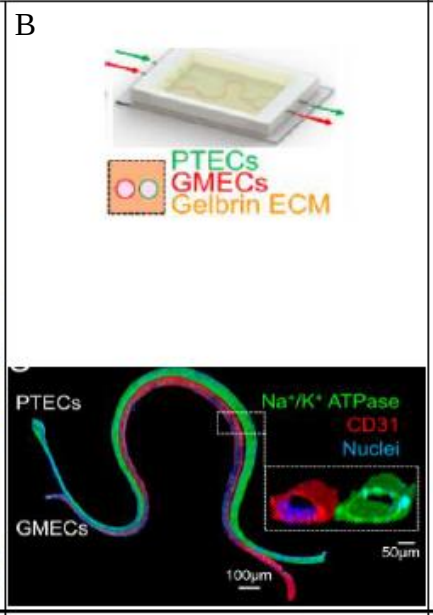	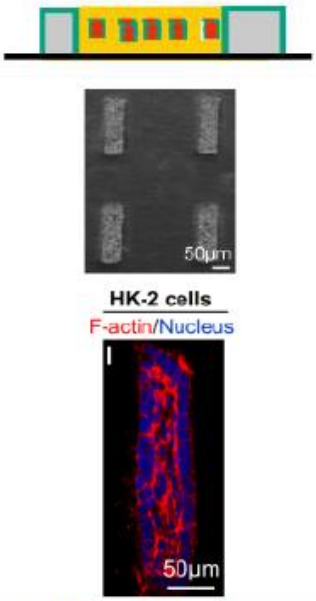
Cell type	PTEC-TERT1	PTEC-TERT1 and GMEC	mIMCD, HK-2 and human embryonic kidney epithelial cells
Flow?	Peristaltic pump: 1µl/min		No flow
Channel size	400 - 550 µm		50 µm
Channel shape	Convoluted tubules		Array of rectangular micropatterns
Coating?	Hydrogel: Fibrinogen and gelatin mix		Hydrogel: Collagen I and Matrigel mix

Figure 27: Table comparing different Kidney-on-chips. Model 4A: 239, model 4B: 240, model 5: 242.
Source: adapted from Source: adapted from [239; 240; 242]

Eventually, a fifth kidney-on-chip model can be depicted relying on natural hydrogel-based device to direct tubule formation: this is the **guided-kidney-tubules-on-chip (gKT)**. Using soft photolithography and photolithography, a mold with an array of 50 µm width micropatterns was designed, and on which PDMS is poured to form a stamp. In parallel, a well

in PDMS was filled with a mix of collagen I and Matrigel, before stamping it with the micropatterns. After gelation, cells were put on the mixed hydrogel, and covered with a layer of the same hydrogel (Fig.27_Model 5). The behaviour of three cell types embedded in this hydrogel was determined: mouse inner medullary collecting duct cells (mIMCD), human proximal tubule cells (HK-2) and human embryonic kidney epithelial cells. Assessing the microenvironment composition, different cell behaviours were observed: in collagen I alone, cells formed disorganized tubular networks that branched, whereas in Matrigel alone, cells form spheroids that collapse. A combination of both components was needed for *in vivo*-like structural (tubule formation) and functional features, with integrated physicochemical cues. For the first time, an array with physiological scale micropatterns allowing tubulogenesis, and recapitulating uniformly the functional human kidney tubules, was developed [242].

Consequently, at this day, no platform gathering all nephron segments to recapitulate its whole functions exists. However, with each of the model aforementioned, the assessment of drug safety and efficacy is strongly promoted.

ii) Kidney-on-chips application: nephrotoxicity evaluation

Kidney is one of the most transplanted organs, as a consequence of a renal disorder and/or drug-induced injury [127][133]. Indeed, kidney is highly susceptible to drug injury during toxic waste elimination [243]. In this context, a company named Nortis Bio from Washington University was created to commercialize microfluidic devices with tubular microchannels embedded within a hydrogel, such as the guided-kidney-tubules-on-chip previously mentioned [164]. In the academic domain, most of the research focuses on the reproduction of the proximal tubule functions to assess drug nephrotoxicity. Indeed, as the smallest and most important functional unit of the kidney, this segment receives the highest local drug or metabolite concentration which may induce nephrotoxicity, and do cause drug failure during clinical trials [162]. In the next part, we will focus on three main studies relating a drug toxicity evaluation.

Jang and co-workers were among the first ones to use their dynamic proximal tubule-on-chip to assess the effect of cisplatin, the widely used chemotherapeutic drug, and known as a proximal tubule nephrotoxin (cf.Fig.26_model 1) [216], [244], [245]. In particular, this drug displays species-specific cytotoxicity differences in drug transporters expression, which is why this first study on a human renal cellular model was required [246]. Indeed, reabsorbed in the proximal tubule *via* the OCT2 transporter, cimedine, an OCT2 inhibitor prevented cisplatin-induced injury and promoted complete recovery of the damage under flow, which was demonstrated for the first time *in vitro*. Similarly, most of the patients taking cisplatin causing kidney failure, ultimately recover, which is not often predictable in animal models [247], [248]. Thus, this human proximal tubule-on-chip mimics *in vivo*-like physiology, pathophysiology, and drug nephrotoxicities studies with high fidelity, under fluidic conditions compared to conventional static cultures.

Another approach, using the 3D bioprinting perfusable proximal tubule-on-chip described earlier (Fig.27_Model 4A), evaluated cyclosporine A (CysA) dosage effects on human proximal tubule cells [217]. Indeed, CysA is a drug usually given after transplant surgery to prevent rejection. However, it is also a known nephrotoxin for which the concentration used is important in kidney injury. Indeed, this 3D proximal tubule device, recapitulating the 3D microenvironment of renal cells, highlighted a dose-dependent response of CysA-induced renal epithelium integrity disruption.

In the same vein, with the gKT embedded in collagen I-Matrigel matrix, the authors determined cisplatin drug and forskolin treatment effects on renal epithelial tubular cells. As previously described, cisplatin induced increased apoptosis with high expression of kidney injury markers (KIM-1), in addition to epithelium phenotypical changes, and metabolic activities of the cells. Nevertheless, contrary to the Jang's device, there was no monitored flow in this embedded tubular structure. Moreover, as a platform for drug screening and diseases modelling, the authors also tried to model cyst formation in the tubules. Indeed, polycystic kidney diseases gather an important group of renal disorders such as ADPKD. Treating mouse cells with forskolin to stimulate cAMP, cystogenesis was observed [242]. In line with this initiation, King and al induce fibrosis with high doses of TGFβ involved in cellular homeostasis, in their 3D non-perfused proximal tubule system developed with 3D bioprinting [249].

Recently, advances in iPCs technologies progressively led to disease modelling, with individual patients personalized therapies [250]. For instance, iPSCs derived from kidney organoids models exhibiting connected tubules were used to study phenotypic modifications in disease conditions [251]. However, the internal lumen is not easily accessible because of their self-organization capability, the contamination with other cell types and batch-to-batch variability between donors and patients need more refinement [3], [214], [242].

Hence, the models of kidney-on-chips developed over the past decades have their advantages and limits. It is noteworthy that they promoted a relevant and significant expression of tubular markers for their metabolic activities (transports of solutes and fluids). Besides, they kept renal tubular epithelial cells architecture and functions over time (more than two months [240]) to enable drug screening, and drug development process. However, none of them precisely reproduced a specific renal disorder within an improved and more biomimetic device (with closer tubules scale). To this end, for this project, we designed an innovative kidney-on-chip to mimic ADPKD (cf. I) 2), which is described in the chapter II.

Aims of the project:

Based on the snowball effect theory, we hypothesised that primary cysts might induce mechanotransduction perturbations (orientation, polarity, proliferation), and subsequent tubule deformation (Fig.28). Theses deformations support cyst propagation within the kidney. Modifications of the tubule geometry are associated, among other things, with actin and microtubule cytoskeletons rearrangement [22]. Moreover, this physical mechanism could favor somatic mutations aforementioned within proliferating cystic cells [12]. Occasionally, cysts can collapse which induces a decrease of renal volume in ADPKD patients, and more often in mouse models of polycystic kidney diseases [252], [253].

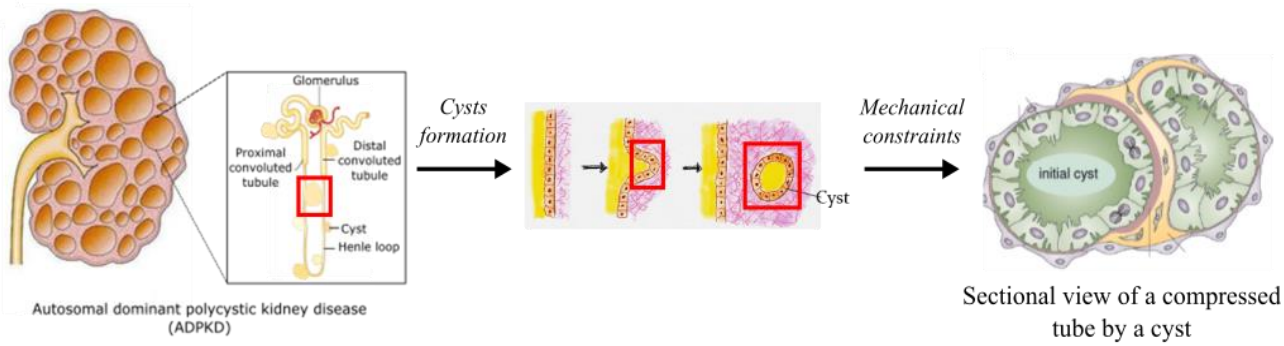

Figure 28: Schematic illustrating the "snowball effect" during ADPKD. Primary cyst formation compress adjacent tubules which may influence the formation of new cysts nearby. The combination of genetic and somatic mutations associated with local pressure may affect the cystogenesis.
Source: Drawn on Inkscape software.

Many studies mainly focus on genetic and molecular factors involved in cysts formation and propagation during ADPKD. The prominent influence of geometrical and mechanical factors on renal tubules requires further study, and an *in vitro* biomimetic system in which one can mimic these complex physiological processes. Our hypothesis is that those parameters could play a major role in renal cyst formation. In particular, the snowball effect could be due to local mechanical constraints. To this end, we need an *in vitro* model mimicking the architectural organization of the nephrons in order to reproduce the snowball effect, which means the mechanical compressions induced by cysts formation and propagation in arrays of densely packed tubules.

Conclusion:

This chapter was an overview on kidney anatomy and physiology, from the discovery of their functions to one of the most common renal disorder existing, the ADPKD. Lacking strong ADPKD models, and targeted therapeutic treatments, the emergence of the Organ-on-chip field to recapitulate individual organs architecture coupled with their functions was then investigated. Born a decade ago, many organs were individually developed, with the lung-on-chip as the first one. They were progressively connected to get closer to the human body organization, which led to the multiorgan-on-chip. Among those organs, some kidney-on-chips were also designed, but few are combined to a specific renal disorder such as ADPKD.

To start with, we will focus on two main aspects: the kidney-on-chip development and the ADPKD cellular models characterization on 2D and in our microphysiological device designed.

In the Chapter II, we detailed the fabrication processes to design and develop an innovative microphysiological device with nephron architecture. Mimicking the tightly packed nephron organization, our system consists of micrometric, aligned and parallel multitubes to mold tubules in a biocompatible hydrogel. Open and ready for further implementations to get closer to the physiological conditions, this novel kidney-on-chip was optimized with the MDCK cells, a wild-type renal epithelial cell line.

In line with this first approach, we then characterized the ADPKD cellular models in our bioartificial kidney-on-chip. In the chapter III, those cells were analyzed on flat surfaces before being seeded in three-dimensional tubular scaffold. We noticed that the homozygous cell line inactivated for *Pkd1* gene highly proliferated and deformed the tubes over time compared to the heterozygous or control cell line. While lining tubes, both cell lines shaped a well-defined cell monolayer surrounding a hollow lumen. However, the homozygous cells displaying cystic features as expected, the next step will be to promote cystogenesis and cyst propagation under flow within our kidney-on-chip.

This aspect, in addition to those about future improvements of the device and biological assays to further characterize the ADPKD cellular models within our system, will be described in the last chapter of this manuscript, the chapter IV.

Chapter II: Development of a renal biomimetic system

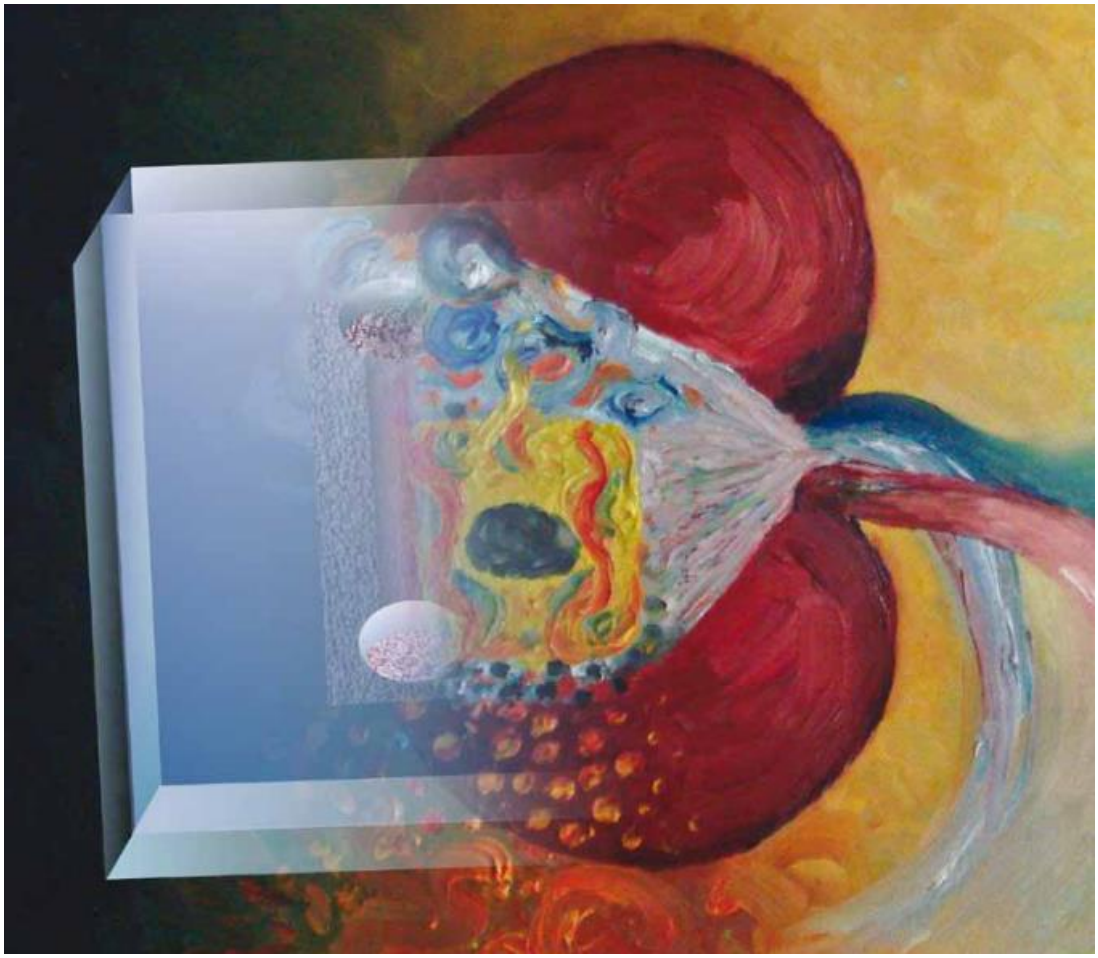

Lab-on-a-Chip journal cover representing an artistic illustration of a kidney-on-chip, drawn by Suh.

Source: Lab-On-a-Chip journal, Volume 10 | Number 1 | 7 January 2010 | Pages 1–132

1) Kidney-on-chip development: prototypes

The aforementioned kidney-on-chip aimed to gradually recapitulate nephrons architecture within its three-dimensional microenvironment. Interestingly, this field applied to acute kidney injury (AKI) has been further investigated recently. However, this adverse effect is due to other pathologies and/or therapeutic treatments. Regarding our project, another relevant aspect is missing: the reproduction and understanding of renal disorders in microphysiological devices such as ADPKD. Indeed, this pathology is characterized by two main phases: the formation and the propagation of cysts through the kidney. To study and decipher those phases, we developed a microfluidic chip with specific features.

a) Kidney-on-chip specifications

To achieve the best functional design, several prototypes have been developed during the first year of my PhD. For that purpose, a PhD student in the MMBM team, Bastien Venzac, trained and mentored me on the different microfabrication techniques needed to carry out this ambitious project. Working together, and based on a previous design he realized to mimic the diameter changes between the proximal or distal tubule and the Henle loop, we developed the ones I will describe below [254].

i) Chip scaffold

It all started when, inadvertently, Bastien Venzac dropped a hair in the PDMS mix, before its polymerization. Picking his chips up from the oven, he gently removed his hair from the PDMS, and noticed a circular microchannel. From this unexpected experiment, the development of a new chip to mimic the functional unit of the kidney is born. Indeed, for our project on ADPKD, the idea was to create a chip recapitulating the tightly packed nephrons organization in the kidney, and more particularly, the first segment of the nephron, or proximal convoluted tubule. To this end, several parameters have to be taken into account, and combined within the same chip. First of all, we need a device with circular micrometric multitubes molded in a biocompatible and deformable hydrogel. Those tubes, in which the local formation of renal cysts might promote the formation of secondary cysts in the adjacent tubules, have to be aligned, parallel and regularly spaced in a controlled manner. Indeed, intrigued by the cystogenesis process and its expansion through the system, those multitubes have to be straight

in our case, and not convoluted as described by Homan and al [217], [255]. Moreover, their diameter should be as close as possible to the renal tubules diameters in the physiological conditions, which means between 40 and 75 µm [237], [254], [256]. Similarly, as a scaffold for the renal epithelial tubular cells, the multitubes should be moulded in a natural and biocompatible hydrogel, with a biomimetic porosity, elasticity and stiffness (5-10 kPa). Eventually, the material, on which this architecture will be moulded, should be biocompatible with optical transparency to ease real-time imaging from below and above, and with a low thickness. For the sake of reproducibility, the material used as a chip base should not be easily deformable compared to the PDMS. For this reason, we decided to use the COC or cyclic olefin copolymer, which could be molded by injection or hot embossed in our case. This polymer is one of the often used for microfluidic chip fabrication because of its transparency and low autofluorescence [257], [258]. However, this thermoplastic is also hydrophobic: it needs a surface treatment to favour proteins specific adsorption, and to increase cell adhesion.

ii) Device handling

Furthermore, it is of interest to note that the final device should be easy to handle, and portable. To this end, the inlet and outlet through which the cells will be seeded, should be on both sides of the chip. Indeed, in most of the renal microphysiological devices previously described (cf. I) 3)b)), the cells seeding takes place on the top of the chip, within small holes punched in the PDMS [216], [223], [254], [259]. This orientation promotes a fast cell sedimentation: the cells do not enter the tubes, which reduces initial cell density within the tubes, and imposes the application of a high pressure that could destroy the tubes made in a soft hydrogel. Therefore, exerting a monitored flow through the device should be achievable in our system. In addition, to provide nutrients, and to favour gas exchanges between the cells and their reconstituted microenvironment, the whole system should be open, and immersed in a culture medium. This specific aspect is highly critical, as COC is not permeable to gas. The cells will be able to interact between each other, while being fed with a small medium volume (6 ml in a Petri dish).

Hence, to mimic the first segment of the proximal tubule as observed in the physiological conditions, we developed several prototypes with micrometric, aligned and parallel cylindrical multitubes. Regularly disposed, they were moulded in a biocompatible and flexible hydrogel relying on the wires molding technique, on an open scaffold made in COC.

b) Conception of prototypes

i) Structure of the design

The conception of the different prototypes relies on different subsequent steps. Indeed, briefly summarized, a sketch of the design is drawn on specific softwares (SolidWorks and Catya) to allow its reproduction on a mold made in brass by the micromilling technique. Then, the COC is hot embossed under a big press, on the brass mold to stamp its patterns, before being mounted to form an operable and functional chip, which will be detailed just below. Three designs were developed, each of them displaying advantages and drawbacks, which led us to the fourth prototype I used during the two next years of my thesis project. This last one was improved, and a fifth prototype was developed lately to get closer to the *in vivo*-like conditions.

First, we designed a mold that contained the patterns to reproduce the appropriate structures for the multitubes molding, which constituted the bottom part of the chip. The patterns were subdivided into three main and symmetrical sections, from the outside to the inside of the mold: the connectors, in which the tubings can be positioned to inject liquids, the slope ending up with grooves to position three to five wires, and a chamber in which the wires were regularly and parallel hanged. The chamber was in the middle of the brass mold, and flanked on both sides with the connectors and grooves (Fig.29A). Each of this pattern was gradually improved to further refine the device and obtained an operable one. The chamber consisted of a 300 µm depth rectangle in which the wires will be positioned to generate the multitube system. Eventually, the hydrogel was poured in this chamber to mold around the wires and shape tubes. This rectangle, corresponding to a chamber, had a length of 5 mm, and a width of 1 mm, which means that the tubes molded in it have a final length of 1 mm. As the rectangle length is of 5 mm, it is possible to add more grooves afterward, in order to increase the number of tubes molded. On both sides of the chamber, grooves regularly spaced of 200 µm were milled to position the wires around which the hydrogel will be poured. Those grooves of 100 µm depth went on with a slope and connectors to gather, and maintained the wires during the polymerisation of the hydrogel around them (Fig.29A).

Once the mold optimized and micromilled, the structures were transferred on a piece of COC using the hot embossing process. Indeed, this technique promotes microstructures fabrication with a high accuracy and reliability [260]. A piece of COC of 2 mm thickness was

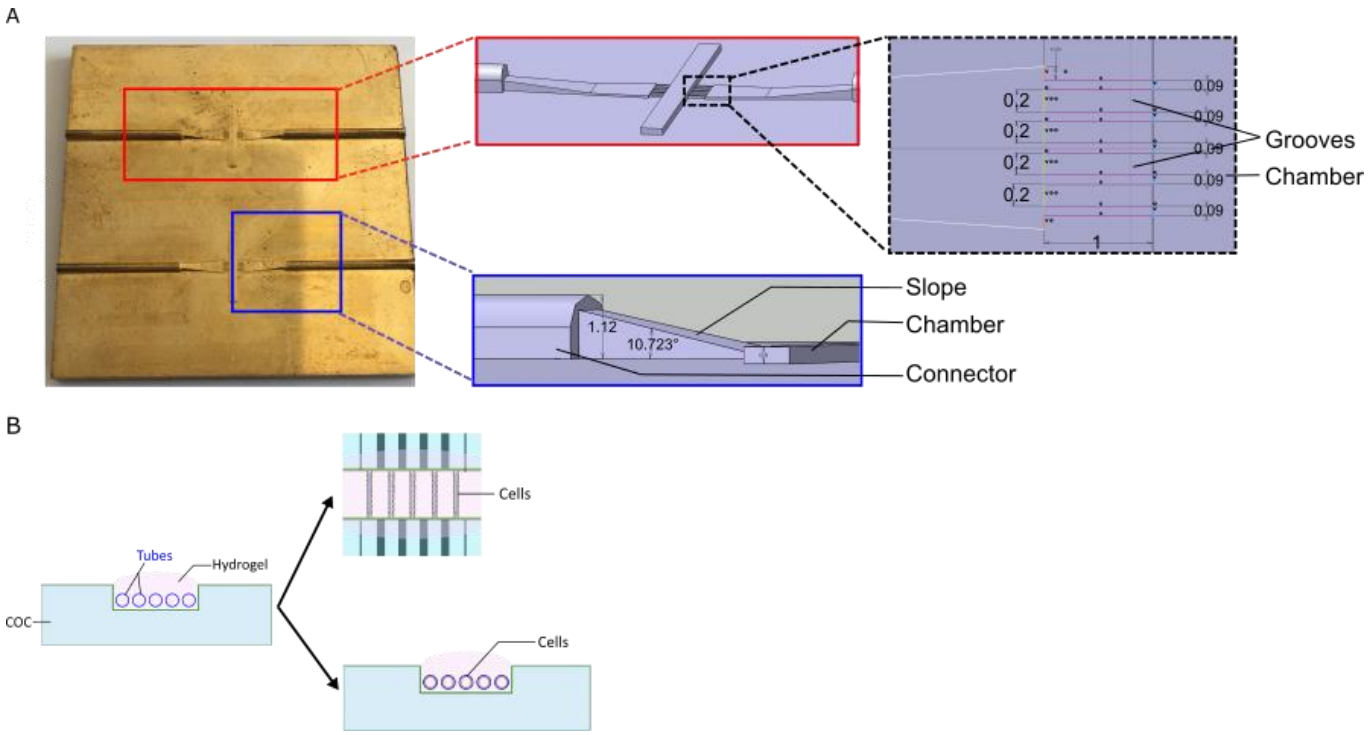

Figure 29: Sketch of the final patterns (A) and of different views, with and without cells lining the tubes (B). A: Brass mold with sketches illustrating its patterns. In the red inset, a top view focusing on the chamber of 300 µm, and the grooves of 90 µm depth on both sides to hold the wires (details in the black inset). The blue inset represents a side view of the macrostructures. B: Illustration of different sections showing the tubes lined with cells on the right. Top: top view of the tubes; bottom: cross section showing cells within the tubes, in the chamber.

pressed on the brass mold, under a monitored temperature and pressure to replicate the microstructures (cf. Annex 3). In other words, the microstructures milled on the brass mold dug on the COC to shape it. Once this bottom part fabricated, it was used to manually position and align the wires in the grooves, in addition to maintain them using different methods described below (cf. II) 1) a) ii))), The hydrogel was then poured and polymerized in the main chamber (Fig.29B). It is noteworthy to mention that this design combines micrometric and millimetric structures, which required the use of milling tools of different diameters. Moreover, for adjacent microstructures below 200 µm, the milling cutters are more fragile and breakable: that is why the space between the tubes was not less than 200 µm for the first prototypes. This small chip's base, of 4 cm* 2 cm size, was then ready to be mounted.

Keeping these patterns in mind, three molds were designed with slight modifications on two of the sections mentioned earlier: the connectors and the grooves. The connectors in which

tubings were disposed to gather the wires, and then to inject the liquids, were improved in two ways. The first version displayed a location to put a seal and prevent leakages, extending towards the chamber without any slope (Fig.30A, left). Kept for the two first designs, these patterns were not efficient enough. Therefore, the connectors were modified: becoming straight and going on with a slope to guide the wires and liquids towards the chamber, they were deepened to ease tubings positioning and prevent leakages (Fig.30A, right). Furthermore, the grooves in which three wires are positioned were refined. Spaced of 400 µm for the two first prototypes with 100 µm depth, and 300 µm length, they were adjusted to ease the fabrication process. Indeed, to be closer to the physiological conditions, the inter-grooves spacing was half reduced (200 µm) (Fig.30B, left). In addition, the grooves length was increased from 300 µm to 1 mm, and they were excavated of 90 µm depth to firmly hold the wires. Grooves were added to promote the investigation of cystogenesis process during ADPKD evolution (Fig.30B, right).

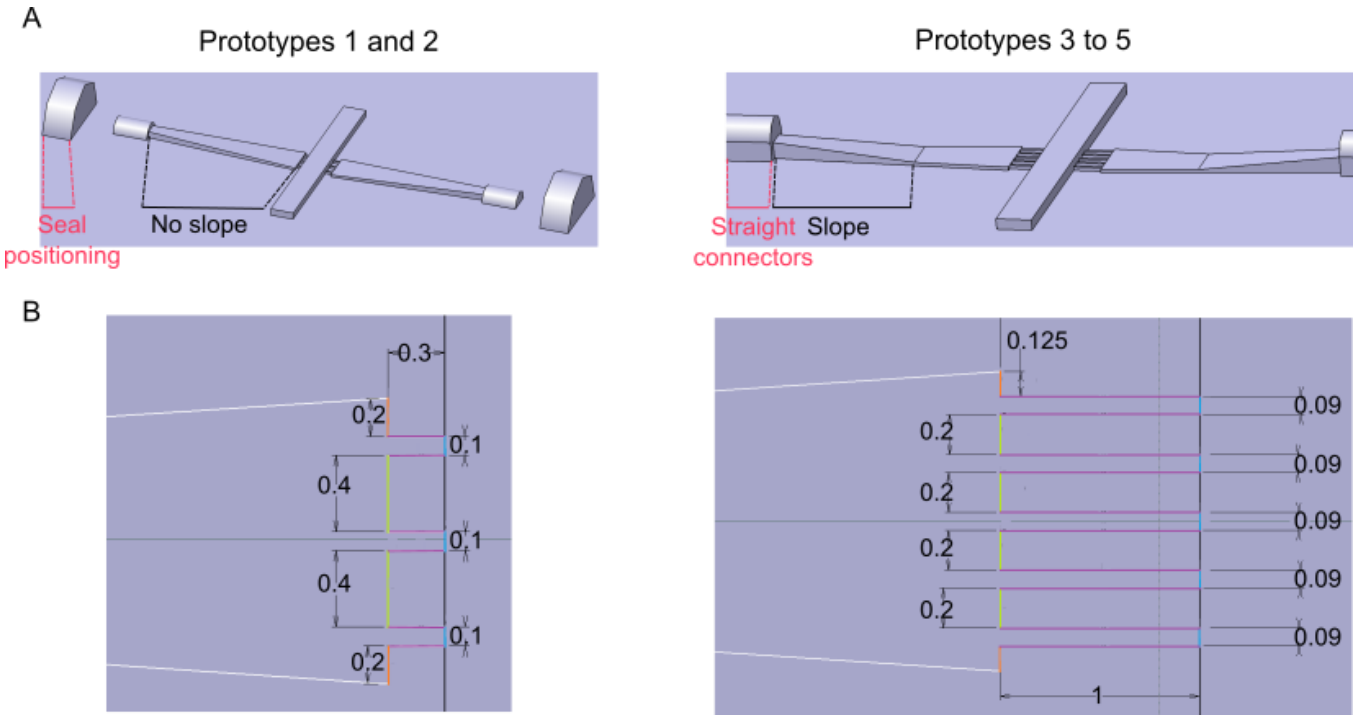

Figure 30: Sketch of the patterns representing the bottom part of the chip improvements. A: General view of the patterns and their differences all the prototypes developed. B: Magnifications on the grooves with in green, the inter-grooves spacing, in purple, the grooves length, and in blue, their depth in mm.

Based on this bottom part gradually optimized, we then focused on the top part essential to hold the wires, and kept the chamber, in which the tubes are shaped, open.

In the next subchapter of this part, the prototypes developed will be described, mainly focusing on the top part implementation.

ii) Prototypes developed

Now that we have the bottom part of the device that will be used to mimic the tightly packed first segments of the nephrons architecture, four different prototypes were developed, including different top parts of the chip (in terms of structure, material, chip bonding…).

Two parameters are crucial for these first steps of the chip development: the wires needed to shape the tubes have to be tightly hold on this base, and the fluids have to flow through the connectors to reach the chamber without any leakages.

The **first prototype** consisted of this base in COC covered with a PDMS layer exhibiting the same patterns. Indeed, using another brass mold reproducing the patterns previously defined, PDMS was poured and cured on it: the PDMS layer features a reservoir of 300 µm depth below which the tubes will be molded, in a chamber. Over it, a top in resin printed in 3D printing displayed a rectangular opening placed above the reservoir made in PDMS. Those two parts were then put on top of a COC piece exhibiting a seal positioning, and three grooves to dispose three wires spaced of 400 µm. Superimposing the COC piece, the PDMS layer and then the resin part, the device was maintained thanks to four screws positioned at the four corners of the chip (Fig.31A). Each layer supported an issue: the PDMS holded the wires on the COC part, while the resin top deepened the final reservoir above the PDMS and the chamber in which the tubular scaffold was molded. Indeed, both reservoirs made in PDMS and resin displayed a total depth of 600 µm, which locally promoted the use of small hydrogel and culture medium volumes (around 300 µl). This opening, on top of the chip, should favor the pouring of enough hydrogel, and should keep it immersed in the culture medium. However, the alignment of the three parts of the chip was not as reliable and accurate as it should have been to ease the visualization within the chip, among other things. Realized under binoculars, and by hand, the

rectangular shapes of each part were supposed to overlap. Besides, the connectors were not tight enough, which promoted fluid leakages.

Therefore, to address these weaknesses while ensuring the operating features, a **second prototype** entirely made in COC was designed. Composed of two parts overlapping, it also exhibited a reservoir of 300 µm depth, in addition to the chamber of the same size and in which the tubes were molded, such as the first prototype. Moreover, the three wires were put between the two parts in COC, within the connectors still exhibiting a seal positioning (Fig.31B). Unfortunately, the chemical bonding between the two COC pieces using hexadecane was not strong enough, which induced fluids leakage. As aforementioned, the alignment of the two COC parts realized under binoculars was not accurate and easily reproducible. Furthermore, the COC top, hot embossed the same way as the bottom part, presented a huge amount of tiny bubbles trapped within the COC. Pressure and temperature are two parameters monitored during the hot embossing process. In association with the air in the big press, all of this may contribute to this unexpected bubbles formation trapped within the COC top. Consequently, those bubbles could prevent an efficient imaging of the tubes through the top of the chip, as well as its thickness.

Relying on these observations, **another device** presenting a different top part to maintain the wires and confine the chamber was designed. To this end and to make the fabrication process easier, a biocompatible and transparent PCR film daily used in the MMBM team was diverted and used as chip roof [261]. Indeed, the chamber space (opening) was accurately cut by hand in this PCR film, and was positioned at the top of the COC base. Remarkably, a simple manual pressure on this film induced its reversible bonding on the COC bottom device. Therefore, the chamber had now 300 µm of depth in which the tubes were to be shaped. Easy to handle, this film allowed the reliable positioning of the wires on the COC base (Fig.31C). Although the three wires were put between the COC part and the PCR film, the connectors shape was still not efficient. Previously composed of a site to position a seal, they were now straight to avoid the leakages. However, fluids fled between the PCR film, and the COC, which suggested that the connectors depth was not optimal. Besides, at the edges of the chip, especially at the inlet of the connectors, fluids also leaked.

	A Prototype 1	B Prototype 2	C Prototype 3
Top brass mold	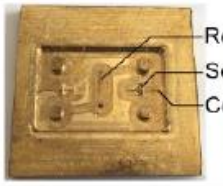		No need
Bottom brass mold			
Chip schematic	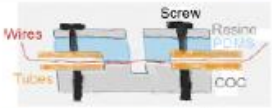		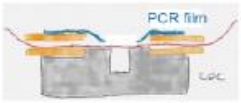
Picture of the top view			
Picture of the side view	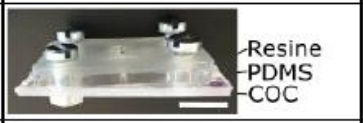		
Improvements	*Triple layers: COC-PDMS-Resine *Reservoir of 600 µm depth	*Double layers: COC-COC *Reservoir of 600 µm depth	*Double layers: PCR film-COC *Chamber of 300 µm depth *Straight connectors *5 grooves of 100 µm depth to mold 5 tubes

Figure 31: Table comparing the three first prototypes developed, with the improvements/changes between each. A: First prototype; B: Second prototype; C: Third prototype. For A-C: brass mold size is 50*50 mm. Scale bar: 1 cm

Eventually, as this approach was the most efficient with a friendly and faster protocol to build it, the connectors were deepened, and two glue points were added during the fabrication process of the chip to achieve a functional system (Fig.32A). Moreover, the depth grooves were improved, and decreased from 100 µm to 90 µm in order to better hold the five introduced wires. This **fourth prototype** is the optimal one used during most of this thesis project, with more tubes to assess tubes interaction, and cystogenesis process as a second step.

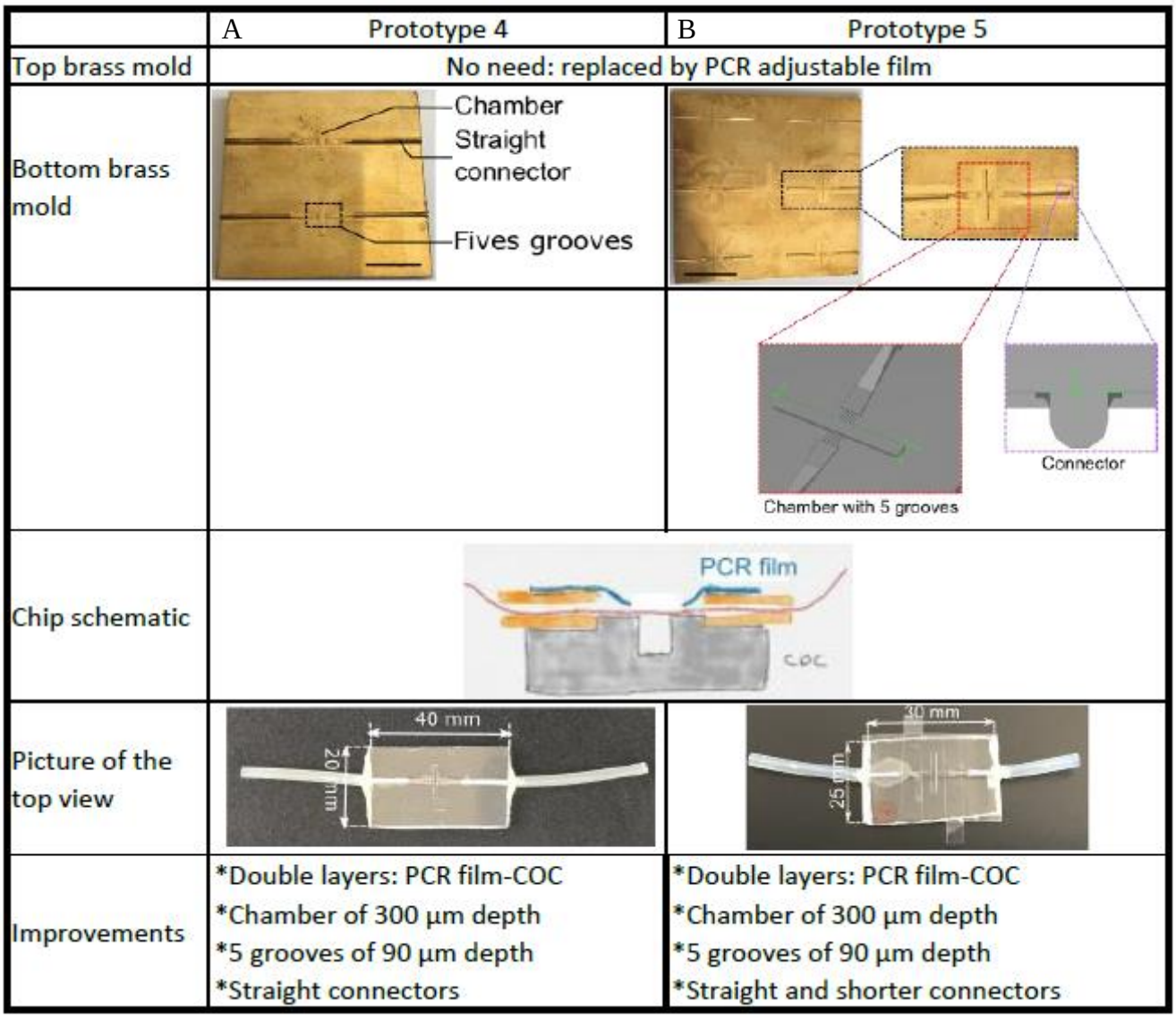

Figure 32: Table illustrating the last prototypes designed, and used for this project first. A: Fourth prototype on a brass mold of 50*50 mm; B: Fifth prototype on a brass mold of 80*80 mm, with 100 µm intertube spacing. Scale bar: 1 cm

Hence, an optimized chip with micrometric, parallely-aligned wires spaced of 200 µm were established to mimic ADPKD events (Fig.32B). Most of the experiments that will be

described thereafter were performed with this design. Nevertheless, to get closer to the tightly packed organization of nephrons within the kidney, another brass mold was lately developed by Giacomo Gropplero. Indeed, to improve the interactions between tubes, the spacing between them was half reduced, from 200 to 100 µm (Fig.32B). Moreover, to reduce air bubbles presence within the connectors, and thus in the tubes molded in collagen I, the length of the connectors was shortened. It is worth noting that to be reproducible, and have several chips all at once, six patterns were milled on the brass mold instead of two. This **last prototype** was used in a few experiments that will be next related (cf. chapter III).

c) Three-dimensional scaffold of biocompatible hydrogels

i) Tests of hydrogels

To reproduce the microcylindrical architecture of the renal epithelial cells microenvironment, several hydrogels were assessed. Indeed, the ECM (extracellular matrix) is an elaborated network composed of many proteins and factors providing spatial and temporal cues on the cells behaviour and functions. Specific to the tissue composing an organ, the ECM influences cell proliferation, differentiation, and migration [3], [262], [263].

First of all, we assessed the ability of different type of wires to be used in our device. Indeed, several wires with a diameter of 80 µm, and made in different materials were handled: nylon, steel and tungsten. The nylon and steel wires are more flexible than the tungsten, which induces uncontrolled curvature within the chamber, instead of straight and uniform wires disposal. Consequently, we decided to select the tungsten wires, as they are sufficiently stiff.

Then, to investigate adequate tubes formation in the chip, we performed the wires molding technique with different hydrogels. Indeed, this crucial feature depends on the mechanical hydrogel properties to shape stable microstructures. Besides, potential interactions between the wires and the hydrogel material can occur [164]. The wires molding technique consists of gently pulling off the wires, by hand, to prevent hydrogel detachment from the COC surface, after the hydrogel polymerization around them.

We first checked the device functionality with PDMS as bulk material, PDMS being an elastomeric material in microfluidics and having a Young modulus in the range of MPa. To do so, we poured PDMS in the chamber, above the aligned tungsten wires. We showed that PDMS stiffness favours tubes formation, as shown in the Fig.33A [264]. Next, we tested several hydrogels that are commonly used for cell culture, or as organ-on-chip based materials. These hydrogels are expected to be softer and porous. Moreover, we also expect them to have different types of interactions with the wire surface. These hydrogels have been used at different concentrations: agarose, Matrigel, and collagen I from rat tails [265], [266]. Agarose is a stiff (range of kPa) and inert hydrogel on which the cells cannot adhere without a coating with a basal membrane component [267]. Between 1 and 4% (m/v or v/v), this matrix shaped regular and straight tubes, but not at 0.8% (Fig.33B). However, agarose did not stick to the COC surface when we injected liquids, in particular when we injected ethanol to sterilize the inner tubes. To get closer to *in vivo* conditions, Matrigel, composed of ECM components such as fibronectin, laminin or collagen IV and other growth factors, was tested. It is derived from the basal lamina secreted by a murine tumour [268]. Although being used pure or half-diluted in culture medium, Matrigel was exceedingly soft to shape the tubes (Fig.33C). Besides, it did not anchor on the COC neither on the PCR film, which suggests that Matrigel is not compatible with the COC lacking a surface treatment. Thereafter, we investigated collagen I, the main component of the

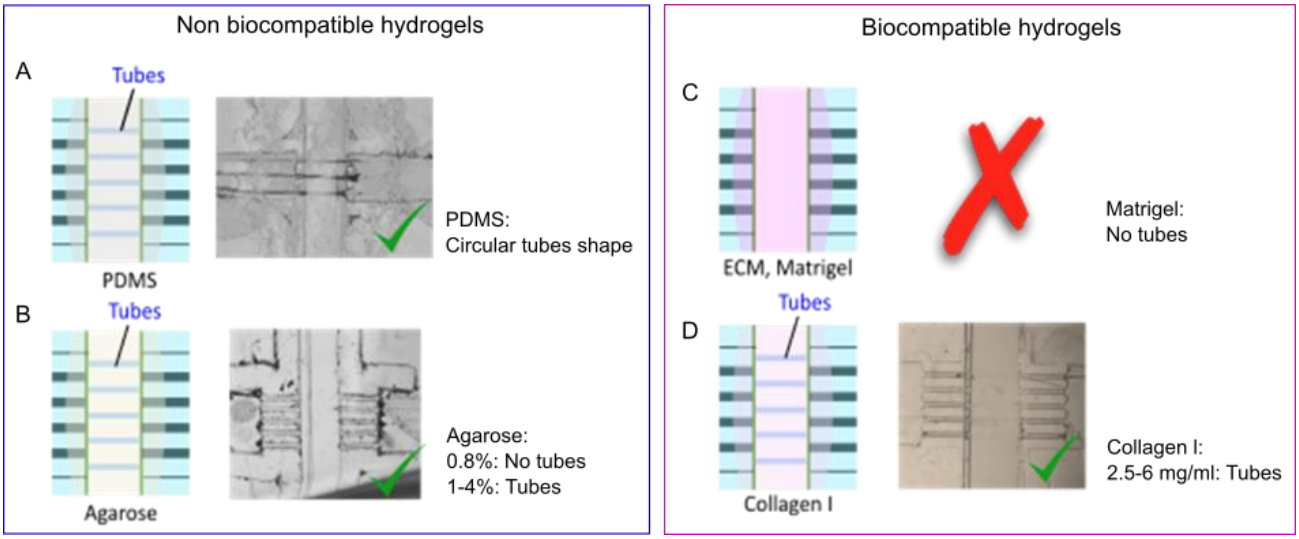

Figure 33: Diagram representing the formation of circular tubes depending on the type of hydrogel and its concentration. In the purple frame are the not biocompatible hydrogels, and in the pink one, the biocompatible hydrogels are gathered. A: PDMS; B: Agarose; C: Matrigel; D: Collagen I.

ECM, at three increasing concentrations: 2.5 mg/ml, 4 and 6 mg/ml. Although tubes were shaped for each concentration, below 6 mg/ml, the microcircular tubes were not stable and uniform. Indeed, some of them collapsed. Thus, we decided to keep the last condition to mold the tubes: collagen I from rat tail, made at 6 mg/ml, as used by Weber and colleagues to fabricate their microphysiological model [219] (Fig.33D).

ii) Fabrication of the kidney-on-chip

The chip design and the biocompatible hydrogel to shape the adjacent tubes were now implemented. The next step was to fabricate the device, and to test its sealing before the cell seeding within the empty tubes. The final protocol is detailed in Annex 3. To this end, three essential steps were improved: wire removal, collagen I mix preparation and polymerization on the COC base, and liquid injection technique.

Briefly, the five tungsten wires of 80 µm diameter were positioned in the grooves of the COC base. Fixed with the PCR film, the chamber top was open and the wires were reachable by the collagen I. Then, this collagen solution was poured on top of the wires, and could thus polymerize around the wires. Thereafter, the empty tubes could be seeded with the renal epithelial cells. However, when we gently pulled out the wires from the collagen I, on both sides of the chip, the collagen I detached from the COC surface. Moreover, the wires took away the collagen I with it, destroying the tubes at the same time. To tackle this problem, the tungsten wires were incubated with a solution of PBS-1% BSA, at room temperature during 30 minutes. Coated this way before being fixed on the COC, the wires did not impair the tubes when we removed them. Meanwhile, we noticed many air bubbles trapped in the collagen I during the polymerization process, and mainly on both sides of the tubes or next to them. As the collagen I mix is very sensitive to temperature and mixing, the solution was kept on ice at 4°C, and was gently blended with an appropriate spatula to prevent air bubble trapping. Then, it was centrifuged less than 30 seconds to pull up the air bubbles, and poured on the COC base. Nonetheless, the COC base was incubated with a solution of PBS-1%BSA at 37°C, during one hour, beforehand. Indeed, this solution was then removed before the collagen I mix pouring in the chamber, to decrease air bubbles formation on both sides of the tubes. Finally, the collagen I mix was poured above the wires, and incubated at 37°C during two hours. To prevent the drying and ease the wires removal, the polymerized collagen I was then immersed in PBS before the cell seeding process. This liquid immersion also prevented air entry, and thus air bubbles

formation within the tubes during fluids injection. This aspect is a major one: air bubbles can destroy the tubes made in a soft collagen I compared to PDMS for instance. For this reason, a liquid-liquid interface is crucial when we inject a fluid through the inlet.

To assess the sealing of the fabricated chip, more particularly the tubes integrity, microbeads of 10 µm diameter were injected within the empty tubes. Beads went through the tubes, albeit crossing the tubes from one extremity to the opposite one. In other words, beads crossed the tubes and went underneath the collagen matrix at the same time. To bypass this problem, the COC surface was first treated with a silane (2% of APTES followed by 0.5% of glutaraldehyde, independently diluted in the PBS) to promote collagen I cross-linking, and then set up with the other elements.

Thus, those different technical improvements allowed us to refine the device, and to move on to the next essential step: cell seeding within the empty tubes made in collagen I at 6 mg/ml.

2) Kidney-on-chip development: Bottom-up approach

a) Cellular model and basal membrane components

Of further interest, the renal epithelial cells are lined on a basal membrane (BM) which provides a structural and functional support. In direct contact with the cells, it acts as a scaffold constantly remodelled, and a barrier between the epithelial and endothelial cells. This basal membrane or basement membrane is a highly specialized ECM whom composition is organ-specific. Indeed, in the kidney, the ECM is composed of around 220 different and specific proteins. They are mostly synthesized, and degraded, by the epithelial and endothelial cells lining on this BM, in a well-balanced process. As the BM composition constantly evolves over time, it also depends on renal development, and pathological conditions [263], [269].

The kidney BM is mainly composed of collagen IV and laminin, in addition to glycoproteins such as nidogen, perlecan and fibronectin. To improve the physiological relevance of our system, and cell performance, we coated the empty tubes made in collagen I with different proteins of the ECM: laminin, collagen IV and Matrigel. In parallel, similar experiments with various coating were performed on a 2D collagen layer. Indeed, before investigating renal cells

behaviour in 3D, we first assessed their behaviour in 2D. The collagen I condition corresponds to the control condition in each experiment. Working on two aspects of the project in parallel, the fabrication of the chip, and the characterization of the ADPKD cellular models, the coating tests were realized on the ADPKD cell lines, which will be detailed in the next chapter (III).

Moreover, in line with other studies that started to work with renal cell lines to recapitulate kidney functions, we first tested our system with Madin-Darby Canine Kidney tagged with Lifeact-GFP construct (MDCK-Lifeact-GFP), and derived from the distal convoluted tubule. This renal cell line stably expresses a construct, which labelled actin filaments to allow the visualization of their intracellular organization. Indeed, depending on their environment, flat or spatially structured, F-actin cytoskeleton rearrangements occur, as well as cells shape.

b) MDCK cell behaviour on 2D

With a preliminary approach, we focused on MDCK-Lifeact-GFP behaviour on glass in regards with their morphology on glass covered with a thin layer of collagen I. Indeed, renal epithelial cells do not proliferate, migrate and spread the same way depending on the substrate on which they adhere. Those cells were seeded on a 12-well plate with glass bottom coated or not with a thin layer of collagen I at 6 mg/ml, at different cell densities: 5.10^3, 10.10^3 and 20.10^3 cells/ml. After two days of culture, they were imaged in phase contrast and with a laser exciting the GFP, under a spinning disc microscope to compare their morphology, and density (Fig.34). A stack of images at different z plans was acquired to observe whether there was an overlap of multilayers, and/or whether they entered in the collagen I layer.

On glass, MDCK cells (which did not uniformly express the Lifeact-GFP construct) overlaid most of the surface at 10.10^3 and 20.10^3 cells/ml (Fig.34A). The cells were small, and constricted with a hexagonal shape (Fig.34A). At a lower cell density, 5000 cells/ml, they formed small islets all over the glass surface: the cells spread, and were taller than at higher density. However, we also observed that on glass covered with a thin layer of collagen I at 6 mg/ml, the concentration prepared to mold tubes, the cell density and spreading was significantly reduced (Fig34.B). Cells did not adhere as fast as on glass or plastic substrate: they migrated faster on glass than on a collagen I layer [270]. Isolated or at the edges of the small islets, the cells had slightly long cytoplasmic extensions, like filopodia, going into the collagen I gel (Fig.34C). At 5000 cells/ml, we barely noticed some isolated cells, suggesting

that this initial cell density was not enough to favour their proliferation. Moreover, we noticed that cells forming domain-like structures exhibited leader cells with a fibroblastic phenotype [270], [271]. Indeed, Haga and al reported that those fusiform cells guide the following cells, or followers, composing the monolayer, on both glass and collagen I substrates to initiate cell collective movement. On collagen I, this cell collective displacement went along with wide lamellipodium formation, as we sometimes observed too (data not shown) [270]. However, albeit the aforementioned study was done with collagen I, this ECM was not extracted from the same animal species, neither used at the same concentration in our experiences. A gel of collagen I from porcine tendon at 1.75 mg/ml was used, instead of collagen I from rat tail at 6 mg/ml in our experimental approach.

Reaching 80-90% of confluence, the cells formed waves on the collagen I layer, which implies that they tended to deform the gel, and to sink into the collagen I to favour other cell adhesion. In contrast to cells seeded on a soft hydrogel such as Matrigel, on a stiffer collagen I layer, cells did not shape as a three-dimensional tulip hat-like structure. They did not manage to pull on enough the soft substrate to remodel it, like in the work of Imai and collaborators [272].

Furthermore, we determined percentage of cell confluency on a flat glass surface covered or not with a thin layer of collagen I at 6 mg/ml, depending on the initial cell density, and three days post-seeding. For this purpose, we measured the area covered with the cell monolayer for each initial cell density, and normalized per the total area (Fig.34D). We noticed that MDCK cells overlaid around 90-100% of the area, when plated between 10.10^3 and 20.10^3 cells/ml on glass. However, only approximately 50% of the area coated with collagen I was covered with cells seeded at 20.10^3 cells/ml. Below, they barely overlaid 30% of the area. Thus, MDCK cells adhered, and proliferated more slowly on a flat layer of collagen I than on a glass substrate. An initial amount of cell seemed to be required to promote cell spreading on the substrate.

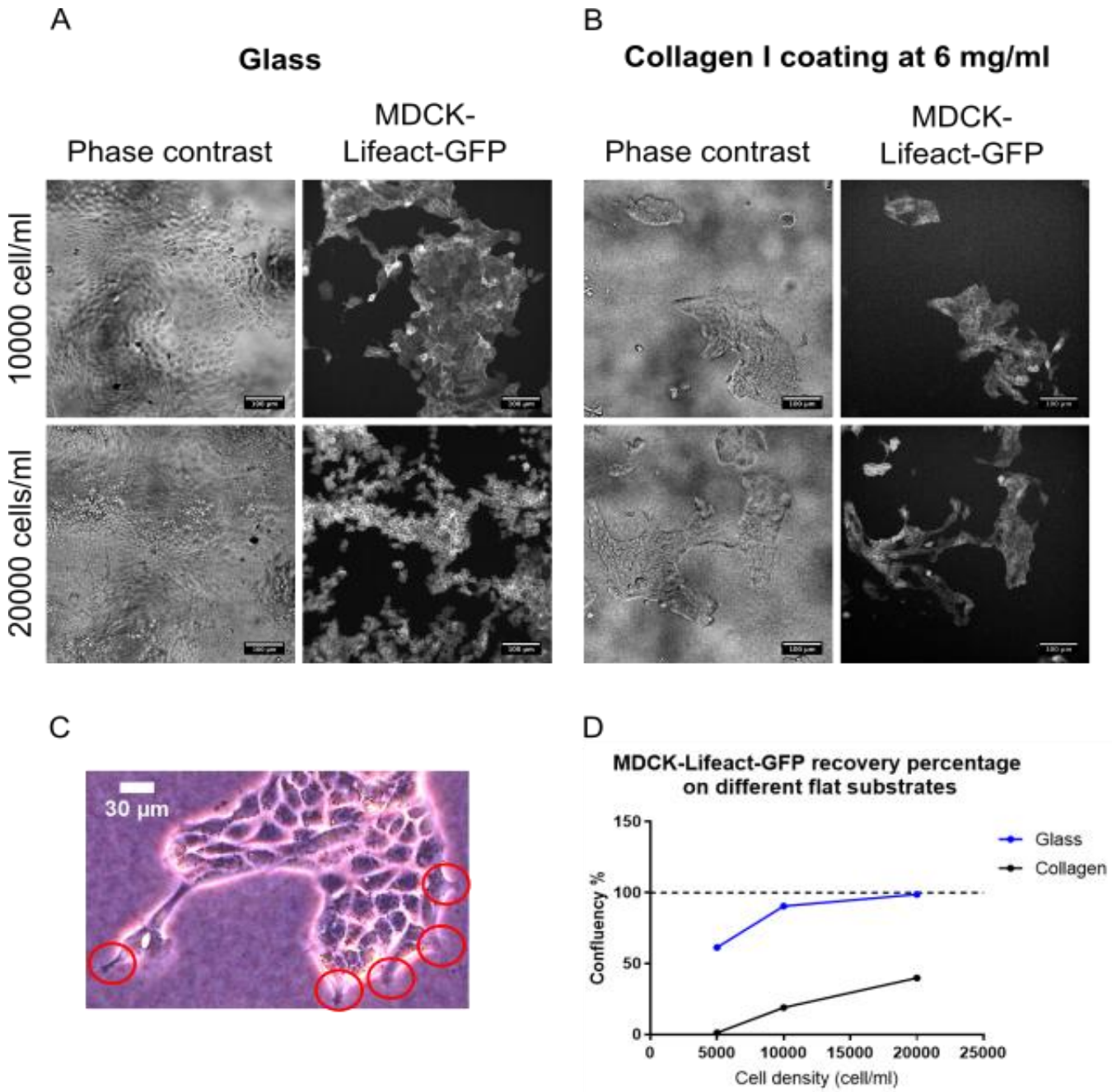

Figure 34: Images illustrating one *z* plan of MDCK-Lifeact-GFP cells on glass (A), and on glass coated with a thin layer of collagen I at 6 mg/ml (B), acquired under a spinning disc microscope. For each panel, the initial cell density is 10.10^3 cells/ml on the top, and 20.10^3 cells/ml on the bottom. A: MDCK-Lifeact-GFP cells seeded on glass. The cells cover almost all the surface. B: MDCK-Lifeact-GFP cells seeded on glass covered with collagen I. However, for the sake of clarity, the cells plated at 5000 cells/ml are not shown. C: Magnification on the MDCK cytoplasmic extensions (red circles) in the collagen I layer. D: Graph representing the MDCK cells confluency percentage on glass, and collagen I layer, 3 days post-seeding. Scale bar: 100 µm.

c) MDKC behaviour in 3D structures

The MDCK renal epithelial cells adhered to the collagen I, and unsurprisingly, did not have the same phenotype as on flat glass: they proliferated and spread slower than on glass surface. Nevertheless, as previously noted, it is well known that cell behaviour on flat substrates does not mimic the physiological conditions as well as the three dimensional scaffold. Indeed, their phenotype as well as their functions strongly depend on their structured microenvironment, exhibiting or not submicron topographical patterns [219], [223]. Relying on these observations, we seeded 5.10^6 cells/ml in the tubes molded in collagen I at 6 mg/ml, and followed them during several weeks, without flow application.

An example on how MDC colonized the tubes is presented in Figure 35A, with a chip exhibiting a fast colonization. The five microcircular multitubes had a diameter of approximately 80 µm after wires removal. However, in this example the fourth tube was larger than the other ones since the beginning of the experiment (Fig.35A). The seeding was not initially uniform, neither was the cell density at day1 (D1) because the cells crossed each tube at different velocity rate without adhering. Thereafter, they took here three days to form a confluent monolayer in almost all the tubes, and to self-assemble in a 3D tubular structure. The epithelial cells seemed to be tightly associated, and to form a barrier lining the tubes. They kept proliferating and lining the tubes until the 59^{th} day. Between days 3 and 59, they slightly distorted the tubes in the example depicted, even though they did not invade the collagen I scaffold. Cells proliferated, and formed clusters gradually detaching from tubes, while pushing the previous clusters on both sides, as we can notice on D31 and D59. In other words, cells growing within tubes, and obstructing the lumen, pushed the current cells towards the tubes extremities. Besides, MDCK cells seeded on collagen I, and not embedded in a gel made in collagen I, might form cysts, like previous studies reported in softer collagen gel [273].

In parallel, we determined different parameters that will be described to characterize MDCK cells dynamics within the tubes over time, as well as the ADPKD cellular models behaviour (cf. Chapter III) 2)). To this end, phase contrast images of the same chips were acquired at different time points. From these raw images, a 2D projection of cells and tubes edges were drawn on a tablet, and processed into binary masks thanks to an ImageJ program developed by Isabelle Bonnet (researcher in the PBME team, Institut Curie, UMR168). The two types of masks, cells or tubes edges, were then analysed with a homemade program written on Matlab

by Sylvie Coscoy (researcher in the PBME team, Institut Curie, UMR168) (cf. Annex 4 for more details).

First of all, we investigated the mean MDCK cell density over time, within tubes made in collagen I. Cell and tube masks intersection highlights cell areas within the tubes, and a ratio between cells area and tubes area at the same time was estimated. This method gives an information on the area filled with cells over time. For these measurements, as the time acquisition scale was not regular, measurements were binned on each 3-days period, and the mean values for several chips is then computed.

Cell colonization appeared to be heterogeneous between chips, with some chips reaching fast confluency (as in Fig. 35A), others reaching it in 1-2 weeks, and few of them never reaching it. Therefore, we observed a growth phase from days D0 to D10, and a plateau up to D38 corresponding to cells filling almost all the tube (ratio between cells area and tubes area at the same time close to 0.8, suggesting that confluency was not reached in some chips). Indeed, they could either contract the tubes when they reach their maximal confluency, or retract the tubular walls when they detach from them, form cell clusters or die. Cells did not seem to distort significantly the tubes.

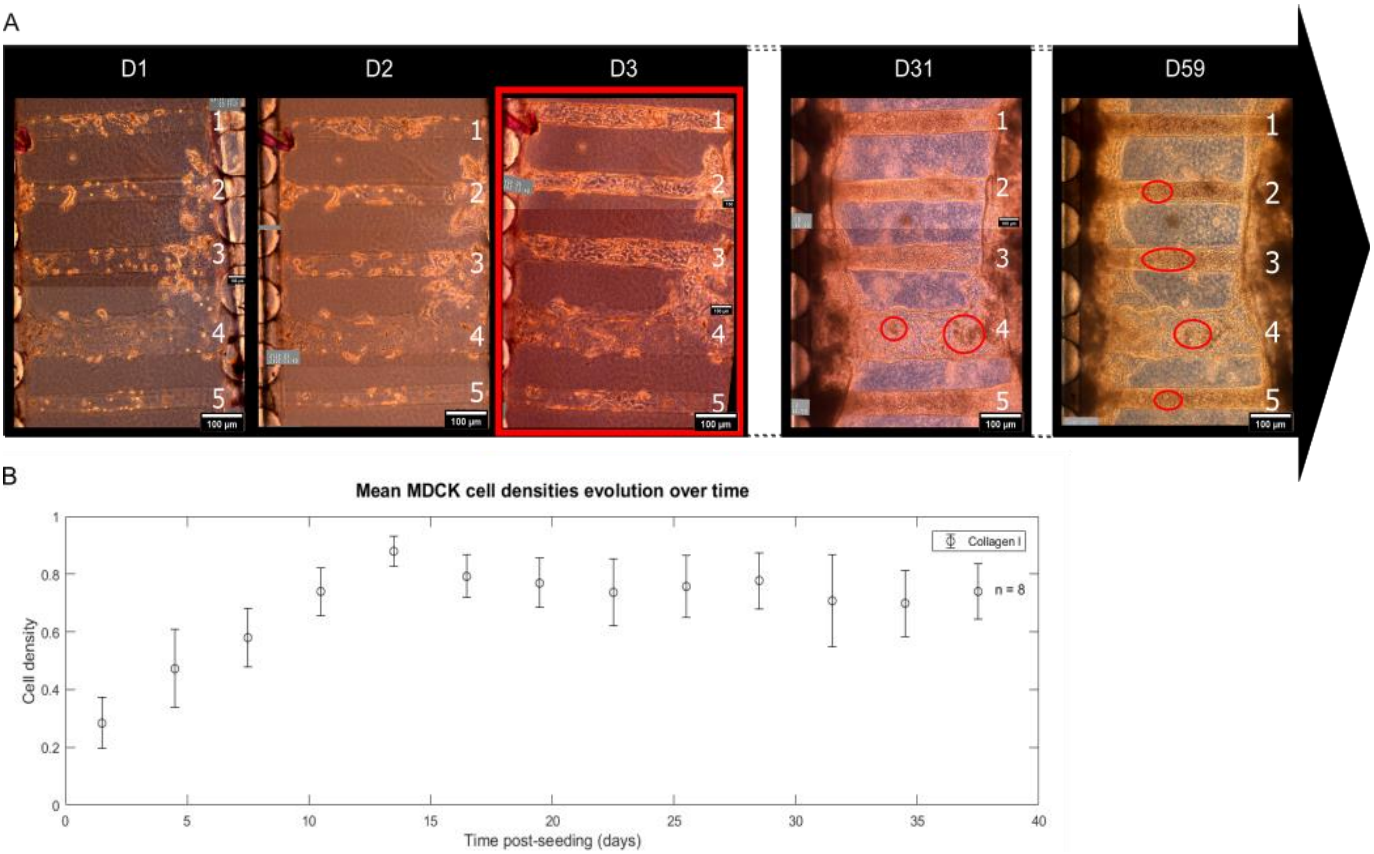

Figure 35: A: Arrow illustrating the growth kinetic of MDCK-Lifeact-GFP cells seeded within tubes molded in collagen I at 6 mg/ml, and observed under an optical microscope over time. At D3, we note some tubes with a confluent cell layer (tubes 1-3). At D31, cells continue to proliferate, and to form clusters (red circles) within the tubes. Scale bar: 100 µm. B: Graph representing the mean cell density evolution over time bined (black dots) of tubes molded in collagen I, and seeded with MDCK cells (n = 8 independent experiments). SEM are represented.

To determine the monolayer structure, as well as the cell integrity, we observed them under a confocal microscope (Fig.36). These preliminary observations allowed us to refine the imaging techniques, in order to determine morphological parameters with the ADPKD cellular models. We noted here that four days after seeding, cells lined all the tubes, and were cohesive between them. At the tube edges, we noticed cells with cobblestone-like structures (Fig.36A and B). Expanding within the tubes, cells quickly formed significant cell clusters slightly obstructing and distorting the tubes. They started to come off the tubes after thirty-one days of culture, and to die by apoptosis, among other cell death programming events (Fig.36C and D). However, we could not characterize the precise cell death mechanism because of technical issues described in the next chapter (III) 2)). After fifty-nine days, the period of the cell culture

evolution within the system, most of the tubes were empty. Some scattered round cells stayed caught on the tubes.

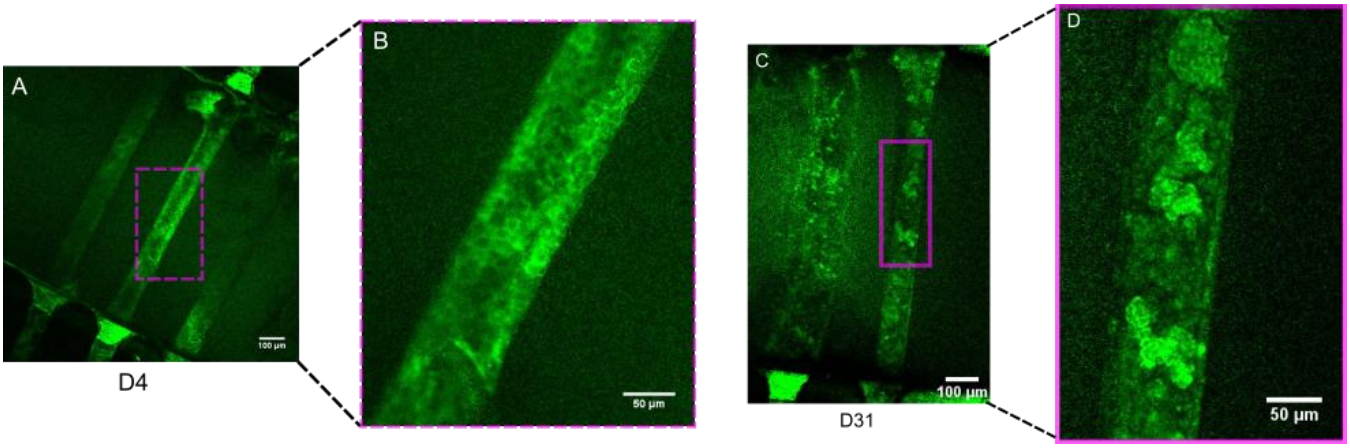

Figure 36: Images representing the MDCK-Lifeact-GFP actin cytoskeleton organization, lining with tubes molded in collagen I at 6 mg/ml, and observed under a confocal microscope at D4 and D31post-seeding. A: General view on three tubes. B: Magnification on the second tube. C: Focus on two tubes at D31. D: Inset on one part of the tube and highlighting MDCK cells clusters. A and C: Scale bar: 100 µm. B and D: Scale bar: 50 µm.

Thereafter, to reproduce the basal membrane on which renal epithelial cells adhere, we first coated the tubes shaped in collagen I at 6 mg/ml with laminin. To check the reliability and

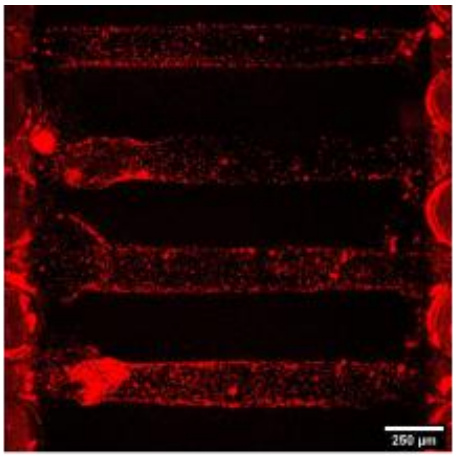

Figure 37: Images showing tubes molded in 6 mg/ml collagen I, and uniformly coated with laminin-Rhodamin. Scale bar: 250 µm.

reproducibility of the coating technique, we injected laminin coupled to Rhodamin fluorophore. As we can notice on Figure 37, the coating with laminin-Rhodamin was uniform in each tube.

We then seeded those tubes with MDCK-Lifeact-GFP cells, and compared their behaviour to the ones seeded in tubes without coating, meaning in collagen I only (Fig.38).

On the laminin coating, the initial cell density was lower than in the tubes made in collagen I. Thus, cells lined the tubes and formed a confluent monolayer belatedly (around 7 days post-seeding). Moreover, they kept proliferating, but formed less cell clusters within the tubes coated than within the tubes without coating (Fig.38A and B). They did not seem to fill the tubes as in the collagen I tubes, suggesting that laminin could enhance the cell adhesion, and could maintain them in direct contact with the scaffold. Moreover, as within tubes made in collagen I alone, the MDCK cell density over time in tubes coated with laminin was evaluated. Similarly to the control condition, we note a growth curve of the cell density over time (Fig.38C). There was no significant differences between the control and the coated conditions: cells seem to colonize the tubes with the same dynamics in both conditions. As previously observed, cells did not seem to dilate the tubes, a parameter described later in this subchapter.

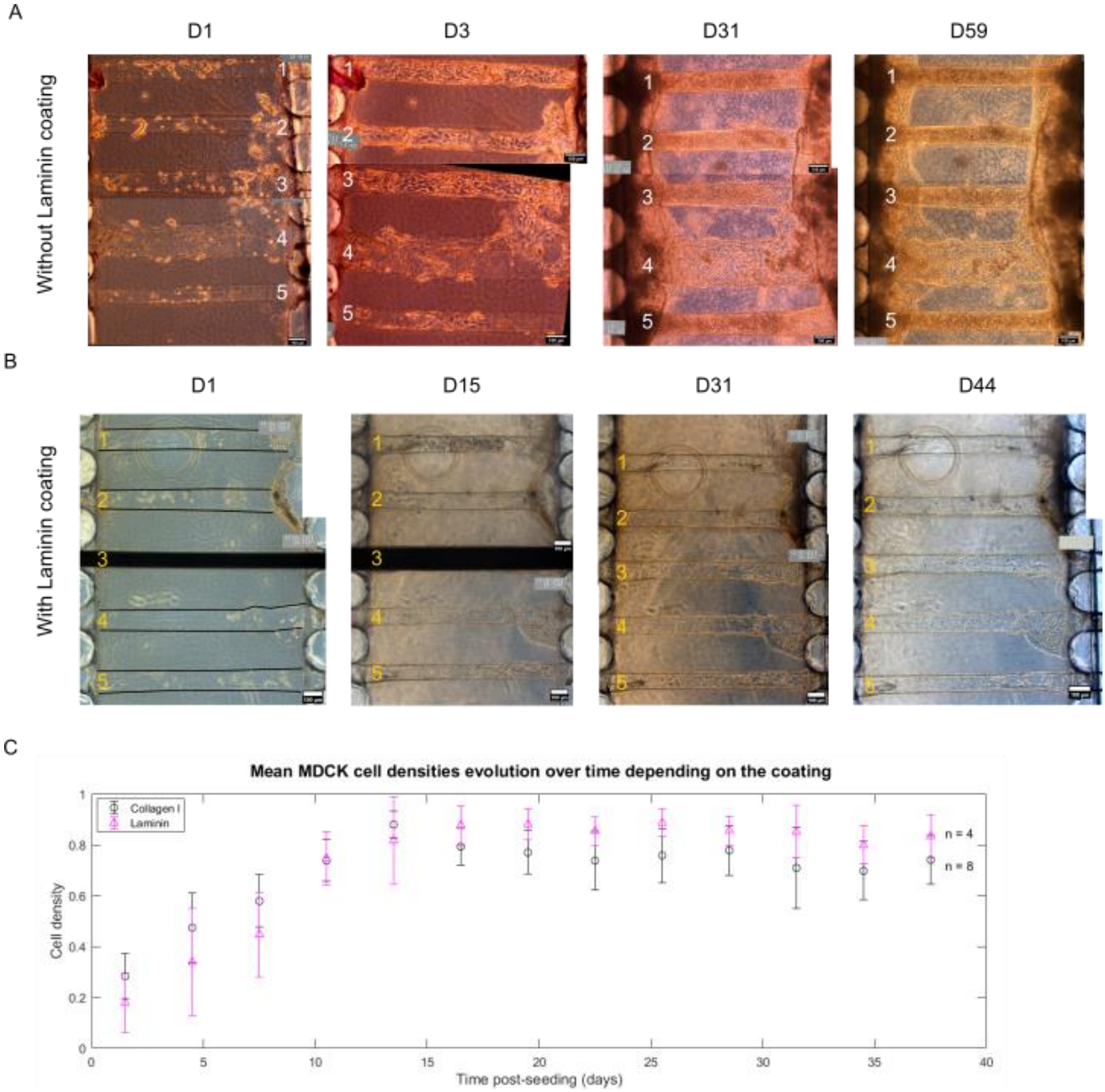

Figure 38: Images illustrating the MDCK-Lifeact-GFP cells within tubes molded in collagen I at 6 mg/ml, and observed under an optical microscope over time. In red, cell clusters coming off from tubes are highlighted. A: Cells adhering to tubes in collagen I, without any coating. B: Cells lining with tubes shaped in collagen I and coated with the laminin protein. The wire has been removed eighteen days post-seeding. Scale bar: 100 µm. C: Graph representing a comparison of the mean cell densities of tubes molded in collagen I (black dots) with or without laminin coating (magenta dots), and seeded with MDCK cells, over time. SEM are represented.

We measured more accurately cell clusters number and size depicted earlier, in association with cell proliferation within the tubes. Using ImageJ software, those two parameters were quantified by hand, on raw images acquired over time after cell confluency. Indeed, cell clusters represent buds of cells that look like small cysts within the tubes. As qualitative images assumed, MDCK cell clusters formation is around three times more important in collagen tubes than in tubes coated with laminin (61 *vs* 26 clusters in laminin coated tubes) (Fig.39A). Besides, their perimeter is significantly less important in the coated tubes, with a 1.57 fold-decrease (Fig.39B). Clusters shaping within tubes coated have a mean perimeter of around 70 µm (+/- 10 µm) while those formed in collagen tubes are bigger (~ 110 µm). Those observations could imply that cells adhere more on laminin coating for long-term culture than on collagen I alone. The basal membrane reconstitution seems to have an effect on MDCK cells behaviour within the tubes, even if the coating does not play a role on their colonization rate [268].

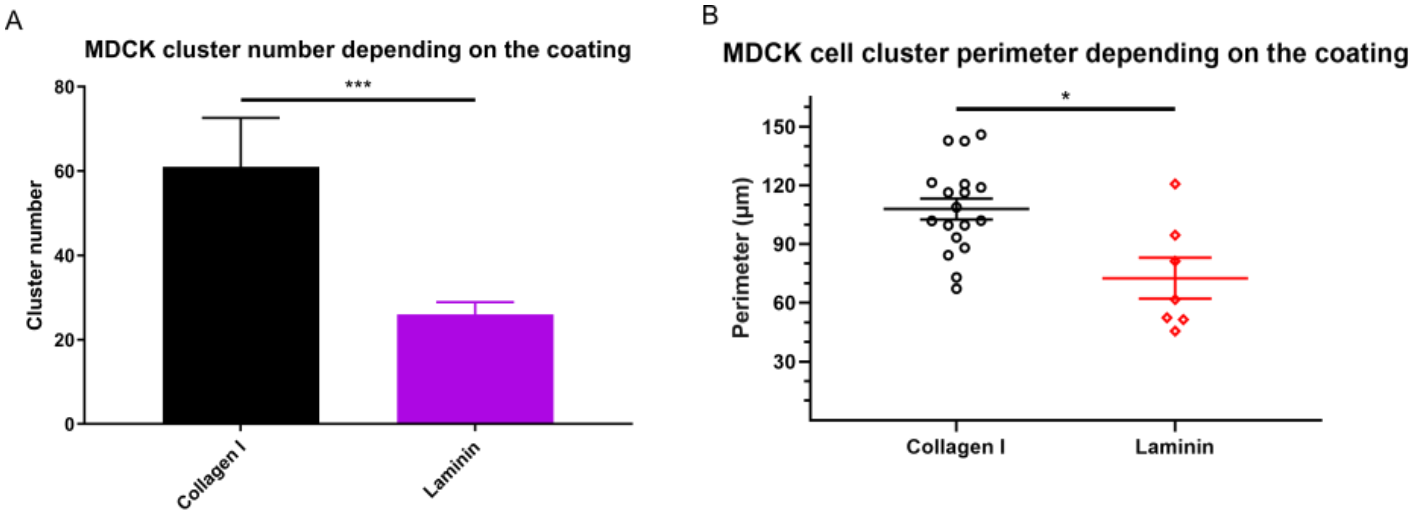

Figure 39: Plots representing MDCK-Lifeact-GFP cell clusters and clusters perimeter depending on the coating. A: Graph of MDCK cell clusters number in collagen I tubes compared to those coated with laminin. One-way ANOVA test was performed for statistical analysis. B: Plot comparing MDCK cell clusters perimeter within tubes made in collagen I alone and coated with laminin. Statistical analysis were performed with an unpaired t-test (Welch's correction), $p < 0.05$. Collagen I: n = 6 independent experiments, laminin: n = 4 independent experiments. SEM are represented.

Besides, we also examined MDCK intracellular organization within laminin coated tubes. We investigated the tight junctions formation characterized by the expression of the ZO-1 (Zonula Occludens-1) protein by confocal microscopy. Indeed, this intracellular marker plays a role in the epithelium barrier functions, which is essential for fluid reabsorption, secretion and transport [268]. On this preliminary image (Fig.40), we observed that the ZO-1 exhibits a network pattern that is similar to chicken wire-like pattern. On the tube edges, they slightly displayed a squamous structure, which is a common feature of renal epithelium *in vivo*-like phenotype. The basal membrane recapitulation could thus induce the cell differentiation into epithelial renal cells with phenotypical features.

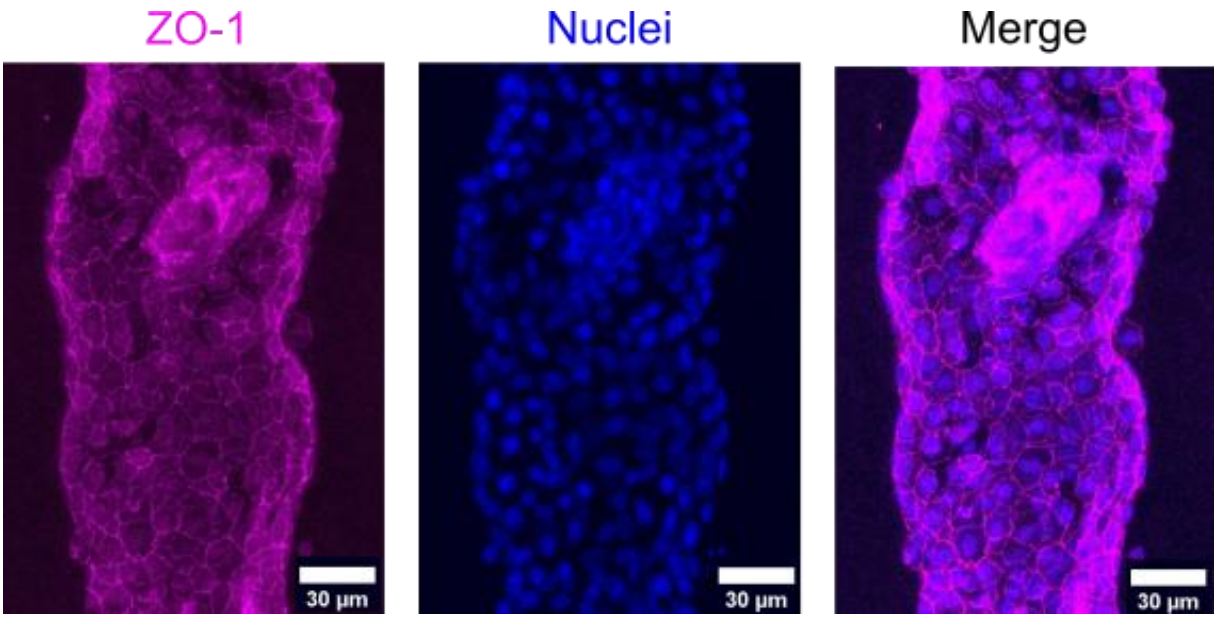

Figure 40: Images illustrating MDCK cells lining with tubes molded in 6 mg/ml collagen I, and coated with laminin, observed under a confocal microscope. In purple: the ZO-1 marker, in blue: the nuclei, and the merge on the third image. All the pictures are a *z*-projection of the maximum intensity signal.

Going back to the global tubes shape, we then determined the mean of tubes diameter over time, after the MDCK cells seeding in different conditions. Based on one plan of phase contrast images acquired, the *z* projection of each image was approximated as the local cylinder diameter (see analysis details in Annex 4). For each following graphs, the dots represent the mean tubes diameters of several independent experiments. These values were normalized with the day 0 (D0) corresponding to tubes size after the seeding.

In tubes made of collagen I, as well as in those coated with laminin, we noticed that the tubes did not dilate over time. Indeed, few variations of the mean tubes diameters over time were observed, with a slight global tendency to retraction. The mean diameter ratio varied between 1 and 0.85 from D10 to D20, which could be due to cell growth within the tubes and their progressive attachment to tubes walls while duplicating (Fig.41A). Then, this ratio fluctuated between 0.9 and 1.05 from days 25 to 38, which could be due to cell detachment from the tubes walls. It is worth noting that more experiments were done without coating than with the laminin coating, as a first implementation. Furthermore, to assess tubes deformation over time more accurately and relevantly, we quantified the mean of the minimal and maximal tubes diameter in each condition (Fig.41B and C respectively). Knowing that the initial tube diameter is 80 µm before the seeding, we noticed that the mean of the maximal tubes diameter varies between 100 and 120 µm over time, but remained quite constant (Fig.41B). In the meantime, the minimal tubes diameter tended to decrease, following the same tendency as the mean normalized tubes diameter. Overall, we observed the same dynamics in tubes coated with laminin compared to the control condition, meaning in tubes molded in collagen I without coating (Fig.41C). Those observations suggest that MDCK cells slightly deformed the tubes during the first two weeks corresponding to the proliferation phase. They seemed to exert a pulling force to retract the tubes during this period. Then, they seemed to proliferate less and less, to detach from the tubes walls and form clusters within the tubes. These following events seemed to decrease the pulling force applied by the cells, which promotes tubes enlargement during the next two weeks.

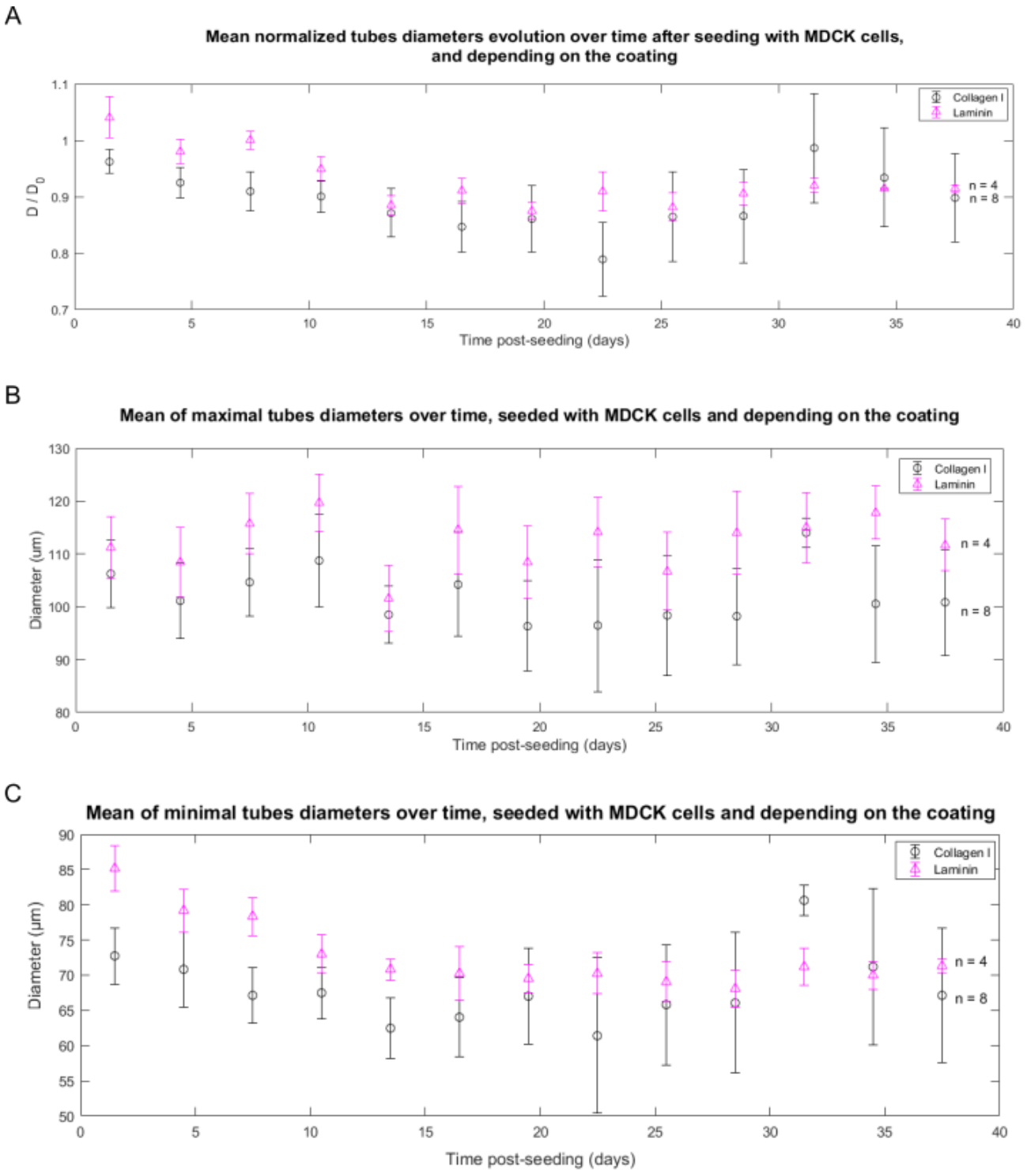

Figure 41: Plots representing mean diameter of tubes seeded with MDCK-Lifeact-GFP cells in different conditions, and over time bins. Tubes made in 6 mg/ml of collagen I were coated or not with laminin. A: Normalized values of mean tubes diameter with in black, mean on chips made in collagen I (n = 8), in magenta, chips with tubes coated with laminin (n = 4). B: Plot of mean of minimal tubes diameter over time. C: Graph illustrating mean of maximal tubes diameter over time. Chips without coating (collagen I), n = 8, and tubes with coating (laminin), n = 4. SEM are represented.

Furthermore, to investigate whether MDCK cell proliferation promotes a mechanical interplay between tubes in a chip coated with laminin, we left the third wire located in the middle. Indeed, cell growth within adjacent tubules might induce the deformation of the empty tube overtime, by contracting or enlarging it for instance. By preventing cell growth within the middle tube from the beginning, we could induce a monitored, and local constraint. It was also done in a tube without coating, as a control experiment. As soon as the adjacent tubes were lined with cells, the wire located in between was gently pulled off. The result was the same in both conditions: albeit the cells grew within the tube after the wire removal, and lined with it, the tube shape did not seem to have a mechanical effect on the other tubes located on both sides. It is worthy to note that MDCK cells can even line with the tube in presence of the wire and that the wire removal did not take away the lining cells.

Conclusion:

Hence, this first approach in an innovative kidney-on-chip, with regularly spaced multitubes molded in collagen I at 6 mg/ml, will provide several cues to mimic renal cell organisation and the ADPKD hallmarks. Indeed, in our novel system, the initial scaffold in collagen I is suitable to gradual improvements. We reproduced the basal membrane with a laminin coating that seems to induce renal epithelial cell differentiation and a characteristic phenotype over a long period (more than thirty days of culture). Cells were able to line tubes, and to recapitulate the tubule-like structure found in physiological conditions. Although we did not apply a constant and monitored flow, the 3D microstructures defined a base to allow the implementation of the epithelium renal features.

Chapter III: A 3D scaffold to mimic the ADPKD

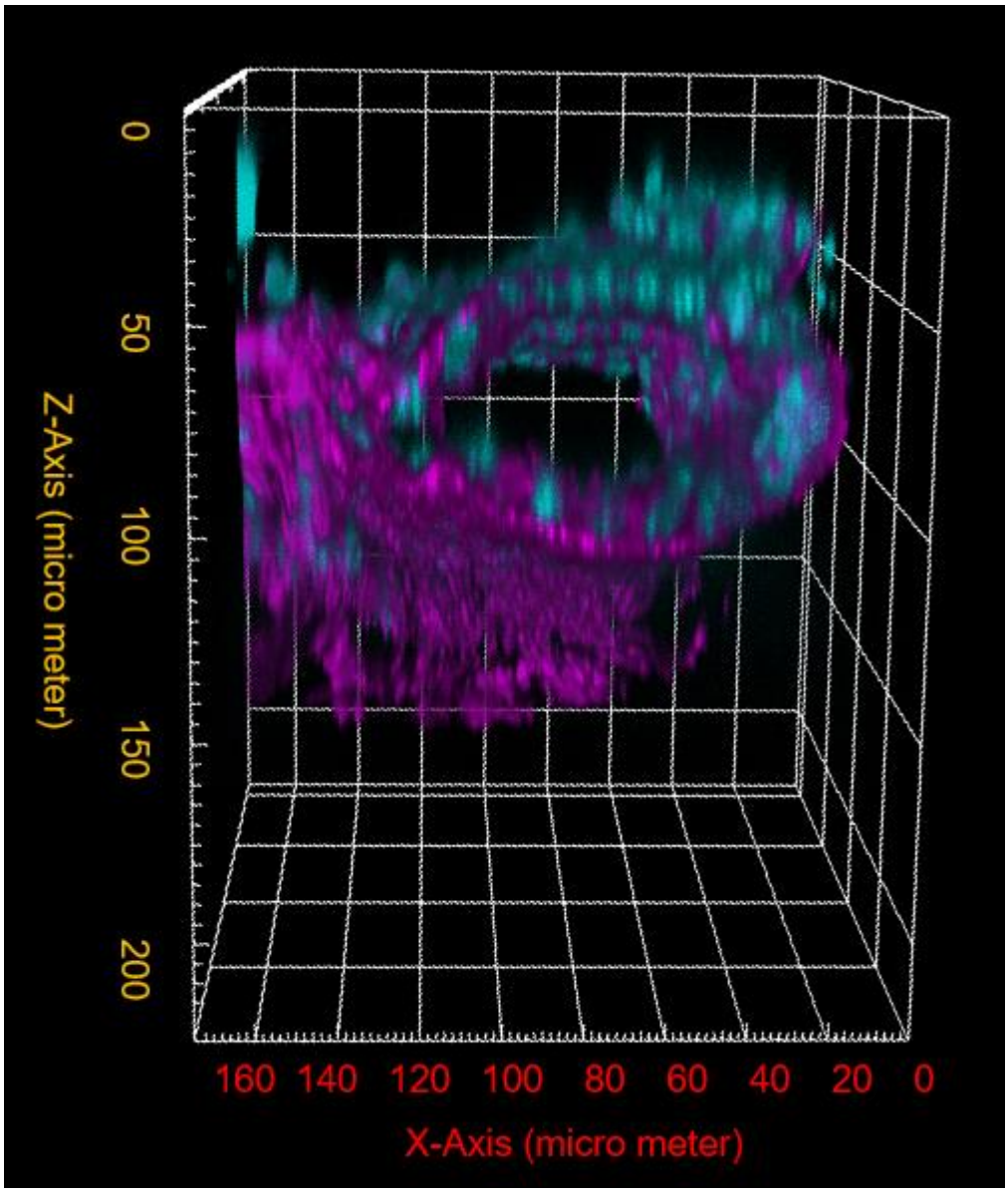

Figure illustrating a tube section lined with *Pkd1*$^{-/-}$ cells with in magenta, F-actin cytoskeleton and in cyan, nuclei. Cells were fixed ten days post-seeding. Processed on Icy software with the help of Lauriane Geremie, PhD student in the MMBM team.

1) Cellular models of the ADPKD

a) Proximal convoluted tubular cell lines

Over the past decades, many kidney-on-a-chip platforms mimicking the first section of the nephron as the renal functional unit were developed [216], [217], [219], [222], [223], [238], [242]. Mainly assessing drug-induced toxicity and drug screening with those microphysiological devices connected or not to other organs, none of them were used to model a specific renal disorder. Indeed, directly in contact with the highest concentration of drugs and their toxic metabolites compared to the following nephrotic segments, the proximal convoluted tubule (PCT) is the most sensitive to renal injury and impairment [3], [216], [217], [219]. Therefore, now that we have designed an operable kidney-on-a-chip device with relevant renal features, we will use it to model one of the most inherited renal disease, the ADPKD or Autosomal Dominant Polycystic Kidney Disease. As cellular models of this pathology, we worked with mice renal cell lines coming from the proximal convoluted tubular cells that reabsorb around 65% of filtered water, solutes and nutrients from the filtrate [8], [263].

To this end, we used three different cell lines from two distinctive mice, and provided by two teams (cf. Annex 1). One of them reproduces the ADPKD major hallmarks, while the two others are used as control cell lines.

The first one is a control cell line expressing the *Pkd1* wild-type gene given by E.Honoré and A.Patel team, from Sophia Antipolis. To get it, kidneys from C57Bl/6 wild-type mice were microdissected to isolate PCT cells from the nephrons, by hand. These tubular segments, detected under binoculars, are immediately located at 1 to 1.5 mm after the glomerulus. This primary culture was then transfected with the SV3-neo plasmid in order to immortalize it [274].

Moreover, S.Somlo team from Yale New Haven Hospital in the USA kindly gave us two immortalized proximal convoluted tubular cell lines carrying a heterozygous or a homozygous mutation in the *Pkd1* gene were put in culture. Indeed, in 85% of ADPKD cases, there is a germinal and/or somatic mutation in the *Pkd1* gene encoding the polycystin-1 protein (PC1). Both of those cell lines were derived from single parental *Pkd1*$^{flox/-}$ clones. The first segment of the nephrons was extracted and PCT cells were isolated. Cells were then transiently

transfected or not with the Cre recombinase enzyme. The PCT cells transient transfection led to *Pkd1*$^{-/-}$ or null (PN24) cell line, whereas its absence gave rise to the heterozygous *Pkd1*$^{+/-}$ (PH2) cell line. Those cells also express the conditionally immortalizing Immortomouse (H-2K-tsA58) transgene, a construct sensitive to the temperature and the presence of γ-interferon. Indeed, cells undergo reversible immortalization under permissive conditions, at 33°C. They decrease their proliferation rate and differentiate into epithelial cells at a higher and physiological temperature, 37°C, in a γ-interferon-free medium to suppress the large T antigen expression from the Immortomouse. Beyond seven days of culture in this medium, the cells differentiate to express an epithelial phenotype (for more details, cf. Annex 1). It is worthwhile that Wei and co-workers studied those cell lines embedded in a mix of collagen I and Matrigel (a ratio of 70:30). They noticed that *Pkd1*$^{+/-}$ cells mainly shape tubules with cord-shaped structures, while *Pkd1*$^{-/-}$ cells form cysts displaying a lumen. Besides, those homozygous cells proliferate faster and exhibit low apoptosis potential than *Pkd1*$^{+/-}$ cells [57], [275]. For the results explained below, *Pkd1* cells were maintained in the differentiation medium during at least seven days, before being used in the different experiments.

We used PCT-Wt as a control of *Pkd1*$^{+/-}$cells, and *Pkd1*$^{+/-}$ cells as a control of *Pkd1*$^{-/-}$ cells. Indeed, the two cell lines carrying a conditional allele for *Pkd1* gene derived from the same mice models. Besides, they were maintained in identical culture media, compared to the PCT-Wt cell line. For the sake of clarity, we will similarly name *Pkd1*$^{+/-}$cells or heterozygous cells, and refer *Pkd1*$^{-/-}$ cells as homozygous cells.

To start with, we characterized the cell lines phenotype when cultured in the differentiation medium and maintained in 2D, on glass or usual plastic surface. We first observed PCT-Wt cells compared to *Pkd1*$^{+/-}$, and *Pkd1*$^{-/-}$ cells, seeded at different cell densities on plastic, without any labelling. At over confluency, PCT-Wt and *Pkd1*$^{+/-}$ cells behaved similarly: they formed multilayers and alveolar structures above the cell monolayer (Fig.42A). The alveolar structures looked like cylinders more or less elliptical, and often linked to each other. Cells grew on each other to shape walls constituting the alveoli, on a cell monolayer. *Pkd1*$^{-/-}$ cells exhibited cell extrusions when they were over confluent, and detached from the plastic surface (Fig.42A). To further investigate these surprising and characteristic phenotypes, we also checked the intracellular organization of the actin cytoskeleton within those three cell lines (Fig.42B). Cells were seeded at 5.10^4 cells/ml on glass coverslips put in a 12-well plate, and fixed two days later. F-actin or filamentous actin was then labelled with phalloidin-TRITC,

when cell density reached around 70% of confluency, and before complete cell detachment from the surface (cf. detailed protocol in Annexe 2). Phalloidin staining also indicates the basal and apical sides of the cells [276]. We note that the actin shapes a circular geometry on a layer of small cells, with long and bent stress fibres in PCT-Wt and *Pkd1*$^{+/-}$ cells. The homozygous cell line tended to form big cell buds from a cell monolayer, with disorganized and microfilaments actin fibres (Fig.42B).

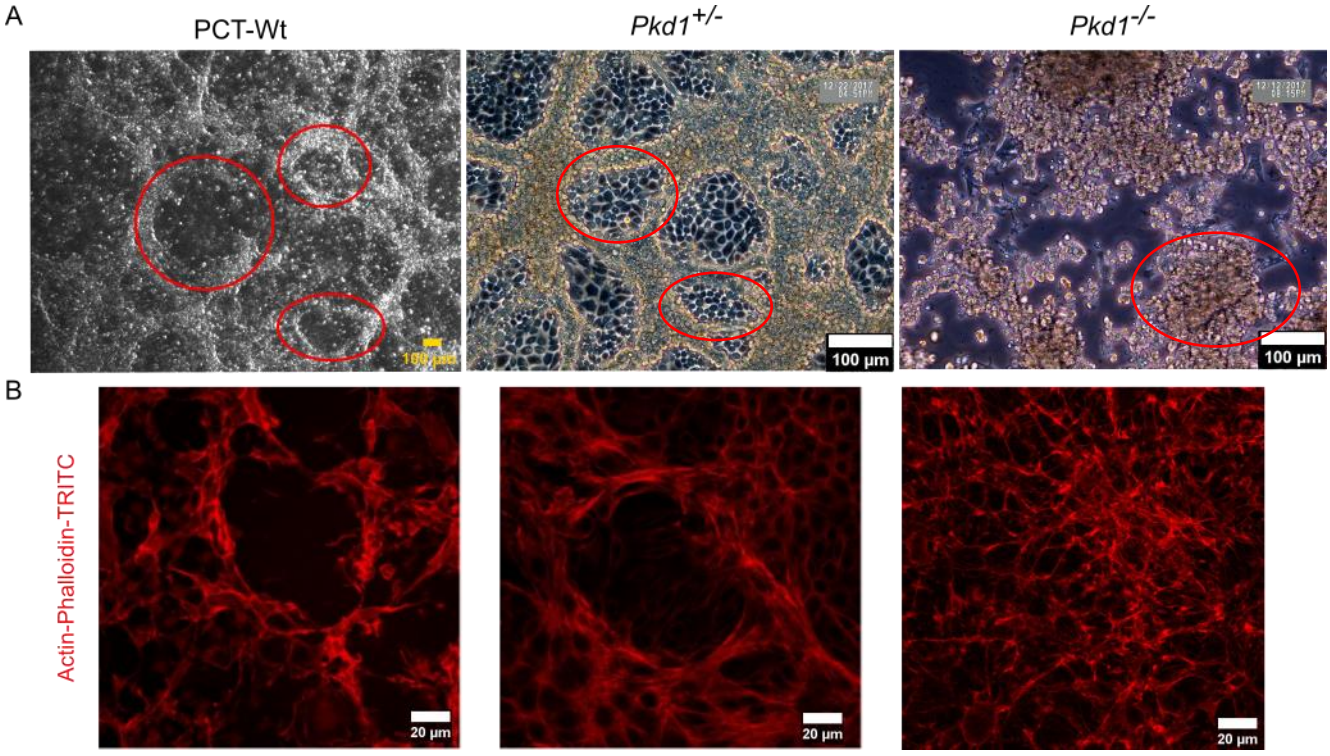

Figure 42: Morphology of the APDKD cellular models. The different cell types were seeded on a plastic support, and observed under a phase contrast microscope at over confluency. A: PCT-Wt cells visualized at high density, with alveolar structures surrounded in red. Scale bar: 100 µm. On the right and the middle, PCT-Wt cells and heterozygous cells respectively, with alveoli circled in red. On the left, *Pkd1*$^{-/-}$ cells morphology, with cell extrusions highlighted in red. Scale bar: 100 µm for the first image, and 250 µm for the two others. B: ADPKD cellular models plated on a glass coverslip, and acquired under a confocal microscope. Images for each cell line is the maximum signal intensity projection in z. The actin cytoskeleton, stained in red, exhibit different rearrangements in the *Pkd1*$^{-/-}$ cell line compared to the two other ones. Scale bar: 20 µm.

It is worth mentioning that *Pkd1* cells display different morphologies depending whether they were cultured in a proliferation or differentiation medium (Fig.43). Indeed, seeded in the proliferation medium, both cell types became smaller and smaller over time, which is associated with the cell proliferation. Although the cells also organized to shape alveolar structures or cell clusters on cell multilayers with *Pkd1*$^{+/-}$ or $^{-/-}$ cells respectively, the dynamics and the cell morphologies were quite different. Indeed, plated in the differentiation medium, both cell lines exhibited distinctive features. The heterozygous cells shaped alveolar structures above a well-defined monolayer of renal epithelial cells, whereas the homozygous cells formed clusters extruding from the monolayer. Those extrusions looked like small cysts.

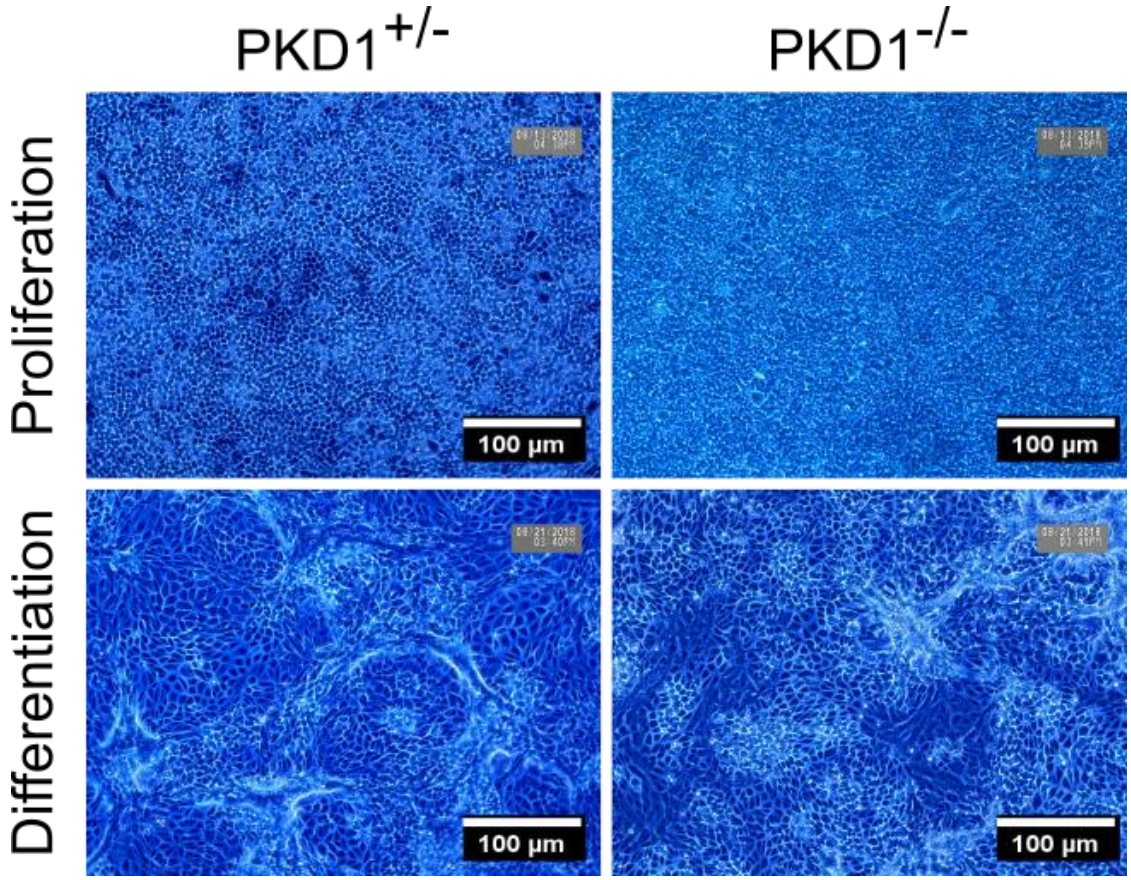

Figure 43: Morphology of the *Pkd1*$^{+/-}$ and $^{-/-}$ cells cultured in different mediums for at least two weeks. Both cell lines were plated on a plastic surface, and observed under a phase contrast microscope, at high density. On the top, we observe the phenotype of the cells put in the proliferation medium, while the bottom panel illustrates the cells cultured in the differentiation medium. As previously, we note two surprising geometries for each cell type: alveoli and buds of *Pkd1*$^{+/-}$ and $^{-/-}$ cells respectively. Scale bar: 100 µm.

Moreover, as the three cell lines did not display an identical dynamics, we realized a doubling test to determine the proliferation rate of each cell line. To this end, all the cell types were plated at different cell densities in a 6-well plate: 5.10^3, 10.10^3, 20.10^3, 40.10^3, and 80.10^3 cell/ml. They were then trypsinized, and counted at different time points, every 24 hours to define a proliferation curve over time (Fig.34). For each cell type, we distinguish two main phases: an exponential phase during which the cells duplicate, and a plateau corresponding to the latency period reached by the cells. The duplication rate was determined during the exponential phase. We noticed that the different cell lines did not proliferate at the same velocity: *Pkd1*$^{-/-}$ cells grew faster than the control cell lines, with a two-fold increase in each medium (Fig.44A and B). It is consistent with the fact that cystogenesis, among other things, is induced by an increased proliferation rate of *Pkd1*$^{-/-}$ cells [275]. The PCT-Wt cells duplicated in around 35 hours, such as *Pkd1*$^{+/-}$ cells in the proliferation medium (Fig.44A and C). Nevertheless, both mutated cell lines grew slower in the differentiation medium: around 48h of doubling time for the heterozygous compared to 25h for the homozygous cell line (Fig.44D).

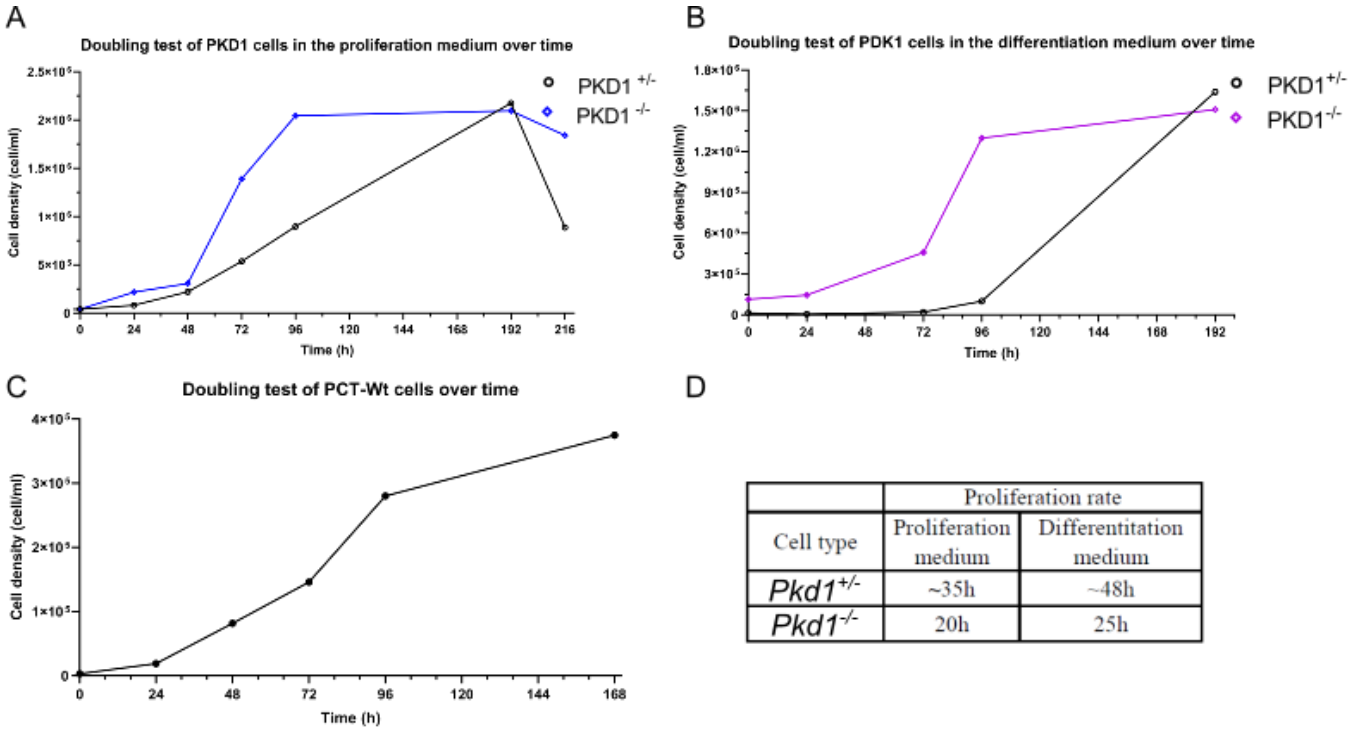

Cell type	Proliferation rate	
	Proliferation medium	Differentitation medium
Pkd1$^{+/-}$	~35h	~48h
Pkd1$^{-/-}$	20h	25h

Figure 44: Doubling test on the ADPKD cellular models. Plots representing cell density over time, for the three cell lines. A: Graph on *Pkd1* cells growth in the proliferation medium. B: Plot on *Pkd1* cells' growth in the differentiation medium. C: Graph of the PCT-Wt cells proliferation. D: Table summarizing the duplication time of the *Pkd1* cells in each medium.

Then, intrigued by the specific and singular phenotype of the ADPKD cellular models, we examined the formation of the alveolar structures and the cell clusters extrusions over time. For this purpose, cells were seeded at a lower cell density in a T25 flask and followed during several days under a phase contrast microscope (Fig.45). Although the medium of

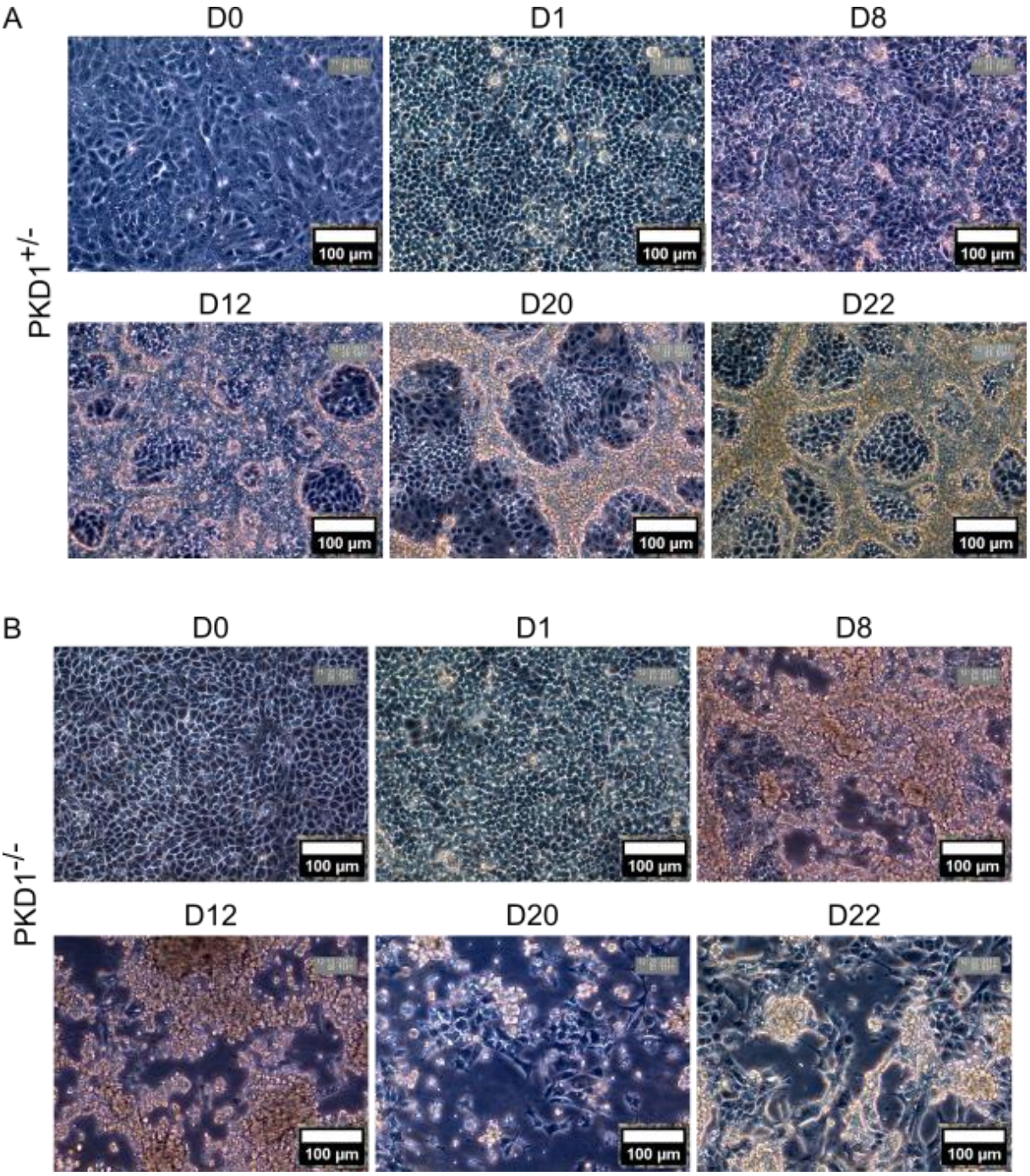

Figure 45: *Pkd1* cells morphology in the differentiation medium, observed under a phase contrast microscope, over time. A: Formation of *Pkd1*$^{+/-}$ cells alveoli over time. B: *Pkd1*$^{-/-}$ cells shaping buds and detaching from the surface. Scale bar: 100 µm.

differentiation was changed every two days, the cells were not passaged in another flask over time.

After eight days, *Pkd1*$^{+/-}$ cells coordinated to build the walls composing the alveoli that strengthened over time (Fig.45A). In parallel, the homozygous cell line joined to form a cohesive cell layer and shaped clusters extruding from the cell monolayer. The remaining cells were elongated, and slowly came off the surface after 22 days of culture (Fig.40B).

Therefore, studied under a phase contrast microscope over time, the three cell lines chose as ADPKD cellular models, and the associated control, displayed interesting and surprising phenotypes. As expected, PCT-Wt and *Pkd1*$^{+/-}$ exhibited a similar phenotype: we will next focus on a deeper characterization of the cell lines carrying a conditional *Pkd1* allele, *Pkd1*$^{+/-}$, and *Pkd1*$^{-/-}$ cells. Indeed, to better define their renal epithelial features, we assessed the expression of specific intracellular markers in 2D, before studying it within the tubes made in collagen I.

b) Renal cell characterizations in 2D, on glass

Renal epithelial cells are known to exhibit a morphology specific to their localization within the nephron tubule, and related to their function [8]. Similarly, we observed that *Pkd1*$^{+/-}$ cells organized differently from the homozygous cells seeded on a flat substrate, at high density [277]. While the heterozygous cells tended to shape a three-dimensional cylinder on an underlying cell layer, the *Pkd1*$^{-/-}$ cells formed buds that looked like small cysts coming off the cohesive cell monolayer.

In order to study the intracellular organization and to decipher the cystogenesis process, immunofluorescence experiments were realized on the ADPKD cellular models in 2D, before putting those cells within a three-dimensional tubular scaffold. *Pkd1* cells were seeded on glass coverslips dropped off a 12-well plate bottom, at a density of 5.10^5 cells/ml for two days, in the differentiation medium. The cells were then fixed, and stained for different proteins (cf. Annex 2). Some epithelial cell specific markers were investigated, under static condition: the polarity (apical and basal), focal contacts, intercellular junctions (*adherens* and tight junctions), as well as F-actin cytoskeleton [276], [278]–[280]. In addition to their distribution within both cell types, those proteins were also quantified by RT-qPCR normalized with GAPDH, a

housekeeping gene whom expression is stable and similar in the three cell types (n = 2 independent experiments performed in the same conditions by the BMBC technological platform from Institut Curie, thanks to the help of Aude Battistella).

Several intercellular junctions were stained and quantified: ZO-1 (Zonula Occludens), Occludin, E-cadherin, and N-cadherin. Apico-basal polarity markers are of great importance to define cyst formation, in particular within tubes. We used two markers: the actin-membrane linker ezrin localized in the apical side of cells, and the Na/K ATPase pump, a specific marker of renal epithelial cells located in the cellular baso-lateral part. Moreover, Aquaporin 1, a water channel expressed in the proximal segment of nephrons, was quantified to assess the function and tubular origin of the cell lines studied.

In each cell line, F-actin arrangement highlighted the three-dimensional cell shape and their orientation within the tissue. We noted that the amount of mRNA encoding the β-actin was not statistically different in both cell lines [278] (Fig.52A).

The results obtained clearly highlighted that the localization and quantification of the intercellular junctions vary depending on the cell type analysed: PCT-Wt and *Pkd1*$^{+/-}$ versus *Pkd1*$^{-/-}$. For the results described below, we will exclusively focus on the *Pkd1* cells behaviour.

ZO-1 and occludin were localized at the plasma membrane in the three cell types: they colocalised perfectly with F-actin cytoskeleton (Fig.46). F-actin was shaped as a thin circumferential network between cells, in the apico-lateral side. Moreover, the amount of mRNA encoding ZO-1 was not different between *Pkd1*$^{+/-}$ and $^{-/-}$ cell lines (Fig.52). This result was expected as it was already reported that this protein expression was similar in both cell types. Noteworthy, the literature mentions a tight junction reorganization under flow: ZO-1 distribution was reported to be punctuated and discontinuous under flow [44], [276], [281]. Other studies performed in slightly different experimental conditions indicated that the tight junctions composition was, on the contrary, strengthened under flow [281]. It could be interesting to study if tight junctions reinforce over time under flow, as our experiments were realized under static condition. Indeed, epithelium leakiness reduction is essential for reabsorption, secretion and solutes transport in PCT.

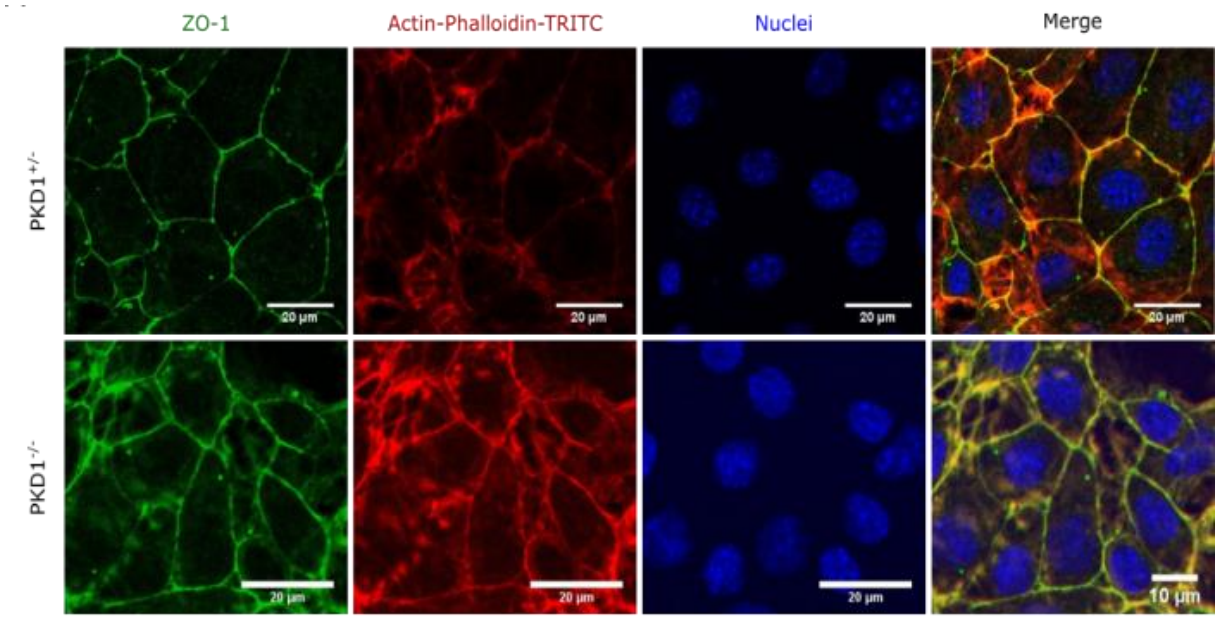

Figure 46: ZO-1 distribution within the ADPKD cellular models. Both cell lines (*Pkd1* $^{+/-}$ on the top, and *Pkd1*$^{-/-}$ cells on the bottom) were immunostained with anti-ZO-1 antibody in green, phalloidin-TRITC in red for F-actin labeling, and Hoechst for nuclei labeling. Scale bar: 20 µm, except for the last picture for which the scale bar is 10 µm.

Then, analysing further the junctional complexes involved in intercellular interactions, E-cadherin intracellular localization was also examined. This *adherens* junctions protein was distributed in the cytoplasm, under vesicular forms, and along the plasma membrane of the heterozygous cells. In contrast, it seemed mainly cytoplasmic in the homozygous cells (Fig.47). Besides, its mRNA level was very low in the homozygous cells compared to its amount in the heterozygous cell line: 0.032 fold change in the *Pkd1*$^{-/-}$ cells compared to 1, which means around thirty times lower in the homozygous cells (Fig.52).

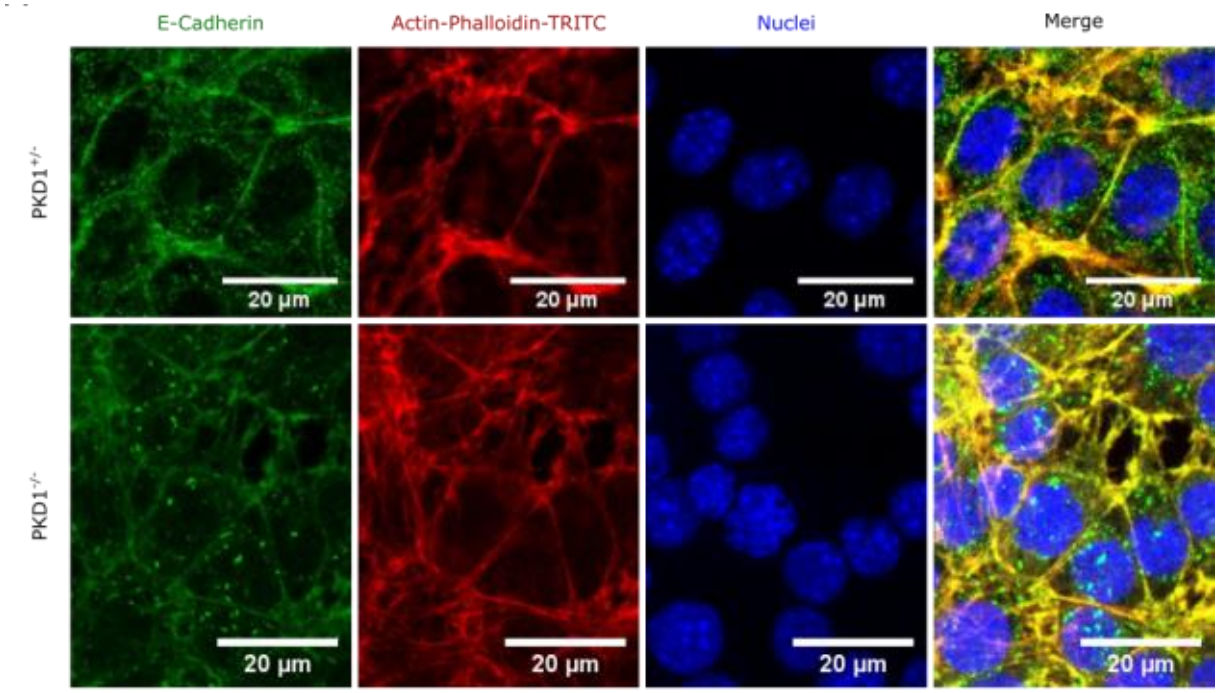

Figure 47: E-cadherin localization within the ADPKD cellular models. Both cell lines (*Pkd1*$^{+/-}$ on the top, and *Pkd1*$^{-/-}$ cells on the bottom) were immunostained with anti-E-cadherin antibody in green, phalloidin-TRITC in red for F-actin, and Hoechst for nuclei. Scale bar: 20 µm.

Moreover, we noticed that N-cadherin, another *adherens* junction protein, was predominantly localized at the plasma membrane of the *Pkd1*$^{-/-}$ cell line. Close to it under vesicular form, its repartition could explain E-cadherin distribution (Fig.48A). Comparing the E-cadherin and N-cadherin expression levels in the *Pkd1*$^{-/-}$ cells, we noticed that the ratio of N-cadherin/E-cadherin mRNA level was six times more important in *Pkd1*$^{-/-}$ *cells*. Besides, N-cadherin mRNA transcript amount was 4.8-fold decreased compared to *Pkd1*$^{+/-}$ cells (Fig.48B). Wilson and co-workers mentioned that E-cadherin is internally sequestered in the cytoplasm and replaced by N-cadherin during ADPKD evolution [282]. This phenomenon could support the E-cadherin repartition observed in ADPKD cellular models. It is noteworthy that the actin filaments formed a dense peripheral actin band, surrounding the cells at the level of *adherens* junction, which is a major site of contact between adjacent cells (Fig.47A and 48A) [281].

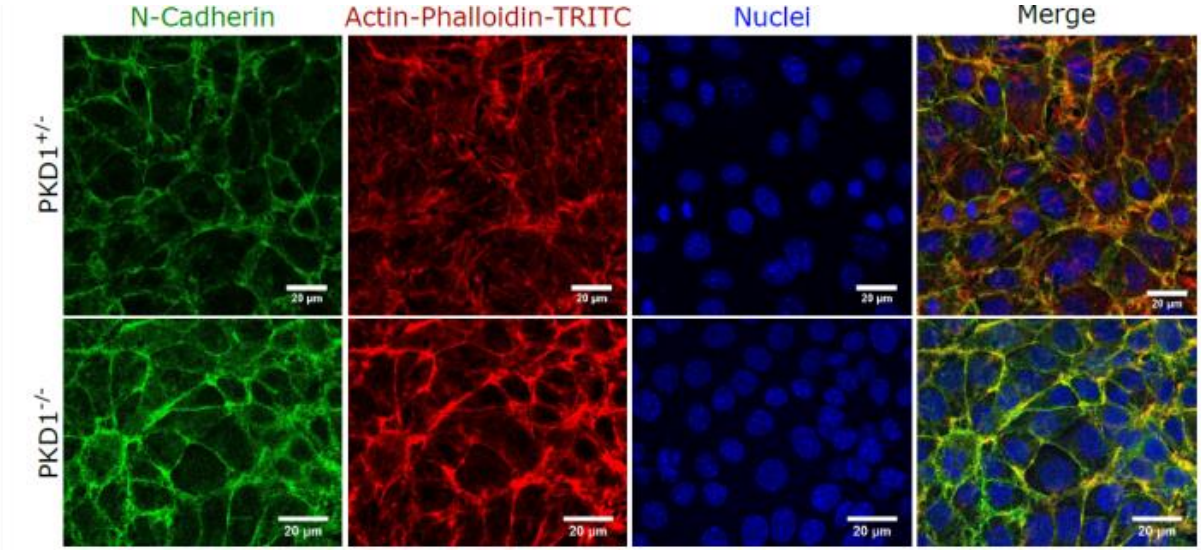

Figure 48: N-cadherin distribution within the ADPKD cellular models. Both cell lines (*Pkd1*$^{+/-}$ on the top, and *Pkd1*$^{-/-}$ cells on the bottom) were immunostained with anti-N-cadherin antibody in green, phalloidin-TRITC in red for F-actin, and Hoechst for nuclei. Scale bar: 20 µm.

Furthermore, focal contact proteins, vinculin and paxillin, were studied. They were localized, as expected, along the stress fibres of *Pkd1*$^{+/-}$ cells [44], [276], [280]. As for occludin protein aforementioned, we only depict the vinculin distribution that is similar to the paxillin one. The staining was more diffuse and mostly in *Pkd1*$^{-/-}$ cells edges, at cell-

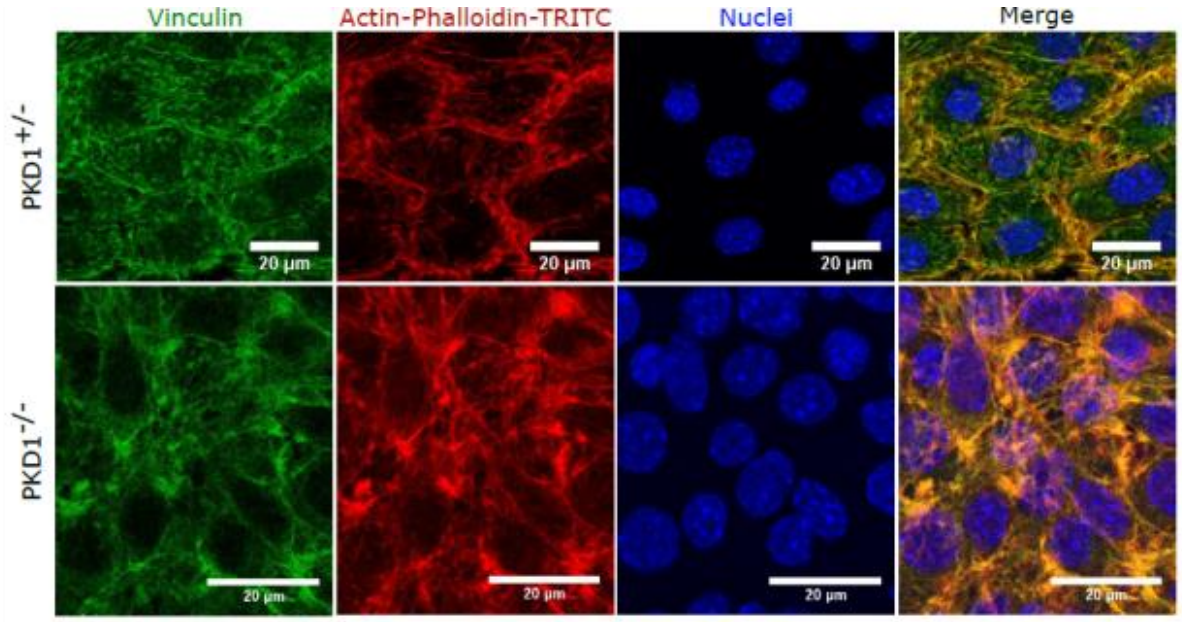

Figure 49: Vinculin distribution within the ADPKD cellular models. Both cell lines, *Pkd1*$^{+/-}$ on the top, and *Pkd1*$^{-/-}$ cells on the bottom, were immunostained with anti-vinculin antibody in green, phalloidin-TRITC in red for F-actin, and Hoechst for nuclei. Scale bar: 20 µm.

cell contacts (Fig.49). This protein, in association with the strong girdle of actin at the plasma membrane, tends to buttress cell-cell contacts instead of cell-ECM adherence. Vinculin gene expression level was also evaluated and displayed no significant difference between both cell lines (Fig.52). The vinculin redistribution in cells would imply that homozygous cells adhesion is weaker, which could ease cells detachment from the surface and cluster formation under cyst shape.

Eventually, polarity markers were examined in both cell types, starting with the apical marker: ezrin. We noted that this protein localized at the plasma membrane of heterozygous cells where it perfectly colocalised with F-actin cytoskeleton. The membrane edge seemed to form much smaller microvilli, or no microvilli, in the *Pkd1*$^{-/-}$ cell line (Fig.50). Besides, this protein spread in a diffuse manner in both cell types, and the encoding mRNA was two times less expressed in the *Pkd1*$^{-/-}$ cells than in the heterozygous one (Fig.52). Ezrin distribution suggested that homozygous cells could partially lose their apico-basal polarity over time.

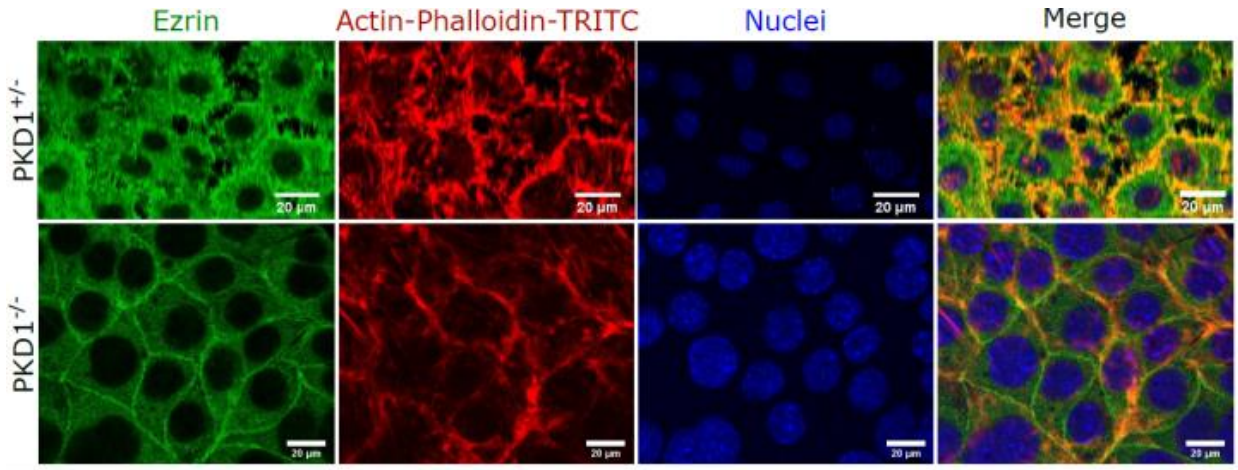

Figure 50: Ezrin repartition within the ADPKD cellular models. Both cell lines, *Pkd1*$^{+/-}$ on the top, and *Pkd1*$^{-/-}$ cells on the bottom, were immunostained with anti-ezrin antibody in green, phalloidin-TRITC in red for F-actin, and Hoechst for nuclei. Scale bar: 20 µm.

Na/K ATPase pump distribution was also investigated: in the heterozygous cell line, this marker distributed in the baso-lateral part, interspersed. However, this protein spanned in the cytoplasm of the homozygous cells, from the apical to the basal side of the cells (Fig.51). The mRNA amount encoding this pump was 2.3 fold-decreased for *Pkd1*$^{-/-}$ cells compared to *Pkd1*$^{+/-}$ cells (Fig.52). These results suggests that Na/K ATPase transporter is mislocalized to

the apical side of *Pkd1* $^{-/-}$ cell line that are cystic epithelial cells, which would invert the polarity for fluid absorption, in line with other studies [1], [109], [110], [283].

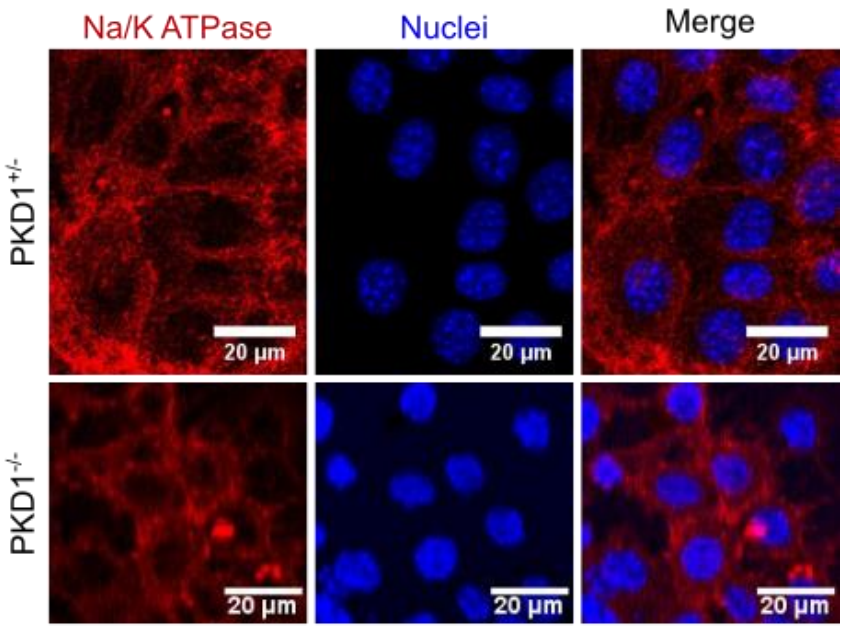

Figure 51: Na/K ATPase distribution within the ADPKD cellular models. Both cell lines (*Pkd1* $^{+/-}$ on the top, and *Pkd1* $^{-/-}$ cells on the bottom) were immunostained with anti-NA/K ATPase antibody in red, and Hoechst for nuclei. Scale bar: 20 µm.

Moreover, to further characterize the ADPKD cellular models, other transcripts were quantified by RT-PCR. We observed that *Pkd1* gene was indeed less expressed in *Pkd1* $^{-/-}$ cells than in the heterozygous cell line: we noted a 3-fold decrease of *Pkd1* gene expression in homozygous cells, favouring its use as an ADPKD cellular model (Fig.52). Nevertheless, as this result was not expected, we started to investigate the reasons for which we still have *Pkd1* gene expression. To delete this gene with the Cre Recombinase enzyme, two loxP sequences framed the exons 2 to 4 of this gene. It turns out that the primers used to realize the RT-PCR targeted the exons 6 to 7 and not the exons 2 to 4, probably producing a transcript encoding for a truncated and not functional protein. Other investigations to confirm the *pkd1* gene depletion with another couple of primers targeting the exons 2 to 4 sequences are on going. In addition, focusing on the proximal tubule, we checked the predominant expression of the water channel AQP1 compared to the AQP2: it is almost not expressed in the PCT cells, as expected (data not shown).

It is noteworthy that ADPKD could be part of the diseases called ciliopathies, as PC1-PC2 complex is expressed in the primary cilium (cf. Chapters I). To begin the investigation of this disease molecular aspect, we also studied Arl13b, a primary cilium marker. We noticed that the mRNA level expression of this marker was not significantly different in both cell lines (Fig.52).

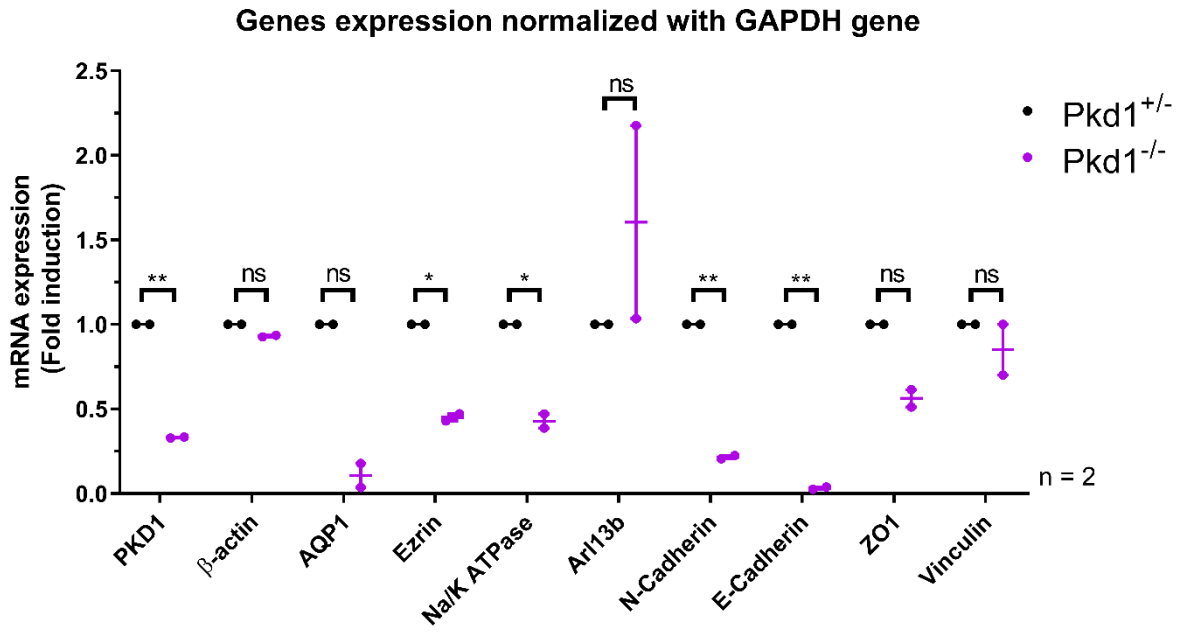

Figure 52: Quantification of markers gene expression within the ADPKD cellular models. A: Transcript level of markers such as actin (cytoskeleton), *Pkd1*, N-Cadherin and E-Cadherin (intercellular junction) was quantified by real-time PCR. Results were expressed as the fold induction compared to the control cell line *Pkd1*$^{+/-}$. Data represent mean ± SEM of 2 independent experiments. p-value< 0.05.

Hence, all those observations raise some hypothesis regarding the cystogenesis mechanism. Indeed, scrutinizing the epithelial cells hallmarks, we focused on the tight and *adherens* junctions, polarity and focal contact markers, as well as on the actin cytoskeleton arrangement within both cell lines, under static conditions. Unlike *Pkd1*$^{+/-}$ cells, *Pkd1*$^{-/-}$ cells have a cystic cell dynamics, with a high growth rate: their intracellular organisation exhibits specific characteristics distinguishing them from normal renal epithelial cells. In particular, the different immunostainings suggest that homozygous cells could display tight junctions reinforcement instead of *adherens* junctions, illustrated by E-cadherin exchanging its homologue N-cadherin, an mesenchymal marker. Those cells could have an impaired apico-basal polarity, and a weak adhesion to the substrate, which could ease more and more the *Pkd1*$^{-}$

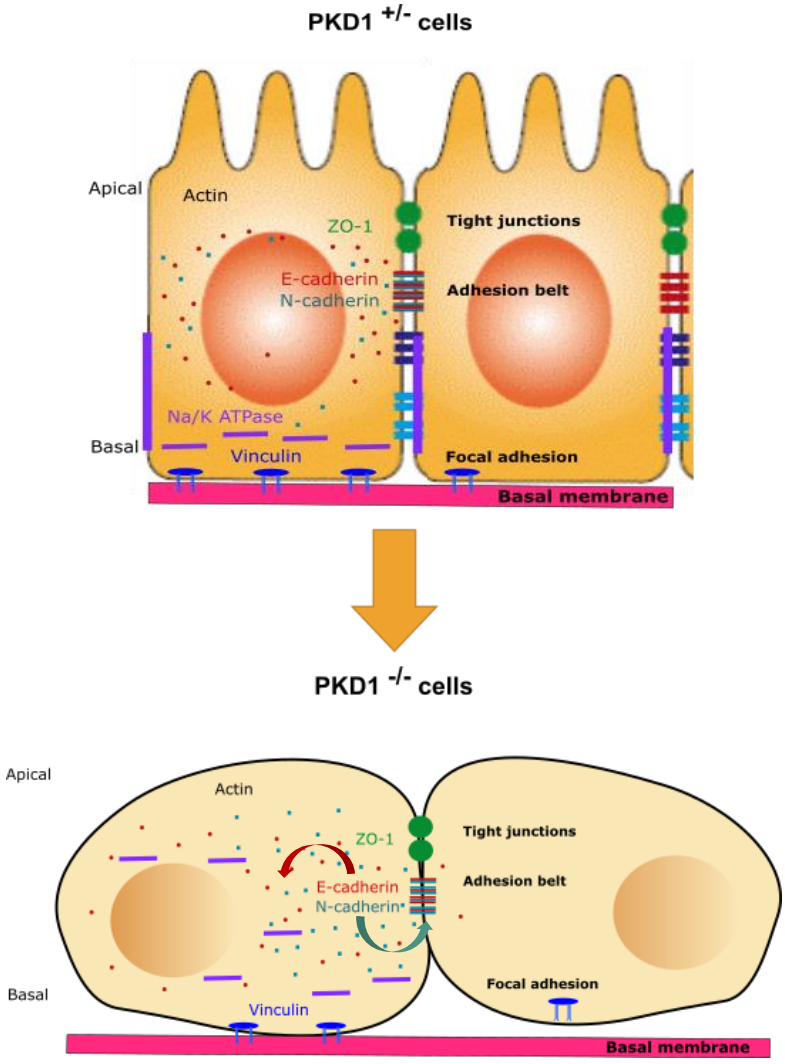

Figure 53: Diagram simulating the localization of epithelial markers within *Pkd1*$^{+/-}$ and $^{-/-}$ cell lines. Cystic cells exhibit a polarity reversal illustrated by Na/K ATPase redistribution. *Adherens* junctions are buttressed to favor intercellular contacts, and focal contacts are impaired to promote cell detachment from the basal membrane. Taken all together, impairment of the different epithelial markers could induce cystogenesis during the ADPKD.

$^{/-}$ cell cluster formation. Moreover, the ions and solutes flow within homozygous cells could be disrupted and temporarily inverted, which could favour the beginning of cystogenesis during the ADPKD evolution [1]. In other words, *Pkd1*$^{-/-}$ cells lose their epithelial phenotype over time, to dedifferentiate and become cystic cells (Fig.53).

c) Cell characterization on flat substrates

In order to reproduce the physical and mechanical support on which renal epithelial cells adhere in the different nephrotic tubular segment, and in order to investigate cells behavior in 2D before moving to 3D tubular scaffold, we seeded *Pkd1*$^{+/-}$ and $^{-/-}$ cells on wells (from a 24-well plate) covered with a thin layer of collagen I. This layer (around 100 µm thickness) was previously coated with adhesion molecules such as laminin, collagen IV or Matrigel. Collagen I alone was the control of the other coating conditions, in 2D as well as in 3D, within the tubes. Cells at subconfluent density do not reabsorb, secrete and transport solutes efficiently because they do not form a cohesive layer. For these reasons, cells phenotype was assessed when they formed a confluent monolayer, and not embedded in the hydrogel, which means three or four days after the seeding (n = 2 independent experiments).

We noticed that the cell monolayer entirely covered the bottom well and was uniform on laminin, collagen I and Matrigel. Cells formed a confluent monolayer, and were packed to each other (Fig.54A). This observation is particularly striking on Matrigel: homozygous, as well as heterozygous cells behaved this way. Those different coatings are known to have a strong positive effect on cell growth and survival. Previous studies reported that epithelial renal cells grew slowly but steadily on laminin coating compare to collagen I or IV coatings [268], [284]. Although cells were seeded on laminin, our experiment was not performed during several weeks, which did not allow us to conclude on this observation in 2D. Nevertheless, on collagen IV, one of the most abundant protein in the basal membrane, both cell types formed a heterogeneous monolayer. Cell-cell contacts were lost, with many gaps appearing in the monolayer, leading to the formation of areas devoid of cells. Cells still adhering to the substrate were more elongated, with long cytoplasmic extensions going through collagen IV. Moreover, we noticed many dead round and floating cells in the medium.

Furthermore, the cell numbers from two different fields of view taken on the pictures were quantified using the Tissue Analyzer plugin on ImageJ. Briefly, cells borders were detected by the plugin from the initial images and corrected by hand to generate a file with the cell number, size, shape and other parameters to characterize a tissue. As the initial images are phase contrast images, cells accurate characterisation was not relevant for this study. We decided to focus on cell density in order to determine the best coating for the kidney-on-chip experiments. We noticed no significant difference between collagen I, Matrigel, and laminin coating on *Pkd1*$^{+/-}$ cell density. Besides, there was a 1.4-fold decrease of the cell number between Matrigel and collagen IV coating. The homozygous cell density on laminin was 1.5 fold-increased compared

to the one on collagen I coating. They were also significantly more numerous on laminin coating than on Matrigel (1.5-fold increase) (Fig.54B). Therefore, the different coating molecules seem to have a moderate effect on the formation and maintenance of a confluent cell monolayer, whether the heterozygous or homozygous cells are assessed.

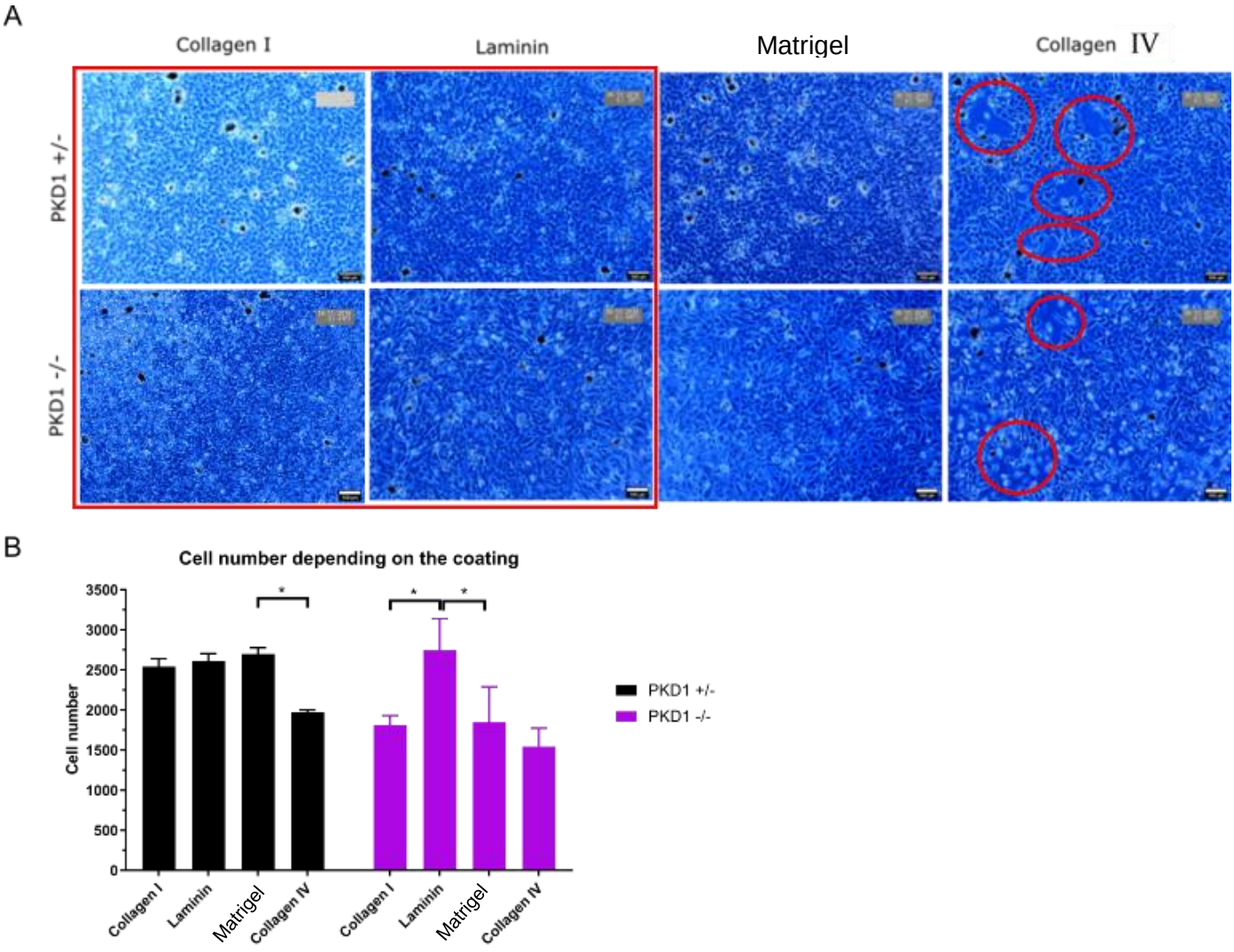

Figure 54: ADPKD cellular models dynamics in response to different basal membrane coatings. A: On the top panel, *Pkd1*$^{+/-}$ cells compared to *Pkd1*$^{-/-}$ cells behavior on the bottom panel, depending on the coating protein. Pictures acquired under a phase contrast microscope, with two fields of view quantified. Scale bar: 100 µm. B: Graph representing cell number depending on the coating protein. Statistical analysis were performed with an unpaired t-test (Welch's correction) * $p < 0.05$. SEM are represented.

Moreover, to determine whether the cell monolayer was cohesive and well differentiated into an epithelium or not depending on the coating, we performed immunostaining (Fig.55). As previously done on glass coverslips, we stained different epithelial markers such as tight and *adherens* junction proteins, focal contacts proteins or polarity markers, as well as F-actin cytoskeleton. Cells were then observed under a spinning-disc microscope to visualize their intracellular organization on the different coatings. However, the method used to observe the immunostained cells was not efficient enough: we were not able to acquire images of cells plated on the different coatings covering the collagen I layer. Indeed, the focus of the microscope remained blurred and inaccurate during the acquisitions. For these reasons, only the actin cytoskeleton organization in both cell lines seeded on a thin layer of collagen I is shown here. We noted that F-actin shaped a circumferential girdle at the plasma membrane, and

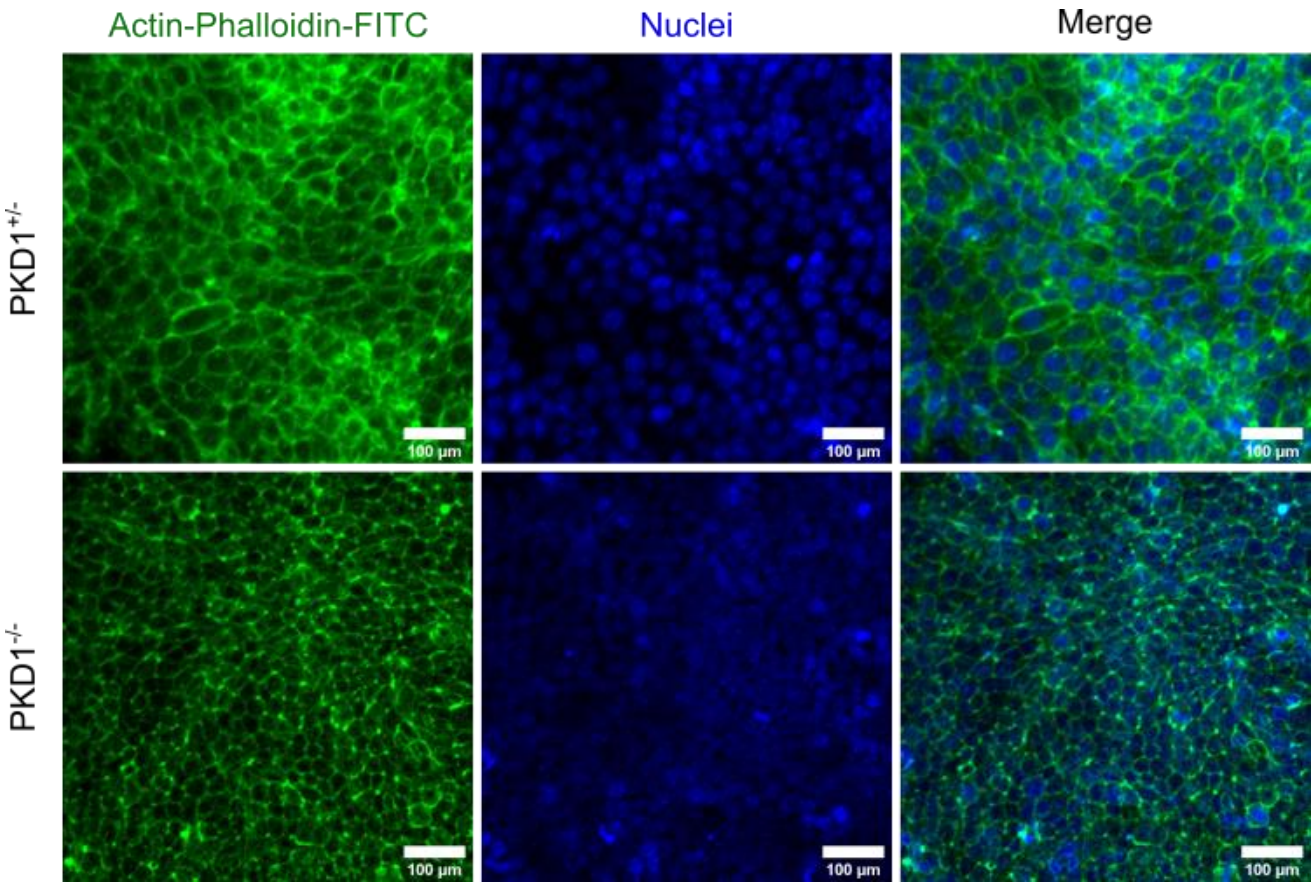

Figure 55: *Pkd1* cell layer phenotype on a thin layer of collagen I, observed under a spinning-disc microscope, four days post-seeding. Both cell lines, *Pkd1* $^{+/-}$ on the top, and *Pkd1*$^{-/-}$ cells on the bottom, were immunostained with phalloidin-FITC in green for F-actin, and Hoechst for nuclei. Each picture is a projection on the z-axis of the fluorophore maximal signal intensity. Scale bar: 100 µm.

connected neighbouring *Pkd1*$^{+/-}$ cells, as well as the smaller and more numerous *Pkd1*$^{-/-}$ cells. This cytoskeleton arrangement suggests that the epithelium is not impaired, but tight, which plays a part in leakages reduction when expanded on collagen I. Moreover, as the coating proteins used were part of the basal membrane composition, the actin cytoskeleton network should be similar and strengthened.

Thus, it seems that *Pkd1*$^{+/-}$ as well as *Pkd1*$^{-/-}$ cells, would rather prefer to lie on laminin than on collagen IV in our experimental conditions, though it is the main component of the renal basal membrane. Similarly, we noticed that the stiffness and thickness of the collagen I in association with Matrigel or not, promote their adhesion and proliferation. Relying on this flat substrate approach, the coating test was adjusted in the kidney-on-chip designed to mimic ADPKD. Indeed, it is of great importance that *Pkd1* cells form a differentiated epithelial monolayer within the tubes, to properly promote their functions.

2) Cell characterization in a 3D structure

Over the last decade, the intricate kidney architecture within its physiological microenvironment has been further developed in the kidney-on-chip domain. In most of them, renal epithelial cells lined the tubule, exhibiting polarized epithelium able to transport solutes and water bidirectionally between the lumen and the interstitium. The first nephrotic segment displays renal structural characteristics with cuboidal or columnar proximal convoluted tubular cells in contact with each other, well-defined nuclei and uniform cytoplasm [285]. To reproduce those phenotypical features reported in several studies, we added a new stone to the building with our innovative tightly packed multitube device to recapitulate the ADPKD major hallmarks.

a) Bottom-up approach

In the previous subchapter, the basal membrane recapitulation on 2D surfaces displayed an effect on our ADPKD cellular models, acting on cell growth and their phenotype. Playing a role on their epithelialization and lifetime, the basal membrane composition provides a chemical and mechanical support to properly promote their functions. In line with other various works on renal microphysiological devices further refined to reproduce the basal membrane, we improved our system to monitor renal tissue formation [219], [268]. To this end, we assessed

the effects of different basal membrane proteins aforementioned in our biomimetic kidney device, before seeding with the ADPKD cellular models: laminin, collagen IV and Matrigel, compared with collagen I alone.

The behaviours of *Pkd1*$^{+/-}$ cells and *Pkd1*$^{-/-}$ cell lines, also referred as heterozygous and homozygous cell lines respectively, were first examined in the control condition, meaning within tubes made in collagen I, coating-free. Cell dynamics (such as cell growth, phenotype, and interplay between tubes) within the three-dimensional tubular scaffold was evaluated without flow application for several weeks, and at least two weeks. Briefly, both cell lines were trypsinized in parallel, and concentrated at 5.10^6 cells/ml in differentiation medium mixed with 4% Dextran (70kDa). They were slowly and gently injected manually in the tubes, with a pipette, to prevent air bubbles entry as much as possible with a liquid-liquid interface between the connector and the pipette tip (Annexes 1 and 3). The seeding was usually realized on both sides of the chip, through the two connectors (cf. details in the Chapter II, and Annex 3). For all the different conditions described below, we noted that the seeding was not perfectly homogeneous, with random cells distribution along each tube. Indeed, some of the tubes contained more cells than others, and a few of them were even empty in the beginning. Although the seeding method was further refined between each experiments, it will still require more optimizations to be reproducible in the future experiments.

In the next subsections, we will first depict the *Pkd1* cells behavior in each coating condition, before describing the quantitative parameters determined to characterize them.

<u>Collagen I tubular scaffold</u>:

We noticed that one day post-seeding, *Pkd1*$^{+/-}$ cells adhered and spread along the tubes. They proliferated and filled the tubes in around ten days. Two weeks after seeding, in some cases, the heterozygous cells started to invade the collagen I from D17 (tube3), and tended to establish cytoplasmic extensions in the collagen I scaffold that looked like filopodia (Fig.56A). With proliferation going on, cells lined the tubes; at this stage, the tube deformation by the cells over time is not obvious. In some tubes, we notice that cells proliferated and formed a tissue on both sides; the tissue then joined in the middle of them. *Pkd1*$^{-/-}$ cells grew and seemed to fill the tubes faster than *Pkd1*$^{+/-}$ cells, as early as seven days post-seeding (not shown). In this example,

homozygous cells did not invade the collagen I matrix. Becoming smaller and smaller, they packed and seemed to strongly dilate tubes starting from D16 (Fig.56B).

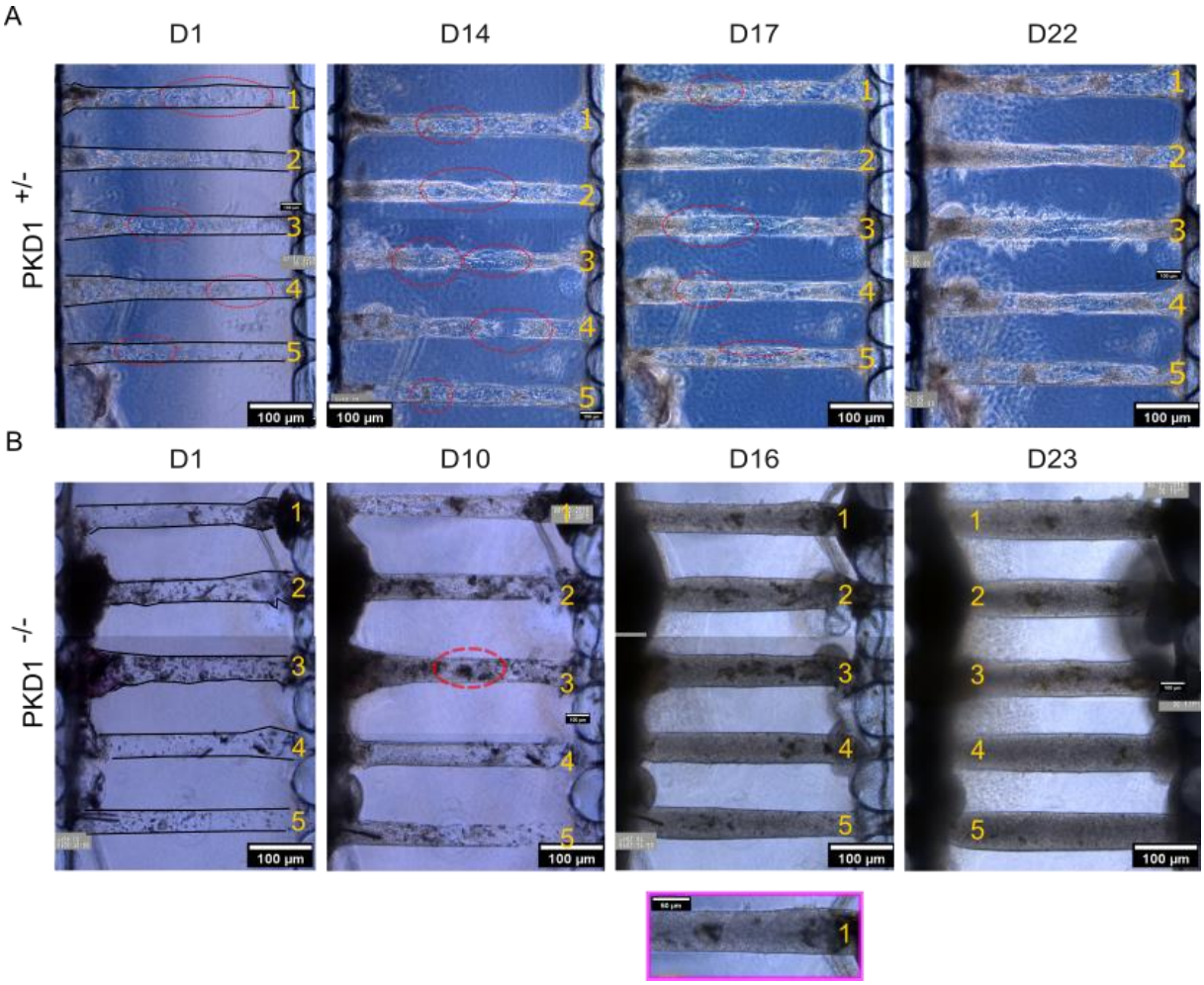

Figure 56: Images illustrating *Pkd1*$^{+/-}$ and *Pkd1*$^{-/-}$ cells evolution after seeding within tubes made in collagen I at 6 mg/ml, and observed under a phase contrast microscope during several weeks. A: *Pkd1*$^{+/-}$ cells observed during three weeks, and trying to invade or branching out of the tubes from D17 (tube 3). Red circles highlight cells lining the tubes and cell tissue joining in the middle. B: *Pkd1*$^{-/-}$ cells keep proliferating without invading the collagen I scaffold, and dilated tubes from D17. Scale bar: 100 µm.

Collagen IV coating**:**

The renal basal membrane is mainly composed of collagen IV and laminin proteins, among others. Therefore, we investigated their impact on the 3D ADPKD cellular models. Knowing that the coating is homogeneous, which has been previously shown in the chapter II) 2), tubes were coated with collagen IV and seeded *Pkd1*$^{+/-}$ and *Pkd1*$^{-/-}$ cells, without flow application. As previously, we noticed that the heterozygous cells started to adhere, proliferate and migrate within the tubes, more than the homozygous cells two days after seeding (Fig.57A and B). However, they all detached from the tubes walls between the second and the eighth day post-seeding, suggesting that both cell types displayed a weak adherence on this coating, and did not survive. This observation is in agreement with those obtained on flat collagen IV coated surface. Unexpectedly, our cell lines did not behave like other cell types seeded on collagen IV, while this coating was successfully used in other kidney-on-chips [216], [219], [223], [237], [254]. The reason for this discrepancy remains unknown: the experiments with our cell lines were performed twice and ended up with the same result, whereas the same collagen IV stock was successfully used with intestinal cell lines in the MMBM team.

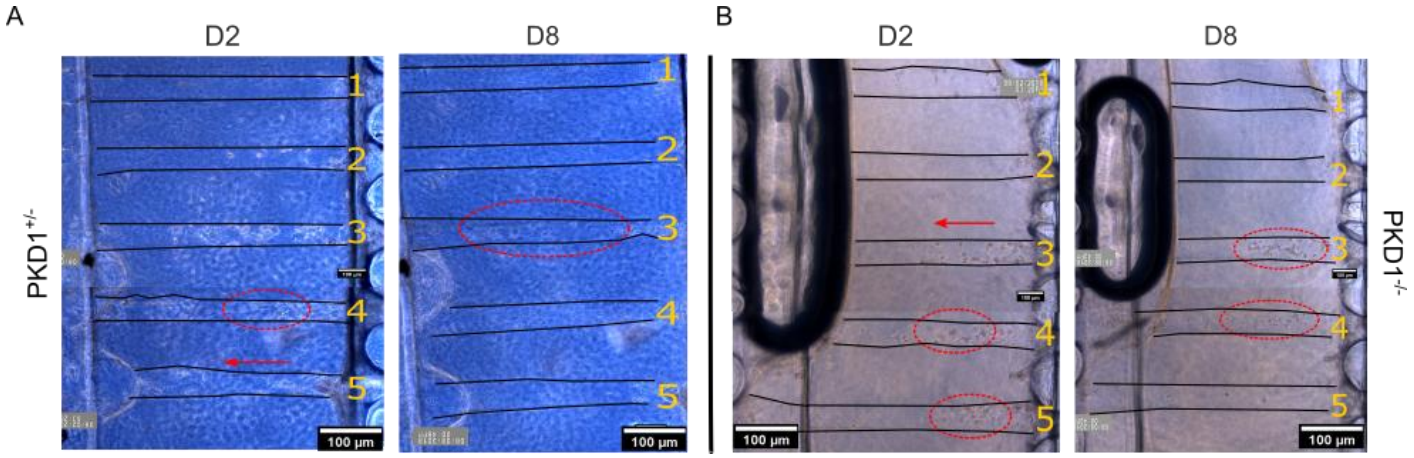

Figure 57: Images representing *Pkd1*$^{+/-}$ and $^{-/-}$ cells evolution after seeding within tubes made in collagen I at 6 mg/ml , and coated with collagen IV. Images were acquired under a phase contrast microscope, at regular time points, during two weeks. A: *Pkd1*$^{+/-}$ cells detached from the tubes walls before 8 days post-seeding, just like the *Pkd1*$^{-/-}$cells in B. Scale bar: 100 µm.

Matrigel coating effect:

Furthermore, on the Matrigel coated tubes, we observed that *Pkd1*$^{+/-}$ cells grew and quickly lined the tubes in around ten days. Eleven days post-seeding, cells shaped a well-defined layer with a tendency to contract the tubes (Fig.58A). In contrast, *Pkd1*$^{-/-}$ cells did not exhibit the same behavior: proliferating faster, they quickly filled the tubes and distorted them over time. In ten days (3 to 13), cells significantly increased tube diameter as shown in the Figure 58B. Both cell lines did not invade collagen I, even if the homozygous cells occasionally exhibited tiny cytoplasmic extensions.

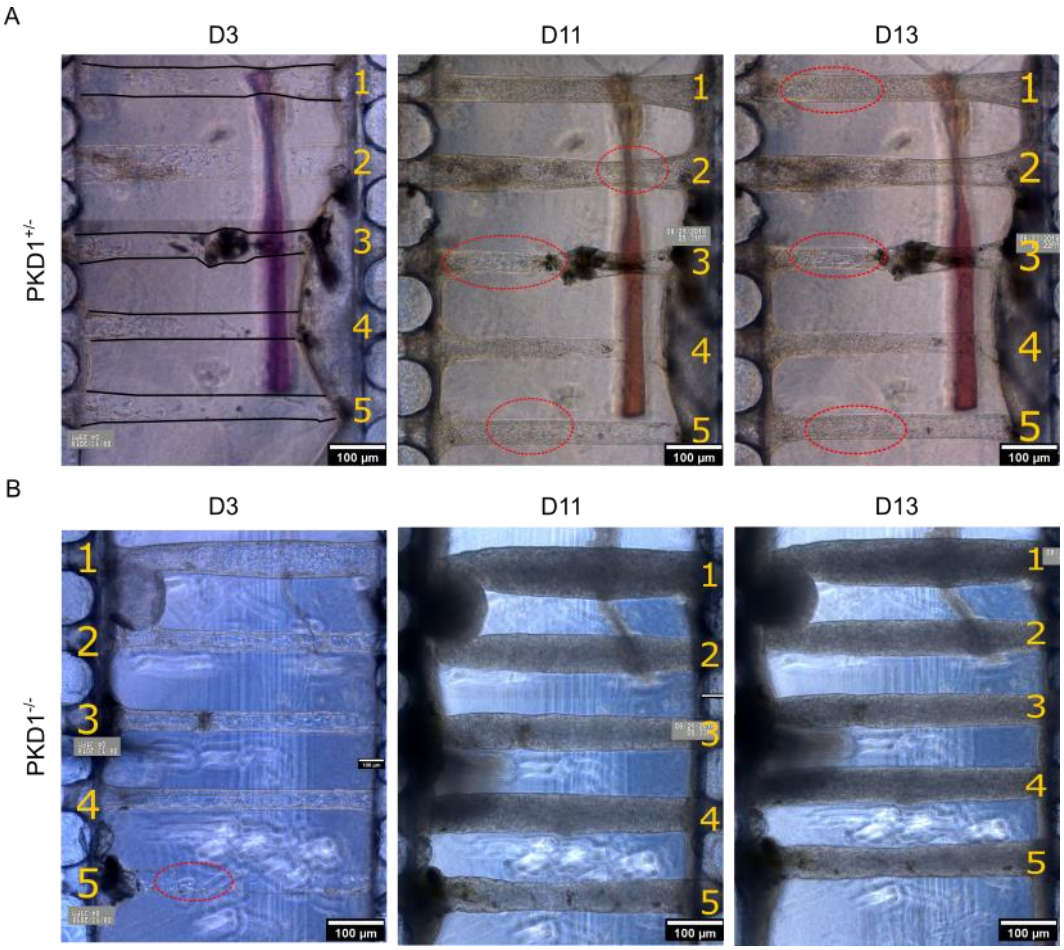

Figure 58: Images illustrating *Pkd1*$^{+/-}$ and $^{-/-}$ cells kinetics after seeding within tubes molded in collagen I at 6 mg/ml, and coated with Matrigel. Images were acquired under a phase contrast microscope, at regular time points, during two weeks. A: *Pkd1*$^{+/-}$ cells lined tubes and seemed to retract them at D13, which is highlighted with red dashed circles. B: *Pkd1*$^{-/-}$cells quickly filled the tubes. Three days after the seeding, almost all the tubes were lined with cells. They kept proliferating and enlarged tubes over time. Scale bar: 100 µm.

Laminin coating effect:

Eventually, the laminin coating effect on the ADPKD cellular models was determined. Similarly to the other coating protein, we noted that both cell lines distribution was not homogeneous within the tubes one day after seeding. The heterozygous cells adhered and progressively spread along tubes: they proliferated and migrated from one side to the other side of the tubes (Fig.59A). After fourteen days, we noted that cells seemed well defined and differentiated: we could distinguish their nuclei and their morphology on the tube walls. They did not invade the three-dimensional tubular scaffold, even if some cytoplasmic extensions were sometimes present. They slightly distorted some parts of the tubes over time. Moreover, as well as previously observed on the Matrigel coating, the homozygous cells rapidly grew and filled the tubes over time, deforming them without significantly invading collagen I (Fig.59B).

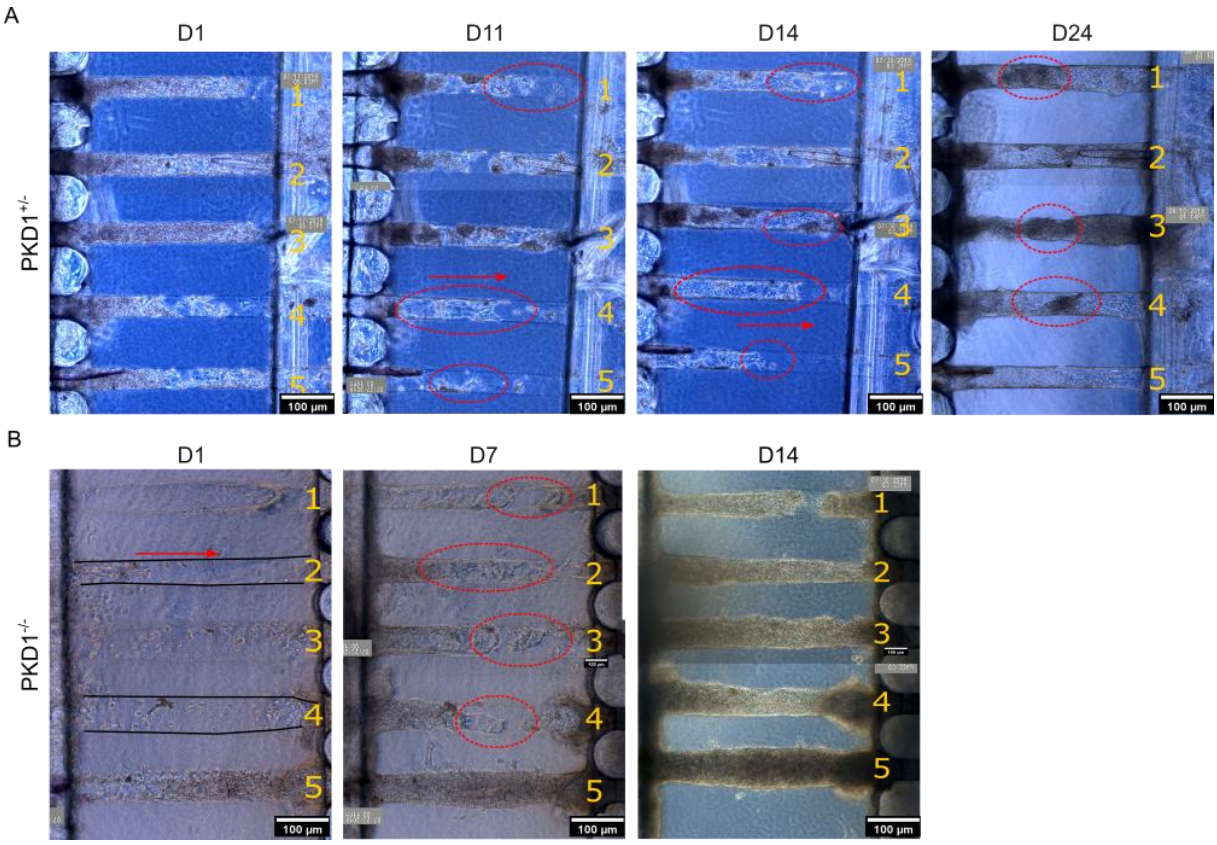

Figure 59: Images illustrating *Pkd1*$^{+/-}$ and $^{-/-}$ cells kinetics after seeding within tubes molded in collagen I at 6 mg/ml , and coated with laminin. Images were acquired under a phase contrast microscope, at regular time points, during three weeks. A: *Pkd1*$^{+/-}$ cells progressively lined tubes and were well defined after D11 (red circles). B: *Pkd1*$^{-/-}$cells quickly filled tubes and kept proliferating, which enlarged them over time. Scale bar: 100 µm.

Altogether, we showed that in tubes molded in collagen I, with laminin or Matrigel coatings, *Pkd1*$^{+/-}$ and *Pkd1*$^{-/-}$ cells did not exhibit the same behavior: they did not seem to exhibit cell contact inhibition, as well as on 2D surfaces. Indeed, cell kept proliferating while they filled all the free space within tubes. As observed on a flat surface, *Pkd1*$^{-/-}$ cells proliferated faster than *Pkd1*$^{+/-}$ cells within the tubes, and strikingly, led to an important tubular dilation over time. The slight invasive behavior observed in some experiments was not systematic, and different quantitative ongoing measurements partly mentioned at the end of this paragraph suggest that this behavior might be similar in collagen I, coated or not with basal membrane proteins. As laminin coating was suitable for our ADPKD cell lines, we decided to perform more experiments with this coating. Indeed, to get closer to the physiological conditions, it is of great interest to accurately control the different improvements made in our system. Therefore, Matrigel consisting of various growth factors at different concentrations, in addition to many proteins was not used in the next steps. Moreover, currently lacking a flow system in our kidney-on-chip to apply a monitored and continuous flow within the tubes, the cells completely fill them in two to three weeks, blocking the lumen initially present. Thus, albeit the basal membrane proteins overlap seems to maintain the cells within the tubes, the collagen I alone also seems to support this biochemical and mechanical aspect in a lesser extent.

b) ADPKD cellular models within a 3D tubular scaffold

Subsequently, relying on the ADPKD cellular models behavior plated on different basal membrane components, we optimized our multitube system. Different quantitative parameters previously described for MDCK cells in the Chapter II, 2) c) were determined to characterize the *Pkd1*$^{+/-}$ and $^{-/-}$ cell lines dynamics on laminin coating compared to collagen I alone as a control. It is worth noting that more experiments were performed with laminin coating than in the control conditions. In particular for *Pkd1*$^{-/-}$ cells, 4 independent experiments were realized with collagen I alone, and 9 with laminin coating, while 4 independent experiments were performed in collagen I seeded with *Pkd1*$^{+/-}$ cells, and 6 with laminin coating. In terms of experimental conditions, all chips were not monitored up to 30 days (about half of chips were not monitored after 15-20 days). Besides, phase contrast images were acquired at different time points that were binned in 3 days intervals. To evaluate tubes evolution and features over time, those images representing a 2D projection of cells and tubes edges were processed (cf. Annex 4).

Cell colonization within the tubes:

We first examined the **mean *Pkd1*$^{+/-}$ and *Pkd1*$^{-/-}$ cell density** or cell covering normalized to the tube surface density in tubes over time (Fig.60). In both conditions, control and laminin coating, we noted that the curves displayed the same tendency: error bars *(s.e.m. are shown)* of both conditions overlapped, suggesting that there were no significant differences between colonization rates with or without laminin coating. Figure 60 illustrates that the colonization kinetics was slower for *Pkd1*$^{+/-}$ than for *Pkd1*$^{-/-}$ cells: we observed a plateau around 23 days post-seeding (both in the laminin and control conditions) for *Pkd1*$^{+/-}$ cells, and around 17 days post-seeding for *Pkd1*$^{-/-}$ cells (Fig.60A, B). This is in line with the previous observation on a 2D (glass) substrate where *Pkd1*$^{-/-}$ cells proliferated two times faster than *Pkd1*$^{+/-}$ cells.

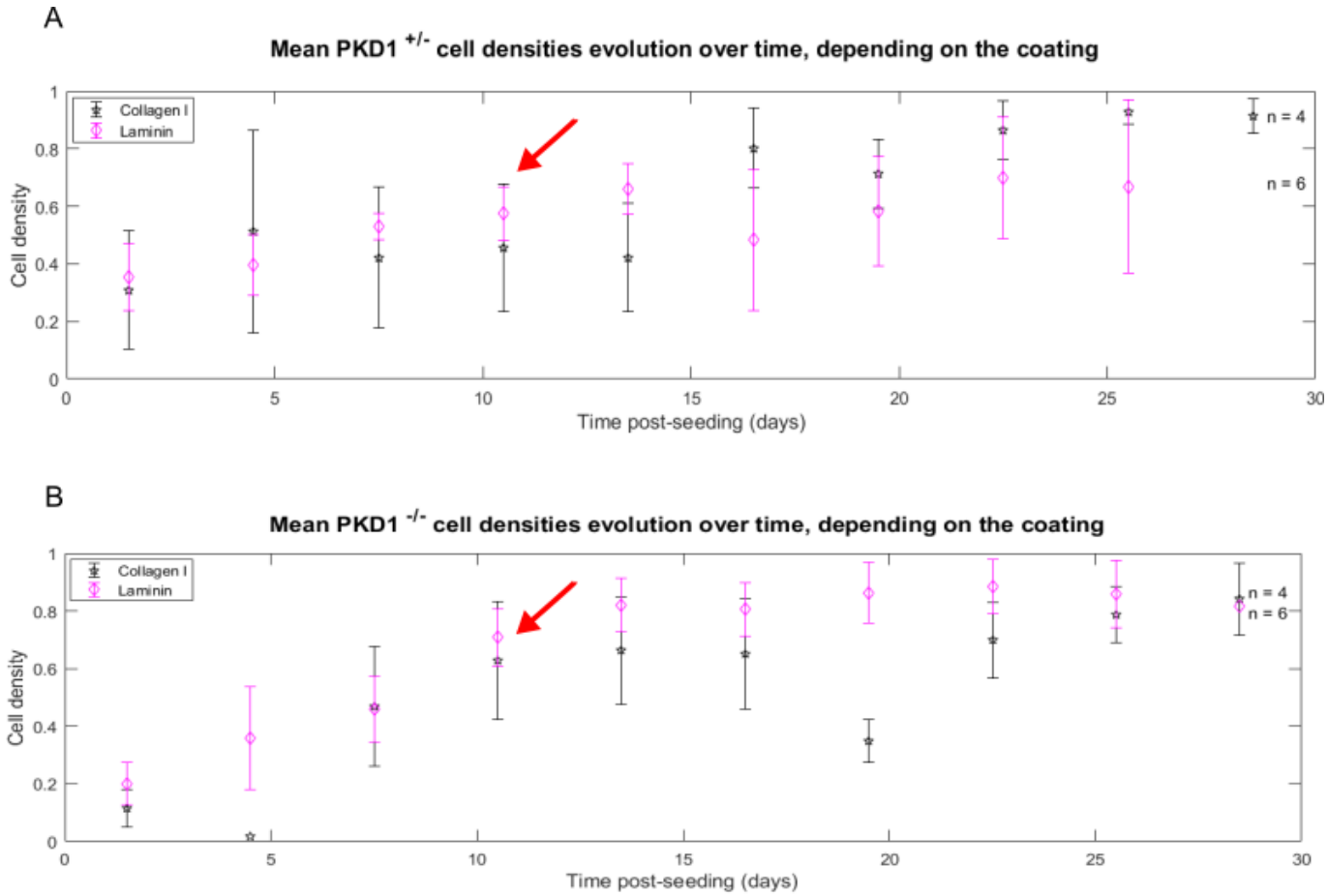

Figure 60: Graphs illustrating the *Pkd1*$^{+/-}$ and $^{-/-}$ cell densities over time after seeding within tubes molded in collagen I at 6 mg/ml, and coated (magenta diamonds) or not (black stars) with laminin. Red arrows points the end of the high proliferative phase before reaching a plateau. A: Plot of *Pkd1*$^{+/-}$ cell density evolution. B: Plot depicting *Pkd1*$^{-/-}$cells colonizing rate tubes over time. n = 4 independent experiments with collagen I, and n = 6 independent experiments with laminin. SEM are represented.

Tube diameter characterization:

To quantify how cells deform the tubes, we measured **the mean tube normalized diameter** evolution over time for the *Pkd1*$^{+/-}$ cell line (Fig.61). For collagen I and laminin conditions, we observed that the mean tube normalized diameter ratio oscillated around one, suggesting that it did not change significantly during the thirteen first days (Fig.61A). From D17 to D28, the mean tube normalized diameter even slightly declined to 0.9 in the tubes molded in collagen I, before reaching one. Within tubes coated with laminin, the mean tube normalized diameter was slightly higher than the initial value after 15 days seeding, reflecting a slight deformation in some chips. Beyond 15 days post-seeding, this small mean dilation was not observed for the collagen condition, even if the differences between collagen I alone or with laminin coating were not statistically different.

Furthermore, to deepen the study of tubes deformation over time, we examined the **minimal and maximal local diameters** (determined for each tube), depending on the cell type and the coating conditions (Fig.61). Keeping in mind that the tube diameter was initially around 80-90 µm, we noted that the mean of the minimal collagen I tubes diameter fluctuated between 70 and 80 µm during the whole experiment (Fig.61B), with a slight decrease after D17 (paralleling the evolution of mean diameter). In tubes coated with laminin, the mean of minimal tube diameter stayed steady along the experiment, fluctuating between 80 and 90 µm. This last observation implies that cells lining on laminin grow quite steadily [286]. In addition to the minimal, we assessed the mean of the maximal value of the tubes diameter over time (Fig.61C). We noticed that it varied between 100 and 120 µm in both conditions, but stayed quite stable over time. All those results indicate that *Pkd1*$^{+/-}$ cells grow in tubes without drastically deforming them over time.

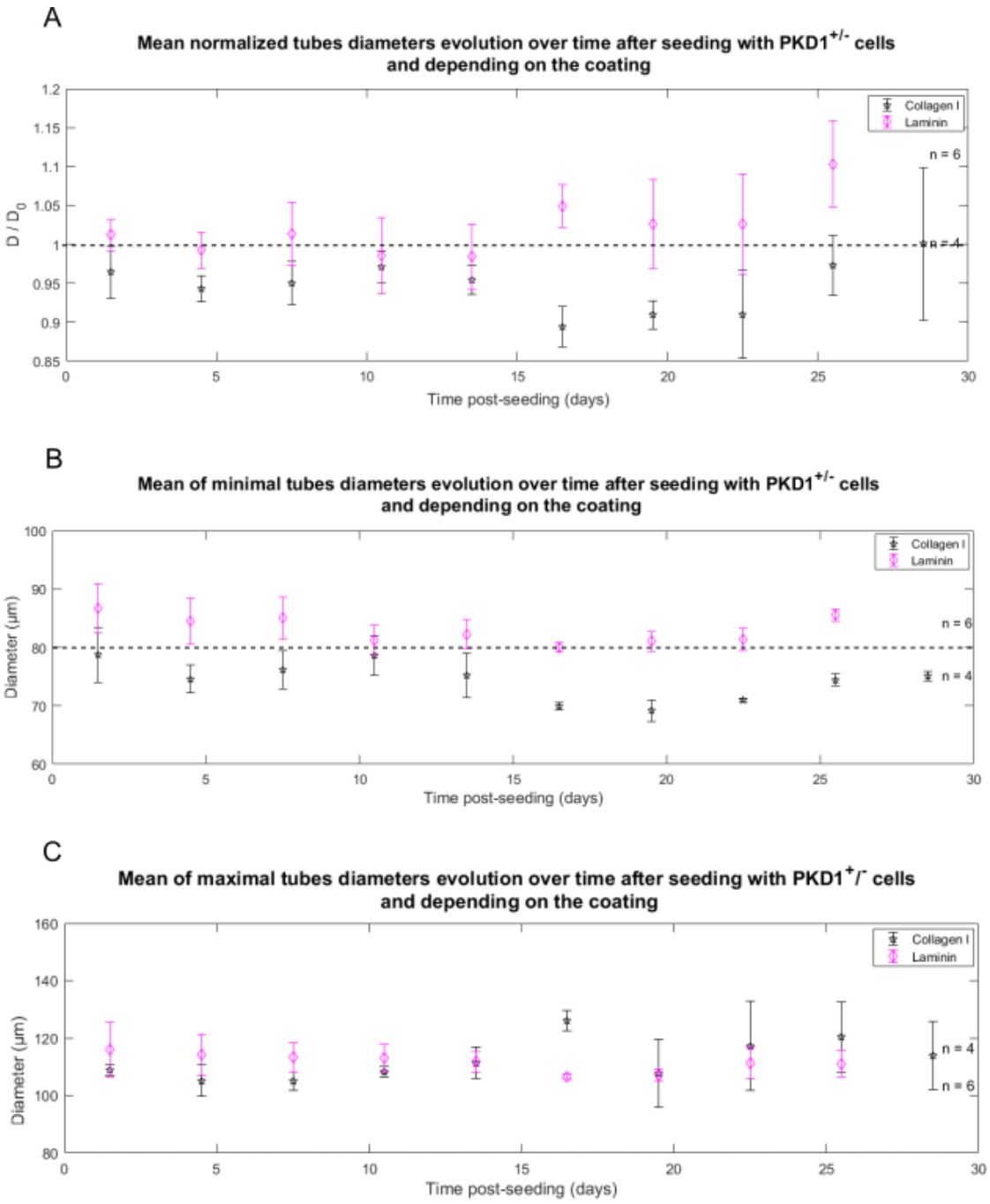

Figure 61: Plots comparing mean tube diameters after seeding with the heterozygous *Pkd1*$^{+/-}$ cell line within collagen I tubular scaffold coated with laminin (magenta diamonds) or not (black stars). A: Graph of mean tubes normalized diameter filled with *Pkd1*$^{+/-}$ cells over time. B: Plot showing the mean minimal of tubes diameter seeded with *Pkd1*$^{+/-}$ cells over time. C: Graph illustrating the mean maximal tubes diameter evolution over time. n = 4 independent experiments with collagen I, and n = 6 independent experiments with laminin. SEM are represented.

Likewise, we analyzed the same parameters with ***Pkd1*$^{-/-}$ cells**, starting with the **mean tubes normalized diameter** over time, in collagen I tubular scaffold coated or not with laminin (Fig.62). As aforementioned, we noted that that the tube deformations were similar with both coatings (Fig.62A). Nevertheless, *Pkd1*$^{-/-}$ cells led to a strong tube dilation, whatever the coating (up to 1.3-fold) at 25 days, and corresponding to a mean diameter of 120 µm. **Minimal mean of the tube diameters** values (from 85 to 100 µm) and **maximal values** (up to 135 µm) followed a parallel evolution (Fig.62B,C). Ongoing analyses of local diameter distributions suggest a slight widening of diameter distribution inside individual tubes as they enlarge. Statistical tests were performed to assess the difference between *Pkd1*$^{+/-}$ and *Pkd1*$^{-/-}$ tube diameters: the difference was significant ($p<0.05$) from the fourth time interval (9-12 days) to the end. Thus, the homozygous *Pkd1*$^{-/-}$ cells significantly deformed tubes over time, whatever the coating. It seems that during the ten first days, they proliferate and fill the tubes, widening them during the ten following days. The confinement and the lack of nutrients within the tubes probably contribute to the cell growth decline and to the tubes narrowing 25 days post-seeding.

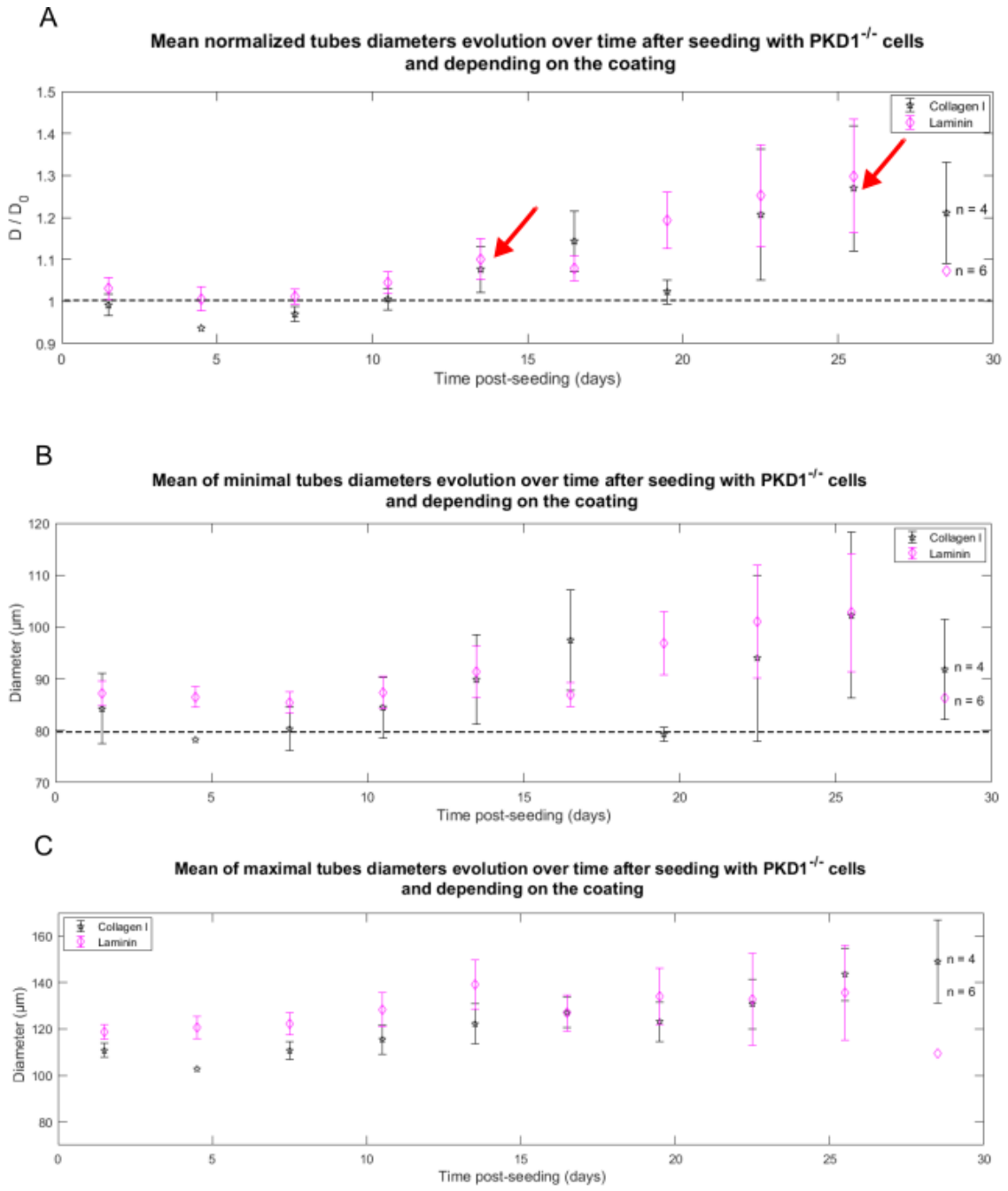

Figure 62: Plots comparing mean tube diameters after seeding with the homozygous *Pkd1*$^{-/-}$ cell line within collagen I tubes (black stars) or laminin coated tubes (magenta diamonds). A: Graph of mean tube normalized diameter filled with *Pkd1*$^{-/-}$ cells over time. Red arrows highlight the tubular deformation period. B: Plot showing mean minimal tube diameter after seeding with *Pkd1*$^{-/-}$cells over time. C: Graph illustrating mean maximal tube diameter evolution over time. n = 4 independent experiments with collagen I, and n = 96 independent experiments with laminin. SEM are represented.

Hence, the ADPKD cellular models displayed two distinct behaviors within our multitube implemented system. Lining on collagen I tubular scaffold coated or not with laminin, both cell types kept their intrinsic dynamics and did not seem to be affected by the adhesion molecules nature. Nevertheless, and as observed in 2D, each of them behaved differently within the tubes. Homozygous *Pkd1*$^{-/-}$ cells colonized faster the tubes, and significantly dilated tubes over time, in contrast to *Pkd1*$^{+/-}$ cells. Altogether, those results suggest that *Pkd1*$^{+/-}$ proliferate and line the tubes in around ten days, slightly deforming the tubes for the next ten days, but not significantly. However, *Pkd1*$^{-/-}$ cells progressively lined the tubes while proliferating and filling the tubes during the following two weeks. Cells distorted the tubes before contracting them after three weeks (Fig.63). Both cell lines were confined: they started to lack nutrients and space after the two first weeks of proliferation within the tubes. Albeit they lined with the tubes, they continued to duplicate and to fill them: they did not seem to display cell contact inhibition mechanism to prevent them from growing.

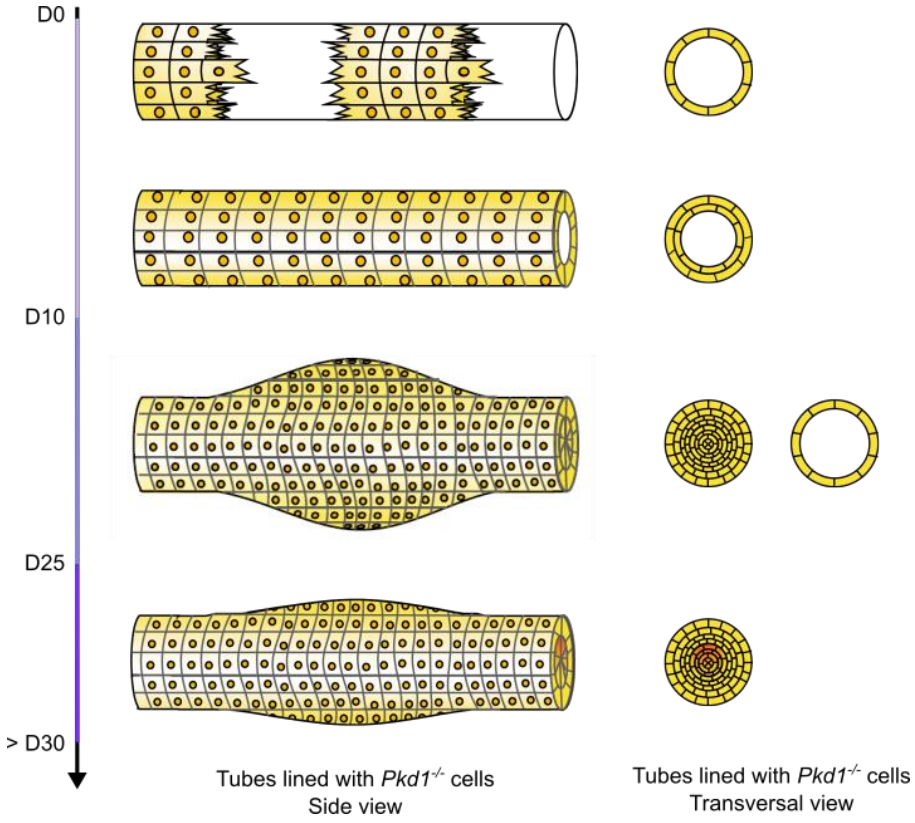

Figure 63: Schematic depicting *Pkd1*$^{-/-}$ cells behavior within collagen I tubes coated or not with laminin over time. Between days 10 and 25, tubes deform either because of tubes filling with *Pkd1*$^{-/-}$ cells or cell monolayer exerting a mechanical force on them (cf.part 3 of this chapter) Beyond 25 days, cells localized in the middle of the tubes could die, lacking nutrients and oxygen. Schematic realized with the help of Audric Jan, PhD student in the MMBM team.

Tubular interplay: 200 µm spacing feature

Based on these first observations, we thus scrutinized on the **distance and the interplay between tubes** seeded with the homozygous cells. In a few words, the distance between tubes edges previously processed from raw phase contrast images was assessed with a Matlab written program (cf. Annex 4 for more details). As the coating did not affect the homozygous cell dynamics, the control condition and laminin coating were pooled to study **the spacing between tubes** variation (Fig.64). We noticed a decreasing trend with two main phases. The intertube spacing stayed quite constant during the ten first days of the cell proliferative growth, around 195 µm, knowing that the initial intertubular spacing (before demolding) is 200 µm. This distance gradually decreased during the following ten days, in line with the tube enlargement, and reach a mean value of 160 µm. The tubes widening corroborated with the retraction of the surrounding collagen I, and did not seem to propagate to adjacent tubes: all behaved as if effects exerted on collagen I were very local. This could correspond to local collagen I rearrangements at immediate proximity of tubes.

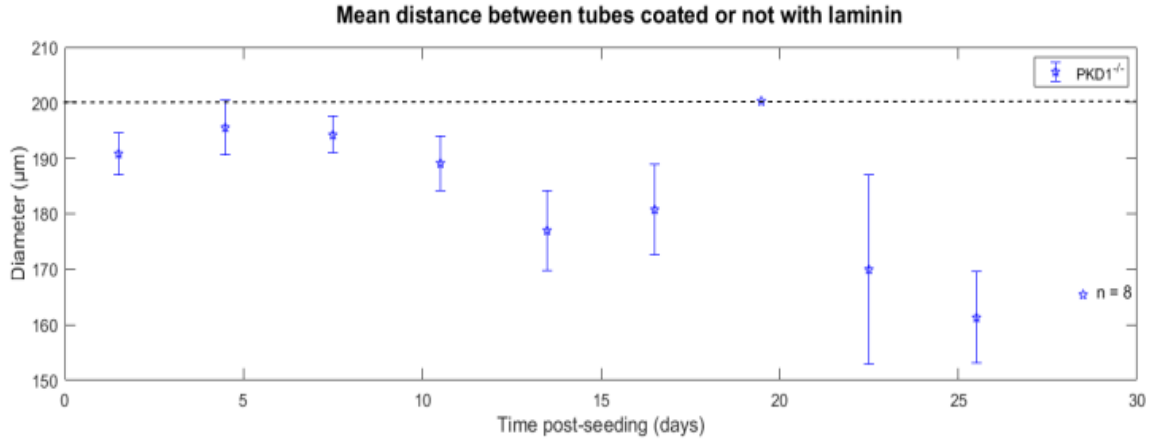

Figure 64: Graphs characterizing the mean intertubes distance over time, with the initial tubes spacing of 200 µm. Collagen I tubes coated and not coated with laminin were seeded with homozygous cells. n = 8 independent experiments with collagen I and laminin coating. SEM are represented.

Therefore, the filling and the distortion of one tube by *Pkd1*$^{-/-}$ cells did not seem to interplay with the adjacent tubes that remained globally straight and uniform over time. This tubular organization could be due to the constraints exerted between the tubes during cell filling.

At this stage, we can assume that the deformation of one tube in one direction did not induce local distortion of adjacent ones in the same direction.

Tubular interplay: 100 µm spacing feature

Since tube deformation did not seem to propagate between adjacent tubes with 200 µm spacing, we decided to decrease this distance. Instead of 200 µm spacing between tubes, this feature was half reduced to 100 µm. We first assessed the ADPKD cellular model behavior in collagen I tubular structures coated with laminin. We observed that, as previously shown, the *Pkd1*$^{+/-}$ cells proliferated and progressively lined the tubes, migrating from one side of the tube to the other one (Fig.65A). After 19 days post-seeding, they seemed well-defined and differentiated. They kept growing and slightly deformed the tubes over time. It is worth noting that tubes 1 and 2 left extremities were merged, which probably occurred during the fabrication processes. Exhibiting some cytoplasmic extensions within those tubes, cells did not invade the collagen I scaffold. Besides, the *Pkd1*$^{-/-}$ cells highly proliferated from the seeding day to day 10 where they formed a confluent and well-defined cell layer (Fig.65B). Further filling the tubes over time, they significantly widened them between D10 and D19 post-seeding, also forming bigger cytoplasmic extensions towards the outer tubes. Locally enlarged at D19, we noticed that tubes filled between D19 and D29, without invading the collagen I. Remarkably, adjacent tubes shaped a straight interface in contact, which we did not observe within tubes spaced of 200 µm. This straight curve was also present at the edges of the tubes positioned at the limit of the chip, meaning tubes 1 and 5. In between, tubes were straight and not locally enlarged or globally convex. Thus, as observed within 200 µm intertubular spacing chips, *Pkd1*$^{+/-}$ cells did not significantly deform tubes over time while they progressively lined and proliferated within them. In contrast, it seemed that the forces exerted by the homozygous cell growth homogeneously enlarged the tubes. They seemed to apply a uniform constraint between adjacent tubes that became straight over time. This observation suggests that a tubular interplay could occur between tubes filled with homozygous cells over time, triggering their shape.

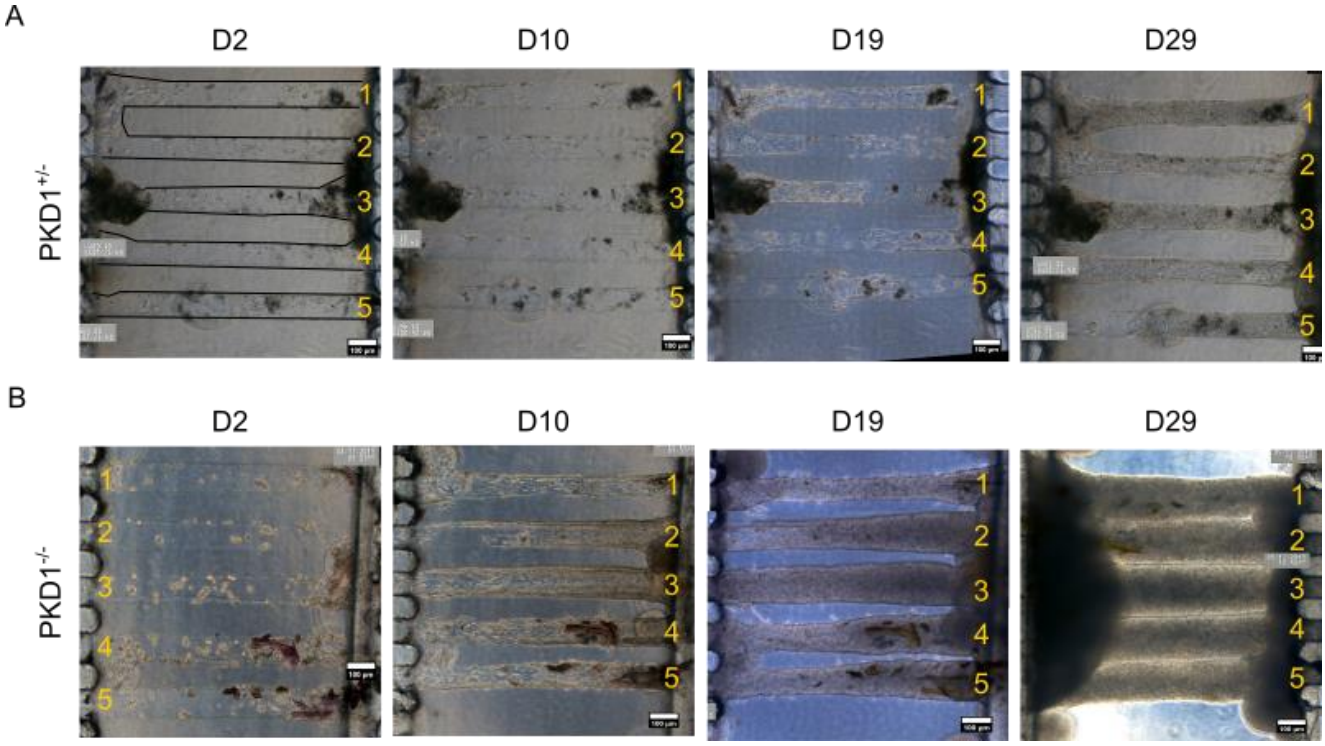

Figure 65: Images illustrating *Pkd1*$^{+/-}$ and $^{-/-}$ cells kinetics after seeding within tubes molded in collagen I at 6 mg/ml spaced of 100 µm, and coated with laminin. Images were acquired under a phase contrast microscope, at regular time points, during four weeks. A: *Pkd1*$^{+/-}$ cells progressively lined tubes and were well defined after D19. B: *Pkd1*$^{-/-}$cells quickly filled tubes and kept proliferating, which enlarged them over time. Tubes even interplay with each other at D29, shaping straight interfaces in between. Scale bar: 100 µm.

The parameters previously described were quantified with the *Pkd1* $^{-/-}$ cell line seeded within tubes coated with laminin. They were compared to the results obtained in the previous design (Fig.66). As expected, we first showed that **cell density** displayed similar growth in chips with 100 µm or 200 µm spacing (Fig. 66A). It is worthy of note that more experiments were performed with the 200 µm design than the other one (n = 9 independent experiments versus n = 4 experiments in the 100 µm intertubes spacing chips seeded the same day).

The Figure 72B presents the variation of **mean tube normalized diameter** as a function of time. A 1.3-fold increase of the tubes normalized diameter is observed two weeks after seeding, which is similar to the observations with 200 µm spacing, and a final mean dilation of about 1.5 fold was eventually reached. The mean **minimal and maximal tubes diameters** corroborated these findings, with the minimal fluctuating between 95 and 130 µm during the

filling tubes phase, while the maximal ranges from 130 and 160 µm (Fig.66C and D, respectively). Thus, the homozygous cells behaved the same way within tubes spaced of 100 µm and 200 µm: after the proliferation phase during which they grew and lined with the tubes,

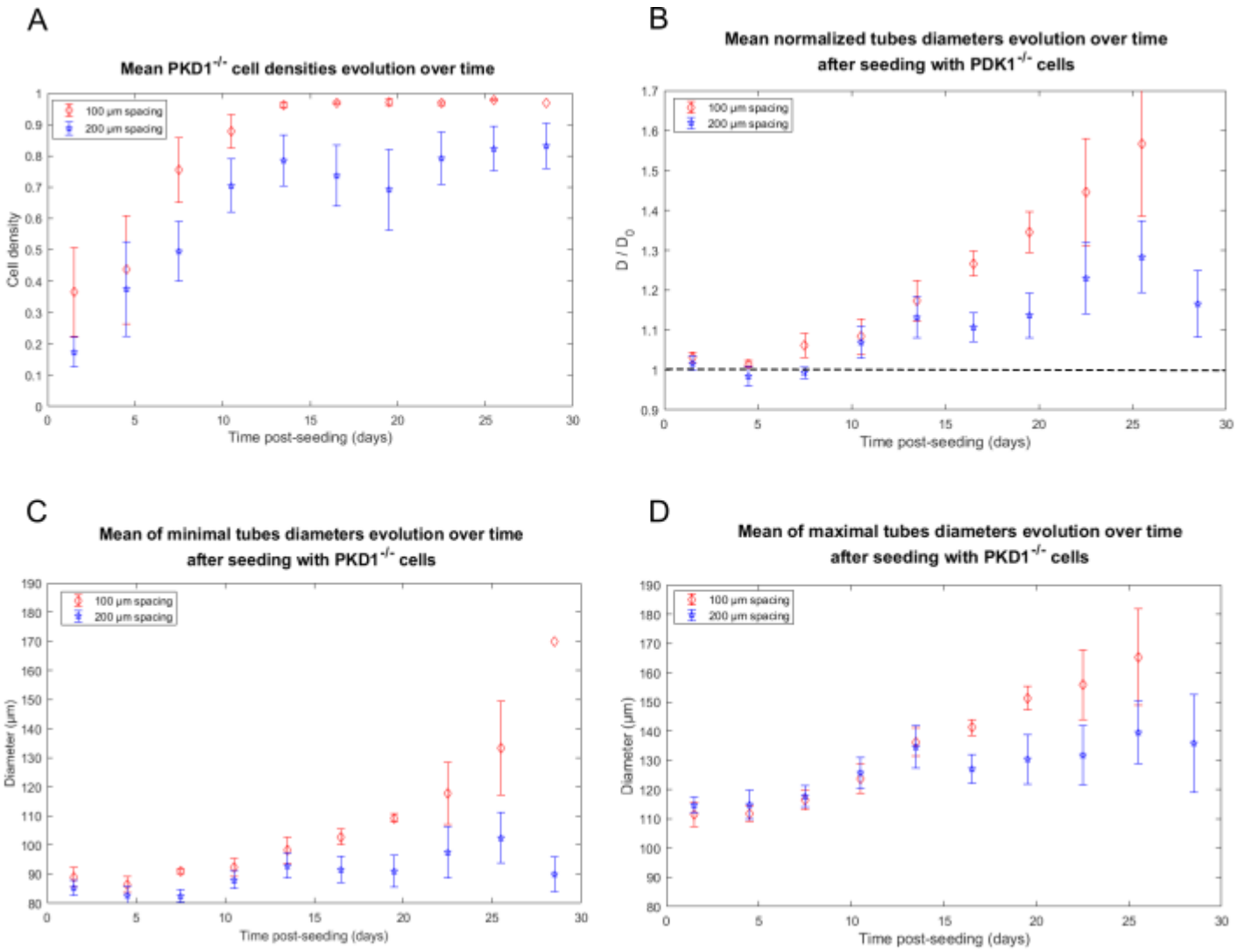

Figure 66: Graphs showing the *Pkd1*$^{-/-}$ cells behavior over time. Collagen I tubes coated and not coated with laminin were seeded with homozygous cells. Both conditions were pooled for the 200 µm spacing design (blue stars), and the laminin condition is represented for the 100 µm spacing device (red diamonds). A: Plot illustrating mean *Pkd1*$^{-/-}$ cell densities over time, and displaying the same tendency. B: Graph of the mean normalized tubes diameter evolution over time. C: Plot depicting mean minimal tubes diameter D: Plot representing mean maximal tube diameter evolution over time. n = 4 independent experiments laminin coating in 100 µm spacing design, and n = 14 independent experiments with collagen I and laminin. SEM are represented.

they kept proliferating to fill and enlarged them during the next two weeks. These results showed that their dynamics is not affected by a decreased distance to other tubes.

Moreover, we assessed the interplay of 100 µm intertube spacing (Fig.67). During the proliferative phase (around ten days), the distance between tubes remained close to 100 µm, ranging from 80 to 90 µm. From D12 to D25, we noted a two-fold decrease of the mean intertube spacing, in accordance with the tubes widening promoted by the cell growth. We also observed interesting features that could relate with tubes interplay. Indeed during the first stage of tube deformation, the deformation does not seem homogeneous along the tube axis, while the more the deformation increases, the more straight the tubes become. It could be correlated with "counter-pressure" due to adjacent tubes and/or on the maximal compression of collagen. These observations should be further investigated to better asses an eventual tubes interaction.

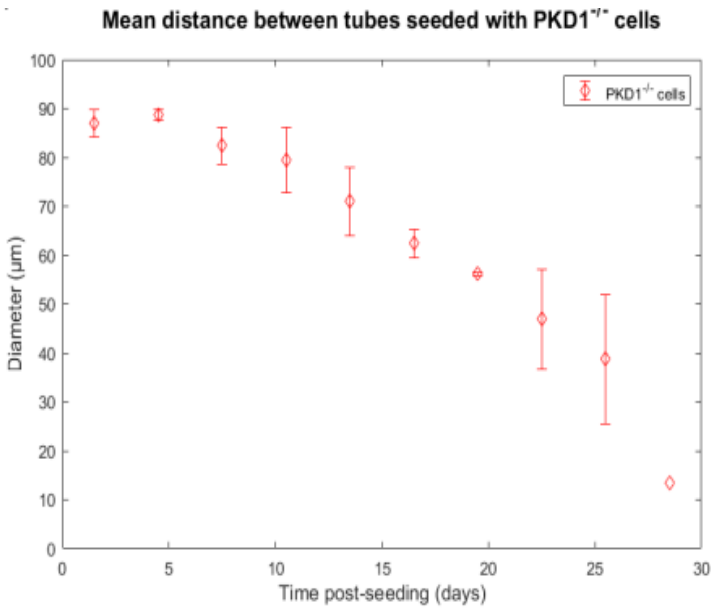

Figure 67: Plot illustrating the mean intertube distance over time, with the initial tubes spacing of 100 µm. Collagen I tubes coated and not coated with laminin were seeded with homozygous cells. n = 4 independent experiments with laminin coating. SEM are represented.

c) Tubular geometry and intracellular organization in a kidney-on-chip

Immunostaining protocol adaptation from 2D to 3D topography:

After the characterization of *Pkd1* cells within the tubular scaffold molded in collagen I coated or not with laminin, we investigated their intracellular organization by performing in-tube immunofluorescence experiments on different epithelial markers.

To this end, the protocol established was based on the one used to stain cells plated on flat surfaces, and consisted of five main steps before the mounting for visualization under confocal microscope. All of those steps were progressively optimized to acquire as resolved and clear stack of images as possible (cf. Annex 2 for more details).

First of all, the tubular scaffold was gently removed from the COC surface with thin tweezes, and placed in a Petri dish filled with PBS. During all the immunostaining protocol, the collagen I scaffold remained immersed in liquid to prevent it from drying. The fixation and permeabilization steps were extended to favor the diffusion of the appropriate buffers within the whole scaffold and cells. It is noteworthy that the detergent concentration used was increased to ease the plasma membrane impairment (from 0.1% to 0.5%). Moreover, the washing buffers, as well as the saturation buffers, contained four times more BSA (4% instead of 1%) and a small amount of goat serum or Tween 20 to prevent non-specific antibodies interactions with the collagen I in particular. Albeit the primary antibodies were incubated over night at 4°C under humidified atmosphere instead of 2 hours at room temperature, the secondary antibodies were incubated for 45 minutes. Indeed, a longer period with the secondary antibodies promoted a lot of background from the collagen I scaffold. In line with the background noises in our hydrogel, the washing steps were of great importance. Realized between the primary and secondary antibodies incubations, three washing steps of ten minutes instead of five minutes were done to remove as much as possible unfixed primary antibodies. The three last washings before the mounting steps were the most crucial: lasting 30 minutes each, they significantly reduced background noises due to secondary antibodies.

Listing those different steps, two of them could be further optimized: the incubation times with antibodies and the washing times. Indeed, we did not manage yet to stain correctly intracellular proteins localized in the cells along the tubes.

Eventually, the last crucial point was to find a way to mount this hydrogel to be able to visualize our stained cells within the tubes. To this purpose, we tried several approaches: starting with an incubation chamber of 50 µm depth, we moved on and designed a homemade incubation chamber made of PDMS adjusted to our hydrogel scaffold. The chamber was made in PDMS (a 1.5 mm thick layer of PDMS was spin-coated, and a square of 1 cm size was punched in the middle of a 2*1.5 mm PDMS piece. This chamber was then bonded on a glass coverslip, both previously plasmated, and half filled with a non-hardening mounting medium. The hydrogel was gently positioned in the middle of the chamber, and immersed in the mounting medium. Afterwards, the chamber was closed with a thin glass coverslip on which cells were usually seeded for immunostaining experiments, and sealed with a transparent nail polish. The whole set-up was horizontally incubated at 4°C to allow the nail polish drying. Tubes faced this top glass coverslip through which they were imaged the following day. It is worth mentioning that the mounting medium used was carefully chosen. It neither hardened nor promoted photobleaching, which maintained the three-dimensional structure integrity and allowed longer time acquisitions under microscope, respectively.

Hence, the immunostaining protocol lasted longer on 3D structures than on flat surfaces: it took two days rather than one.

Image acquisition implementation:

The next step was to acquire stacks of images under a confocal microscope to characterize the intracellular organization of *Pkd1* cells in the tubes. We faced two main limitations: the set-up thickness and the lens working distance that had to be high enough. Indeed, the laser has to cross three different environments: glass, mounting medium and collagen I before reaching the tubes, a set-up of at least 1 mm thick. Two lenses were used to acquire stack of images as resolved and exploitable as possible: a 10X, and a 40X water immersion.

To start with, the whole tubes were imaged under a 10X lens, zooming in to better observe the cell arrangement within the tubes (Fig.68A). For this first test, the actin cytoskeleton was stained with the phalloidin-TRITC to examine *Pkd1*$^{-/-}$ cell organization within tubes molded in collagen I, as well as the nuclei. The chip was fixed before cell confluence. We observed a cell monolayer lining the tube, with well-defined cell membranes on the tubes walls edges: tightly packed, they displayed a cuboidal shape. We also discerned small actin stress fibers distributed along the tube segment, and tiny cytoplasmic extensions elongated towards the outer part of the tube section (Fig.68B). To visualize the cylindrical shape of the tube, we used the orthogonal view on ImageJ software: the stack of images was reoriented under two orthogonal axes (xz and yz) (Fig.68C). However, the resolution was not good enough to ease image analyses such as 3D reconstructions or cell/nuclei counting. The numerical aperture imposed a significant step between each image, which decreased the resolution between each of them and made the analyses harder. Besides, the fluorescent signals above and below the tube were increased, as well as the bleaching during the stack acquisition.

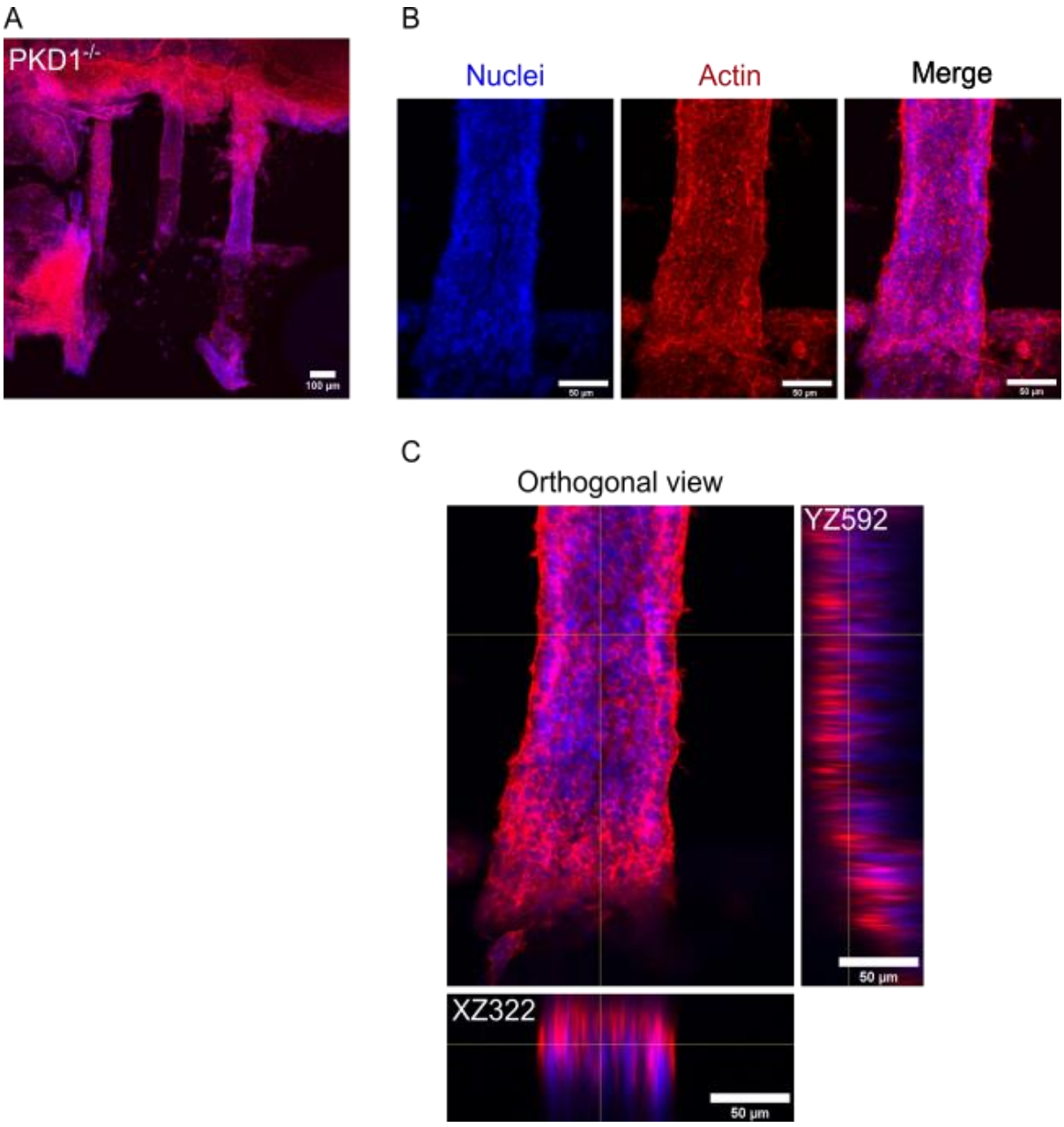

Figure 68: Immunostaining of *Pkd1*$^{-/-}$ cells within tubes molded in collagen I, and imaged with a 10X lens under a confocal microscope two to three weeks post-seeding. A: Maximal projection in z of three adjacent tubes is represented with phalloidin-TRITC in red for F-actin and Hoechst for nuclei. Scale bar: 100 µm. B: Magnification on part of one tube. Images illustrate a z projection of the maximal signal intensity. C: Orthogonal view of the tube section with on the right side, the YZ position and on the bottom, the XZ position depicting the tube geometry. Scale bar: 50 µm.

Therefore, another lens was used, a 40X water immersion, to acquire more resolved images (Fig.69). Surprisingly, this approach was the most relevant and efficient to visualize our tridimensional structures. We clearly distinguished the actin stress fibers and the plasma membranes of the cells lining with the tube (Fig.69A). Importantly, we are also able to observe the absence or presence of a lumen within the tube segment, and along it (Fig.69B). Albeit, the

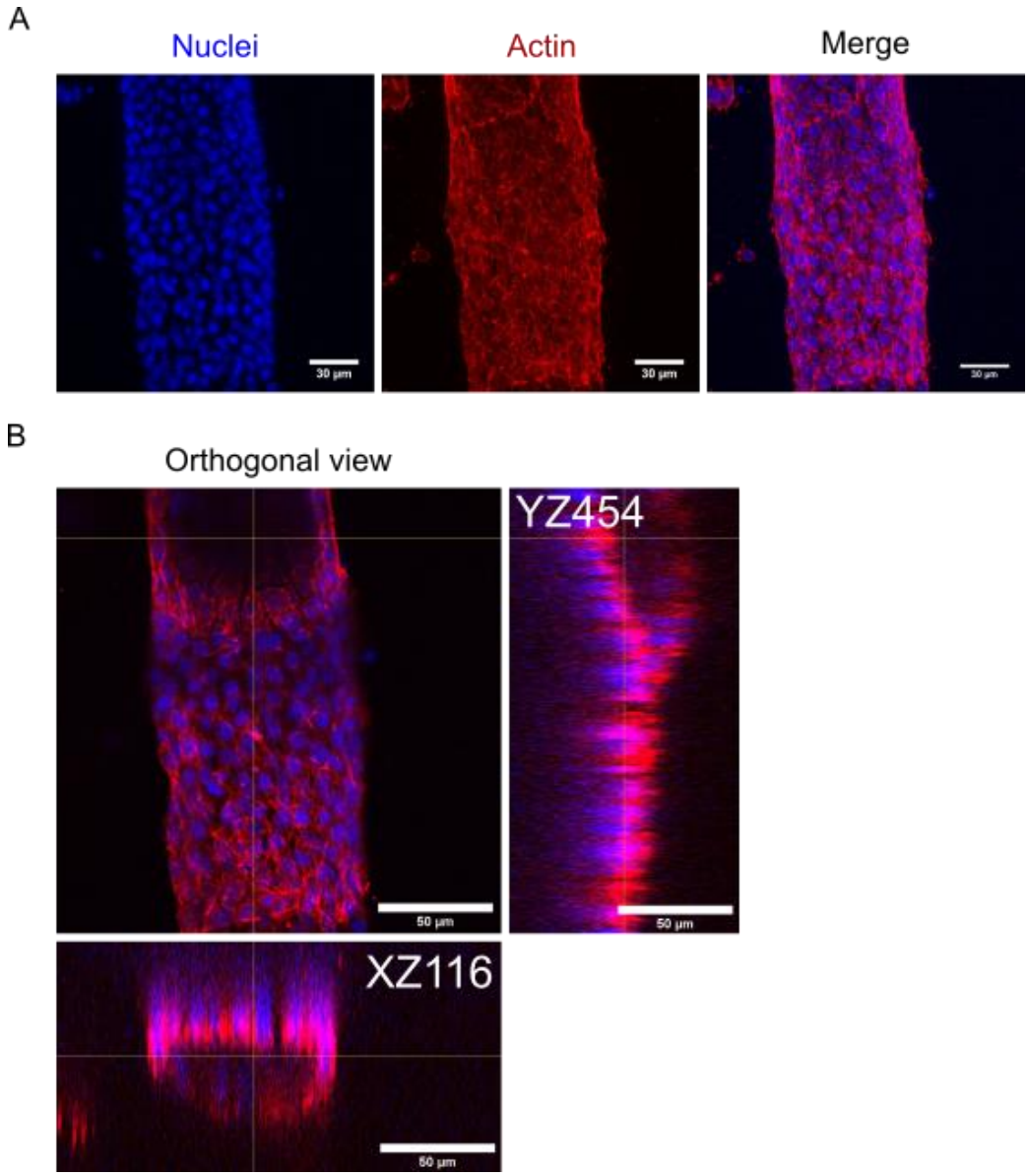

Figure 69: Immunostaining of the same chip as in the figure 68, and imaged with a 40X lens under a confocal microscope. A: Magnification focusing on one part of the tube lines with *Pkd1*$^{-/-}$ cells labelled with phalloidin-TRITC in red for the F-actin and the Hoechst for the nuclei. Scale bar: 30 µm. B: Orthogonal view of the tube section with on the right side, the YZ position and on the bottom, the XZ position depicting a lumen within the tube. Scale bar: 50 µm.

acquisition time was indeed longer than previously, the resolution was also better than with the 10X lens. Moreover, we note less background noises, and more structural details within the tubes.

Thus, after many weeks of improvement of image acquisition at different levels and dialogues with microscopic platforms engineers, we managed to establish an optimized protocol for future acquisitions. To summarize, the entire chip was visualized with a 10X lens, before a magnification on three parts of the tubes of interest with a 40X lens. This method takes part to ease the images treatment and analyses explained below, as well as the immunostaining protocol aforementioned.

Image analyses: program development

In the past few years, many powerful softwares such as Imaris, Icy or even plugins (3D viewer) on the currently used ImageJ software were increasingly developed and daily improved. Nevertheless, quantitative data extraction and three-dimensional reconstructions on our stack of images were not so obvious. After many technical discussions with engineers from different imaging platforms, one of them dared to address this exciting challenge. Engineer at the IPGG technological platform, Bertrand Cinquin wrote and gradually improved an ImageJ macro to extract different quantitative parameters that will be described in more details in the next subsection (cf. Annex 4). He focused on two aspects: the shape of tubes lined with *Pkd1* cells and the characterization of cells within the tubes.

The macro was developed on the F-actin cytoskeleton staining, which was not the most relevant for the segmentation step as our cell lines display many actin stress fibers. Nevertheless, lacking other clean immunostained markers within the cells, we started with that one.

Overall, the macro processed the stacks of images in four main steps, and was adjusted for both magnifications (10X and 40X). First, the **local contrast** of each image was enhanced with a plugin called CLAHE to improve the staining visualization and ease the next images treatment. The **background noises** were then reduced as much as possible to focus on the interested structures. Afterwards, a function called **Fit ellipse** was created to distinguish each tube and produce an envelope of the vertical tube and its transversal section over it length. To this end, the fluorescent signals from the stained cells were detected and an ellipse fit was

applied to the external part of the tube. This one was seen as a convex structure on which the ellipse had to fit and adjust over the entire length of the tube. Thanks to this function, several parameters were determined to describe the shape of the cellular monolayer lining tubes: area, perimeter and circularity ((4π x area) / perimeter²) depending on the tubes length.

Eventually, cell organization and features such as their shape, orientation, and size within the tubes were also important aspects to focus on. For this purpose, the cell plasma membrane staining relying on the F-actin staining was used in order to individualize cells and segment the tissue along the tubes. Based on a plugin on ImageJ, Skeleton, cell edges were partially detected at each step in z: the final result was too rough and inaccurate to be exploited for the moment.

Thus, the lately written macro raised several aspects from the stack of images acquired in order to better characterize our multitubular microphysiological system in 3D, as well as the cellular organization within it. Very preliminary results obtained with this approach are described below.

Cellular organization within the tubes:

Image acquisitions with confocal microscope promote the three-dimensional tubular scaffold characterization, as well as the intracellular organization of the *Pkd1* cells lining the tubes made in collagen I. This approach completed and deepened the previous analyses realized on 2D projections phase contrast images. Indeed, this method provides further details on the architecture of our kidney-on-chip in the three-dimensional space, unlike the 2D one. It will in particular allow us to determine the tube shape depending on the cell type, and the presence or absence of lumen at one time point. In other words, in addition to tubes geometry, it will also be possible to detect whether the cells line tubes or fill them. For this purpose, kidney-on-chips were fixed and stained as soon as they lined tubes.

To investigate the *Pkd1* cell layer epithelialization and its polarity along tubes, several markers also used on 2D flat surfaces were selected: the tight and *adherens* junctions, polarity markers, focal contact protein as well as F-actin cytoskeleton and nuclei. Nevertheless, as aforementioned, F-actin cytoskeleton staining was the only one operable for the moment.

Therefore, we will focus on the preliminary data obtained with this staining in the next part of this chapter, in order to characterize the tubes shape, in parallel to cell organization within tubes. Briefly, the tubes made in collagen I were coated with laminin and seeded with the *Pkd1* cell lines. As a first strategy, the chips were followed from one to three weeks, the minimal period needed for a confluent monolayer formation along the tubes. The chips were then fixed, and the actin cytoskeleton and nuclei were stained with phalloidin-TRITC and Hoechst respectively.

Cells were imaged as soon as they reached confluency, more precisely after they lined tubes and before they filled them. We noted that the heterozygous cells lined the whole tubes, and formed a monolayer. Although we observed five tubes regularly spaced, the two tubes localized on the right and left extremities were more distorted and larger than the ones in the

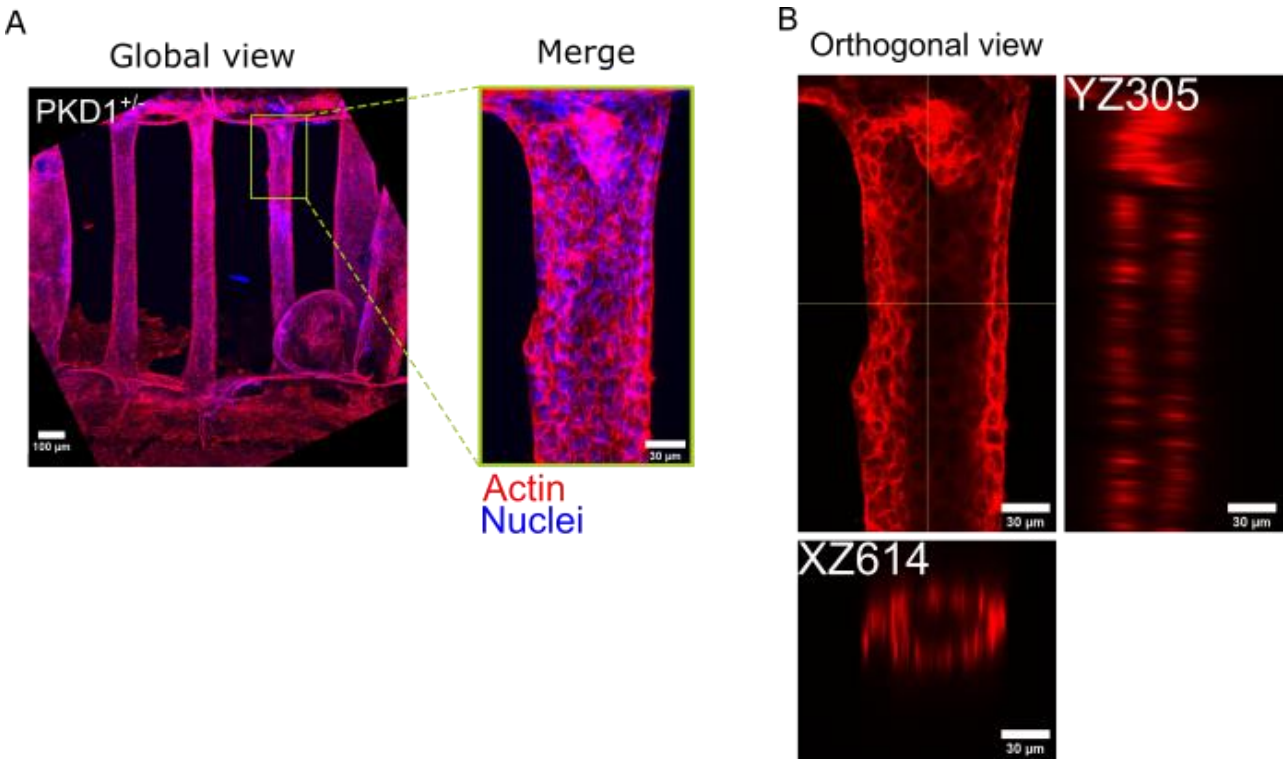

Figure 70: Immunostaining of a chip imaged under a confocal microscope. A: Global view of the five tubes. The three tubes in the middle were easier to visualize, and displayed the same structure. In red, F-actin labelled with phalloidin-TRITC and in blue, nuclei stained with Hoechst. Scale bar: 100 µm. On the right, magnification focusing on one part of the tube lined with *Pkd1*$^{+/-}$ cells (21 days post-seeding): z projection of the maximal signal intensity. Scale bar: 30 µm. B: Orthogonal view of the tube section with on the right side, the YZ position and on the bottom, the XZ position depicting a lumen within the tube. We note the cells cuboidal shape on the tube edge. Scale bar: 30

middle, which was certainly due to the wire removal before the seeding step (Fig.70A). The merge illustrates the actin cytoskeleton arrangement, highlighting the cells cuboidal shape along the tube section, which is more visible on the orthogonal view (Fig.70B). Moreover, we observed some tiny stress fibers oriented along the tube axis. The orthogonal view points the presence of an empty lumen surrounded by a cell monolayer in most of the tube segment, as indicated by the XZ axis (Fig.70B).

In parallel, we also observed the homozygous cells arrangement in the same conditions (Fig.71). We noticed a cell monolayer under three of the five tubes lined with *Pkd1*$^{-/-}$ cells. The two tubes positioned at the edges of the chip were not easily imaged, reason why we did not focus on them. Besides, they displayed a widened shape after the wires removal (Fig.71A).This monolayer displayed long actin stress fibers. Interestingly, the third and fourth tubes, starting from the left of the chip, partially merged on top of one of their extremity (Fig.71A). The magnification on one extremity of the first tube underlines the longest and numerous oriented actin stress fibers along the tube axis, compared to the one observed in the control cell line, which has not been quantified yet (cf. Chapter IV). Moreover, we noticed well-defined cuboidal cells lining tubes, and a lumen surrounded by a cell monolayer (Fig.71B).

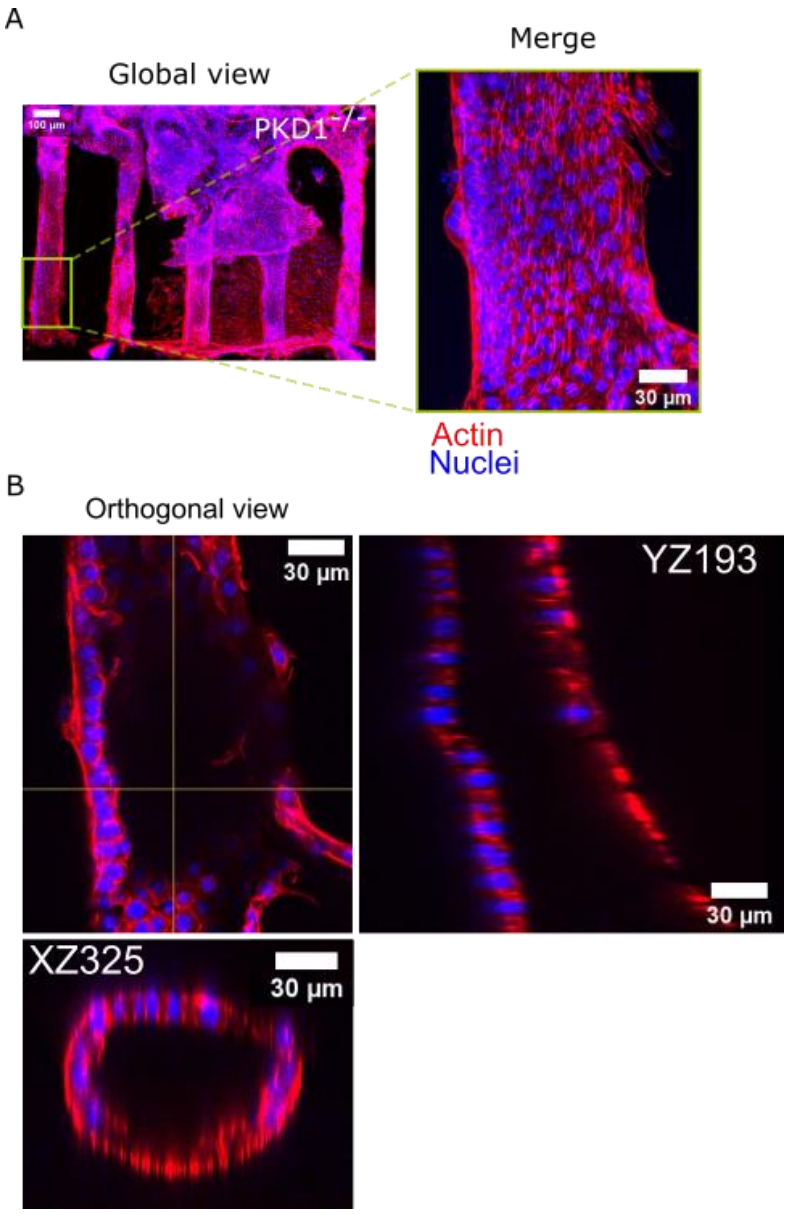

Figure 71: Immunostaining of a chip imaged under a confocal microscope. A: Global view of the five tubes. A cell layer partially obstructed the visualization of two tubes. In red, F-actin labelled with phalloidin-TRITC and in blue, nuclei stained with Hoechst. Scale bar: 100 µm. On the right, magnification focusing on one part of the tube lined with *Pkd1*$^{-/-}$ cells, 19 days post-seeding. It is a projection in z of the maximal signal intensity. Scale bar: 30 µm. B: Orthogonal view of the tube section with on the right side, the YZ position and on the bottom, the XZ position depicting a lumen within the tube. We note the cuboidal shape of cells on the tube edge. Scale bar: 30 µm.

On another note, the three-dimensional tubular analyses raise some questions regarding the interplay between tubes, depending on the cell type. As aforementioned in the previous subsection (III) 2) b)), the chip design was modified to half-reduce the intertube distance from

200 to 100 µm. Cells organization within those tubes spaced of 100 µm were then visualized. The cellular organization of *Pkd1*$^{+/-}$ cells within the tubes was examined as preliminary data (Fig.72). The five tubes were visualized at the same time: we observed a uniform cell monolayer within each tube. The two last tubes, starting from the left, merged at their bottom sides (Fig.72A). On the tube segment magnification, we noticed numerous long actin stress fibers that seemed to orient according to the tube axis. Moreover, on the orthogonal view, we noted the elliptical geometry of the tube lined with the heterozygous cells. It is worth noting that the cells exhibited a well-defined cuboidal shape along the tube (Fig.72B).

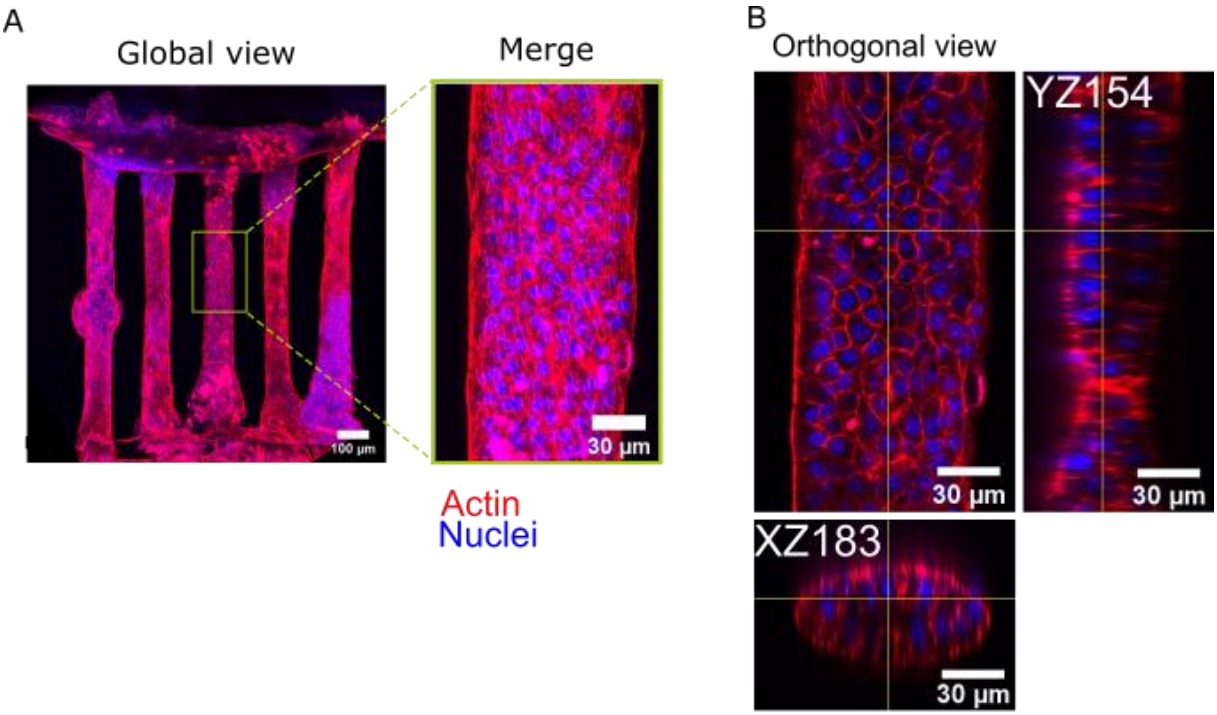

Figure 72: Immunostaining of a chip imaged with a 40X lens under a confocal microscope. A: Global view of the five tubes with 100 µm spacing. On the top, a *Pkd1*$^{+/-}$ cell layer partially covers the tubes. In the middle of the first tube from the left, a round shape due to a bubble air in the collagen I is filled with cells. In red, F-actin labelled with phalloidin-TRITC and in blue, nuclei stained with Hoechst. Scale bar: 100 µm. On the right, magnification focusing on one part of the tube lined with *Pkd1*$^{+/-}$ cells, 39 days post-seeding. It is a projection in z of the maximal signal intensity. Scale bar: 30 µm. B: Orthogonal view of the tube section with on the right side, the YZ position and on the bottom, the XZ position depicting a lumen within the tube. We note the cell cuboidal shape on the tube walls. Scale bar: 30 µm.

Hence, with both cell types fixed and observed as soon as they lined tubes, the tubular scaffold seemed to be maintained: with the control cell line, the tube structure seemed more elliptical than circular, which will be next quantified. In particular, *Pkd1*$^{-/-}$ cells could have an effect on the mechanical properties of the tubular scaffold, playing a role on its deformation by pulling and/or pushing on it. Therefore, to assess these hypotheses, we examined several quantitative parameters thanks to the macro written by Bertrand Cinquin. Measurements were realized along the tube axis in order to define the **cell layer area**, the **perimeter of the tubes** and their **circularity all along the tube**, depending on the cell type. To avoid aberrant measurements, I cropped the tubes at both extremities, and focus only on less than 1 mm tube length. Sometimes, air bubbles created holes in the collagen I, in which cells lined and proliferated: those architectural defaults were also removed when it was possible.

First of all, we determined those parameters within empty tubes molded in collagen I, and coated with laminin coupled to rhodamin in order to characterize the tubes geometry without cells, as a reference (Fig.73). The **tube perimeter** defined by the fluorescent laminin depending on the x position within the tubes was first processed (Fig.73A). We noted that the curve split into three parts, which highlighted three sections along the tubes. The hatched area coincides with the middle of the tubes, the region on which we will focus our descriptions on, while the two others sections illustrate the tubes edges. During the first hundred micrometers,

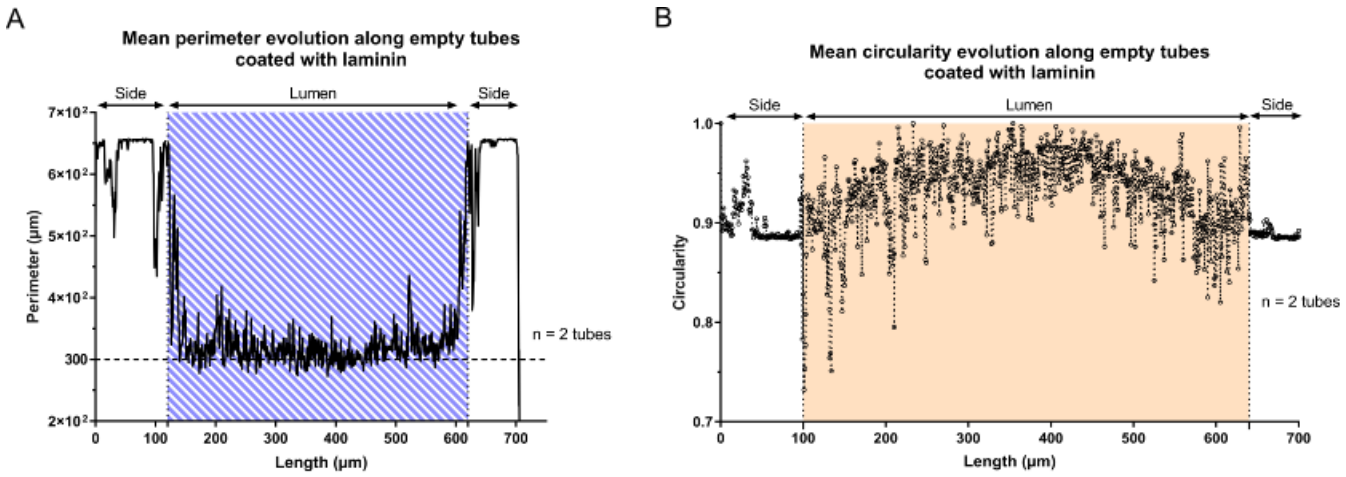

Figure 73: Graphs illustrating the tube shape evolution depending on the position within tube. Tubes molded in collagen I were coated with laminin-Rhodamin before image acquisition under a confocal microscope. A: Graph depicting the coating mean perimeter evolution along tubes. B: Plot of circularity evolution along tubes, with 1 corresponding to a perfect circle, and less than 1, an elliptical shape.

as well as for the last hundred micrometers (from 600 to 700 µm), the tube perimeter was the highest (650 µm). At 100 µm and 610 µm length, the perimeter value drastically declined to 300 µm. Moreover, we investigated **tube circularity** (Fig.73B). Fluctuating between 0.9 and 1, tubes exhibited almost a nearly circular shape. However, as noticed with the perimeter values, the curve displayed three sections, with the middle part of tubes exhibiting a global circularity close to 1.

Those observations suggest a symmetry within the tubes arrangement: on both sides of the tubes where the cells are seeded, tubes seem to be slightly less circular. In between, tubes displayed a roundest shape, as expected in this reference condition. This symmetry could be due to the fabrication process. Indeed, tubes were molded in collagen I around wires that were gently removed after the collagen I polymerization. The wire removal, even carefully and slowly realized, can induce a slight collapse of the tubes. Besides, the coating step, as well as the cell seeding, can slightly deform the tubes at their extremities.

Relying on these observations, we next assessed the **mean cell layer area variation** within the tubes, depending on the cell type and the tube position (Fig.74). In all this part, we present preliminary results corresponding to 3 independent chips for *Pkd1*$^{+/-}$ cells, and 2 independent chips for *Pkd1*$^{-/-}$ cells. We noted that the heterozygous cell line represents a smaller area than the homozygous one, which could be related to the larger tube deformation observed with the homozygous cell line or a difference in the cell shape (Fig.74A). Albeit this measure was not significantly different, it corroborates the previous analyses made on 2D projections phase contrast images.

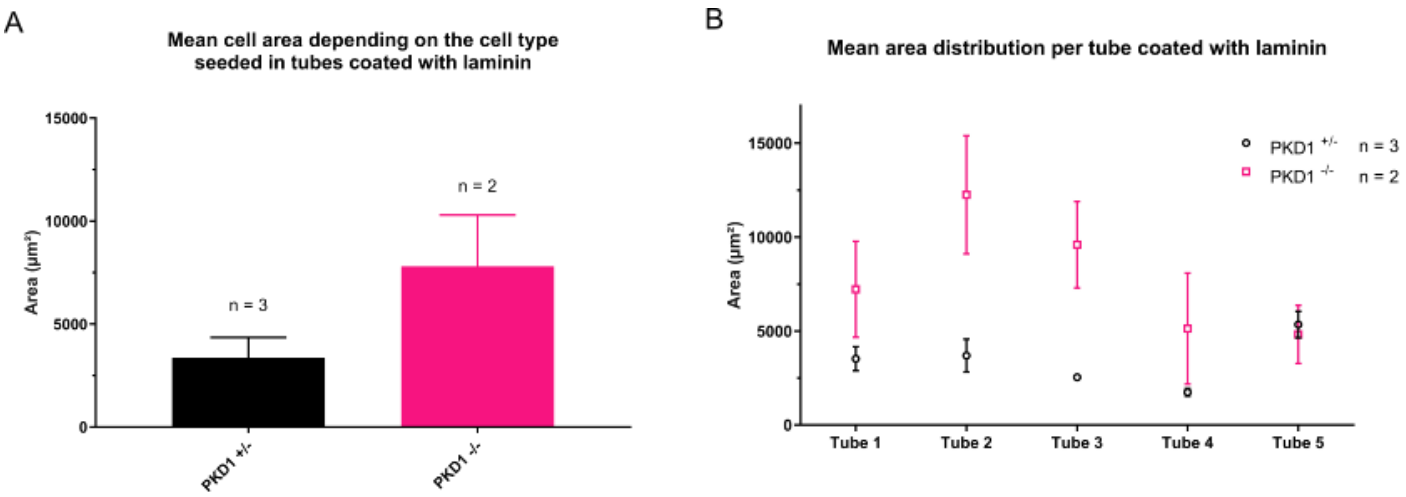

Figure 74: Graphs illustrating the cell area evolution depending on the tubes interplay and the cell type. A: Plot representing the mean area evolution depending on the tube position within the chip, and comparing the ADPKD cellular models. B: Graph depicting the mean cell area evolution depending on the cell type. A statistical unpaired t-test was performed to compare both cell lines, and *p = 0.031<0.05. SEM is represented, with n = 3 independent experiments with the *Pkd1*$^{+/-}$ cells, and n = 2 independent experiments with the homozygous cells.

In parallel, we also investigated the **tube boundaries effects** on tubes localized in the central part of the chip. Indeed, the chip consists of five tubes: two of them face the collagen I unstructured scaffold while the three others, in the central part of the chip, are adjacent to each other. Tubes 1 and 5 refer to the extremities, while tubes 2 to 4 correspond to the ones in between (Fig.74B). We first observed that with the control *Pkd1*$^{+/-}$ cell line, cell area was quite similar in all the tubes whatever its position ($2.5.10^3$ µm^2). In contrast, this parameter varied slightly as function of tubes position with the *Pkd1*$^{-/-}$ cells. Cells in the central tubes seem to occupy a larger surface than in the tubes at the extremities. Those results could suggest that *Pkd1*$^{-/-}$ cells deformed and enlarged more the tubes located in the middle of the chip.

We also measured the **mean perimeter of the tubes** as a function of the cell lines and as function of the tube position (Fig.75). As expected the mean perimeter of the tubes followed the same tendency as the mean cell layer area, with the homozygous cells exhibiting a 1.6 fold-increase of the tubes perimeter compared to the heterozygous cell line (Fig.75A). Similarly to the cell area, the tube perimeters seems to be slightly larger for the tubes located at the extremities of the tube array (Fig.75B). We were initially expecting opposite behavior, as the tubes at the extremities would be less affected by their neighbors, and should thus enlarge more.

This first observation needs to be further confirmed by performing more experiments in similar conditions.

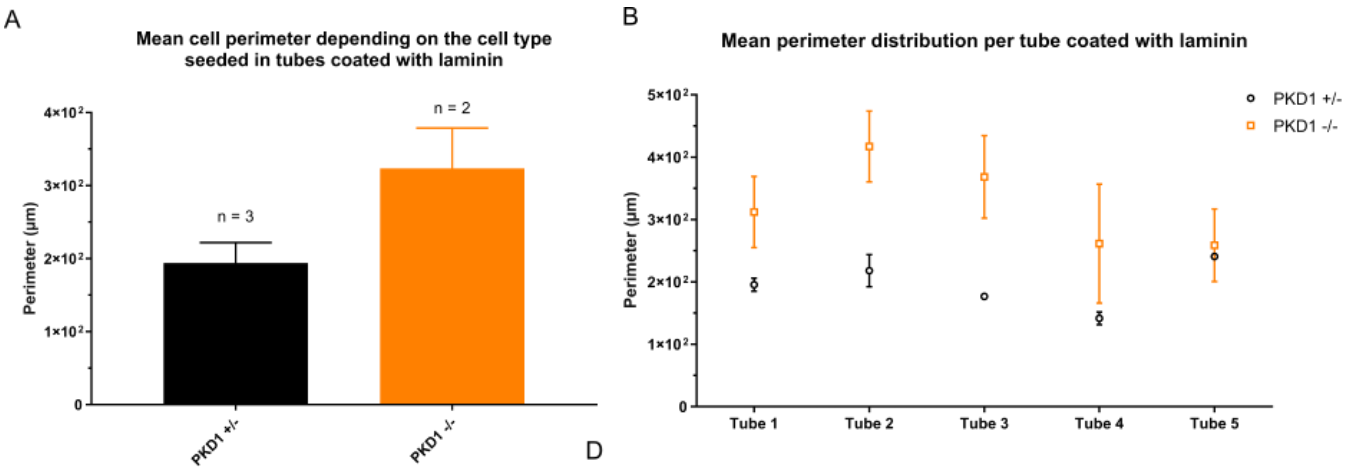

Figure 75: Graphs illustrating the tube perimeter evolution depending on the tubes interplay and the cell type. A: Plot representing the mean perimeter evolution depending on the tube position within the chip, and comparing the ADPKD cellular models. B: Graph depicting the mean perimeter evolution depending on the cell type. A statistical unpaired t-test was performed to compare both cell lines, and **p <0.05. SEM is represented, with n = 3 independent experiments with the *Pkd1*$^{+/-}$ cells, and n = 2 independent experiments with the homozygous cells.

Afterwards, we focused on **the tube geometry** depending on the local position within the tube, starting with the **area of the cells** lining on the tubes (Fig.76A). The area of the heterozygous cells was stable along the tubes, with small variations at the edges (orange arrows). For x ranging from 50 to 500 µm, the mean cell layer area was around 5000 µm². We observed the same steps with the homozygous cell line (red arrows), although the mean cell layer area was significantly higher: this parameter progressively raised with almost a two-fold increase (from 8.10^3 to $1.5.10^4$ µm²). We noted that the tubes lined with the homozygous cells were shorter (around 450 µm length) than the one filled with the control cell line (600 µm length), which was due to the cell growth on both sides of the tubes. Thus, the heterozygous cells lined the tubes shaping a lumen, similarly to the homozygous cells that tended to gradually enlarge the tubes from one extremity towards the middle of the tubes. Besides, the **mean**

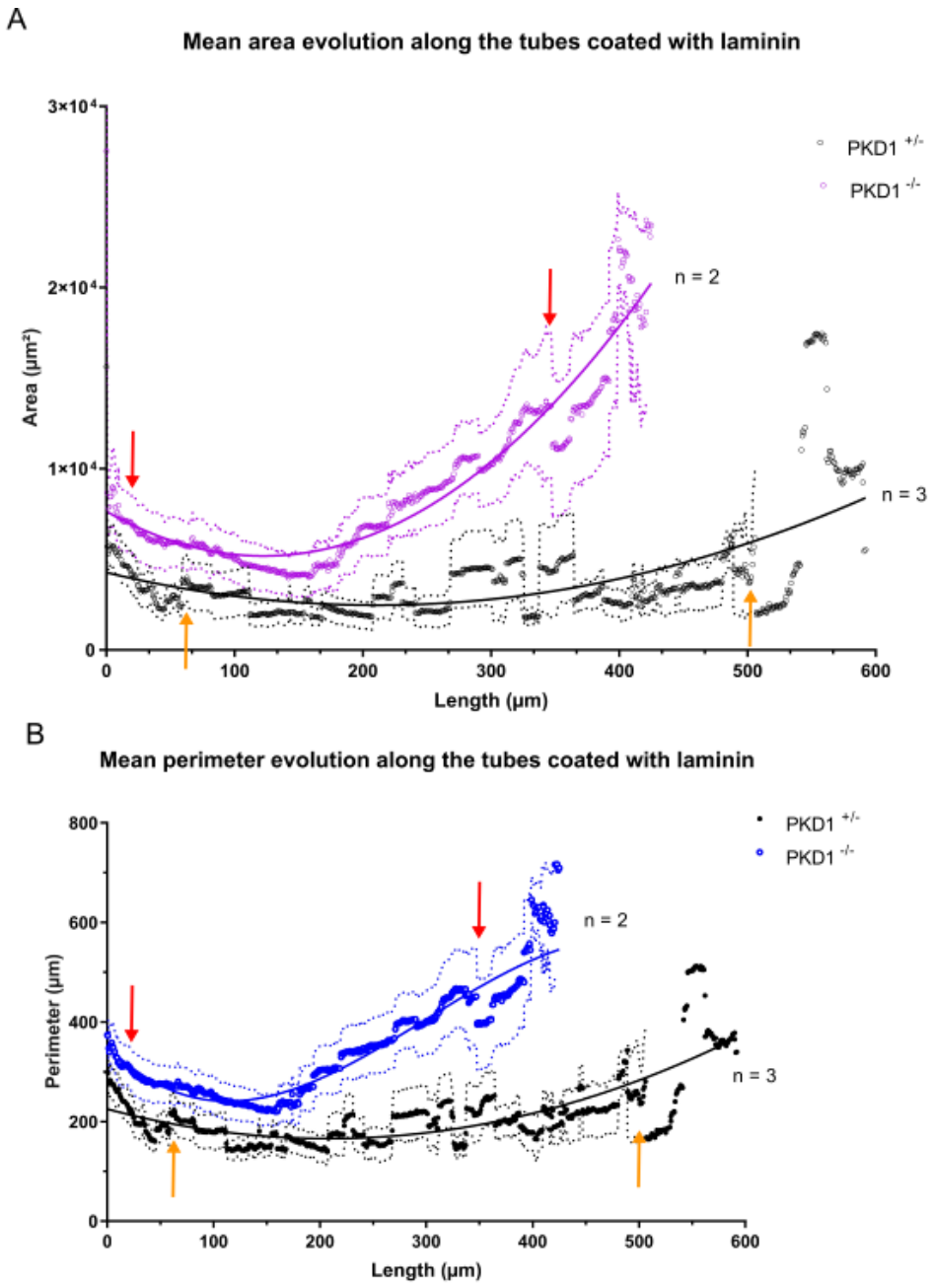

Figure 76: Graphs illustrating the mean cell area evolution and the tube perimeter evolution depending on the cell type. A: Plot representing the mean area evolution depending on the cell type. The *Pkd1*$^{+/-}$ cells curve was fitted with a third order polynomial for visualization (straight black line) while the *Pkd1*$^{-/-}$ cells curve was fitted with a second order polynomial equation (straight purple curve). A statistical unpaired t-test was performed to compare both cell lines, and ***p <0.001. B: Graph depicting the mean perimeter evolution depending on the cell type. The same polynomial equations were fitted as for graph A. SEM are represented as dispersed dashed dots on both sides of the curves, with n = 3 independent experiments with *Pkd1*$^{+/-}$ cells, and n = 2 independent experiments with *Pkd1*$^{-/-}$ cells.

perimeter measurement along the tubes supported these observations (Fig.76B). The tube

perimeter lined with heterozygous cells was quite steady between 50 and 500 µm tubular length, ranging from 200 to 300 µm. With the homozygous cells, it significantly increased between the two extremities of the tubes, with a 1.5 fold-increase compared to the control cell line.

Hence, both cell lines formed a monolayer lining with the tubes that displayed a hollow lumen. Moreover, *Pkd1*$^{+/-}$ cells did not significantly distort the tubes compared to *Pkd1*$^{-/-}$ cells that exhibited a more important lumen. Interestingly, *Pkd1*$^{-/-}$ cells in particular deformed tubes while they just formed a confluent monolayer lining the tubes. Therefore, in parallel to the observations on 2D projection images, tubes were not necessarily filled to be deformed by the homozygous cells. Tubes can either be lined with homozygous cells to shape a hollow lumen cells or filled and obstructed with them.

The **circularity of tubes** was also further investigated (Fig.77). We noticed that the circularity of the tubes lined with *Pkd1*$^{+/-}$ cells fluctuated around 0.9 along the tubes, indicating that the tubes were uniform and nearly round. With *Pkd1*$^{-/-}$ cells the circularity along the tube axis progressively declined, ranging from 0.8 to 0.6, which suggests that *Pkd1*$^{-/-}$ cells distort the tubes by enlarging them at one extremity, and contracting them at the other one. This preliminary study will be repeated and realized on further stacks of images in the near future.

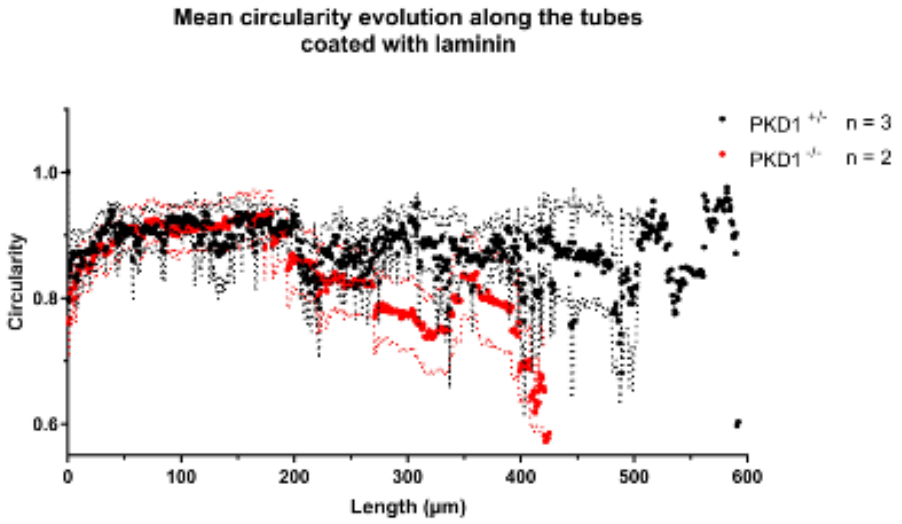

Figure 77: Plot representing the mean circularity varying between 0 and 1, with in black dots, control *Pkd1*$^{+/-}$ cells, and in red dots *Pkd1*$^{-/-}$ cells. SEM are represented as dispersed dashed dots on both sides of the curves, with n = 3 independent experiments with *Pkd1*$^{+/-}$ cells, and n = 2 independent experiments with the *Pkd1*$^{-/-}$ cell line.

Hence, using a 3D approach to characterize our ADPKD cellular models, we deepened the previous analyses made on 2D images. Both cell lines exhibited two specific behaviors defined over time during several weeks, and at one time point, before reaching confluency within the tubes. Going further, this last method refined the tube geometry characterization, depending on the cell type. Indeed, this preliminary data suggest that circular tubes at their extremities were more elliptical in their middle, which was more marked with the *Pkd1*$^{-/-}$ cells that deformed the tubes. They simultaneously enlarged and retracted part of the tubes.

Of another note, those different parameters to characterize tubes deformation, the absence or presence of lumen, in addition to tubes shape (circular or elliptical) will be next performed on tubes spaced of 100 µm filled with both ADPKD cellular models. Furthermore, another aspect is currently being developed to further characterize those cell lines and the tissue they establish within the tubes: nuclei counting and cell segmentation to describe their shape, size and orientation within the tubes.

Conclusion:

Thus, taken all together, the results highlight two distinct behaviors of the ADPKD cellular models in our innovative and gradually implemented multitube device. Embedded in a mix of collagen I and Matrigel (70:30), Wei and co-workers highlighted that *Pkd1*$^{+/-}$ cells mainly form tubular and linear branching structures, while the *Pkd1*$^{-/-}$ cell line displays cystic features with some of them more linear [275]. Moreover, the proliferation rate of both cell types on 2D surface were assessed, indicating that homozygous cells duplicated almost three times faster than the heterozygous cells, in line with our observations. Going further, our approach promoted their characterization in 3D tubular structures mimicking the nephrons architecture. Indeed, both cell lines were characterized by two growth cell regimes, on flat surfaces as well as in 3D structures. The control cell line or *Pkd1*$^{+/-}$ cells proliferated and lined tubes without deforming them, while the homozygous cells grew faster, lined tubes and distorted them over time. Displaying cystic features, those cells gradually enlarged tubes during their proliferative phase, before retracting them over time. Furthermore, albeit the cells leaned on a basal membrane protein, their dynamics was not affected even if they grew more steadily on laminin than on collagen I alone. Relying on this cell kinetics, the tubes geometry and the intracellular

organization were then refined at one time point before they obstructed the tubes. In line with the previous observations, both cell types lined the tubes, shaping a hollow lumen more or less circular. *Pkd1*$^{-/-}$ cells further enlarged tubes without filling them, suggesting that they could exert a mechanical constraint on them. In contrast to control *Pkd1*$^{+/-}$ cell line with which tubes remained stable all along. It is important to note that tube enlargement could have an effect on adjacent tubes, which we started to investigate with our 100 µm intertube spacing design. Indeed, it will favor the study of cyst propagation within the system, one the ADPKD major hallmark. As homozygous cells indeed deformed the tubes, which is the first step for cyst formation, this approach can be further deepened and refined in the near future, which will be discussed in the next chapter (IV).

Chapter IV: Conclusions and perspectives

Painting entitled “Renal Cherry Tree” realized by Lizzy Rainey, and published as magazine cover of the ASRT Radiologic technology, Volume 86, number 4, March/April 2015.

1) Kidney-on-chip achievements and improvements

In recent years, many pharmaceutical industries get interested with the organ-on-chip field, and more specifically with kidney-on-chip development in association or not with liver. Indeed, involved in drugs metabolism and excretion from the body, those organs are of most interest [3], [287]. Taking part in this effort and with a special interest for the ADPKD renal disorder modelling, we designed an innovative kidney-on-chip that can be further improved in the near future.

a) Tightly packed multitubes implementation

Relying on different microfabrication processes, we designed a functional microphysiological device in copolymer (COC) gradually improved in order to get closer the physiological conditions (cf. Chapter II). As an open system to ease the daily maintenance of the ADPKD cell culture, the chip was immersed in the culture medium, which favoured oxygen and nutrients exchanges within the tubes over time.

The device consisted of five micrometric and cylindrical tubes parallel disposed, and regularly spaced. Molded in collagen I, a biocompatible hydrogel, the tubes were then coated to further reproduce the basal membrane on which renal epithelial cells lean on. Coated with collagen IV, Matrigel or laminin to enhance renal cell survival and differentiation within the tubes, it would also be of interest to mix those proteins to mimic *in vivo* conditions [275], [286]. Indeed, controlling this bottom-up approach could reinforce the formation and differentiation of cell monolayer junction, maintaining cells within the tubes. We noticed that both ADPKD cellular models lined tubes coated with Matrigel and laminin. On laminin, cells behaved similarly as on the collagen I alone, which is the control condition, even though they stably grew over time on the laminin coating.

The intertube distance was initially set at 200 µm, and was later half reduced from 200 µm to 100 µm in order to favour the effect of tube vicinity, and thus, their interplay depending on the ADPKD cell type seeded. In particular, we showed for the first time in such condition that the homozygous cells, *Pkd1*$^{-/-}$ cells, displayed cystic characteristics promoting tube distortion over time. Performing further experiments with a low intertube distance will allow us to decipher the influence of one tube deformation on the adjacent one. We will also consider that decreasing this distance will favour both the mechanical and chemical coupling between tubes.

Indeed, with lower distance between tubes lined with homozygous cells in particular, the chemical cues secreted by the cells from one tube might propagate to the surrounding tubes.

Thus, all those different improvements will enhance long-term epithelial renal cell culture within our innovative microphysiological device, and support renal epithelium tissue formation. Nevertheless, the first function of nephrons is to filtrate the blood in order to produce urine, which involves fluid flow through the different tubular segments. Therefore, the next implementation will be to add a flow system in our device.

b) Flow system establishment

We already scrutinized on a flow system development we can implement in our kidney-on-chip device in order to apply a monitored and constant flow rate (and consequently shear stress) for a long-term cell culture period. Four devices were designed: two passive systems based on the gravity versus two active systems.

In 2004, Zhu and co-workers designed an array of horizontally-oriented tubes connected to the inlet and outlet of a microchannel in order to continuously deliver cell culture medium at a constant flow rate, and for long-term cell culture period [288]. To this end, glass pipettes were horizontally-oriented with a defined height difference to induce a constant hydraulic pressure and thus, flow velocity. The top pipettes contained the cell culture medium while the bottom one collected the wastes and factors secreted by the cells seeded within the microchannel. Using gravity force, a steady pulse-free flow was exerted within the horizontal pipettes driving cell culture medium from the reservoir pipettes with higher fluid levels down to the collector pipette. With cell medium flowing towards the collector pipette, the fluid meniscus remained lateral, implying that the channel resistance was constant, as well as the hydraulic pressure. Relying on this **gravity-driven pumping system**, Bastien Venzac, former PhD student in the MMBM team (cf. Chapter II), designed a similar prototype in 3D printed resin (Fig.78).

Figure 78: Illustrations of the gravity-driven pumping system. On the top left, schematic of the device and derived from [4]. On the bottom, picture of the 3D printing prototype based on the schematic.

Composed of two Pasteur glass pipettes parallely disposed with one cm height difference, the top glass pipettes should contain cell culture medium and the lowest one should collect the wastes and the remaining cell culture medium. Each pipette was respectively connected to the inlet and outlet of the kidney-on-chip placed in the middle of the device. Nevertheless, flow rate measurements realized on the weight of small water volume over time were nor sensitive enough neither reproducible. Therefore, we adjusted and refined this device, designing another one (Fig.79). Also composed of two positions to place Pasteur glass pipettes, we used a micromanipulator to modify the height between both pipettes, which was more accurate and easier to adjust depending on the flow rate required within the tubes. As with the previous system, the highest pipette imposed the flow rate through the connected kidney-on-chip, while the other one collected the cellular wastes. Both pipettes were connected to glass capillaries of 100 µm diameter to mimic the resistance within the final collagen I tubular scaffold. Moreover, a resistance was added upstream the chip, connecting a capillary of 1 cm length and 100 µm diameter to begin with, in order to exert the right flow rate. To apply a constant flow rate of 0.75 µl/min within our chip, we assessed the required height between both pipettes measuring the weight of small water volume over time, depending on the inter-pipette height. Starting with a height difference of 6 cm, we measured the weight of volume water at different time point, and determined the flow rate in the range of µl/min. However, as with the previous gravity-driven device, flow rate measurements over time were not enough accurate and reproducible.

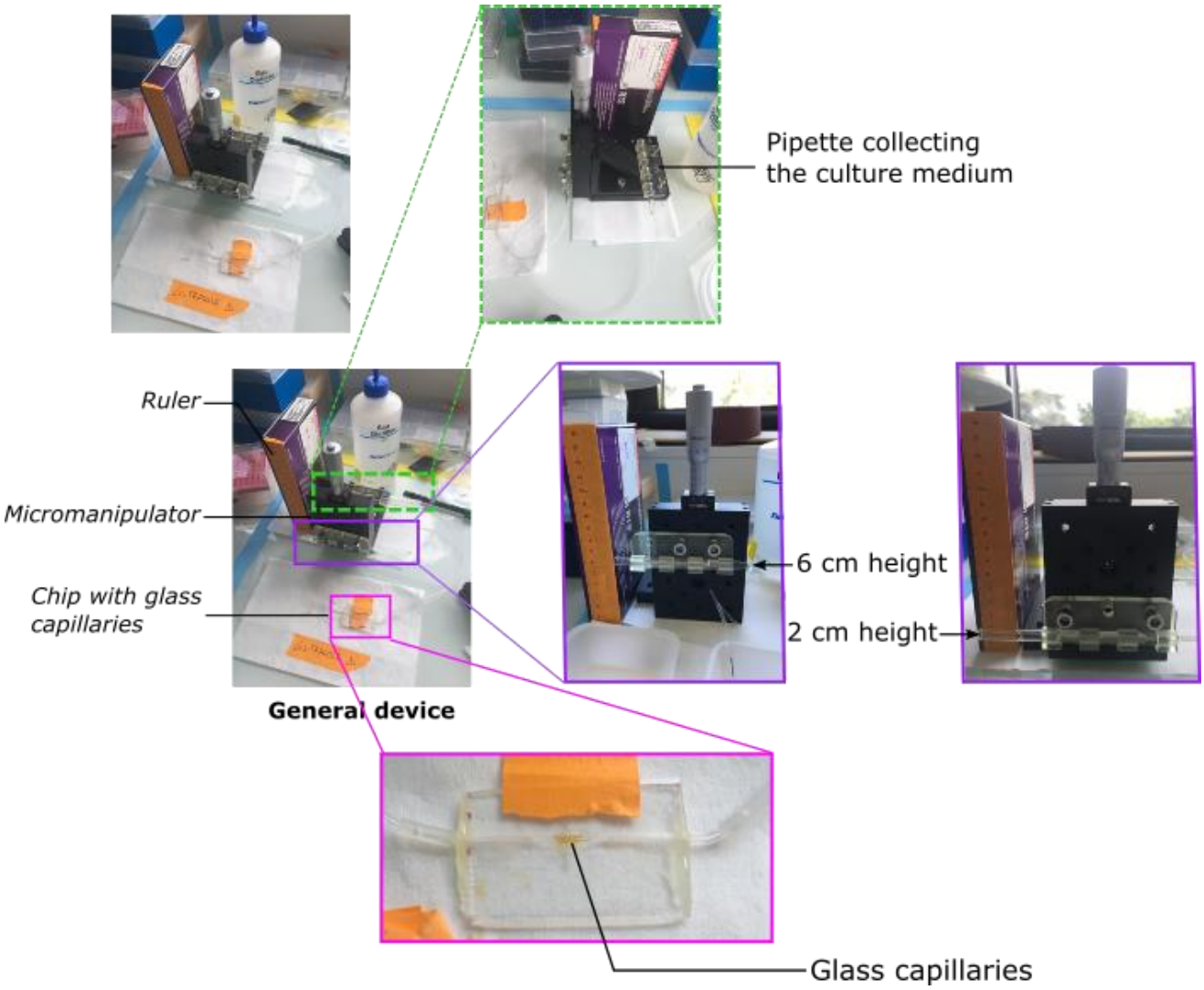

Figure 79: Illustrations of the second design of the gravity-driven pumping system. On the top left, and in the middle left, the general view of the device is pictured. In green dotted line rectangle, focus on the glass collecting pipette, while the purple rectangles represent the glass pipette containing the cell medium and imposing the flow. In front of the micromanipulator, a magnification on the chip with glass capillaries mimicking the collagen I tubes is shown.

Nonetheless, with both developed devices, we had to deal with the same issues: water evaporation in the pipettes and the tubings used to connect the different parts of the device, and air bubble formation along the tubings over time. To limit air bubble formation, the surfaces of pipettes and tubings were passivated with buffer containing 1% BSA, and water was degased before passing through the fluidic system. Evaporation issues were avoided with a droplet of mineral oil above the water, which created an interface between both liquids. Albeit both gravity-driven systems approach were tempting, they were not efficient enough to pursue with them.

Moving on, with the help of Giacomo Gropplero, research engineer in the MMBM team, we evaluated an active system, using a **syringe pump** connected to our kidney-on-chip composed of tubes molded in collagen I (Fig.80). To do so, chips were seeded with the ADPKD cellular models, and let to grow until they adhered and started to form a tissue lining the tube walls. A syringe containing cell culture medium was positioned on the syringe pump, and then connected to the chip inlet via a liquid-liquid interface to avoid bubbles passing through collagen I tubes. Afterwards, a flow rate of 0.75 µl/min was applied in the main channel and split within the five tubes, which theoretically induces a flow rate of 0.15 µl/min within each tube. However, the cells did not line tubes similarly, which means that not all tubes were filled the same way and some of them could be obstructed. Therefore, the flow rate within each tube was not the one initially applied, and varied depending on the tube size, shape and filling that finally set the hydrodynamic resistances of the tubes. Moreover, this system dealt with the similar microfluidic issues than aforementioned: air bubble formation along the tubings, promoting collagen I tubes breaking, and fluctuations of the flow rate distribution within the tubes.

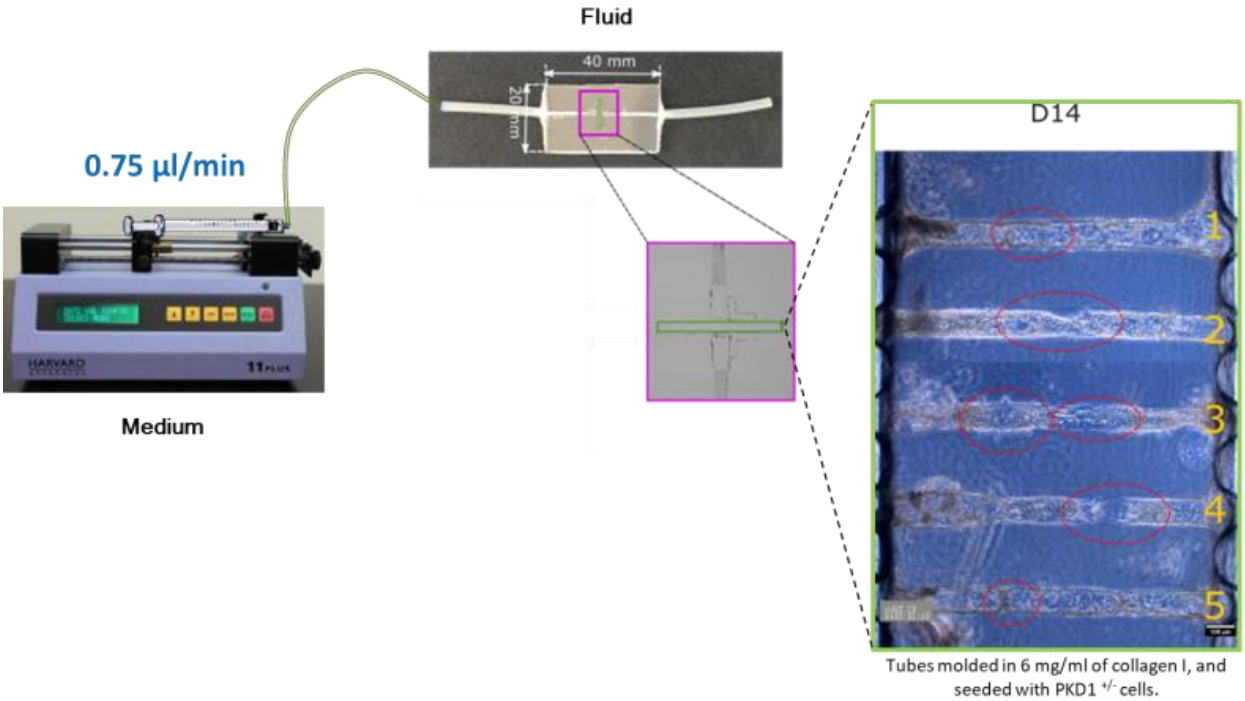

Figure 80: Representation of the syringe pump system connected to the chip. A syringe containing the cell medium is positioned on the syringe pump, and a flow rate of 0.75 µl/min is applied in the following tubings linked to the chip. The green rectangle illustrates a magnification on the theoretical view on the tubes lined with the heterozygous cells. It is worthwhile to note that the cell tissue is not similar within all the tubes.

Eventually, with the help of Manh Nguyen, a PhD student from the MMBM team, we connected the kidney-on-chip to a currently used **microfluidic pressure controller** in addition to a flow unit (MFCS) (Fig.81). Developed by the Fluigent company, those microfluidic systems and components, in particular the pressure pumps, compete with the traditional syringe pumps previously used.

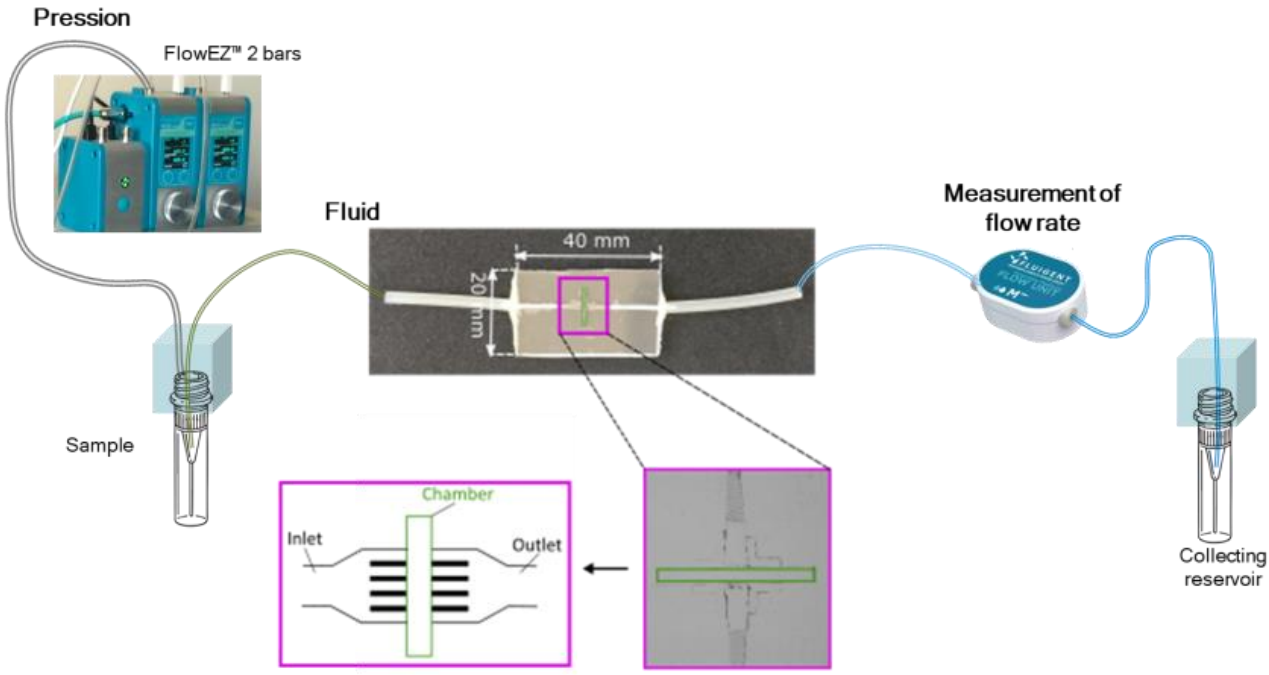

Figure 81: Schematic depicting the connections between the pressure controller, the flow unit and the chip.

In preliminary experiments, the pressure controller was positioned upstream the chip, at the inlet, and the flow unit measuring the flow crossing the whole tubes was placed at the outlet, downstream the chip. Albeit the preliminary tests were not as conclusive as expected within the chip, Manh is currently refining and adjusting this method in the context of the development of a muscle-on-chip.

Furthermore, the flow system addition to the organ-on-chips developed in the MMBM team, and more specifically to the kidney-on-chip, will improve and favour the reproducibility of some important steps. Indeed, this implementation will refine and promote a reproducible and homogeneous tubes coating with basal membrane proteins, as well as the cell seeding process. It will finally provide a controlled renewing of the intratubular medium while applying a controlled shear stress on the cells lining the tube.

Hence, different methods to connect a flow system to our innovative multitube device were assessed. However, all of them dealt with the same limitations: applying a constant and controlled flow rate within the parallel disposed five tubes displaying various hydrodynamic resistance. In other words, the flow rate within each tube would be different and not easily quantifiable: we will experience this injecting microbeads inside the different tubes. To overcome this limitation, one of the possible change is to disconnect each tube individually, which means to change the current design. Then, we can apply a monitored flow rate as soon as the cells form a confluent monolayer lining with the tube or even sooner, when they adhere to the tube walls. Another possibility could be to add a resistance system that will be largely higher than the one of each individual tubes, and then set the flow conditions. Both alternatives will be evaluated.

c) Local compression setup

One of the main challenge of this project is to recapitulate the ADPKD hallmarks within our kidney-on-chip, which means cyst formation and propagation. Indeed, the Snowball effect theory described in Chapter I, assumes that primary cyst formation within one tube could induce secondary cyst formation and propagation from adjacent tubes because of mechanical constraints. To reproduce and decipher the molecular processes involved, three potential approaches to apply a local and controlled compression on the tubes could be attempted.

Succinctly, three methods could be considered: two methods display a direct contact with the seeded tubes, and the other one relies on a biological approach. There are mainly assumptions and need to be further conceptualized.

For the **first method**, the kidney-on-chip device would be modified to integrate tubes made in Ecoflex embedded in the collagen I tubular scaffold [289]. In particular, they could be positioned perpendicularly to the collagen tube to applied a local constraints. These tubes made in Ecoflex, a silicon elastomer softer than the PDMS, would be connected to a pneumatic device that will be filled with air or liquid in order to exert a local constraints on the collagen I tubes.

A **second strategy** relies on a direct compression applied on the collagen tubes with a micropipette using a micromanipulator can be considered. The tubes would preliminarily be surrounded with deformable material to prevent impairments of tubes lined with cells.

A **third more physiological approach** is built on renal MDCK cells mechanical properties when embedded within an extracellular matrix (ECM), like the collagen I scaffold used in our multitube device [290]. Indeed, directly embedded in the collagen I, the MDCK cells would randomly distributed in the scaffold and close to the tubes before shaping spherical cysts. As MDCK cells form fluid-filled expanding cysts when cultured in 3D substrate, they will mimic a local and more *in-vivo* like constraint on the tubes lined with the ADPKD cellular models.

In conclusion, three different approaches to exert a control and local constraint on the tubes can be explored to implement the kidney-on-chip, and recapitulate the Snowball effect.

2) ADPKD modelling: biological functional assays

a) Morphological and molecular assessments of ADPKD cells

As already described, ADPKD is one the most inherited nephropathy and is characterized by the formation of numerous cysts from the nephrons. Epithelial cells composing cysts display impaired polarity leading to the expansion of fluid-filled cysts. To recapitulate this pathology hallmarks, two cell lines carrying a heterozygous or homozygous mutation in *Pkd1* gene were used. We started by characterizing their phenotype on flat substrate (Chapter III) 1)). We investigated the cystogenesis process, comparing the homozygous cells (*Pkd1* $^{-/-}$ cells) to the control cell line (*Pkd1*$^{+/-}$ cells). In the meantime, wild-type proximal convoluted tubular cell line (PCT-Wt) was also used as a control cell line to the *Pkd1*$^{+/-}$ cells. Both behaving similarly on flat surfaces, we chose to focus on *Pkd1*$^{+/-}$ as cell model for further experiments.

For this purpose, we performed immunofluorescence (IF) experiments on different epithelial markers: tight and *adherens* junctions proteins composing the apical junctional complex (ZO-1, E-cadherin and N-cadherin), polarity markers (Na/K ATPase, Ezrin), focal contact protein (Vinculin), and the actin cytoskeleton arrangement [1], [11], [282]. The PC1 protein, encoded by *Pkd1* gene, associates with different partners among which the ones aforementioned, to form protein complexes involved in cell-cell, cell-matrix and cell-cytoskeleton interactions. In addition, the transcript amount of each marker was quantified by

qRT-PCR. From the IF experiments, several aspects were highlighted between the control cell line and the homozygous one. On one hand, apical junctional complex impairment occurred within *Pkd1*$^{-/-}$ cells: the tight junctions appeared reinforced while *adherens* junctions were affected by the mutation. E-cadherin expression was gradually lost at the cell-cell junction, and replaced by its isoform, N-cadherin [282]. One mechanism could be that PC1 binding to E-cadherin/β-catenin/actin complex is disrupted at the apico-lateral part of the cells, which destabilizes the *adherens* junctions. However, E-cadherin internalization and mislocalization could be partially compensated by N-cadherin expression, which could trigger cell dedifferentiation [291]. In addition to impairments in cell-cell interaction, vinculin localization in our IF experiments suggested a decrease in *Pkd1*$^{-/-}$ cell adhesion to the extracellular matrix, which could promote cell shape changes and detachment from the surface (Chapter III) 1)). Indeed, focal contact complexes are also impaired upon *Pkd1* inactivation, as PC1 does not bind to integrin in order to phosphorylate and activate the FAK protein (Focal Adhesion Kinase) [44], [282]. PC1 depletion in *Pkd1* gene-depleted mice also decreases focal adhesion rate turnover, which impairs their maturation and formation [11]. Regulating actin and microtubule cytoskeletons, PC1, in association with other partners, affects their stability and dynamics, during cell migration for instance [44]. On the other hand, it is of great importance to note that apico-basal cell polarity was disrupted in *Pkd1-/-* cells: Na/K ATPase was mislocalized in the apical side of the cells instead of being baso-laterally distributed, which could play a part in ion and fluid secretion inversion towards the inner cysts [283][110][292]. Besides, to demonstrate the proximal origin of the *Pkd1* cells, the AQP1 (aquaporin 1) protein, a water channel, was quantified. It is also one of the markers of interest localized at the plasma membrane and in the cytoplasm of heterozygous cells. Eventually, as PC1 binds to PC2 to form a complex in the primary cilium, the staining and quantification of this organelle with markers like Arl13b could enhance knowledge on its involvement in the cystogenesis mechanism. Thus, *Pkd1*$^{-/-}$ cells exhibit dedifferentiated and defect polarity features that could concur to loss of their epithelialization, leading to cystic behaviour and beginning of cystogenesis during ADPKD evolution.

Furthermore, another aspect is currently being developed to further characterize those cell lines and the tissue they establish within the tubes: nuclei counting and cell segmentation to describe their shape, size and orientation within the tubes. An implementation of the current macro joined the previous one to allow nuclei segmentation in order to count them and to estimate their volume within the tubes. The segmentation process was based on the quality of

images and on their resolution. As these parameters were better on the images acquired with the 40X lens water immersion, the nuclei density will be determined on these images. Indeed, this analysis is still on going.

On one hand, each biomolecular method gave us two different features of the ADPKD cellular models: the IF display the proteins distribution within the cell types, while the qRT-PCR quantify the upstream form of the proteins visualized, or the mRNA expression. This last quantification can be deepened with Western blots to determine the level of protein expression in addition to their transcripts. Indeed, mRNA transcripts can be post-transcriptionally modified, which can change their amount in the cells. This modification can also promote modifications of the post-translational process, and thus, the amount of functional proteins expressed.

On the other hand, PC1 is involved in many protein complexes regulating different signalling pathways such as cell proliferation, differentiation or apoptosis. Among them, PC1 interferes with the Hippo signalling pathways involved in cell proliferation and apoptosis, taking an active part in organ and tissue size control [95]. Last effectors of the Hippo signalling pathway, the transcriptional co-activators YAP (Yes-Associated Protein) and its ortholog TAZ, are localized in the nucleus of cystic cells, and phosphorylated to be sequestered in the cytoplasm of normal cells [293], [294]. Those transcriptional co-activators are also mechanosensors and mechanotransductors, as PC1 senses mechanical stimuli such as urine flow within the nephrotic tubules [76], [79], [80]. They could drive cyst growth, making them a target of interest to characterize the involvement of Hippo signalling pathway in cystogenesis process during ADPKD. Thus, YAP localization in PC1-depleted cell lines is also of great interest.

In the near future, it could be interesting to check the localization and the level of expression of those proteins after long-term culture within our tubular structures, and in response to a controlled and locally mechanical constraint on the tubes. Performing immunostaining experiments on tubes with the same markers already used on flat surfaces, the ADPKD cellular models epithelialization as well as their polarity could be investigated. Proteins and mRNA encoding those proteins could be isolated and collected for both cell types similarly cultured within the tubes made in collagen I with or without coating after collagen digestion. To this end, the cell extraction method has to be efficient in order to collect enough cell samples without

impairing them for the next biochemical assays. Going further, transcriptomic analyses on cells cultured within the tubes, under flow and local mechanical compression or not (control condition) could decipher cyst formation during ADPKD.

Moreover, we can deepen the characterization of the tubular scaffold lined with those cells, over time. Indeed, displaying a cystic behaviour, *Pkd1*$^{-/-}$ cells remodel the extracellular matrix and the basal membrane on which they lean on. Indeed, with a high proliferation rate and inversion of ion and fluid secretion, cysts affect their microenvironment, changing the collagen I and IV expression for instance, or the MMP-2 (metalloproteainase-2) localization [1], [282]. Degradation of the basement membrane and restructuration of the surrounding matrix could promote cyst formation and expansion from one tube to the adjacent ones [295]. In line with this idea, we noticed that *Pkd1*$^{-/-}$ cells tended to form branching out of the tubes (Chapter III) 2)). Therefore, the immunostaining of extracellular matrix proteins and metalloproteinase secreted by renal epithelial cells could be of interest to better understand, and characterize, cyst formation and propagation though the nephrotic tubes.

In line with this idea, and going further in the characterization of ADPKD cellular models, we noticed that cell area around tubes could be globally concave or convex, meaning towards the inner part of the tubes like a cavity, or in the opposite direction and rounded, respectively. Indeed, *Pkd1* cell lines, and more specifically *Pkd1*$^{+/-}$ cells, tend to shape branching towards the outer part of the tubes, like an invasion, as previously described. This analysis putting the scaffold invasion forth, realized with the help of a PhD student from the MMBM team (Institut Curie, UMR 168), Charles Cavaniol, was performed on Matlab. Briefly, relying on the same raw phase contrast images from which masks of cells and tubes edges were processed, he wrote a program to distinguish tubes shape over time (ongoing analysis).

b) ADPKD cellular models hallmarks: functional assays

In addition to the technological improvements we can realize to get closer to *in vivo*-like conditions, we can emphasize the biological aspects of ADPKD modelling within our kidney-on-chip.

We started to characterize their behaviour within the tubular structures, as summarized in the previous subsection. However, further experiments can be realized to assess the kidney-

on-chip recapitulation features, and to decipher the cystogenesis mechanisms during ADPKD. In particular, two aspects can be pursued in the near future: investigate the renal physiological functions on one hand, and refine the ADPKD cellular models behaviour within the tubes on the other hand.

Basic kidney-on-chip functionality:

To investigate the specific renal physiological functions, as performed in many other kidney-on-chip devices developed since a decade (cf.Chapter I) 3)), several assays can be realized [201], [217], [219], [223], [241], [242]. First, we can assess cell monolayer permeability, injecting a coloured and biocompatible solution such as dextran-FITC (70 kDa), inulin-FITC, BSA-FITC, or glucose-D labelled with Rhodamin dye. The last solution, in addition to evaluate cell layer integrity, also assesses the transport capacity of renal cells. Indeed, glucose uptake as well as albumin reabsorption are key aspects of renal epithelial cell functions. From the glucose uptake assay that is an apical transport, the glucose co-transporter SGLT-2 functions can be examined too. Moreover, the injection of specific drugs to inhibit glucose transporters, like quinine, would highlight the ADPKD cellular models functions within tubes [242].

Furthermore, cell viability within the system can be determined using a cell Live/Dead kit staining for instance, or labelings with AnnexinV or Propidium Iodide (PI) for apoptotic cell death. In addition to cell viability, cell proliferation is also important. To monitor it, it would be interesting to check the proliferation rate incubating the kidney-on-chip with EdU, or antibodies against Ki67 or PCNA, two proliferative markers. Among all those assays, the permeability test, the cell death and proliferation were explored. Unfortunately, as the immunostaining protocol in the tubes still needs to be optimized, we could not get relevant and obvious results within our multitube device.

Characterization of the ADPKD cellular models behaviour within the system:

Both *Pkd1* cell lines exhibit specific dynamics within the tubes molded in collagen I, and coated or not with laminin for more than 25 days. As $Pkd1^{+/-}$ cells lined tubes, filled them and slightly deformed them, $Pkd1^{-/-}$ cells highly proliferated in the tubes, filled them and significantly enlarged them.

However, at later stages, when cells reached a certain density within tubes, they slightly retracted them. Intrigued by these shape modifications, it could be of interest to examine whether tube contraction is due to the actin or microtubule cytoskeleton. To this end, drugs inhibitors like LatrunculinA or CytochalasinD, and nocodazole, respectively could be injected through the tubes. In line with this approach, to determine the forces exerted by the cells enlarging or shrinking the tubes, polyacrylamide microbeads could be embedded in the collagen I tubular scaffold, close to the tubes [296]. Those biocompatible beads, acting as stress sensors, could be functionalized to promote cell adhesion on their surface, which is not of interest in our case. With the possibility to adjust their mechanical properties (rigidity) and functionalized ligands on their surface, the forces exerted on the tubes could be measured through the microbeads size and volume at different time points, and locally. Of note, this method could also refine the interplay between the tubes lined with the homozygous cells, and could be used to quantify the mechanical forces involved. Hence, our current innovative multitube open system could allow those different approaches in order to recapitulate the kidney-on-chip basic functions, and to further characterize the ADPKD cellular models, corroborating the features of renal epithelial cells. Unfortunately, to perform those biological functional assays, an optimized and efficient flow system should be connected to the kidney-on-chip designed. Making some changes previously indicated, it would be easier to recapitulate the proximal tubule *in vivo*-like phenotype and functionalities: with polarity, and epithelialization markers, exhibiting biochemical and metabolic activities in a long-term perspective (ions and fluid reabsorption and secretion) [219].

c) ADPKD modelling: next steps

In vivo, ADPKD cysts are composed of $Pkd1^{+/-}$ and $Pkd1^{-/-}$ cells, in different proportions. In a significant proportion of cysts, cystogenesis is triggered by a second hit mutation, which leads to loss of the *Pkd1* functional allele and to the obtention of homozygous cells ($Pkd1^{-/-}$). ADPKD cysts exhibit more $Pkd1^{-/-}$ cells than $Pkd1^{+/-}$ cells when the disease symptoms appear.

Based on this knowledge, and to instigate formation of these primary cysts, stably transfected $Pkd1^{+/-}$ and $Pkd1^{-/-}$ cell lines were established. Expressing a construct labelling the actin cytoskeleton, two different fluorescent proteins were used. Generated by the BMBC

technological platform from Institut Curie (UMR 168), with the CRISPR-Cas9 biomolecular method, several clones of mCherry-beta-actin *Pkd1*$^{-/-}$ cells were obtained, as well as Lifeact-GFP *Pkd1*$^{+/-}$ and *Pkd1*$^{-/-}$ cells, and Lifeact-mScarlett *Pkd1*$^{+/-}$ cells. Several of these cell lines were successfully obtained only recently and could not be characterized in long-term experiments. It could be worthwhile and elegant to co-culture both cell types for the next experiments in order to trigger cystogenesis within the tubes made in collagen I. Another physiological way to drive cyst formation could be the induction of a second hit mutation, using a physical or chemical agent. Indeed, an increased flow rate within the tubes lined with the homozygous cells and/or the co-culture of both cell types. As chemical method, we can inject a drug to alter the renal epithelium, which could enhance this mechanism [95].

Keeping in mind this aspect, kidney-on-chip recapitulation implies several cell types interacting in the same microenvironment, like other kidney-on-chip models aforementioned in the Chapter I) 3) [217], [223], [241]. Keeping the same multitube device, mice fibroblasts could also be embedded in the collagen I scaffold surrounding the tubes lined with the ADPKD cellular models. Indeed, those cells secrete extracellular matrix components and growth factors (such as EGF) that could enhance our ADPKD cellular models metabolism, and further promote a physiological behaviour. In addition, adjusting the current design with independent inlets and outlets, we could alternatively co-culture endothelial cells to mimic the peritubular capillaries surrounding the tubes lined with renal epithelial cells, and *Pkd1* cells in the adjacent tubes. Creating a tubular epithelium-endothelium interface, this architecture could promote exchanges between two distinct compartments in close proximity. Nonetheless, another way to implement our kidney-on-chip could be to embed fibroblasts and endothelial cells within the collagen I tubular scaffold, before seeding the ADPKD cellular models within the tubes. The fibroblasts would secrete various proteins to remodel the scaffold microenvironment, while the endothelial cells could spontaneously shape to form vessels branching towards the tubes lined with the ADPKD cell lines. The cell culture medium for each cell type would probably be one of the limitation for this approach, as for the multiple-organ-on-chips issues met during their establishment.

Eventually, the dynamics of ADPKD cellular models can be daily visualized with live cell imaging acquisitions, an implementation that has already been demonstrated by Brice Lapin, the next PhD student who will pursue on this ambitious thesis project. Indeed, to better characterize the *Pkd1* cells behaviour within the tubes for short-time experiments,

videomicroscopy will be used. Several parameters will then be dynamically determined such as the cell colonization velocity, the cell colonization within the tubes, their orientation, and alignment. Besides, he will also further develop the microfluidic part to add flow within another prototype of our kidney-on-chip design.

Thus, the ADPKD modelling within our innovative multitube device raises several and different approaches, focusing on different aspects of this renal disorder. On one hand, the device modifications to get closer to the renal physiological conditions, with flow implementation and co-culture of different cell types would be of great interest. On the other hand, further characterizations of the ADPKD cellular models within this kidney-on-chip are necessary. With all those different adjustments, it would be possible to screen therapeutic drugs in order to reduce and inhibit the cystogenesis mechanism during ADPKD evolution in the future.

Conclusion:

Through this ambitious organ-on-chip PhD project I worked on during these three last years, we developed a novel kidney-on-chip to model the ADPKD, the most frequent inherited renal disorder. Starting from scratch, we focused on two main aspects of the project, and defined several interesting axes. Indeed, as an interdisciplinary topic, we first developed the microphysiological platform, before starting to reproduce ADPKD hallmarks in it.

In the first chapter, we described the organ-on-chip field, before scrutinizing on the kidney-on-chip domain last technological innovation compared to our design. As disease modelling are not widely studied, in particular renal diseases in appropriate three-dimensional architecture, we relied on the current kidney-on-chip models to design ours. Indeed, we managed to design two functional and innovative microphysiological devices with key renal features, the second one being an improvement of the first one, and detailed in the chapter II.

This kidney-on-chip is composed of micrometric and circular aligned multitubes, regularly spaced, and parallely disposed on a rigid base made in COC, a copolymer. Relying on the technique of wire molding in collagen I, the tubular scaffold can be seeded with the ADPKD cellular models. The multitubes, made in the one of the most abundant proteins of the

conjunctive tissue composing the kidney, joined to end up on one inlet and an outlet. This structure neither promotes a controlled and equivalent flow within each tube, nor eases the biological assays described in the chapter IV. Nevertheless, these dimensions for tubes, and their vicinity has not been achieved yet in other studies. Moreover, as an open and small device easy to handle, the materials used favour imaging acquisitions and initiate new possibilities. Succeeding to grow another epithelial renal cell line (MDCK) within this scaffold, we gradually implemented the tube composition. We added basal membrane proteins to coat the tubes and reproduce the membrane on which renal epithelial cells lean on, in the nephrons. Thus, as other kidney-on-chips developed, our microphysiological device displays advantages and drawbacks.

Pursuing on this aspect, we next focused on the ADPKD cellular models behaviour on 2D flat surfaces, and in our three-dimensional tubular architecture. Highlighting the cystogenesis mechanism on flat surface, we next observed the behaviour of ADPKD cellular models within the tubes. Both cell lines displayed two distinct behaviours: the heterozygous cell line proliferated and slightly deformed the tubes in around 20 days, while the homozygous cells quickly lined with and filled the tubes. Starting to enlarge them in around 10 days, they kept proliferating and distorting the tubes. After 25 days, they slightly retracted the tubes pulling on them or dying within them, which could promote tubes slight collapsing. It is worthwhile that *Pkd1*$^{-/-}$ cells grew faster than *Pkd1*$^{+/-}$ cells, and exhibited a cystic behaviour. Moreover, it turned out that the ADPKD cellular models lined and proliferated similarly with tubes coated with laminin or Matrigel, or only in collagen I. Nonetheless, it is interesting to note that the cells grew more steadily on the laminin coating than on collagen I tubes without coating.

Furthermore, in the chapter III, the intracellular organization of *Pkd1* cells was characterized through preliminary immunofluorescence images acquisition. Focusing on the tubular structure geometry depending on the cell type, we highlighted the circular shape of the tubes seeded with each of the ADPKD cell line. Albeit the *Pkd1*$^{+/-}$ cells slightly flattened the tubes and the *Pkd1*$^{-/-}$ cells enlarged the tubes, both cell types exhibited a well-defined cuboidal shape lining with the tubes.

Hence, during this study, a novel kidney-on-chip with key structural features was developed in order to reproduce the ADPKD major hallmarks: the formation and propagation of renal cyst, relying on the Snowball effect theory. Adding a flow system and a controlled, local constraint on the tubes, we will be able to mimic those aspects in the near future.

Annexes

TABLE OF CONTENTS

Annex 1: Cell culture

1) Cell passage protocol

Regarding the ADPKD cellular models, three cell lines were selected. Two of them carry a conditional allele in the *Pkd1* gene associated with the Immortomouse transgene, while the Wild-type one was obtained in a standard way, by another team.

The first cell line is a control cell line derived from 5-6 weeks old C57Bl/6 mice, and were kindly given by E.Honoré and A.Patel team, from Sophia Antipolis. Briefly, kidneys from wild-type mice were microdissected under sterile conditions to isolate nephrons (Fig.1A). The mouse primary PCT cells were then extracted by hand, under binoculars, and transfected with the SV3-neo plasmid. They were cultured in equal amount of DMEM and F12 (GIBCO) medium supplemented with: 15 mM NaHCO3, 20 mM HEPES adjusted at pH 7.4, 1% FBS (Fetal Bovin Serum from ThermoFisher), 2 mM glutamine, 5 µg/ml insulin (Sigma, ref. I6634), 50 nM dexamethasone (Sigma, ref. D4902), 1 µg/l epidermal growth factor (Sigma, ref. E4127), 5 mg/l transferrin (Sigma, T1283), 30 nM sodium selenite (Sigma, ref.S9133), and 10 nM triiodo-L-thyronine (Sigma, ref. T6397) and 125 µg/ml G418 (Sigma, ref.10131-019) [1], [2].

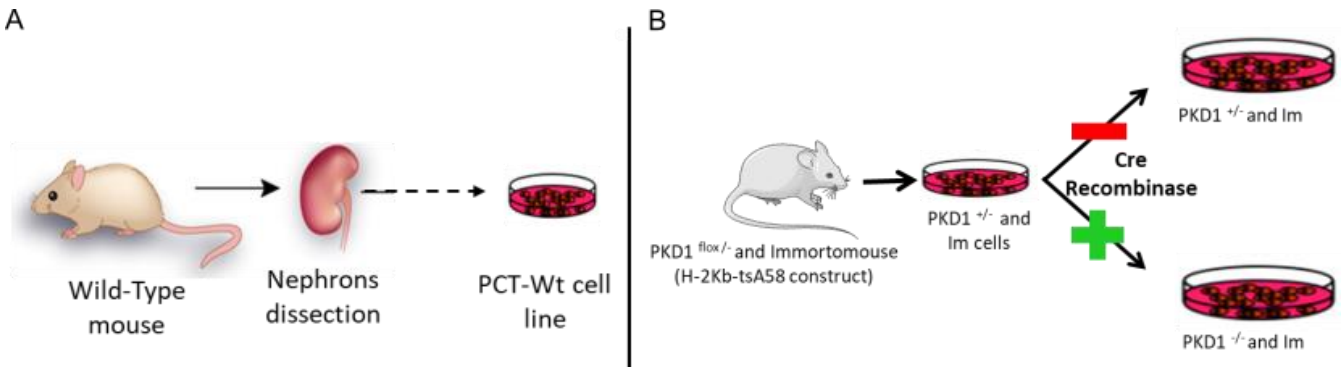

Figure 1: Schematics illustrating the obtention of the cell lines used. A: PCT-Wt cells deriving from wild-type mice, and transfected with SV3-neo plasmid. B: Diagram representing the main steps to obtain *Pkd1* cells used as ADPKD cellular models.

Cells were daily cultured in a T25 flask, and maintained at 37°C, in a 5%CO_2-95% air water-saturated atmosphere. Cells were passaged two times a week, when they reached around 70-80% of confluence. They were rinsed two times with DPBS (Dulbecco's Phosphate

Buffered Saline from Sigma), and trypsinized with 2 ml of 0.05% Trypsin- ethylenediamine tetraacetic acid (EDTA) (Sigma) at 37°C, during 5 minutes in the incubator. Trypsine was then inhibited with 2 ml of medium, and the cell suspension was centrifuged 3 minutes at 1000 rpm to remove the remaining trypsine. Cells were resuspended in 4 ml of medium, and diluted at fiftieth in 5 ml of medium. Every two days, the medium was changed.

Furthermore, two cell lines obtained from a single mouse carrying a conditional allele for *Pkd1* gene in association with the Immortomouse (H-2Kb-tsA58) transgene previously described were used to reproduce the ADPKD hallmarks [1]. Those cell lines are a gift from S.Somlo team, working at Yale New Haven Hospital in the USA. In a few words, PCT cells from the $Pkd1^{flox/-}$ clone were isolated and transiently transfected or not with the Cre recombinase enzyme in order to get the $Pkd1^{-/-}$ or $Pkd1^{+/-}$ cell lines, respectively (Fig.1B). The null cells (PN24) or *Pkd1*-depleted cells, as well as the heterozygous cell line (PH2), were maintained in culture in two types of medium: the proliferation medium composed of 3% of SVF and γ–interferon, a cytokine activating the Immortomouse transgene, and the differentiation containing less SVF (only 1%) and devoid of γ–interferon to reduce the proliferation rate. Under expansion condition, cells were put in the proliferation medium composed of equal amount of DMEM and F12 (GIBCO) medium supplemented with: 3% FBS, 5 mg/ml γ–interferon (Millipore, ref.IF005), 7.5 nM sodium selenite (S9133), 1.9 nM Triiodo-L-Thyronine (T6397), 5 mg/ml insulin (I6634), 5 mg/ml transferrin (T1283), 100 u/ml penicillin- streptomycin, 5 ml/ml nystatin (N1638) (all products from Sigma-Aldrich), at 33°C with 5% CO_2. Cells were changed to the differentiation medium containing the same supplements, but only 1% FBS and γ–interferon-free to inhibit large T antigen expression from the Immortomouse construct, and favor cells epithelialization. Cells were cultured in this medium 7 days before using them in the experiments, at 37°C with 5% CO_2 [1], [2]. Besides, qPCR experiments confirmed the depletion of *Pkd1* gene in the $Pkd1^{-/-}$ cells.

For daily culture, cells were maintained in the proliferation medium at 33°C, in a 5%CO_2-95% air water-saturated atmosphere, in a T75 flask. Cells were passaged twice a week, when they reached around 70-80% of confluence. They were rinsed twice with DPBS (Dulbecco's Phosphate Buffered Saline from Sigma), and split with 2 ml of 0.05% Trypsin- ethylenediamine tetraacetic acid (EDTA) (Sigma) at 33°C, during 10 minutes in the incubator for the $Pkd1^{+/-}$ cells, and 10 minutes for the null cells. Trypsin was then neutralized in 2 ml of proliferation medium, and the cell suspension was centrifuged 3 minutes at 1000 rpm to remove the

remaining trypsin. Cells were resuspended in 4 ml of medium, and diluted at fiftieth in 10 ml of medium for both cell lines. Moreover, cells were resuspended in 4 ml of differentiation medium, and diluted at tenth in 10 ml of medium for the heterozygous cells, and at twentieth for the homozygous cell line. Every two days, both mediums were changed with 10 ml of fresh medium.

The three cell lines were used at a low passage in the different experiments: mostly between passage 6 and 20.

On another note, MDCK-Lifeact-GFP cells were used to implement the kidney-on-chip designed. The Madin-Darby canine kidney cell line also express the Lifeact-GFP construct to stably label filamentous actin. Generated in the laboratory by the BMBC platform, those cells were grown in DMEM medium containing 10% FBS and 0.8% G418 (10131-019) (both from Sigma). Maintained at 37°C, in 5%CO_2 atmosphere, in a T75 flask, cells were split two twice a week, when they reached around 70-80% of confluence. They were rinsed twice with DPBS (Dulbecco's Phosphate Buffered Saline from Sigma), and trypsinized with 2 ml of 0.05% Trypsin- ethylenediamine tetraacetic acid (EDTA) (Sigma) at 37°C, during 10-15 minutes in the incubator. Trypsin was then neutralized in 2 ml of medium, and the cell suspension was centrifuged 3 minutes at 1000 rpm to remove the remaining trypsin. Cells were resuspended in 4 ml of medium, and diluted at thirtieth in 10 ml of medium, that was changed every two days. Those cells were used until passage 20.

2) Cell seeding in 2D and 3D

The four renal cell lines were split as previously described, and 20 µl of the cell suspension was diluted in DPBS at tenth. The dilution was then counted with a cell counter (model Scepter from Millipore). Cells were then plated on a flat surface or within the tubes, which did not rely on the same initial cell density.

On glass coverslips, or the bottom part of well-plate, covered or not with a coating protein composing the basal membrane (laminin, Matrigel, collagen IV) or collagen I, the initial cell density seeded varied between 5.10^3 and 80.10^4 cell/ml, depending on the experiment realized (cf.Chapter III) 1) and 2)). In the well plates used for the coating test, *Pkd1*$^{+/-}$ cells were seeded at 2.10^5 cells/ml while the initial *Pkd1*$^{-/-}$ cell density was 1.10^5 cells/ml.

Within the tubular scaffold made in collagen I, MDCK cells were seeded at an initial cell density of 5.10^6 cell/ml. However, this step was not reproducible and efficient: cells randomly crossed one tube or several tubes at the same time at the expense of other tubes. This crucial step ended up with heterogeneous cell distribution within the tubes. Moreover, albeit the seeding occurred, cells went rashly through the tubes, which sometimes prevented them from staying and adhering to the tube walls. To address this issue in the following tunings, the suspension of *Pkd1* cells at 5.10^6 cells/ml in the culture medium was supplemented with 4% dextran (70kDa, Sigma) to increase the medium viscosity, and enable fine monitoring of the seeding process [3]. Dextran addition slightly slowed down cells, and in particular $Pkd1^{-/-}$ cells, that are smaller than the $Pkd1^{+/-}$, within the tubes. Other details about the procedure to seed cells in the kidney-on-chip are given in the annex 3.

3) Coating protocol on flat surface

The coating test was realized on 24-well plates with glass bottom, with collagen I and several proteins composing the basal membrane. Wells were previously pre-treated with a silane to cross-link the hydrogel to the surface. Briefly, wells were incubated with 500µl of a solution of 2% APTES diluted in DPBS for 30 minutes. They were then washed with 500 µl of water three times during 5 minutes each, before being incubated with 500 µl solution of 0.5% glutaraldehyde diluted in DPBS for 30 minutes. All those steps were realized at room temperature. Eventually, wells were washed with water again, and let in 500 µl of water overnight, at 4°C. Water was removed just before coating proteins deposition in the bottom well.

Different proteins were used: laminin from mouse (1 mg/ml, LifeTechnologies), collagen IV (1 mg/ml), Matrigel (BD), collagen I (between 8 and 12 mg/ml, Corning). The proteins were previously diluted in the differentiation medium at the following concentrations: the collagen I and IV from rat tail were mixed with PBS10X (D1408, Sigma) and NaOH 1N (S2770, Sigma) to reach 6 mg/ml and a pH of 7.4 respectively, laminin at 0.02 mg/ml and Matrigel was twofold diluted. A collagen I volume of 200 µl uniformly covered the bottom of each well, and the well plate was incubated at 37°C, in 5% CO_2 atmosphere for 2 hours. This first layer is either covered with a volume of 100 µl of the different proteins, or 500 µl of PBS for the control wells with collagen I only. Again, the well plate was incubated at 37°C, in 5% CO_2 atmosphere for 30 minutes. After washing with 500 µl of DPBS, cells were seeded on top of the coatings and put

in the incubator, at 37°C, in 5% CO_2 atmosphere for 2 days. The thin layer of proteins was gently and homogeneously distributed with circular movements.

Annex 2: Cell immunostaining

1) Immunostaining protocol in 2D

Cells were washed three times with PBS containing $CaCl_2$ and $MgCl_2$, then fixed with 4% paraformaldehyde (PFA) for 10 minutes at room temperature. Permeabilized with 0.1% Triton X-100 (LifeTechnologies) diluted in PBS for 5 minutes, cells were washed again three times with PBS to remove Triton X-100. Cells were then blocked in a solution of PBS with 1% BSA-0.01% Tween 20 for 2 hours at room temperature, and under humidified atmosphere. Primary antibodies were then applied for 1 hour, at room temperature, and under humidified atmosphere. After three washing steps in the same buffer, fluorescently labeled secondary antibodies were incubated with cells, in a humidified chamber and at room temperature for 30 minutes. Rinsed three times with PBS, cells were then mounted with Shandon Immu-Mount (Fisher Scientific) medium and observed under a confocal microscope (Leica, IPGG Imaging platform). Images acquired were analyzed on ImageJ software.

Primary antibodies: 2D

Name	Generated in...	Dilution factor
ZO-1	Rabbit	100
E-cadherin	Mouse	100
Polyclonal N-Cadherin	Mouse	20
Monoclonal N-cadherin CDH2	Mouse	100
Na/K ATPase	Rabbit	500
Vinculin	Mouse	100
Aquaporin	Mouse	100
Ezrin	Rabbit	200
Arl13b	Rabbit	100
Occludin	Mouse	250
Na/K ATPase	Mouse	20
Ki67	Rabbit	200

Secondary antibodies and additional labellings: 2D

Name	Generated in...	Dilution factor
Mouse IgG	Alexa fluor 488	500
Rabbit IgG	Alexa fluor 488	500
Mouse IgG	Alexa fluor 555	500
Rabbit IgG	Alexa fluor 555	500
Phalloidin	TRITC	500
Phalloidin	FITC	500
	Hoechst	1000
Na/K ATPase-555	Souris	125
Annexin-V-633		100
	Hoechst	1000

Primary antibodies: 3D

Name	Generated in...	Dilution factor
ZO-1	Mouse	50

Secondary antibodies and additional labellings: 3D

Name	Generated in...	Dilution factor
Mouse IgG	Alexa fluor 647	100
Mouse IgG	Alexa fluor 488	100
Mouse IgG	Hoechst	1000
Phalloidin	TRITC	500
	Hoechst	1000

Figure 2: Tables summarizing antibodies tested. A: In 2D on glass coverslips or on coated wells. B: Within tubes in the kidney-on-chips to characterize *Pkd1*$^{+/-}$ and $^{-/-}$ cell lines.

2) Immunostaining protocol in 3D

Similar steps were realized to stain *Pkd1* cells lining the tubes. Nonetheless, each step needed a longer period, and the buffers composition was different.

Chips were washed three times with PBS containing $CaCl_2$ and $MgCl_2$, then fixed with 4% paraformaldehyde (PFA) for 15 minutes at room temperature: 3 ml of each solution were successively deposited on collagen I. Carefully detached from the COC surface (cf. details Chapter III), the collagen I scaffold was then immersed in a permeabilization buffer composed of 0.1% Triton X-100 (LifeTechnologies) and 2% BSA diluted in PBS for 5 minutes. The collagen I scaffold was then washed again three times with PBS to remove Triton X-100, and blocked in a solution of PBS with 4% BSA-0.1% Tween 20 for 2 hours at room temperature, and under humidified atmosphere. Primary antibodies were then incubated for 1 hour, at room temperature, or over night at 4°C and under humidified atmosphere. After three washing in 2%BSA-0.1% Tween 20 diluted in PBS, fluorescent labeled secondary antibodies were incubated with the tubular scaffold, in a humidified chamber and at room temperature for 45 minutes. Between the primary and secondary antibodies incubation steps, collagen I was washed twice with a solution of 2%BSA-0.1% Tween 20 in PBS. Rinsed three times with the blocking buffer for thirty minutes, the collagen I scaffold was then mounted with the VectaShield mounting medium (Vector Laboratories) in a homemade PDMS chamber, as aforementioned in the chapter III, and observed under a confocal microscope (Zeiss, BDD Imaging platform from Institut Curie). Images acquired were analyzed on ImageJ software.

Annex 3: Chip fabrication

1) Fabrication of the chip

To decipher the cystogenesis mechanism during ADPKD, and more particularly early steps which are the formation and the propagation of renal cysts from one tubule to the adjacent one, we designed an innovative multitube device described in the chapter II. Open and composed of microcircular tubes regularly spaced and parallely aligned, those tubes were molded in collagen I according to the following steps (Fig.3).

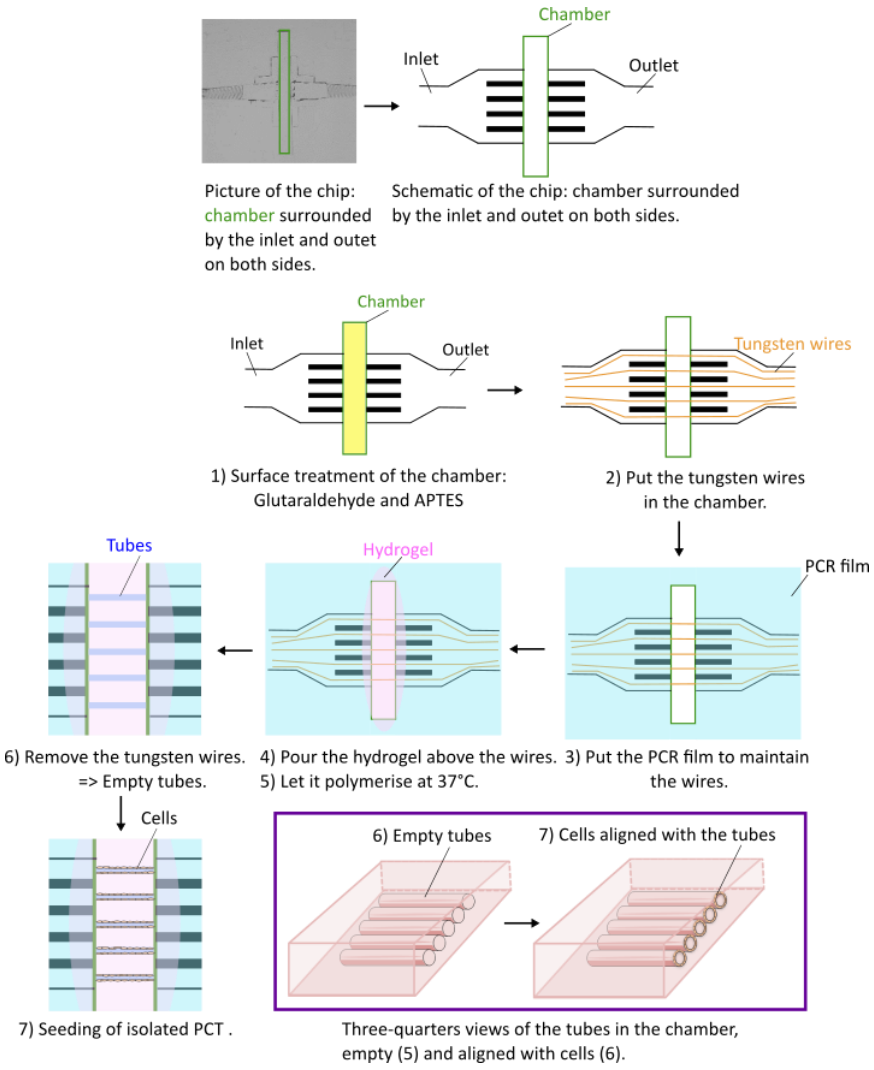

Figure 3: Schematic illustrating the different steps to make the chip, from the surface treatment to the seeding step. On top, picture and drawing representing the chip patterns with the central chamber and the connectors on both sides. On the bottom, the purple framed depicted empty tubes, and tubes lined with cells.

The chip, made in COC (Cyclic Olefin Copolymer), a transparent and rigid copolymer of 2 mm thickness, displayed an optimal optical index to visualize the tubes lining cells behavior above or below, under a microscope. This COC piece of 4cm x 2cm consisted of a central chamber of 300 µm depth in which the tubes were molded in collagen I, and surrounded by two set of five grooves in which the wires to mold the tubes were positioned, and going on with two connectors through which liquids and cells were injected (Fig.3, black rectangles).

The chamber surface was treated with a silane in order to allow collagen I covalent adhesion, whatever the cell forces exerted on the tubular scaffold and over time. Using a yellow scotch tape to delineate the chamber, this one was first incubated with 50 µl of 2% APTES diluted in PBS during thirty minutes, at room temperature. After three washing steps during five minute with deionized water, the chamber was then incubated with 50 µl of 0.5% glutaraldehyde in PBS during thirty minutes at room temperature. The chamber was washed twice in deionized water before immersing it in water, and incubating it at 4°C over night. The following day, tungsten wires of 80 µm diameter were incubated in 1%BSA-PBS buffer during thirty minutes at room temperature. They were then put within silicon tubings themselves bonded on the connectors with epoxy glue (Sader). Tungsten wires were next gently and manually disposed within the parallel, regularly spaced and aligned grooves of the chamber, under a binocular magnifier. Anchored on the COC chip with a PCR film open at the chamber position, the chamber and its connectors were then incubated in degassed and filtered PBS for one hour, at 37°C [5]. Indeed, the degassed PBS absorbed bubbles forming at the grooves position in order to decrease their formation during collagen I polymerization. Moreover, to avoid thermal shock between the collagen I mix prepared at 4°C and the chamber surface covered with PBS at 37°C, the chip was placed at 4°C for fifteen minutes. Afterwards, the degassed PBS was removed and replaced with the collagen I mix, gently poured above the open chamber. The collagen I polymerized at 37°C, in 5% CO_2 atmosphere and under humidified atmosphere for two hours, before placing a PBS droplet above it to keep it wet. This last step was crucial to shape empty tubes. Eventually, after collagen I polymerization, wires were gently removed through the connectors in order to get empty microcircular tubes through which cells were seeded and followed during several weeks. After the cell seeding, the chip was immersed in 6 ml of cell culture medium, in a Petri dish placed in the incubator, at 37°C, 5% CO_2 atmosphere. The medium was changed every two days.

2) Collagen I and coating proteins mixing

Several biocompatible hydrogels were assessed before selecting collagen I, one of the main component of the extracellular matrix (ECM), in which tubes were molded. Indeed, the stiffness of the chip (range of 5-10 kPa), its porosity as well as its composition have to be as close as possible to the extracellular matrix of nephrons in order to reach an adequate biomimetic system.

For this purpose, a mix composed of collagen I (Corning), PBS10X, NaOH 1N and distilled water was gently combined with a spatula on ice, at 4°C. Especially sensitive to temperature changes, the collagen I mix was continuously kept at 4°C. Indeed, large collagen I fibers indicating stiffness and porosity modifications of the collagen I could appear when the polymerization begins at room temperature. Moreover, to avoid bubbles formation during the polymerization step, the collagen I mix was centrifuged less than thirty seconds to degas it. Eventually, 80 µl of this mix was carefully poured in the central chamber, around the wires. The whole set-up was then incubated at 37°C, 5% CO_2 atmosphere, and under humidified atmosphere for two hours before wires removal.

Once empty tubes in collagen I were shaped, they were covered with a thin layer of different proteins composing the ECM for one hour, at 37°C, before cell seeding. Indeed, the basal membrane play a significant role in cell proliferation, growth and adhesion [6]. Several proteins were individually investigated: collagen IV (main component of the ECM), laminin and Matrigel composed of many different proteins. To this end, laminin coupled or not with a fluorescent dye was diluted in culture medium (0.02 mg/ml), as well as Matrigel (50:50). Collagen IV was mixed with water and NaOH 1N to reach a final concentration of 0.5 mg/ml. An acid acetic solution was used to adjust its pH to 7.4 (neutral pH). Afterwards, 50 µl of those different coating proteins were injected within the collagen I tubes. The chip was then immersed in PBS, and incubated at 37°C, under humidified atmosphere, with 5% CO2 for one hour. The tubes were finally washed twice with PBS, and seeded.

3) Cell seeding within the tubes

The cell seeding process was progressively improved: first realized with MDCK cells, it was then performed with the ADPKD cellular models, using another method.

Briefly, all the cell lines were trypsinized in parallel, and concentrated at 5.10^6 cells/ml in the appropriate culture medium. The MDCK cells were directly and carefully injected by hand within the tubes. However, they quickly crossed the tubes, decreasing the cell adhesion probability on the tubes walls. Consequently, *Pkd1* cells that were smaller after the trypsinization step, were concentrated at 5.10^6 cells/ml in differentiation medium mixed with 4% Dextran (70kDa). They were slowly and gently injected manually in the tubes, with a pipette, to prevent air bubbles entry as much as possible with a liquid-liquid interface between the connector and the pipette tip. The seeding was usually realized on both sides of the chip, through the two connectors.

Annex 4: Data analysis

1) 3D tubular structures analyses: masks drawing

To analyze the cells behavior over time and investigate different parameters (cell density, mean tube diameter, minimal and maximal of the mean tubes diameter, as well as the intertube distance), phase contrast images of the same chip were acquired at different time points. From these raw images, a 2D projection of cells and tubes edges were drawn on a tablet, and processed

```
// Written by I.Bonnet
// January 2019

// Purpose: Sarah Myram
// Draw Contour of channel for each slices of all stacks in a given folder

// Sanity clearing
run("Close All");


// User selects the file to analyze
path = File.openDialog("Select an image file");
inputdir = File.getParent(path);
filenameWithExt = File.getName(path);
filenameWithOutExt = File.nameWithoutExtension;



// for a single file
DrawChannelContours(inputdir, filenameWithExt);

// Define a function that executes DrawChannelContours
function DrawChannelContours(inputdir, file) {
        // REMOVE SUFFIX FROM FILENAME
        dotIndex = indexOf(file, ".");
        filename = substring(file, 0, dotIndex);

        // OPEN STACK
        open(inputdir +File.separator+ file);
        nbslices = nSlices;
        close();

        //ASK USER HOW MANY CHANNELS
        //nbchannel= getNumber("How many channel for this stack ?", 3);

        // DRAW ROI
        for (kk=1; kk<=nbslices;kk++) {
            open(inputdir+File.separator+file,kk);
            //Stack.setSlice(kk);;
            setTool("freehand");
            //waitForUser("Mask", "Draw the contour of the " + nbchannel+ " channels");
            waitForUser("Mask", "Draw the contour of the channels");
            setForegroundColor(255, 255, 255);
            run("Fill", "slice");
            setBackgroundColor(0, 0, 0);
            run("Clear Outside");
            run("Make Binary");
            run("Invert LUT");
            run("Duplicate...", "use");
            rename("tempo" + kk);
            wait(500);
  }

        //SAVE
        run("Images to Stack", "name=Stack title=tempo use");
        saveAs("Tiff", inputdir+File.separator+"Mask_"+ filenameWithOutExt);
        close();
}

run("Close All");

```

Figure 4: ImageJ program written by Isabelle Bonnet to draw the tubes edges, and cells area within the tubes, and create binary masks.

into binary masks thanks to an ImageJ program developed by Isabelle Bonnet (researcher in the PBME team, Institut Curie, UMR168) (Fig.4).

The two types of masks, cells or tubes edges, were then analysed with a homemade program written on Matlab by Sylvie Coscoy (researcher in the PBME team, Institut Curie, UMR168) and described below.

2) 3D tubular structures analyses: 2D images projection

After acquisition of time movies (Δt=2-5 days, *typical images in fig. 5A*), masks of tube contours *(example in fig.5B, left, day1 corresponding to fig. 5A)* and masks of regions filled with cells *(example in fig.5B, right)* were drawn thanks to a CINTIQ drawing tablet and a home-written ImageJ macro. Superimposed images of mask_tubes (green) and mask_cells (red) are shown in *Fig. 5C*: the yellow part corresponds to cells present in tubes, the green part inside tubes to empty tube regions, the red part above or under tube "invasion" (protrusions or cells extending in collagen matrix, see *fig. 5H*). The analysis shown here is focused on the part of tubes that is common to all tubes and all times (*Fig. 5D, left*), although total individual tube data (*fig. 5D, left*) were also collected, with only marginal differences for the different results.

A home-written Matlab softwares was used for data analysis (local tube diameters *(fig. 5E)*, cell densities (*fig. 5F*), intertube distances (*fig. 5G*), in function of the *x* position along the tube (for each pixel, with pixel size=1.65 μm), invasive area (*fig. 5H*) and derived statistics).

In more details: first, for a given stack, horizontal contours were extracted from tube masks for diameter analysis (*fig. 5E*), with the approximation that tubes were revolution surfaces and that the projection visible on images corresponded to local cylinder diameter. For cell density *(fig. 5F)* and invasion *(fig. 5H)* analysis, we determined the intersection between cell masks and tube masks (cell areas inside tubes), and cell masks with the exclusion of this intersection (cell invasion); global areas were calculated, as well as local cell densities (in function of *x*), defined as the sum of contributions of the different cell masks (cell density between 0 and 1, with 1 corresponding to local confluency, *fig. 5F*).

Data generated by the analysis of individual stacks were afterwards aggregated for global statistics. Tubes with wire left after cell seeding were treated separately. Tubes with

important deformations at initial times were excluded for the analysis (for the whole analysis, it concerned 25 out of 48X5 = 240 tubes).

Mean diameters or densities correspond to following sequential operations: 1. mean of each tube local diameters along x; 2. for each time, mean on the selected tubes in each individual chip; 3. for each time bin (]0 3[days, [3 6[days…), mean of the different values if the considered chip has several time points in the considered bin, 4. mean and s.e.m. of the different chips.

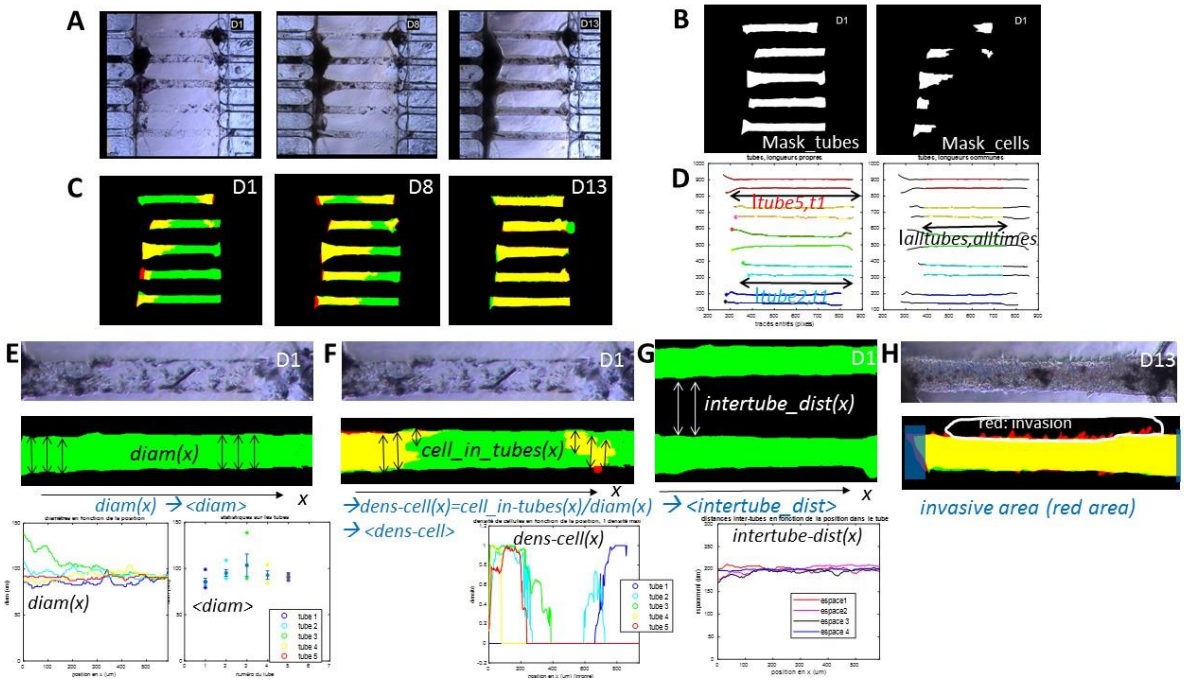

Figure 5: Illustration for tube analysis method.

3) 3D images processing: tubes geometry

Immunofluorescence experiments realized within tubes seeded with *Pkd1* cells were analyzed with an ImageJ macro developed by an engineer from the IPGG technological platform, Bertrand Cinquin (cf. description in the Chapter III). Using confocal images, the cell layer area, the tube perimeter and circularity were assessed (Fig.6). In the near future, it will also be possible to determine cell density within the tubes, in addition to tube spacing.

```
//Denoising
run("Enhance Local Contrast (CLAHE)", "blocksize=127 histogram=256 maximum=3 mask=*None*");
run("Subtract Background...", "rolling=30 stack");

//Select the tube
run("Properties...", "channels=1 slices="+nSlices+" frames=1 unit=microns pixel_width=0.32 pixel_height=0.32 voxel_depth=5");
run("Reslice [/]...", "output=5.000 start=Top avoid");
makeRectangle(512, 0, 1024, 30);
//Manually change the rectangle to fit the tube
run("Duplicate...", "title=[Reslice of Actin_SkeletonPruned-ROI2] duplicate");
//La suite du code doit être sélectionner et lancer entièrement pour fonctionner…
Name = "Reslice of Actin_SkeletonPruned-ROI2";
selectWindow(Name);
for (i = 1; i < nSlices; i++) {
                setSlice(i);
                setAutoThreshold("Default dark");
                run("Measure");
                selectWindow("Results");
                Int = getResult("Mean", i-1);
                selectWindow(Name);
                if (Int != 0) {
                                CanalEllipse();
                }

}

 //Fit Ellipse function
function CanalEllipse(){

run("Create Selection");
run("Convex Hull");
run("Fit Ellipse");
roiManager("add");
}

//Draw Tube Enveloppe
newImage("Tube Enveloppe2", "8-bit black", 512, 29, nSlices);
for (i = 1; i < roiManager("count"); i++) {
                roiManager("Select",i);
                setSlice(i+1);
                run("Draw",  "slice");
}
run("Select All");
run("Reslice [/]...", "output=1.000 start=Top avoid");



//Dessine le graph Area Ellipse
selectWindow("Results");

EllipseArray = newArray(nResults);
Length = newArray(nResults);
for (i = 0; i < nResults; i++) {

EllipseArray[i] = getResult("Area",i);
Length[i] = i*0.5;
}
Plot.create("Tube Area", "Length (µm)", "TubeArea (µm²)", Length, EllipseArray);
```

Figure 6: ImageJ program written by Bertrand Cinquin to analyze 3D confocal images of tubes geometry lined with *Pkd1* cells. Another version implemented to the cell density and tubes spacing was also realized but not shown here.

Bibliography:

[1] J. Ghata and B. D. Cowley, “Polycystic kidney disease,” *Compr. Physiol.*, vol. 7, no. 3, pp. 945–975, 2017.

[2] A. Li, “Diagnosis and Treatment Status and Progress of Autosomal Dominant Polycystic Kidney Disease -,” vol. 3, no. November, pp. 40–45, 2017.

[3] S. Ahadian *et al.*, “Organ-On-A-Chip Platforms: A Convergence of Advanced Materials, Cells, and Microscale Technologies,” *Adv. Healthc. Mater.*, vol. 7, no. 2, pp. 1–53, 2018.

[4] D. W. Fishman, Alfred P.Richards, *Circulation of the bood: men and ideas*. 1982.

[5] W. Bowman, “On the Structure and Use of the Malpighian Bodies of the Kidney, with Observations on the Circulation through That Gland.,” *Proc. R. Soc. London*, vol. 4, no. 0, pp. 374–377, 1837.

[6] and G. H. G. Carl W. Gottschalk, Robert W. Berliner, *Renal physiology: people and ideas*. .

[7] R. L. Jamison, “Resolving an 80-yr-old controversy: the beginning of the modern era of renal physiology,” *Adv. Physiol. Educ.*, vol. 38, no. 4, pp. 286–295, 2014.

[8] Tortora, Derrickson, G. J., and Bryan, *Principles of Anatomy & Physiology, Cardiovascular System: Blood Vessels and Hemodynamics". Principles of Anatomy & Physiology (13th ed.). John Wiley & Sons. p. 816. ISBN 978-0470-56510-0*. 2012.

[9] A. J. Vander Douglas Eaton, John Pooler, *Vander ’ s Renal Physiology*. 2009.

[10] C. J.Lote, “PRINCIPLES OF RENAL PHYSIOLOGY, 4TH EDITION,” *Shock*, vol. 15, no. 1, p. 80, Jan. 2001.

[11] H. C. Chapin and M. J. Caplan, “The cell biology of polycystic kidney disease,” *Journal of Cell Biology*, vol. 191, no. 4. pp. 701–710, 2010.

[12] E. Cornec-Le Gall, M.-P. Audrézet, Y. Le Meur, J.-M. Chen, and C. Férec, “Genetics and pathogenesis of autosomal dominant polycystic kidney disease: 20 years on.,” *Hum. Mutat.*, vol. 35, no. 12, pp. 1393–406, 2014.

[13] E. Cornec-Le Gall, A. Alam, and R. D. Perrone, “Autosomal dominant polycystic kidney disease,” *Lancet*, vol. 393, no. 10174, pp. 919–935, 2019.

[14] T. Mochizuki, K. Tsuchiya, and K. Nitta, “Autosomal dominant polycystic kidney disease: Recent advances in pathogenesis and potential therapies,” *Clinical and Experimental Nephrology*, vol. 17, no. 3. pp. 317–326, 2013.

[15] E. C.-L. Gall *et al.*, “The PROPKD score: A new algorithm to predict renal survival in autosomal dominant polycystic kidney disease,” *J. Am. Soc. Nephrol.*, vol. 27, no. 3, pp.

942–951, 2016.

[16] E. C.-L. Gall *et al.*, “Type of PKD1 mutation influences renal outcome in ADPKD,” *J. Am. Soc. Nephrol.*, vol. 24, no. 6, pp. 1006–1013, 2013.

[17] K. Hopp *et al.*, “Functional polycystin-1 dosage governs autosomal dominant polycystic kidney disease severity,” *J. Clin. Invest.*, vol. 122, no. 11, pp. 4257–4273, Nov. 2012.

[18] S. V. Fedeles *et al.*, “A genetic interaction network of five genes for human polycystic kidney and liver diseases defines polycystin-1 as the central determinant of cyst formation,” in *Nature Genetics*, 2011, vol. 43, no. 7, pp. 639–647.

[19] Y. H. Hwang *et al.*, “Refining genotype-phenotype correlation in autosomal dominant polycystic kidney disease,” *J. Am. Soc. Nephrol.*, vol. 27, no. 6, pp. 1861–1868, Jun. 2016.

[20] G. M. Fick *et al.*, “Characteristics of very early onset autosomal dominant polycystic kidney disease,” *Pediatr. Nephrol.*, vol. 7, no. 6, p. 757, Dec. 1993.

[21] K. Zerres, S. Rudnik-Schoneborn, and F. Deget, “Childhood onset autosomal dominant polycystic kidney disease in sibs: clinical picture and recurrence risk. German Working Group on Paediatric Nephrology (Arbeitsgemeinschaft fur Padiatrische Nephrologie.,” *J. Med. Genet.*, vol. 30, no. 7, pp. 583–588, Jul. 1993.

[22] W. N. Leonhard *et al.*, “Scattered Deletion of PKD1 in Kidneys Causes a Cystic Snowball Effect and Recapitulates Polycystic Kidney Disease,” *J. Am. Soc. Nephrol.*, vol. 26, no. 6, pp. 1322–1333, 2015.

[23] E. Cornec-Le Gall, A. Alam, and R. D. Perrone, “Autosomal dominant polycystic kidney disease,” *The Lancet*, vol. 393, no. 10174. Lancet Publishing Group, pp. 919–935, 02-Mar-2019.

[24] S. A. Grampsas *et al.*, “Anatomic and metabolic risk factors for nephrolithiasis in patients with autosomal dominant polycystic kidney disease,” *Am. J. Kidney Dis.*, vol. 36, no. 1, pp. 53–57, 2000.

[25] Z. H. Bajwa, K. A. Sial, A. B. Malik, and T. I. Steinman, “Pain patterns in patients with polycystic kidney disease,” *Kidney Int.*, vol. 66, no. 4, pp. 1561–1569, 2004.

[26] J. L. Nishiura, S. R. M. Eloi, and I. P. Heilberg, “Pain determinants of pain in autosomal dominant polycystic kidney disease,” *J. Bras. Nefrol.*, vol. 35, no. 3, pp. 242–243, Oct. 2013.

[27] Z. H. Bajwa, S. Gupta, C. A. Warfield, and T. I. Steinman, “Pain management in polycystic kidney disease,” *Kidney Int.*, 2001.

[28] M. C. Hogan and S. M. Norby, “Evaluation and Management of Pain in Autosomal

Dominant Polycystic Kidney Disease," *Advances in Chronic Kidney Disease*, vol. 17, no. 3. May-2010.

[29] P. A. Gabow, I. Duley, and A. M. Johnson, "Clinical Profiles of Gross Hematuria in Autosomal Dominant Polycystic Kidney Disease," *Am. J. Kidney Dis.*, vol. 20, no. 2, pp. 140–143, 1992.

[30] A. M. Johnson and P. A. Gabow, "Identification of Patients With Autosomal Dominant Polycystic Kidney Disease at Highest Risk for End-Stage Renal Disease," *J. Urol.*, p. 952, Sep. 1998.

[31] V. B. Delaney, S. Adler, F. J. Bruns, M. Licinia, D. P. Segel, and D. S. Fraley, "Autosomal Dominant Polycystic Kidney Disease: Presentation, Complications, and Prognosis," *Am. J. Kidney Dis.*, vol. 5, no. 2, pp. 104–111, 1985.

[32] M.-S. G., C. G., M. R., J. A., and Lord R., "Abdominal wall hernia in autosomal dominant polycystic kidney disease," *British Journal of Surgery*, vol. 84, no. 5. pp. 615–617, 1997.

[33] G. J. E. R. Monique H M Vlak, Ale Algra, Raya Brandenburg, "Prevalence of unruptured intracranial aneurysms, with emphasis on sex, age, comorbidity, country, and time period: a systematic review and meta-analysis," *Artic. Lancet Neurol*, vol. 10, no. 8, pp. 626–636, 2011.

[34] H. W. Xu, S. Q. Yu, C. L. Mei, and M. H. Li, "Screening for intracranial aneurysm in 355 patients with autosomal-dominant polycystic kidney disease," *Stroke*, vol. 42, no. 1, pp. 204–206, Jan. 2011.

[35] E. D. Lederman, D. J. Conti, N. Lempert, T. P. Singh, and E. C. Lee, "Complicated diverticulitis following renal transplantation," *Dis. Colon Rectum*, vol. 41, no. 5, pp. 613–618, May 1998.

[36] Y. Pei *et al.*, "Imaging-Based Diagnosis of Autosomal Dominant Polycystic Kidney Disease," *J. Am. Soc. Nephrol.*, vol. 26, no. 3, pp. 746–753, Mar. 2015.

[37] I. A. Iliuta *et al.*, "Polycystic kidney disease without an apparent family history," *J. Am. Soc. Nephrol.*, vol. 28, no. 9, pp. 2768–2776, Sep. 2017.

[38] A. B. Chapman *et al.*, "Autosomal-dominant polycystic kidney disease (ADPKD): Executive summary from a Kidney Disease: Improving Global Outcomes (KDIGO) Controversies Conference," *Kidney Int.*, 2015.

[39] P. C. Harris and S. Rossetti, "Molecular diagnostics for autosomal dominant polycystic kidney disease," *Nature Reviews Nephrology*, vol. 6, no. 4. pp. 197–206, Apr-2010.

[40] The International Polycystic Kidney Disease Consortium, "Polycystic kidney disease:

The complete structure of the PKD1 gene and its protein," *Cell*, vol. 81, no. 2, pp. 289–298, 1995.

[41] T. C. Burn *et al.*, "Analysis of the genomic sequence for the autosomal dominant polycystic kidney disease (PKD1) gene predicts the presence of a leucine-rich repeat: The AMERICAN pkd1 consortium (apkd1 consortium)," *Hum. Mol. Genet.*, vol. 4, no. 4, pp. 575–582, Apr. 1995.

[42] P. C. H. Jim Hughes, "The polycystic kidney disease 1 (PKD1) gene encodes a novel protein with multiple cell recognition domains," *Nat. Genet.*, vol. 10, pp. 151–160, 1995.

[43] T. Mochizuki *et al.*, "PKD2, a gene for polycystic kidney disease that encodes an integral membrane protein," *Science (80-.).*, vol. 272, no. 5266, pp. 1339–1342, May 1996.

[44] M. Castelli *et al.*, "Regulation of the microtubular cytoskeleton by Polycystin-1 favors focal adhesions turnover to modulate cell adhesion and migration," *BMC Cell Biol.*, vol. 16, no. 1, pp. 1–16, 2015.

[45] J. Van Adelsberg, "Peptides from the PKD repeats of polycystin, the PKD1 gene product, modulate pattern formation in the developing kidney," *Dev. Genet.*, vol. 24, no. 3–4, pp. 299–308, 1999.

[46] O. Ibraghimov-Beskrovnaya, "Strong homophilic interactions of the Ig-like domains of polycystin-1, the protein product of an autosomal dominant polycystic kidney disease gene, PKD1," *Hum. Mol. Genet.*, vol. 9, no. 11, pp. 1641–1649, Jul. 2000.

[47] A. J. Streets, B. E. Wagner, P. C. Harris, C. J. Ward, and A. C. M. Ong, "Homophilic and heterophilic polycystin 1 interactions regulate E-cadherin recruitment and junction assembly in MDCK cells," *J. Cell Sci.*, vol. 122, no. 10, pp. 1702–1702, May 2009.

[48] C. Xu *et al.*, " Human ADPKD primary cyst epithelial cells with a novel, single codon deletion in the PKD1 gene exhibit defective ciliary polycystin localization and loss of flow-induced Ca 2+ signaling ," *Am. J. Physiol. Physiol.*, vol. 292, no. 3, pp. F930–F945, Mar. 2007.

[49] N. Nims, D. Vassmer, and R. L. Maser, "Transmembrane Domain Analysis of Polycystin-1, the Product of the Polycystic Kidney Disease-1 (PKD1) Gene: Evidence for 11 Membrane-Spanning Domains," *Biochemistry*, vol. 42, no. 44, pp. 13035–13048, Nov. 2003.

[50] F. Qian *et al.*, "Cleavage of polycystin-1 requires the receptor for egg jelly domain and is disrupted by human autosomal-dominant polycystic kidney disease 1-associated mutations," *Proc. Natl. Acad. Sci.*, vol. 99, no. 26, pp. 16981–16986, Dec. 2002.

[51] W. Wei, K. Hackmann, H. Xu, G. Germino, and F. Qian, "Characterization of cis-

autoproteolysis of polycystin-1, the product of human polycystic kidney disease 1 gene," *J. Biol. Chem.*, vol. 282, no. 30, pp. 21729–21737, Jul. 2007.

[52] Y. Yu *et al.*, "Structural and molecular basis of the assembly of the TRPP2/PKD1 complex," *Proc. Natl. Acad. Sci.*, vol. 106, no. 28, pp. 11558–11563, Jul. 2009.

[53] V. Chauvet *et al.*, "Mechanical stimuli induce cleavage and nuclear translocation of the polycystin-1 C terminus," *J. Clin. Invest.*, vol. 114, no. 10, pp. 1433–1443, 2004.

[54] V. A. Low, P. Sandroni, R. D. Fealey, and P. A. Low, "Detection of small-fiber neuropathy by sudomotor testing," *Muscle and Nerve*, vol. 34, no. 1, pp. 57–61, 2006.

[55] Y. Huan and J. Van Adelsberg, "Polycystin-1, the PKD1 gene product, is in a complex containing E- cadherin and the catenins," *J. Clin. Invest.*, vol. 104, no. 10, pp. 1459–1468, 1999.

[56] B. K. Yoder, X. Hou, and L. M. Guay-Woodford, "The polycystic kidney disease proteins, polycystin-1, polycystin-2, polaris, and cystin, are co-localized in renal cilia," *J. Am. Soc. Nephrol.*, vol. 13, no. 10, pp. 2508–2516, Oct. 2002.

[57] D. Joly, S. Ishibe, C. Nickel, Z. Yu, S. Somlo, and L. G. Cantley, "The polycystin 1-C-terminal fragment stimulates ERK-dependent spreading of renal epithelial cells," *J. Biol. Chem.*, vol. 281, no. 36, pp. 26329–26339, Sep. 2006.

[58] M. Boca, L. D'Amato, G. Distefano, R. S. Polishchuk, G. G. Germino, and A. Boletta, "Polycystin-1 Induces Cell Migration by Regulating Phosphatidylinositol 3-kinase-dependent Cytoskeletal Rearrangements and GSK3beta-dependent Cell Cell Mechanical Adhesion," *Mol. Biol. Cell*, vol. 18, no. 10, pp. 4050–4061, Aug. 2007.

[59] C. J. Ward *et al.*, "Polycystin, the polycystic kidney disease 1 protein, is expressed by epithelial cells in fetal, adult, and polycystic kidney.," *Proc. Natl. Acad. Sci.*, vol. 93, no. 4, pp. 1524–1528, Jul. 2002.

[60] G. S. Markowitz *et al.*, "Polycystin-2 expression is developmentally regulated," *Am. J. Physiol. Physiol.*, vol. 277, no. 1, pp. F17–F25, Dec. 2017.

[61] D. J. M. Peters *et al.*, "Cellular localization and tissue distribution of polycystin-1," *J. Pathol.*, vol. 188, no. 4, pp. 439–446, 1999.

[62] S. Gonzalez-Perrett *et al.*, "Polycystin-2, the protein mutated in autosomal dominant polycystic kidney disease (ADPKD), is a Ca2+-permeable nonselective cation channel," *Proc. Natl. Acad. Sci.*, vol. 98, no. 3, pp. 1182–1187, Jul. 2012.

[63] L. Tsiokas, T. Arnould, C. Zhu, E. Kim, G. Walz, and V. P. Sukhatme, "Specific association of the gene product of PKD2 with the TRPC1 channel," *Proc. Natl. Acad. Sci.*, vol. 96, no. 7, pp. 3934–3939, Jul. 2002.

[64] A. Ćelić, E. T. Petri, B. Demeler, B. E. Ehrlich, and T. J. Boggon, “Domain mapping of the polycystin-2 C-terminal tail using de novo molecular modeling and biophysical analysis,” *J. Biol. Chem.*, vol. 283, no. 42, pp. 28305–28312, Oct. 2008.

[65] G. Product *et al.*, “Identification and Characterization of Polycystin-2, the PKD2 Gene Product,” vol. 274, no. 40, pp. 28557–28565, 1999.

[66] L. Foggensteiner *et al.*, “Cellular and subcellular distribution of polycystin-2, the protein product of the PKD2 gene.,” *J. Am. Soc. Nephrol.*, vol. 11, no. 5, pp. 814–27, May 2000.

[67] Y. Li, J. M. Wright, F. Qian, G. G. Germino, and W. B. Guggino, “Polycystin 2 interacts with type I inositol 1,4,5-trisphosphate receptor to modulate intracellular Ca2+ signaling,” *J. Biol. Chem.*, vol. 280, no. 50, pp. 41298–41306, Dec. 2005.

[68] F. Qian, T. J. Watnick, L. F. Onuchic, and G. G. Germino, “The molecular basis of focal cyst formation in human autosomal dominant polycystic kidney disease type I,” *Cell*, 1996.

[69] P. Koulen *et al.*, “Polycystin-2 is an intracellular calcium release channel,” *Nat. Cell Biol.*, vol. 4, no. 3, pp. 191–197, 2002.

[70] P. M. Vassilev *et al.*, “Polycystin-2 is a novel cation channel implicated in defective intracellular Ca2+ homeostasis in polycystic kidney disease,” *Biochem. Biophys. Res. Commun.*, 2001.

[71] D. Douguet, A. Patel, and E. Honoré, “Structure and function of polycystins: insights into polycystic kidney disease,” *Nature Reviews Nephrology*, vol. 15, no. 7. Nature Publishing Group, pp. 412–422, 01-Jul-2019.

[72] M. Silberberg, A. J. Charron, R. Bacallao, and A. Wandinger-Ness, “Mispolarization of desmosomal proteins and altered intercellular adhesion in autosomal dominant polycystic kidney disease,” *Am. J. Physiol. Physiol.*, vol. 288, no. 6, pp. F1153–F1163, Jun. 2005.

[73] G. I. Anyatonwu, M. Estrada, X. Tian, S. Somlo, and B. E. Ehrlich, “Regulation of ryanodine receptor-dependent calcium signaling by polycystin-2,” *Proc. Natl. Acad. Sci.*, vol. 104, no. 15, pp. 6454–6459, Apr. 2007.

[74] Y. Li, N. G. Santoso, S. Yu, O. M. Woodward, F. Qian, and W. B. Guggino, “Polycystin-1 interacts with inositol 1,4,5-trisphosphate receptor to modulate intracellular Ca2+ signaling with implications for polycystic kidney disease,” *J. Biol. Chem.*, vol. 284, no. 52, pp. 36431–36441, Dec. 2009.

[75] D. R. Rundle, G. Gorbsky, and L. Tsiokas, “PKD2 interacts and co-localizes with mDia1 to mitotic spindles of dividing cells: Role of mDia1 in PKD2 localization to mitotic

spindles," *J. Biol. Chem.*, vol. 279, no. 28, pp. 29728–29739, Jul. 2004.

[76] S. M. Nauli *et al.*, "Polycystins 1 and 2 mediate mechanosensation in the primary cilium of kidney cells," *Nat. Genet.*, vol. 33, no. 2, pp. 129–137, Feb. 2003.

[77] Q. Su *et al.*, "Structure of the human PKD1/PKD2 complex," *Science (80-.).*, vol. 9819, p. eaat9819, 2018.

[78] A. Patel and E. Honoré, "Polycystins and renovascular mechanosensory transduction," *Nat. Rev. Nephrol.*, vol. 6, no. 9, pp. 530–538, 2010.

[79] M. C. Hogan *et al.*, "Characterization of PKD Protein-Positive Exosome-Like Vesicles," *J. Am. Soc. Nephrol.*, vol. 20, no. 2, pp. 278–288, Feb. 2009.

[80] P. G. Decaen, M. Delling, T. N. Vien, and D. E. Clapham, "Direct recording and molecular identification of the calcium channel of primary cilia," *Nature*, vol. 504, no. 7479, pp. 315–318, 2013.

[81] W. B. G. & G. G. G. Kazushige Hanaoka*[2], Feng Qian[23], Alessandra Boletta[23], Anil K. Bhunia[3], Klaus Piontek[3], Leonidas Tsiokas§, Vikas P. Sukhatmek, "Co-assembly of polycystin-1 and -2 produces unique cation-permeable currents," *Nature*, vol. 408, no. 21/28, pp. 990–994, 2000.

[82] D. Douguet, A. Patel, and E. Honoré, "Structure and function of polycystins: insights into polycystic kidney disease," *Nat. Rev. Nephrol.*, 2019.

[83] B. Pelucchi *et al.*, "Nonspecific Cation Current Associated with Native Polycystin-2 in HEK-293 Cells," *J. Am. Soc. Nephrol.*, vol. 17, no. 2, pp. 388–397, Jan. 2006.

[84] L. J. Newby, A. J. Streets, Y. Zhao, P. C. Harris, C. J. Ward, and A. C. M. Ong, "Identification, characterization, and localization of a novel kidney polycystin-1-polycystin-2 complex," *J. Biol. Chem.*, vol. 277, no. 23, pp. 20763–20773, 2002.

[85] M. Castelli *et al.*, "Polycystin-1 binds Par3/aPKC and controls convergent extension during renal tubular morphogenesis," *Nat. Commun.*, vol. 4, 2013.

[86] V. E. Torres and P. C. Harris, "Autosomal dominant polycystic kidney disease: The last 3 years," *Kidney International*. 2009.

[87] J. J. Grantham, J. L. Geiser, and A. P. Evan, "Cyst formation and growth in autosomal dominant polycystic kidney disease," *Kidney Int.*, vol. 31, no. 5, pp. 1145–1152, 1987.

[88] C. P. Bleeker-Rovers, R. G. L. d. Sévaux, H. W. van Hamersvelt, F. H. . Corstens, and W. J. . Oyen, "Diagnosis of renal and hepatic cyst infections by 18-F-fluorodeoxyglucose positron emission tomography in autosomal dominant polycystic kidney disease," *Am. J. Kidney Dis.*, 2003.

[89] J. J. Grantham, "The etiology, pathogenesis, and treatment of autosomal dominant

polycystic kidney disease: Recent advances," *American Journal of Kidney Diseases*. 1996.

[90] J. P. Calvet, B. D. Cowley Jr., J. J. Grantham, and L. J. Chadwick, "Elevated proto-oncogene expression in polycystic kidneys of the C57BL/6J (cpk) mouse," *J. Am. Soc. Nephrol.*, vol. 1, no. 8, pp. 1048–1053, 1991.

[91] B. D. Cowley, F. L. Smardo, J. J. Grantham, and J. P. Calvet, "Elevated c-myc protooncogene expression in autosomal recessive polycystic kidney disease.," *Proc. Natl. Acad. Sci.*, vol. 84, no. 23, pp. 8394–8398, May 2006.

[92] T. Yamaguchi *et al.*, "Cyclic AMP activates B-Raf and ERK in cyst epithelial cells from autosomal-dominant polycystic kidneys," *Kidney Int.*, 2003.

[93] T. Yamaguchi *et al.*, "cAMP stimulates the in vitro proliferation of renal cyst epithelial cells by activating the extracellular signal-regulated kinase pathway," in *Kidney International*, 2000.

[94] T. Yamaguchi, D. P. Wallace, B. S. Magenheimer, S. J. Hempson, J. J. Grantham, and J. P. Calvet, "Calcium restriction allows cAMP activation of the B-Raf/ERK pathway, switching cells to a cAMP-dependent growth-stimulated phenotype," *J. Biol. Chem.*, vol. 279, no. 39, pp. 40419–40430, Sep. 2004.

[95] H. Happé *et al.*, "Altered Hippo signalling in polycystic kidney disease," *J. Pathol.*, vol. 224, no. 1, pp. 133–142, 2011.

[96] E. Fischer *et al.*, "Defective planar cell polarity in polycystic kidney disease," *Nat. Genet.*, vol. 38, no. 1, pp. 21–23, Jan. 2006.

[97] S. Nishio *et al.*, "Loss of Oriented Cell Division Does not Initiate Cyst Formation," *J. Am. Soc. Nephrol.*, vol. 21, no. 2, pp. 295–302, Feb. 2010.

[98] D. P. Wallace, J. J. Grantham, and L. P. Sullivan, "Chloride and fluid secretion by cultured human polycystic kidney cells," *Kidney Int.*, 1996.

[99] D. P. Wallace, L. A. Rome, L. P. Sullivan, and J. J. Grantham, "cAMP-dependent fluid secretion in rat inner medullary collecting ducts," *Am. J. Physiol. Physiol.*, vol. 280, no. 6, pp. F1019–F1029, Dec. 2017.

[100] B. S. Magenheimer *et al.*, " Early Embryonic Renal Tubules of Wild-Type and Polycystic Kidney Disease Kidneys Respond to cAMP Stimulation with Cystic Fibrosis Transmembrane Conductance Regulator/Na + ,K + ,2Cl − Co-Transporter–Dependent Cystic Dilation ," *J. Am. Soc. Nephrol.*, vol. 17, no. 12, pp. 3424–3437, Dec. 2006.

[101] R. Montesano, H. Ghzili, F. Carrozzino, B. C. Rossier, and E. Féraille, "cAMP-dependent chloride secretion mediates tubule enlargement and cyst formation by

cultured mammalian collecting duct cells," *Am. J. Physiol. Physiol.*, vol. 296, no. 2, pp. F446–F457, Feb. 2009.

[102] C. J. Davidow, R. L. Maser, L. A. Rome, J. P. Calvet, and J. J. Grantham, "The cystic fibrosis transmembrane conductance regulator mediates transepithelial fluid secretion by human autosomal dominant polycystic kidney disease epithelium in vitro," *Kidney Int.*, 1996.

[103] R. Grosjean *et al.*, "Characterization of human renal stones with MDCT: Advantage of dual energy and limitations due to respiratory motion," *Am. J. Roentgenol.*, vol. 190, no. 3, pp. 720–728, Mar. 2008.

[104] M. Lu, K. Dong, M. E. Egan, G. H. Giebisch, E. L. Boulpaep, and S. C. Hebert, "Mouse cystic fibrosis transmembrane conductance regulator forms cAMP-PKA-regulated apical chloride channels in cortical collecting duct," *Proc. Natl. Acad. Sci.*, vol. 107, no. 13, pp. 6082–6087, Mar. 2010.

[105] B. Yang, N. D. Sonawane, D. Zhao, S. Somlo, and A. S. Verkman, "Small-Molecule CFTR Inhibitors Slow Cyst Growth in Polycystic Kidney Disease," *J. Am. Soc. Nephrol.*, vol. 19, no. 7, pp. 1300–1310, Jul. 2008.

[106] P. D. Wilson *et al.*, "Apical plasma membrane mispolarization of NaK-ATPase in polycystic kidney disease epithelia is associated with aberrant expression of the β2 isoform," *Am. J. Pathol.*, 2000.

[107] O. Devuyst, C. R. Burrow, B. L. Smith, P. Agre, M. A. Knepper, and P. D. Wilson, "Expression of aquaporins-1 and -2 during nephrogenesis and in autosomal dominant polycystic kidney disease," *Am. J. Physiol.*, vol. 271, no. 1 PART 2, 1996.

[108] E. Plaisier *et al.*, "COL4A1 mutations and hereditary angiopathy, nephropathy, aneurysms, and muscle cramps," *N. Engl. J. Med.*, vol. 357, no. 26, pp. 2687–2695, Dec. 2007.

[109] S. R. Brill, K. E. Ross, C. J. Davidow, M. Ye, J. J. Grantham, and M. J. Caplan, "Immunolocalization of ion transport proteins in human autosomal dominant polycystic kidney epithelial cells.," *Proc. Natl. Acad. Sci.*, vol. 93, no. 19, pp. 10206–10211, Jul. 2002.

[110] E. D. Avner, W. E. Sweeney, and W. J. Nelson, "Abnormal sodium pump distribution during renal tubulogenesis in congenital murine polycystic kidney disease.," *Proc. Natl. Acad. Sci.*, vol. 89, no. 16, pp. 7447–7451, May 2006.

[111] K. I. Swenson-Fields *et al.*, "Macrophages promote polycystic kidney disease progression," *Kidney Int.*, 2013.

[112] M. H. T. Ta, D. C. H. Harris, and G. K. Rangan, “Role of interstitial inflammation in the pathogenesis of polycystic kidney disease,” *Nephrology*, vol. 18, no. 5. pp. 317–330, May-2013.

[113] C. Lebeau, K. Hanaoka, M. L. Moore-Hoon, W. B. Guggino, R. Beauwens, and O. Devuyst, “Basolateral chloride transporters in autosomal dominant polycystic kidney disease,” *Pflugers Arch. Eur. J. Physiol.*, vol. 444, no. 6, pp. 722–731, Sep. 2002.

[114] B. P. Baur and C. J. Meaney, “Review of tolvaptan for Autosomal dominant polycystic kidney disease,” *Pharmacotherapy*, vol. 34, no. 6. Pharmacotherapy Publications Inc., pp. 605–616, 2014.

[115] J. M. Shillingford, K. B. Piontek, G. G. Germino, and T. Weimbs, “ Rapamycin Ameliorates PKD Resulting from Conditional Inactivation of Pkd1 ,” *J. Am. Soc. Nephrol.*, vol. 21, no. 3, pp. 489–497, Mar. 2010.

[116] J. M. Shillingford, C. P. Leamon, I. R. Vlahov, and T. Weimbs, “Folate-Conjugated Rapamycin Slows Progression of Polycystic Kidney Disease,” *J. Am. Soc. Nephrol.*, vol. 23, no. 10, pp. 1674–1681, Oct. 2012.

[117] I. Zafar, K. Ravichandran, F. A. Belibi, R. B. Doctor, and C. L. Edelstein, “Sirolimus attenuates disease progression in an orthologous mouse model of human autosomal dominant polycystic kidney disease,” *Kidney Int.*, 2010.

[118] M. . Min Ye, M.D, and Jared J.Grantham, “The secretion of fluid by renal cysts from patients with autosomal dominant polycystic kidney disease,” *N. Engl. J. Med.*, vol. 329, no. 5, pp. 310–313, 1993.

[119] M. Y. Chang and A. C. M. Ong, “Autosomal dominant polycystic kidney disease: Recent advances in pathogenesis and treatment,” *Nephron - Physiology*, vol. 108, no. 1. Feb-2008.

[120] V. H. Gattone, X. Wang, P. C. Harris, and V. E. Torres, “Inhibition of renal cystic disease development and progression by a vasopressin V2 receptor antagonist,” *Nat. Med.*, vol. 9, no. 10, pp. 1323–1326, Oct. 2003.

[121] V. E. Torres, X. Wang, Q. Qian, S. Somlo, P. C. Harris, and V. H. Gattone, “Effective treatment of an orthologous model of autosomal dominant polycystic kidney disease,” *Nat. Med.*, vol. 10, no. 4, pp. 363–364, Apr. 2004.

[122] X. Wang, V. Gattone, P. C. Harris, and V. E. Torres, “Effectiveness of Vasopressin V2 Receptor Antagonists OPC-31260 and OPC-41061 on Polycystic Kidney Disease Development in the PCK Rat,” *J. Am. Soc. Nephrol.*, vol. 16, no. 4, pp. 846–851, Apr. 2005.

[123] V. E. Torres, “Role of vasopressin antagonists,” *Clin. J. Am. Soc. Nephrol.*, vol. 3, no. 4, pp. 1212–1218, Jul. 2008.

[124] S. Horie, “Will introduction of tolvaptan change clinical practice in autosomal dominant polycystic kidney disease?,” *Kidney International*. 2015.

[125] V. E. Torres *et al.*, “Multicenter, open-label, extension trial to evaluate the long-term efficacy and safety of early versus delayed treatment with tolvaptan in autosomal dominant polycystic kidney disease: The TEMPO 4:4 Trial,” *Nephrol. Dial. Transplant.*, vol. 33, no. 3, pp. 477–489, Mar. 2018.

[126] R. Peces, E. Cuesta-López, C. Peces, V. Pérez-Dueñas, C. Vega-Cabrera, and R. Selgas, “Octreotide reduces hepatic, renal and breast cystic volume in autosomal-dominant polycystic kidney disease,” *Int. Urol. Nephrol.*, vol. 43, no. 2, pp. 565–569, Jun. 2011.

[127] I. Zafar, Y. Tao, S. Falk, K. McFann, R. W. Schrier, and C. L. Edelstein, “Effect of statin and angiotensin-converting enzyme inhibition on structural and hemodynamic alterations in autosomal dominant polycystic kidney disease model,” *Am. J. Physiol. Physiol.*, vol. 293, no. 3, pp. F854–F859, Sep. 2007.

[128] M. C. Hogan *et al.*, “Randomized Clinical Trial of Long-Acting Somatostatin for Autosomal Dominant Polycystic Kidney and Liver Disease,” *J. Am. Soc. Nephrol.*, vol. 21, no. 6, pp. 1052–1061, Jun. 2010.

[129] T. J. G. Gevers, J. C. Hol, R. Monshouwer, H. M. Dekker, J. F. M. Wetzels, and J. P. H. Drenth, “Effect of lanreotide on polycystic liver and kidneys in autosomal dominant polycystic kidney disease: An observational trial,” *Liver Int.*, vol. 35, no. 5, pp. 1607–1614, May 2015.

[130] A. Caroli *et al.*, “Effect of longacting somatostatin analogue on kidney and cyst growth in autosomal dominant polycystic kidney disease (ALADIN): A randomised, placebo-controlled, multicentre trial,” *Lancet*, vol. 382, no. 9903, pp. 1485–1495, 2013.

[131] G. Bullich *et al.*, “A kidney-disease gene panel allows a comprehensive genetic diagnosis of cystic and glomerular inherited kidney diseases,” *Kidney Int.*, vol. 94, no. 2, pp. 363–371, Aug. 2018.

[132] G. Distefano *et al.*, “Polycystin-1 Regulates Extracellular Signal-Regulated Kinase-Dependent Phosphorylation of Tuberin To Control Cell Size through mTOR and Its Downstream Effectors S6K and 4EBP1,” *Mol. Cell. Biol.*, vol. 29, no. 9, pp. 2359–2371, May 2009.

[133] P. R. Wahl, A. L. Serra, M. Le Hir, K. D. Molle, M. N. Hall, and R. P. Wüthrich, “Inhibition of mTOR with sirolimus slows disease progression in Han:SPRD rats with

autosomal dominant polycystic kidney disease (ADPKD)," *Nephrol. Dial. Transplant.*, vol. 21, no. 3, pp. 598–604, Mar. 2006.

[134] J. M. Shillingford *et al.*, "The mTOR pathway is regulated by polycystin-1, and its inhibition reverses renal cystogenesis in polycystic kidney disease," *Proc. Natl. Acad. Sci.*, vol. 103, no. 14, pp. 5466–5471, Apr. 2006.

[135] A. L. Serra *et al.*, "Sirolimus and kidney growth in autosomal dominant polycystic kidney disease," *N. Engl. J. Med.*, vol. 363, no. 9, pp. 820–829, Aug. 2010.

[136] G. Walz *et al.*, "Everolimus in Patients with Autosomal Dominant Polycystic Kidney Disease," *N. Engl. J. Med.*, vol. 363, no. 9, pp. 830–840, Aug. 2010.

[137] V. E. Torres *et al.*, "Angiotensin blockade in late autosomal dominant polycystic kidney disease," *N. Engl. J. Med.*, vol. 371, no. 24, pp. 2267–2276, Dec. 2014.

[138] N. O. Bukanov, L. A. Smith, K. W. Klinger, S. R. Ledbetter, and O. Ibraghimov-Beskrovnaya, "Long-lasting arrest of murine polycystic kidney disease with CDK inhibitor roscovitine," *Nature*, vol. 444, no. 7121, pp. 949–952, Dec. 2006.

[139] W. Lu *et al.*, "Perinatal lethality with kidney and pancreas defects in mice with a targetted pkd1 mutation," *Nature Genetics*, vol. 17, no. 2. pp. 179–181, 1997.

[140] P. C. Harris, "What Is the Role of Somatic Mutation in Autosomal Dominant Polycystic Kidney Disease?," *J. Am. Soc. Nephrol.*, vol. 21, no. 7, pp. 1073–1076, Jul. 2010.

[141] I. S. Lantinga-van Leeuwen *et al.*, "Lowering of Pkd1 expression is sufficient to cause polycystic kidney disease," *Hum. Mol. Genet.*, vol. 13, no. 24, pp. 3069–3077, Dec. 2004.

[142] S. T. Jiang *et al.*, "Defining a link with autosomal-dominant polycystic kidney disease in mice with congenitally low expression of Pkd1," *Am. J. Pathol.*, 2006.

[143] S. Rossetti *et al.*, "Incompletely penetrant PKD1 alleles suggest a role for gene dosage in cyst initiation in polycystic kidney disease," *Kidney Int.*, 2009.

[144] R. I. Botulinum and R. Study, "A polycystin-centric view of cyst formation and disease: the polycystins revisited," vol. 4, no. 1, pp. 139–148, 2014.

[145] A. Takakura, L. Contrino, A. W. Beck, and J. Zhou, " Pkd1 Inactivation Induced in Adulthood Produces Focal Cystic Disease ," *J. Am. Soc. Nephrol.*, vol. 19, no. 12, pp. 2351–2363, Dec. 2008.

[146] G. Aguiari *et al.*, "Deficiency of polycystin-2 reduces Ca2+ channel activity and cell proliferation in ADPKD lymphoblastoid cells.," *FASEB J.*, vol. 18, no. 7, pp. 884–886, 2004.

[147] K. Piontek, L. F. Menezes, M. A. Garcia-Gonzalez, D. L. Huso, and G. G. Germino, "A

critical developmental switch defines the kinetics of kidney cyst formation after loss of Pkd1," *Nat. Med.*, vol. 13, no. 12, pp. 1490–1495, Dec. 2007.

[148] J. L. Brasier and E. P. Henske, "Loss of the polycystic kidney disease (PKD1) region of chromosome 16p13 in renal cyst cells supports a loss-of-function model for cyst pathogenesis," *J. Clin. Invest.*, vol. 99, no. 2, pp. 194–199, Jan. 1997.

[149] A. P. Bastos *et al.*, " Pkd1 Haploinsufficiency Increases Renal Damage and Induces Microcyst Formation following Ischemia/Reperfusion ," *J. Am. Soc. Nephrol.*, vol. 20, no. 11, pp. 2389–2402, Nov. 2009.

[150] V. Patel *et al.*, "Acute kidney injury and aberrant planar cell polarity induce cyst formation in mice lacking renal cilia," *Hum. Mol. Genet.*, vol. 17, no. 11, pp. 1578–1590, Jun. 2008.

[151] H. Happé *et al.*, "Toxic tubular injury in kidneys from Pkd1-deletion mice accelerates cystogenesis accompanied by dysregulated planar cell polarity and canonical Wnt signaling pathways," *Hum. Mol. Genet.*, vol. 18, no. 14, pp. 2532–2542, 2009.

[152] S. Nishio *et al.*, "Pkd1 regulates immortalized proliferation of renal tubular epithelial cells through p53 induction and JNK activation," *J. Clin. Invest.*, vol. 115, no. 4, pp. 910–918, 2005.

[153] L. Pritchard, "A human PKD1 transgene generates functional polycystin-1 in mice and is associated with a cystic phenotype," *Hum. Mol. Genet.*, vol. 9, no. 18, pp. 2617–2627, Nov. 2000.

[154] A. Takakura *et al.*, "Renal injury is a third hit promoting rapid development of adult polycystic kidney disease," *Hum. Mol. Genet.*, vol. 18, no. 14, pp. 2523–2531, 2009.

[155] X. Liu, T. Vien, J. Duan, S. H. Sheu, P. G. DeCaen, and D. E. Clapham, "Polycystin-2 is an essential ion channel subunit in the primary cilium of the renal collecting duct epithelium," *Elife*, vol. 7, 2018.

[156] I. Orhon *et al.*, "Primary-cilium-dependent autophagy controls epithelial cell volume in response to fluid flow," *Nat. Cell Biol.*, vol. 18, no. 6, pp. 657–667, 2016.

[157] K. Zimmerman and B. K. Yoder, "Snap Shot: Sensing and signaling by cilia," *Cell*, vol. 161, no. 3. Cell Press, pp. 692-692.e1, 23-Apr-2015.

[158] S. Weinbaum, Y. Duan, L. M. Satlin, T. Wang, and A. M. Weinstein, "Mechanotrans-duction in the renal tubule," *Am J Physiol Ren. Physiol*, vol. 299, pp. 1220–1236, 2010.

[159] V. Raghavan and O. A. Weisz, "Discerning the role of mechanosensors in regulating proximal tubule function," *Am J Physiol Ren. Physiol*, vol. 310, pp. 1–5, 2016.

[160] N. E. Brown and N. S. Murcia, "Delayed cystogenesis and increased ciliogenesis

associated with the re-expression of polaris in Tg737 mutant mice," 2003.

[161] J. J. Grantham, J. L. Geiser, and A. P. Evan, "Cyst formation and growth in autosomal dominant polycystic kidney disease," 1987.

[162] A. Dietzel, "Microsystems for Pharmatechnology: Manipulation of Fluids, Particles, Droplets, and Cells," *Microsystems for Pharmatechnology: Manipulation of Fluids, Particles, Droplets, and Cells*, Springer International Publishing, pp. v–vi, 01-Jan-2016.

[163] L. P. Lee, "Microphysiological Analytic Platforms (MAPs): Precision Organs on Chip," *Adv. Healthc. Mater.*, vol. 7, no. 2, pp. 2–3, 2018.

[164] B. Zhang, A. Korolj, B. F. L. Lai, and M. Radisic, "Advances in organ-on-a-chip engineering," *Nat. Rev. Mater.*, vol. 3, no. 8, pp. 257–278, 2018.

[165] Dongeun Huh, "Reconstituting Organ-Level Lung Functions on a Chip," *Science (80-.).*, vol. 328, no. 5986, pp. 1658–1662, Jun. 2010.

[166] A. D. Van Der Meer and A. Van Den Berg, "Organs-on-chips: Breaking the in vitro impasse," *Integrative Biology*, vol. 4, no. 5. pp. 461–470, May-2012.

[167] D. Huh, Y. S. Torisawa, G. A. Hamilton, H. J. Kim, and D. E. Ingber, "Microengineered physiological biomimicry: Organs-on-Chips," *Lab on a Chip*, vol. 12, no. 12. Royal Society of Chemistry, pp. 2156–2164, 21-Jun-2012.

[168] D. Huh *et al.*, "Acoustically detectable cellular-level lung injury induced by fluid mechanical stresses in microfluidic airway systems," *Proc. Natl. Acad. Sci. U. S. A.*, vol. 104, no. 48, pp. 18886–18891, Nov. 2007.

[169] H. Kimura, T. Yamamoto, H. Sakai, Y. Sakai, and T. Fujii, "An integrated microfluidic system for long-term perfusion culture and on-line monitoring of intestinal tissue models," *Lab Chip*, vol. 8, no. 5, pp. 741–746, 2008.

[170] S. G. H. and M. L.Shuler, "Growth Of Endothelial Cells On Microfabricated silicon nitride membranes for an In vitro model of the blood-brain-barrier," *Biotechnol. Bioprocess Bioeng.*, vol. 8, no. 246–251, 2003.

[171] D. Huh *et al.*, "Microfabrication of human organs-on-chips," *Nat. Protoc.*, vol. 8, no. 11, pp. 2135–2157, 2013.

[172] D. E. Ingber, "Cellular mechanotransduction: Putting all the pieces together again," *FASEB J.*, vol. 20, no. 7, pp. 811–827, May 2006.

[173] H. J. Kim, D. Huh, G. Hamilton, and D. E. Ingber, "Human gut-on-a-chip inhabited by microbial flora that experiences intestinal peristalsis-like motions and flow," *Lab Chip*, vol. 12, no. 12, pp. 2165–2174, Jun. 2012.

[174] G. Stacey, "Primary Cell Cultures and Immortal Cell Lines," in *Encyclopedia of Life*

Sciences, John Wiley & Sons, Ltd, 2006.

[175] Y. I. Wang, H. E. Abaci, and M. L. Shuler, "Microfluidic blood–brain barrier model provides in vivo-like barrier properties for drug permeability screening," *Biotechnol. Bioeng.*, vol. 114, no. 1, pp. 184–194, Jan. 2017.

[176] C. Zhang, Z. Zhao, N. A. Abdul Rahim, D. Van Noort, and H. Yu, "Towards a human-on-chip: Culturing multiple cell types on a chip with compartmentalized microenvironments," *Lab Chip*, vol. 9, no. 22, pp. 3185–3192, 2009.

[177] P. Gangatirkar, S. Paquet-Fifield, A. Li, R. Rossi, and P. Kaur, "Establishment of 3D organotypic cultures using human neonatal epidermal cells," *Nat. Protoc.*, vol. 2, no. 1, pp. 178–186, Feb. 2007.

[178] Y. C. Toh, T. C. Lim, D. Tai, G. Xiao, D. Van Noort, and H. Yu, "A microfluidic 3D hepatocyte chip for drug toxicity testing," *Lab Chip*, vol. 9, no. 14, pp. 2026–2035, 2009.

[179] D. Hare, S. Collins, B. Cuddington, and K. Mossman, "The importance of physiologically relevant cell lines for studying virus-host interactions," *Viruses*, vol. 8, no. 11. MDPI AG, 01-Nov-2016.

[180] D. Howard, L. D. Buttery, K. M. Shakesheff, and S. J. Roberts, "Tissue engineering: Strategies, stem cells and scaffolds," *Journal of Anatomy*, vol. 213, no. 1. pp. 66–72, Jul-2008.

[181] C. Pan, C. Kumar, S. Bohl, U. Klingmueller, and M. Mann, "Comparative proteomic phenotyping of cell lines and primary cells to assess preservation of cell type-specific functions," *Mol. Cell. Proteomics*, vol. 8, no. 3, pp. 443–450, Mar. 2009.

[182] L. Yang *et al.*, "Human cardiovascular progenitor cells develop from a KDR+ embryonic-stem-cell-derived population," *Nature*, vol. 453, no. 7194, pp. 524–528, May 2008.

[183] E. Matsa, J. H. Ahrens, and J. C. Wu, "Personalized and Precision Cardiovascular Medicine," *Physiol Rev*, vol. 96, pp. 1093–1126, 2016.

[184] T. Aasen *et al.*, "Efficient and rapid generation of induced pluripotent stem cells from human keratinocytes," *Nat. Biotechnol.*, vol. 26, no. 11, pp. 1276–1284, Nov. 2008.

[185] M. Stadtfeld, K. Brennand, and K. Hochedlinger, "Reprogramming of Pancreatic β Cells into Induced Pluripotent Stem Cells," *Curr. Biol.*, 2008.

[186] J. Yu *et al.*, "Induced pluripotent stem cell lines derived from human somatic cells," *Science (80-.).*, vol. 318, no. 5858, pp. 1917–1920, Dec. 2007.

[187] K. Takahashi and S. Yamanaka, "Induction of Pluripotent Stem Cells from Mouse Embryonic and Adult Fibroblast Cultures by Defined Factors," *Cell*, 2006.

[188] C. R. Hooijmans, “Progress in Using Systematic Reviews of Animal Studies to Improve Translational Research,” vol. 10, no. 7, pp. 1–4, 2013.

[189] P. R. L. Debra S. Echt, M.D., “Mortality and morbidity in patients receiving encainide, flecainide, or placebo,” *N. Engl. J. Med.*, vol. 324, no. 12, pp. 781–788, 1991.

[190] D. E. Ingber, “Reverse Engineering Human Pathophysiology with Organs-on-Chips,” *Cell*. 2016.

[191] E. W. Esch, A. Bahinski, and D. Huh, “Organs-on-chips at the frontiers of drug discovery,” *Nature Reviews Drug Discovery*, vol. 14, no. 4. Nature Publishing Group, pp. 248–260, 01-Apr-2015.

[192] A. M. Ghaemmaghami, M. J. Hancock, H. Harrington, H. Kaji, and A. Khademhosseini, “Biomimetic tissues on a chip for drug discovery,” *Drug Discovery Today*, vol. 17, no. 3–4. pp. 173–181, Feb-2012.

[193] N. S. Bhise *et al.*, “Organ-on-a-chip platforms for studying drug delivery systems,” *Journal of Controlled Release*, vol. 190. Elsevier B.V., pp. 82–93, 28-Sep-2014.

[194] B. Zhang and M. Radisic, “Organ-on-A-chip devices advance to market,” *Lab on a Chip*, vol. 17, no. 14. Royal Society of Chemistry, pp. 2395–2420, 2017.

[195] G. J. Mahler, M. B. Esch, R. P. Glahn, and M. L. Shuler, “Characterization of a gastrointestinal tract microscale cell culture analog used to predict drug toxicity,” *Biotechnol. Bioeng.*, vol. 104, no. 1, pp. 193–205, Sep. 2009.

[196] “Harris-Shuler2003_Article_GrowthOfEndothelialCellsOnMicr.”

[197] A. Carraro *et al.*, “In vitro analysis of a hepatic device with intrinsic microvascular-based channels,” *Biomed. Microdevices*, vol. 10, no. 6, pp. 795–805, 2008.

[198] P. J. Lee, P. J. Hung, and L. P. Lee, “An artificial liver sinusoid with a microfluidic endothelial-like barrier for primary hepatocyte culture,” *Biotechnol. Bioeng.*, vol. 97, no. 5, pp. 1340–1346, Aug. 2007.

[199] K. Jang, K. Sato, K. Igawa, U. Il Chung, and T. Kitamori, “Development of an osteoblast-based 3D continuous-perfusion microfluidic system for drug screening,” *Anal. Bioanal. Chem.*, vol. 390, no. 3, pp. 825–832, Feb. 2008.

[200] J. W. Song, W. Gu, N. Futai, K. A. Warner, J. E. Nor, and S. Takayama, “Computer-controlled microcirculatory support system for endothelial cell culture and shearing,” *Anal. Chem.*, vol. 77, no. 13, pp. 3993–3999, Jul. 2005.

[201] K. J. Jang and K. Y. Suh, “A multi-layer microfluidic device for efficient culture and analysis of renal tubular cells,” *Lab Chip*, vol. 10, no. 1, pp. 36–42, 2010.

[202] K. W. Garey and G. W. Amsden, “Norfloxacin-induced cholestatic jaundice,” 2000.

[203] P. B. Watkins, M. Merz, M. I. Avigan, N. Kaplowitz, A. Regev, and J. R. Senior, “The Clinical Liver Safety Assessment Best Practices Workshop: Rationale, Goals, Accomplishments and the Future,” *Drug Safety*, vol. 37, no. 1, Springer International Publishing, pp. 1–7, 2014.

[204] D. V. LaBarbera, B. G. Reid, and B. H. Yoo, “The multicellular tumor spheroid model for high-throughput cancer drug discovery,” *Expert Opinion on Drug Discovery*, vol. 7, no. 9. pp. 819–830, Sep-2012.

[205] Y. Imamura *et al.*, “Comparison of 2D- and 3D-culture models as drug-testing platforms in breast cancer,” *Oncol. Rep.*, vol. 33, no. 4, pp. 1837–1843, Apr. 2015.

[206] M. B. Esch, A. S. T. Smith, J. M. Prot, C. Oleaga, J. J. Hickman, and M. L. Shuler, “How multi-organ microdevices can help foster drug development,” *Advanced Drug Delivery Reviews*, vol. 69–70. Elsevier, pp. 158–169, 2014.

[207] L. Shintu *et al.*, “Metabolomics-on-a-chip and predictive systems toxicology in microfluidic bioartificial organs,” *Anal. Chem.*, vol. 84, no. 4, pp. 1840–1848, Feb. 2012.

[208] W. SUN *et al.*, “Organs-on-chips and Its Applications,” *Chinese Journal of Analytical Chemistry*, vol. 44, no. 4. Chinese Academy of Sciences, pp. 533–541, 01-Apr-2016.

[209] I. Maschmeyer *et al.*, “A four-organ-chip for interconnected long-term co-culture of human intestine, liver, skin and kidney equivalents,” *Lab Chip*, vol. 15, no. 12, pp. 2688–2699, 2015.

[210] E. Iori, B. Vinci, E. Murphy, M. C. Marescotti, A. Avogaro, and A. Ahluwalia, “Glucose and fatty acid metabolism in a 3 tissue in-vitro model challenged with normo- and hyperglycaemia,” *PLoS One*, vol. 7, no. 4, 2012.

[211] J. H. Sung and M. L. Shuler, “A micro cell culture analog (CCA) with 3-D hydrogel culture of multiple cell lines to assess metabolism-dependent cytotoxicity of anti-cancer drugs,” *Lab Chip*, vol. 9, no. 10, pp. 1385–1394, 2009.

[212] K. Viravaidya and M. L. Shuler, “Incorporation of 3T3-L1 cells to mimic bioaccumulation in a microscale cell culture analog device for toxicity studies,” *Biotechnol. Prog.*, vol. 20, no. 2, pp. 590–597, Mar. 2004.

[213] S. Kim and S. Takayama, “Organ-on-a-chip and the kidney,” *Kidney Res. Clin. Pract.*, vol. 34, no. 3, pp. 165–169, 2015.

[214] M. J. Wilmer, C. P. Ng, H. L. Lanz, P. Vulto, L. Suter-Dick, and R. Masereeuw, “Kidney-on-a-Chip Technology for Drug-Induced Nephrotoxicity Screening,” *Trends Biotechnol.*, vol. 34, no. 2, pp. 156–170, 2016.

[215] U. Meyer, T. Meyer, J. Handschel, and H. P. Wiesmann, “Preface,” *Fundamentals of*

Tissue Engineering and Regenerative Medicine, Springer Berlin Heidelberg, 2009.

[216] K. J. Jang *et al.*, "Human kidney proximal tubule-on-a-chip for drug transport and nephrotoxicity assessment," *Integr. Biol. (United Kingdom)*, vol. 5, no. 9, pp. 1119–1129, Sep. 2013.

[217] K. A. Homan *et al.*, "Bioprinting of 3D Convoluted Renal Proximal Tubules on Perfusable Chips," *Sci. Rep.*, vol. 6, pp. 1–13, 2016.

[218] G. Ligresti *et al.*, "A novel three-dimensional human peritubular microvascular system," *J. Am. Soc. Nephrol.*, vol. 27, no. 8, pp. 2370–2381, 2016.

[219] E. J. Weber *et al.*, "Development of a microphysiological model of human kidney proximal tubule function," *Kidney Int.*, vol. 90, no. 3, pp. 627–637, 2016.

[220] M. Zhou *et al.*, "Development of a Functional Glomerulus at the Organ Level on a Chip to Mimic Hypertensive Nephropathy," *Sci. Rep.*, vol. 6, Aug. 2016.

[221] S. Musah *et al.*, "Mature induced-pluripotent-stem-cell-derived human podocytes reconstitute kidney glomerular-capillary-wall function on a chip," *Nat. Biomed. Eng.*, vol. 1, no. 5, May 2017.

[222] K. J. Jang and K. Y. Suh, "A multi-layer microfluidic device for efficient culture and analysis of renal tubular cells," *Lab Chip*, vol. 10, no. 1, pp. 36–42, Jan. 2010.

[223] E. M. Vedula, J. L. Alonso, M. A. Arnaout, and J. L. Charest, "A microfluidic renal proximal tubule with active reabsorptive function," *PLoS One*, vol. 12, no. 10, 2017.

[224] E. M. Frohlich, J. L. Alonso, J. T. Borenstein, X. Zhang, M. A. Arnaout, and J. L. Charest, "Topographically-patterned porous membranes in a microfluidic device as an in vitro model of renal reabsorptive barriers," *Lab Chip*, vol. 13, no. 12, pp. 2311–2319, Jun. 2013.

[225] J. L. Charest, A. J. García, and W. P. King, "Myoblast alignment and differentiation on cell culture substrates with microscale topography and model chemistries," *Biomaterials*, vol. 28, no. 13, pp. 2202–2210, May 2007.

[226] J. L. Charest, M. T. Eliason, A. J. García, and W. P. King, "Combined microscale mechanical topography and chemical patterns on polymer cell culture substrates," *Biomaterials*, vol. 27, no. 11, pp. 2487–2494, Apr. 2006.

[227] C. J. Bettinger, R. Langer, and J. T. Borenstein, "Engineering substrate topography at the Micro- and nanoscale to control cell function," *Angewandte Chemie - International Edition*, vol. 48, no. 30. pp. 5406–5415, 13-Jul-2009.

[228] J. L. Charest, L. E. Bryant, A. J. Garcia, and W. P. King, "Hot embossing for micropatterned cell substrates," *Biomaterials*, vol. 25, no. 19, pp. 4767–4775, Aug. 2004.

[229] A. Blattmann, L. Denk, R. Strehl, H. Castrop, and W. W. Minuth, “The formation of pores in the basal lamina of regenerated renal tubules,” *Biomaterials*, vol. 29, no. 18, pp. 2749–2756, Jun. 2008.

[230] E. M. Frohlich, X. Zhang, and J. L. Charest, “The use of controlled surface topography and flow-induced shear stress to influence renal epithelial cell function,” *Integr. Biol.*, vol. 4, no. 1, pp. 75–83, 2012.

[231] L. A. Bruggeman, R. P. Doan, J. Loftis, A. Darr, and A. Calabro, “A cell culture system for the structure and hydrogel properties of basement membranes: Application to capillary walls,” in *Cellular and Molecular Bioengineering*, 2012, vol. 5, no. 2, pp. 194–204.

[232] C. P. Ng, Y. Zhuang, A. W. H. Lin, and J. C. M. Teo, “A Fibrin-Based Tissue-Engineered Renal Proximal Tubule for Bioartificial Kidney Devices: Development, Characterization and In Vitro Transport Study,” *Int. J. Tissue Eng.*, vol. 2013, pp. 1–10, 2013.

[233] H. D. Humes, S. M. MacKay, A. J. Funke, and D. A. Buffington, “Tissue engineering of a bioartificial renal tubule assist device: In vitro transport and metabolic characteristics,” *Kidney Int.*, vol. 55, no. 6, pp. 2502–2514, 1999.

[234] A. Tourovskaia, M. Fauver, G. Kramer, S. Simonson, and T. Neumann, “Brief Communication: Tissue-engineered Microenvironment Systems for Modeling Human Vasculature HHS Public Access,” *Exp Biol Med*, vol. 239, no. 9, pp. 1264–1271, 2014.

[235] T. M. DesRochers, L. Suter, A. Roth, and D. L. Kaplan, “Bioengineered 3D Human Kidney Tissue, a Platform for the Determination of Nephrotoxicity,” *PLoS One*, vol. 8, no. 3, Mar. 2013.

[236] L. H. Lash, D. A. Putt, and H. Cai, “Membrane transport function in primary cultures of human proximal tubular cells,” *Toxicology*, vol. 228, no. 2–3, pp. 200–218, Dec. 2006.

[237] W. Xi, S. Sonam, T. Beng Saw, B. Ladoux, and C. Teck Lim, “Emergent patterns of collective cell migration under tubular confinement,” *Nat. Commun.*, vol. 8, no. 1, p. 1517, 2017.

[238] D. B. Kolesky, R. L. Truby, A. S. Gladman, T. A. Busbee, K. A. Homan, and J. A. Lewis, “3D bioprinting of vascularized, heterogeneous cell-laden tissue constructs,” *Adv. Mater.*, vol. 26, no. 19, pp. 3124–3130, May 2014.

[239] D. B. Kolesky, K. A. Homan, M. A. Skylar-Scott, and J. A. Lewis, “Three-dimensional bioprinting of thick vascularized tissues,” *Proc. Natl. Acad. Sci.*, vol. 113, no. 12, pp. 3179–3184, 2016.

[240] K. A. Homan *et al.*, “Bioprinting of 3D Convoluted Renal Proximal Tubules on

Perfusable Chips," *Sci. Rep.*, vol. 6, pp. 1–13, 2016.

[241] N. Y. C. Lin *et al.*, "Renal reabsorption in 3D vascularized proximal tubule models," *Proc. Natl. Acad. Sci.*, vol. 116, no. 12, pp. 5399–5404, 2019.

[242] B. Subramanian, O. Kaya, M. R. Pollak, G. Yao, and J. Zhou, *Guided tissue organization and disease modeling in a kidney tubule array*, vol. 183. Elsevier Ltd, 2018.

[243] N. Poornejad, L. B. Schaumann, E. M. Buckmiller, B. L. Roeder, and A. D. Cook, "Current Cell-Based Strategies for Whole Kidney Regeneration," *Tissue Engineering - Part B: Reviews*, vol. 22, no. 5. Mary Ann Liebert Inc., pp. 358–370, 01-Oct-2016.

[244] N. Pabla and Z. Dong, "Cisplatin nephrotoxicity: Mechanisms and renoprotective strategies," *Kidney International*, vol. 73, no. 9. Nature Publishing Group, pp. 994–1007, 2008.

[245] X. Yao, K. Panichpisal, N. Kurtzman, and K. Nugent, "Cisplatin nephrotoxicity: A review," *American Journal of the Medical Sciences*, vol. 334, no. 2. pp. 115–124, Aug-2007.

[246] Y. Lu, A. Kawashima, I. Horii, and L. Zhong, "Cisplatin-induced cytotoxicity in BSO-exposed renal proximal tubular epithelial cells: Sex, age, and species," *Ren. Fail.*, vol. 27, no. 5, pp. 629–633, 2005.

[247] J. Uetrecht, "Role of animal models in the study of drug-induced hypersensitivity reactions," *AAPS Journal*, vol. 7, no. 4. 13-Jan-2006.

[248] N. Pabla, R. F. Murphy, K. Liu, and Z. Dong, "The copper transporter Ctr1 contributes to cisplatin uptake by renal tubular cells during cisplatin nephrotoxicity," *Am. J. Physiol. - Ren. Physiol.*, vol. 296, no. 3, Mar. 2009.

[249] S. M. King *et al.*, "3D proximal tubule tissues recapitulate key aspects of renal physiology to enable nephrotoxicity testing," *Front. Physiol.*, vol. 8, no. MAR, 2017.

[250] B. S. Freedman *et al.*, "Modelling kidney disease with CRISPR-mutant kidney organoids derived from human pluripotent epiblast spheroids," *Nat. Commun.*, vol. 6, no. May, pp. 1–13, 2015.

[251] M. Takasato *et al.*, "Kidney organoids from human iPS cells contain multiple lineages and model human nephrogenesis," *Nature*, vol. 526, no. 7574, pp. 564–568, Oct. 2015.

[252] D. Woo, "Apoptosis and Loss of Renal Tissue in Polycystic Kidney Diseases," *N. Engl. J. Med.*, vol. 333, no. 1, pp. 18–25, Jul. 2002.

[253] H. Happé *et al.*, "Cyst expansion and regression in a mouse model of polycystic kidney disease," *Kidney Int.*, 2013.

[254] B. Venzac *et al.*, "Engineering small tubes with changes in diameter for the study of

kidney cell organization," *Biomicrofluidics*, vol. 12, no. 2, Mar. 2018.

[255] N. Y. C. Lin *et al.*, "Renal reabsorption in 3D vascularized proximal tubule models," *Proc. Natl. Acad. Sci.*, vol. 116, no. 12, pp. 5399–5404, 2019.

[256] M. A. Knepper, R. A. Danielson, G. M. Saidel, and R. S. Post, "Quantitative analysis of renal medullary anatomy in rats and rabbits," *Kidney Int.*, vol. 12, no. 5, pp. 313–323, 1977.

[257] S. Roy, C. Y. Yue, S. S. Venkatraman, and L. L. Ma, "Fabrication of smart COC chips: Advantages of N-vinylpyrrolidone (NVP) monomer over other hydrophilic monomers," *Sensors Actuators, B Chem.*, vol. 178, pp. 86–95, 2013.

[258] P. M. Van Midwoud, A. Janse, M. T. Merema, G. M. M. Groothuis, and E. Verpoorte, "Comparison of biocompatibility and adsorption properties of different plastics for advanced microfluidic cell and tissue culture models," *Anal. Chem.*, vol. 84, no. 9, pp. 3938–3944, May 2012.

[259] E. J. Weber, "Development of a Microphysiological Model of the Kidney Proximal Tubule and Application in Predictive Toxicity Testing of Polymyxin Antibiotics," 2018.

[260] M. Heckele, W. Bacher, and K. D. Müller, "Hot embossing - The molding technique for plastic microstructures," *Microsyst. Technol.*, vol. 4, no. 3, pp. 122–124, 1998.

[261] M. Serra, I. Pereiro, A. Yamada, J. L. Viovy, S. Descroix, and D. Ferraro, "A simple and low-cost chip bonding solution for high pressure, high temperature and biological applications," *Lab Chip*, vol. 17, no. 4, pp. 629–634, 2017.

[262] W. P. Daley, S. B. Peters, and M. Larsen, "Extracellular matrix dynamics in development and regenerative medicine," *Journal of Cell Science*, vol. 121, no. 3. pp. 255–264, 01-Feb-2008.

[263] A. M. van Genderen, J. Jansen, C. Cheng, T. Vermonden, and R. Masereeuw, "Renal Tubular- and Vascular Basement Membranes and their Mimicry in Engineering Vascularized Kidney Tubules," *Adv. Healthc. Mater.*, vol. 7, no. 19, pp. 1–13, 2018.

[264] W. Zheng, Z. Wang, W. Zhang, and X. Jiang, "A simple PDMS-based microfluidic channel design that removes bubbles for long-term on-chip culture of mammalian cells," *Lab Chip*, vol. 10, no. 21, p. 2906, 2010.

[265] T. Walimbe, A. Panitch, and P. M. Sivasankar, "A Review of Hyaluronic Acid and Hyaluronic Acid-based Hydrogels for Vocal Fold Tissue Engineering," *J. Voice*, vol. 31, no. 4, pp. 416–423, 2017.

[266] M. Verhulsel, M. Vignes, S. Descroix, L. Malaquin, D. M. Vignjevic, and J. L. Viovy, "A review of microfabrication and hydrogel engineering for micro-organs on chips,"

Biomaterials, vol. 35, no. 6, pp. 1816–1832, 2014.

[267] S. J. Park, M. B. Goodman, and B. L. Pruitt, "Measurement of mechanical properties of Caenorhabditis elegans with a piezoresistive microcantilever system," *2005 3rd IEEE/EMBS Spec. Top. Conf. Microtechnology Med. Biol.*, vol. 2005, no. June 2005, pp. 400–403, 2005.

[268] D. Z. Huishi Zhang, Farah Tasnim, Jackie Y. Ying, "The impact of extracellular matrix coatings on the performance of human renal cells applied in bioartificial kidneys Huishi," *Biomaterials*, vol. 3, no. 8. Elsevier Ltd, pp. 257–278, 2009.

[269] K. H. Nakayama, C. C. I. Lee, C. A. Batchelder, and A. F. Tarantal, "Tissue Specificity of Decellularized Rhesus Monkey Kidney and Lung Scaffolds," *PLoS One*, vol. 8, no. 5, May 2013.

[270] H. Haga, C. Irahara, R. Kobayashi, T. Nakagaki, and K. Kawabata, "Collective movement of epithelial cells on a collagen gel substrate," *Biophys. J.*, vol. 88, no. 3, pp. 2250–2256, 2005.

[271] A. Zuk, K. S. Matlin, and E. D. Hay, "Type I collagen gel induces Madin-Darby canine kidney cells to become fusiform in shape and lose apical-basal polarity," *J. Cell Biol.*, vol. 108, no. 3, pp. 903–919, 1989.

[272] M. Imai, K. Furusawa, T. Mizutani, K. Kawabata, and H. Haga, "Three-dimensional morphogenesis of MDCK cells induced by cellular contractile forces on a viscous substrate," *Sci. Rep.*, vol. 5, no. September, pp. 1–10, 2015.

[273] F. Pampaloni, E. H. K. Stelzer, S. Leicht, and M. Marcello, "Madin-Darby canine kidney cells are increased in aerobic glycolysis when cultured on flat and stiff collagen-coated surfaces rather than in physiological 3-D cultures," *Proteomics*, vol. 10, no. 19, pp. 3394–3413, Oct. 2010.

[274] R. Peyronnet *et al.*, "Mechanoprotection by polycystins against apoptosis is mediated through the opening of stretch-activated K2P channels," vol. 1, no. 3, pp. 241–250, 2012.

[275] F. Wei *et al.*, "Neutrophil gelatinase-associated lipocalin suppresses cyst growth by Pkd1 null cells in vitro and in vivo," *Kidney Int.*, vol. 74, no. 10, pp. 1310–1318, 2008.

[276] D. Maggiorani *et al.*, "Shear Stress-Induced Alteration of Epithelial Organization in Human Renal Tubular Cells," *PLoS One*, vol. 10, no. 7, p. e0131416, 2015.

[277] P. L. Smith, D. A. Buffington, and H. D. Humes, "Kidney Epithelial Cells," *Methods Enzymol.*, vol. 419, no. 06, pp. 194–207, 2006.

[278] S. Baranwal *et al.*, "Nonredundant roles of cytoplasmic - and -actin isoforms in regulation of epithelial apical junctions," *Mol. Biol. Cell*, vol. 23, no. 18, pp. 3542–3553,

2012.

[279] Y. Duan *et al.*, “Shear-induced reorganization of renal proximal tubule cell actin cytoskeleton and apical junctional complexes,” 2008.

[280] E. Lever and D. Sheer, “Tight junction composition is altered in the epithelium of polycystic kidneys ASL,” *J. Pathol.*, vol. 220, no. September, pp. 114–125, 2010.

[281] Y. Duan *et al.*, “Shear-induced reorganization of renal proximal tubule cell actin cytoskeleton and apical junctional complexes,” *Proc. Natl. Acad. Sci.*, vol. 105, no. 32, pp. 11418–11423, 2008.

[282] P. D. Wilson, “Apico-basal polarity in polycystic kidney disease epithelia,” *Biochim. Biophys. Acta - Mol. Basis Dis.*, vol. 1812, no. 10, pp. 1239–1248, 2011.

[283] K. Geering, “Functional roles of Na,K-ATPase subunits,” *Curr. Opin. Nephrol. Hypertens.*, vol. 17, no. 5, pp. 526–532, 2008.

[284] N. Kanai, Y. Fujita, T. Kakuta, and A. Saito, “The Effects of Various Extracellular Matrices on Renal Cell Attachment to Polymer Surfaces During the Development of Bioartificial Renal Tubules,” 1999.

[285] E. M. Frohlich and J. L. Charest, “Microfabricated Kidney Tissue Models,” in *Microfluidic Cell Culture Systems*, 2nd ed., Elsevier Inc., 2012, pp. 279–302.

[286] H. Zhang, F. Tasnim, J. Y. Ying, and D. Zink, “The impact of extracellular matrix coatings on the performance of human renal cells applied in bioartificial kidneys,” *Biomaterials*, vol. 30, no. 15, pp. 2899–2911, May 2009.

[287] B. Zhang, A. Korolj, B. F. L. Lai, and M. Radisic, “Advances in organ-on-a-chip engineering,” *Nature Reviews Materials*, vol. 3, no. 8. Nature Publishing Group, pp. 257–278, 01-Aug-2018.

[288] X. Zhu *et al.*, “Arrays of horizontally-oriented mini-reservoirs generate steady microfluidic flows for continuous perfusion cell culture and gradient generation,” *Analyst*, vol. 129, no. 11, pp. 1026–1031, Nov. 2004.

[289] S. Eom and S. Lim, “Stretchable complementary split ring resonator (CSRR)-based radio frequency (RF) sensor for strain direction and level detection,” *Sensors (Switzerland)*, vol. 16, no. 10, Oct. 2016.

[290] N. Elia and J. Lippincott-schwartz, “Culturing Three Dimensional MDCK cells for Analyzing Intracellular Dynamics,” *Curr. Protoc. cell Biol.*, 2009.

[291] T. Roitbak, C. J. Ward, P. C. Harris, R. Bacallao, S. A. Ness, and A. Wandinger-Ness, “A Polycystin-1 Multiprotein Complex is Disrupted in Polycystic Kidney Disease Cells,” *Mol. Biol. Cell*, vol. 15, no. 3, pp. 1334–1346, Mar. 2004.

[292] S. Terryn, A. Ho, R. Beauwens, and O. Devuyst, “Fluid transport and cystogenesis in autosomal dominant polycystic kidney disease,” *Biochim. Biophys. Acta - Mol. Basis Dis.*, vol. 1812, no. 10, pp. 1314–1321, 2011.

[293] B. C. Low, C. Q. Pan, G. V. Shivashankar, A. Bershadsky, M. Sudol, and M. Sheetz, “YAP/TAZ as mechanosensors and mechanotransducers in regulating organ size and tumor growth,” *FEBS Lett.*, vol. 588, no. 16, pp. 2663–2670, 2014.

[294] Y. Huang *et al.*, “Integrin-YAP/TAZ-JNK cascade mediates atheroprotective effect of unidirectional shear flow,” *Nature*, vol. 540, no. 7634, pp. 579–582, 2016.

[295] C. A. Rankin, K. Suzutu, D. M. Ziemer, J. J. Grantham, J. P. Calvet, and H. Nagase, “Matrix metalloproteinases and TIMPS in cultured C57BL/6J-cpk kidney tubules,” 1996.

[296] M. E. Dolega, M. Delarue, F. Ingremeau, J. Prost, A. Delon, and G. Cappello, “Cell-like pressure sensors reveal increase of mechanical stress towards the core of multicellular spheroids under compression,” *Nat. Commun.*, vol. 8, no. May 2016, pp. 1–9, 2017.